Optimizing Large Scale Particle Image Velocimetry using a Multi Camera System

Aiden Mallany-Stanley

Academic Advisors: Dr. Colin Rennie and Dr. Elizabeth Jamieson

A thesis submitted to the University of Ottawa
in partial fulfillment of the requirements for the
Master's of Applied Sciences in Civil Engineering

Department of Civil Engineering
Faculty of Engineering
University of Ottawa

uOttawa

Abstract

Hydrometric monitoring plays a vital role in Canada's environment. It is used for flood monitoring, climate change modelling, water resources engineering design and much more. Environment and Climate Change Canada (ECCC) operates over 2200 hydrometric stations across the country, collecting and publishing near real-time water level and discharge data. Discharge measurements are required to validate rating curves after major rainfall events and periodically throughout the year. Conventional methods can pose safety risks to hydrometric technologists in high flows. Additionally, in flashy streams at remote locations it is challenging to travel to the station in time to obtain the peak discharge. This is where methods such as image velocimetry could be used as an alternative to conventional methods.

Numerous surface velocimetry algorithms have been created and adapted for the field, one of which is large scale particle image velocimetry (LSPIV). LSPIV utilizes video recordings of a river surface to estimate the surface velocity field, based on a cross-correlation technique that identifies the displacement between subsequent image frames of surface roughness or scatterers within individual interrogation areas (IA). This study aimed to tackle challenges of both LSPIV and stereoscopic LSPIV.

A novel multi-camera LSPIV method was created by combining the best portions of the surface velocity field obtained by each camera. The channel was split in the middle and the portions of the surface velocity field for each half of the channel obtained from the respective adjacent camera were retained and then combined across the cross-section. Single camera LSPIV had absolute percent differences of 11.73%, 26.41%, and 21.05% for the gauge house camera, left bank (bridge) camera and right bank (bridge) camera, respectively, compared to ADCP measurements. The multi-camera method resulted in an improvement compared to the best single camera estimates in four of five surveys and had an absolute average difference of 8.19% compared to the ADCP. The results also reinforced the importance of surface texture and environmental conditions in LSPIV analysis.

Acknowledgements

First off, I would like to thank my two supervisors: Dr. Colin Rennie and Dr. Elizabeth Jamieson for accepting me as their Master's student. Dr. Rennie's curiosity and encouragement pushed me to look for creative solutions whenever I hit a roadblock. Dr. Jamieson's meticulous feedback was extremely beneficial when articulating my results and improving the overall communication of this thesis. I am also super thankful for the opportunity to work with ECCC. It was a very rewarding experience to be able to work in collaboration with them on such an exciting project and I am very grateful for that.

Next, I am grateful for the support I received at the University of Ottawa. Qingcheng Yu for always being so willing to help. Xiatong Cai for his suggestions and assistance with field work. Mark Lapointe for his expertise in the laboratory and Saber Ansari for getting this project rolling and his help throughout the study.

There are so many people at ECCC who have assisted me during this study. I am especially thankful to James Bomhof, I could not have had the Castor field site running smoothly without him from the camera installation to his assistance on a variety of challenges I dealt with during this research. Alain Goulet and Eugene Pripa for their help with maintenance and field surveys. I also would like to thank all of my professors both at the University of Ottawa and the University of Guelph where I completed my undergraduate studies. I would not be here today without the support and guidance of many of them, and I am thankful for their mentorship over the years.

Finally, I want to thank my family. My parents Robert and Darcy for always supporting and encouraging me to get me to this point. Thank you to Avery, for being a supportive little sister. Lastly, I would like to thank my wonderful girlfriend Madeline for her support throughout this process.

Contents

Abstract ii
Acknowledgements iii
List of Figures viii
List of Tables xii
List of Equations xiii
Symbols and Abbreviations xiv
1.0 Introduction 1
1.1 Image Velocimetry Techniques 4
1.1.1 Stereoscopic Image Velocimetry 5
1.2 Problem Statement 6
1.3 Objectives 7
1.4 Contributions and Novelty of the Study 8
1.5 Outline 9
2.0 Literature Review 9
2.1 Discharge Measurements 9
2.2 Image Velocimetry 12
2.2.3 Stereoscopic Image Velocimetry 17
2.2.4 Environmental Conditions 18
2.2.6 Camera Characteristics 20
2.2.7 Image Rectification 24
2.2.8 Image Processing 27
3.0 Experimental Methods 32
3.1 Castor River 32
3.1.1 Data Collection 34
3.1.1.2 May 5th, 2023 38
3.1.1.3 May 15th 2024 39
3.1.1.1 ECCC Surveys 40
3.2 Black Canyon Laboratory Experiment 40
3.2.1 Model Creation & Installation 40
3.2.2 Data Collection 42
3.2.2.1 Equipment 43
3.2.2.2 Video Collection 45

3.2.2.3 ADV Velocity Measurements 46
3.2.3.5 Tracer Particles 47
3.3 Multi-Camera LSPIV Processing 50
3.3.1 Camera Calibration 51
3.3.2 Rectification of Image Velocimetry Results (RIVeR) 53
3.3.2.1 Video Input & Image Extraction 54
3.3.2.1 PIVLab 56
3.3.2.3 Image Rectification 57
3.3.2.4 Discharge Computation 59
3.3.2.4.1 Determination of Alpha 61
3.4 Matlab Processing 62
3.4.1 Velocity Difference Code 62
3.4.2 Distance Made Good Code 64
3.4.3 ADCP Variance Code 65
3.4.4 Discharge Optimization Code 66
3.5 Stereoscopic LSPIV Processing 67
3.5.1 Surface Reconstruction 67
3.5.2 Standard Image Velocimetry Processing 69
4.0 Results 70
4.1 Multi-Camera LSPIV 70
4.1.1 Castor River Field Site 70
4.1.1.2 March 18th, 2022 71
4.1.1.3 March 21st, 2022 75
4.1.1.4 April 8th, 2022 81
4.1.1.5 May 5th, 2022 85
4.1.1.6 May 5th, 2023 88
4.1.1.7 March 6th, 2024 97
4.1.1.8 May 15th, 2024 102
4.1.1.9 Combined Discharge Results 117
4.1.1.10 Summary of Surveys 117
4.2 Stereoscopic Image Velocimetry Results 118
4.2.1 Castor River Field Site 118
4.2.2 Black Canyon Lab Model 121

5.0 Discussion 123
5.1 Multi-Camera LSPIV 123
Limitations 141
Integration into ECCC hydrometric network 141
5.2 Stereoscopic Image Velocimetry 142
5.4 Future Work & Recommendations 144
5.4.1 Recommendations for Multi-Camera Systems 144
5.4.2 Recommendations for Stereoscopic Image Velocimetry Systems 144
6.0 Conclusion 145
References 148
Appendices 154
Appendix A – Combined Camera Calculations 154
March 21st, 2022 154
April 8th, 2022 155
May 5th, 2023 156
March 6th, 2024 157
May 15th, 2024 158
Appendix B – Velocity Difference Plots 159
March 18th, 2022 159
March 21st, 2022 162
April 8th, 2022 164
May 5th, 2022 166
May 5th, 2023 169
March 6th, 2024 171
May 15th, 2024 173
Appendix C – Normalized Velocity Difference Plots 184
March 18th, 2022 184
March 21st, 2022 185
April 8th, 2022 185
May 5th, 2022 186
March 6th, 2024 186
May 15th, 2024 186
Appendix D – Velocity Vector Plots 192

March 18th, 2022 192
March 21st, 2022 194
April 8th, 2022 195
May 5th, 2022 196
May 5th, 2023 198
March 6th, 2024 201
May 15th, 2024 202
Appendix E – Other Plots & MATLAB Scripts 212
Velocity Difference Code 216
Combining Discharge Code 236
Vector Plots Code 241
Distance Made Good Code 245
ADCP Variance Code 246

List of Figures

Figure 1: Water Survey of Canada (WSC) Hydrometric Monitoring Network Map (Environment and Climate Change Canada, 2022b) 2
Figure 2: Illustration displaying ADCP Operation (D. Mueller et al., 2013) 10
Figure 3: Rating Curve Example from Perks., 2020 KLT paper where the dashed lines represent a 95% confidence interval, the black circles represent fixed camera KLT-IV measurements, and the red crosses are UAV KLT-IV measurements 12
Figure 4: Example of STIV Processing of the Uono River (Fujita et al., 2007) 14
Figure 5: ADCP vs IR-QIV velocities over a 20hr period (Schweitzer & Cowen, 2021). 16
Figure 6: Stereo Imaging Configuration on the Longxi River where 1 and 2 are the cameras used, 3 is the solar panel used to power the system and 4 is a box where additional equipment is stored (W. Li et al., 2019) 17
Figure 7: Effect of shadows and glare on surface velocity field (Hauet, Kruger, et al., 2008) 19
Figure 8: Typical pinhole camera model and explanation of focal length (Source: Mathworks.com, Accessed 15 Aug. 2024) 21
Figure 9: Different ways images are distorted radially (Source: Mathworks.com, Accessed 15 Aug. 2024) 22
Figure 10: MATLAB single camera calibrator application GUI (Source: Mathworks.com, Accessed 15 Aug. 2024) 22
Figure 11: Analysis of the number of Image pairs versus longitudinal velocity at varying image resolutions (Le Boursicaud et al., 2016) 24
Figure 12: Diagram displaying how ground sampling distance (GSD) is affected by an oblique camera angle (Jolley et al., 2021) 25
Figure 13: Castor River Ground Control Points Setup used for image rectification (Source: James Bomhof, National Hydrological Service, Environment and Climate Change Canada) 26
Figure 14: Example of CLAHE filtering (Kumar et al., 2019) 28
Figure 15: Analysis performed for ECCC displaying how varying video durations affect discharge estimates (Patalano, 2021) 29
Figure 16: Diagram displaying how cross-correlation methods are used to determine particle displacement between image frames (Muste et al., 2008) 30
Figure 17: Google maps image showing fastest route from the University of Ottawa to the Castor River field site ... 32
Figure 18: Castor River flow duration curve using average daily discharge values from the gauging station between 1968 and 2024 33
Figure 19: Left) Bridge cameras installation Top Right) Left bank field of view Bottom Right) Right bank field of view 34
Figure 20: Field of view from the camera mounted on top of the gaugehouse 34
Figure 21: LSPIV camera board setup (Source: James Bomhof, National Hydrological Service, Environment and Climate Change Canada) 36
Figure 22: Ground Control Points and the corresponding surveyed cross-sections at the Castor River from the view of the Gaugehouse Camera. Flow is from right to left. 37
Figure 23: Author and supervisors performing an ADCP zig zag survey from May 5th, 2023 39
Figure 24: Upstream end of the canyon model facing downstream 42
Figure 25: Left) Region of Interest (ROI) in the Black Canyon (Ansari et al., 2018) Right) NADIR view of ROI in lab model 42
Figure 26: Ground Control Points in the section of interest for the canyon model 43
Figure 27: Camera Setups for the canyon model. Left) Stereolabs 2i camera on an adjustable tripod. Right) Acti A310 cameras on adjustable mount 44
Figure 28: Sidelooker and downlooker ADV probes where the right side displays the location of where the four beams intersect to obtain velocities. This is known as the sampling volume. 45

Figure 29: Approximate locations of the ADV sampling, where the black ticks represent the location of each vertical profile sampled and the red lines indicate the cross-section. Spacings of 2cm were used for the near surface measurements which were performed at all red lines. *46*
Figure 30: Multi-Camera LSPIV Workflow Diagram *50*
Figure 31: Calibration checkerboard sitting in laboratory flume *52*
Figure 32: MATLAB Stereoscopic camera calibrator app *52*
Figure 33: Distortion corrected image pair in MATLAB *53*
Figure 34: RIVeR flowchart (Patalano et al., 2017) *54*
Figure 35: Image extraction window in RIVeR from an AXIS camera recording of the Castor River *55*
Figure 36: User-defined region of interest with masked banks for a left bank video at the Castor River *56*
Figure 37: Example of an image frame with the CLAHE pre-processing filter applied *57*
Figure 38: Imported ground control points marked on an image of the Castor River *58*
Figure 39: Left) Median magnitude field of a video at the Castor River produced in RIVeR. Right) Median vector field from the same Castor River video processed through RIVeR. The scale bar unit is in meters. *59*
Figure 40: AreaComp2 GUI after determining discharge of a cross-section *60*
Figure 41: Left) Discharge at the cross-section broken up into verticals. The colour scale represents the percentage of discharge contained in each panel. Right) Verticals shown as velocity vectors on the rectified median image *61*
Figure 42: Discharge vs Alpha at the Castor River from several surveys *61*
Figure 43: Stereoscopic LSPIV Workflow Diagram *67*
Figure 44: Reconstructed point cloud from the Stereolabs camera at the Castor River. The black object represents the camera location along the right bank *68*
Figure 45: Normalized velocity differences between Top) Left and right bank cameras Middle) Gaugehouse camera and right bank camera Bottom) Gaugehouse camera and left bank camera *73*
Figure 46: Normalized velocity differences between Top) Drone (DJI0018) and left bank camera Bottom) Drone (DJI0018) and right bank camera *74*
Figure 47: Left bank camera vs gaugehouse camera vector plot zoomed into the right bank for March 18th, 2022 survey *75*
Figure 48: Normalized velocity difference plots Top) Left bank vs right bank camera Middle) Gaugehouse vs right bank camera Bottom) Gaugehouse vs left bank camera *76*
Figure 49: Top) Right bank vs Gaugehouse camera vector plot Bottom) Frame showing glare from sunlight that impacted the surface texture near the left bank *77*
Figure 50: ADCP versus camera velocity differences Top) Left bank camera comparison Bottom) Right bank camera comparison *78*
Figure 51: Distance versus velocity difference to the ADCP scatterplots Top) Left bank camera Middle) Right bank camera Bottom) Gaugehouse Camera *80*
Figure 52: Normalized velocity differences Top) Left bank versus right bank cameras Middle) Gaugehouse camera versus left bank camera Bottom) Gaugehouse camera versus right bank camera *81*
Figure 53: Zoomed in vector plots displaying the surface velocity differences near the banks for the April 8th, 2022 survey: Left) Zoomed into left bank. Right) Zoomed into right bank *82*
Figure 54: ADCP versus camera velocity differences Top) Left bank vs ADCP Bottom) Right bank vs ADCP *83*
Figure 55: Distance to camera versus velocity differences to ADCP Top) Left bank camera Middle) Right bank camera Bottom) Gaugehouse camera *84*
Figure 56: Normalized velocity differences Top) Right vs left bank camera Middle) Gaugehouse vs left bank camera Bottom) Gaugehouse vs right bank camera *85*
Figure 57: Velocity difference plots comparing drone camera to fixed cameras Top) Left bank camera vs Drone Bottom) Right bank camera vs Drone *86*
Figure 58: Example of Empty PIV vector field in PIVLab where the blue box represents the area being processed and the red indicates areas that have been masked out *87*

Figure 59: Normalized velocity difference plots Top) Left bank vs right bank camera Middle) Gaugehouse vs left bank camera Bottom) Gaugehouse vs right bank camera *89*
Figure 60: ADCP versus camera comparisons Top) Left bank camera versus ADCP Middle) Right bank camera versus ADCP Bottom) Gaugehouse camera versus ADCP *90*
Figure 61: Distance vs Velocity Differences to the ADCP Scatterplots for May 5th, 2023 Top) Left bank camera Middle) Right bank camera Bottom) Gaugehouse camera *92*
Figure 62: Velocity difference plots between left and right bank cameras with varying sensitivities Top Left) 0.25m maximum distance threshold Top Right) 0.5m maximum distance threshold Bottom Left) 0.75m maximum distance threshold Bottom Right) 1.0m maximum distance threshold *94*
Figure 63: Velocity difference plots between right bank camera and single ping ADCP data Top Left) 0.25m maximum distance threshold Top Right) 0.5m maximum distance threshold Bottom Left) 0.75m maximum distance threshold Bottom Right) 1.0m maximum distance threshold *96*
Figure 64: Velocity difference plots between left bank camera and 5-ping boxcar average ADCP data Top Left) 0.25m maximum distance threshold Top Right) 0.5m maximum distance threshold Bottom Left) 0.75m maximum distance threshold Bottom Right) 1.0m maximum distance threshold *96*
Figure 65: Normalized velocity differences between cameras for March 6th, 2024 survey Top) Right bank vs left bank camera Middle) Gaugehouse vs right bank camera Bottom) Gaugehouse vs left bank camera *98*
Figure 66: Top) Left bank vs right bank camera vector plot zoomed in towards left bank. Bottom) Frame from left bank camera showing lack of surface texture along the left bank caused by glare *99*
Figure 67: Camera surface velocity differences compared to the ADCP Top) Right bank camera vs ADCP Bottom) Gaugehouse camera vs ADCP *100*
Figure 68: Distance to the camera versus velocity difference compared to the ADCP for March 6th, 2024 Top) Gaugehouse camera vs ADCP Bottom) Right bank camera vs ADCP *102*
Figure 69: Surface velocity differences between cameras Top) Left bank vs right bank camera Middle) Gaugehouse vs left bank camera Bottom) Gaugehouse vs right bank camera *103*
Figure 70: Surface velocity differences between cameras and ADCP measurements Top) Gaugehouse camera vs ADCP Middle) Left bank camera vs ADCP Bottom) Right bank camera vs ADCP *104*
Figure 71: Velocity differences for DJI054 Top) Frame showing FOV from drone Top Middle) Drone vs ADCP Bottom Middle) Drone vs right bank camera Bottom) Drone vs left bank camera *106*
Figure 72: Zoomed in velocity vector plots showing near-bank surface velocity estimates between bridge cameras and drone estimates Top) Left bank camera zoomed in on the right bank Bottom) Right bank camera zoomed in on left bank *107*
Figure 73: Velocity differences for DJI055 Top) Frame showing FOV from drone Middle) Drone vs right bank camera Bottom) Drone vs left bank camera *108*
Figure 74: Velocity differences for DJI057 Top) Frame showing FOV from drone Middle) Drone vs right bank camera Bottom) Drone vs left bank camera *109*
Figure 75: Velocity differences for DJI058 Top) Frame showing FOV from drone Top Middle) Drone vs ADCP Bottom Middle) Drone vs right bank camera Bottom) Drone vs left bank camera *110*
Figure 76: Distance to camera versus velocity differences to ADCP: Top) Gaugehouse camera. Middle) Left bank camera. Bottom) Right bank camera *112*
Figure 77: All surveys combined distance to drone versus surface velocity differences plot between drone image velocimetry and ADCP *113*
Figure 78: Boxplot of ADCP variance between transects *115*
Figure 79: Depth image of the Castor River taken on the right bank *119*
Figure 80: Snapshot of reconstructed point cloud of the Castor River collected from the right bank *119*
Figure 81: .png nadir image of the Castor River taken from the right bank video converted from .ply *120*
Figure 82: RIVeR median frame from converted point clouds test *120*
Figure 83: Surface reconstruction of the canyon lab model *121*
Figure 84: Nadir view of canyon reconstructed point cloud converted to image file *122*

Figure 85: Median frame of point cloud image files processed in RIVeR 122
Figure 86: Near-surface ADV data overlayed on Black Canyon 122
Figure 87: May 5th, 2023 left bank vs right bank camera vector plot. Left) Zoomed in on the left bank Right) Zoomed in on the right bank..... 123
Figure 88: May 5th, 2023 left bank vs gaugehouse camera zoomed in on the right bank 124
Figure 89: Distortion still affecting images post-distortion correction in the left bank camera..... 125
Figure 90: Individual Camera Frames from May 15th, 2024 Survey. Top Left) DJI_054 Top Right) DJI_055 Middle Left) DJI_056 Middle Right) DJI_057 Bottom Left) DJI_058 Bottom Right) DJI_059..... 127
Figure 91: May 5th drone median velocity comparisons extracted from RIVeR where the top left is associated with the bottom left frame and the top right is associated with the bottom right frame. The velocity results near the power lines have been excluded. 128
Figure 92: Streamwise surface velocity plots across cross-section 2 for March 21st and April 8th, 2022 surveys where x=0m is the location of the upper ground control point (GCP05) on the left bank of the channel. Note that the ADCP data from April 8th was plotted using a five-point moving average while the other surveys used a five-ping boxcar average to reduce noise..... 133
Figure 93: Streamwise surface velocity plots across cross-section 2 for May 15th, 2024 survey where x=0m is the location of the upper ground control point (GCP05) on the left bank of the channel. Note that the ADCP data from April 8th was plotted using a five-point moving average while the other surveys used a five-ping boxcar average to reduce noise..... 134
Figure 94: Results of poor surface texture from March 21st, 2022 survey. A) Vector plot comparing ADCP to the gaugehouse camera B) Field of view from camera with red box highlighting approximate area of poor surface texture 136
Figure 95: Result of poor surface texture from March 6th, 2024 survey. A) Vector plot zoomed in on the left bank comparing right bank camera to the left bank camera B) Field of view from camera with red box highlighting approximate area of poor surface texture..... 137
Figure 96: Distance to the camera versus velocity differences to the ADCP with all surveys combined Top) Gaugehouse camera Middle) Left bank camera Bottom) Right bank camera..... 139
Figure 97: Image pairs of the original stereo image (Top) and the rectified pair (Bottom) from Li et al., 2019 142
Figure 98: Reconstructed 3D Point Cloud of the Canyon Model created with the Stereolabs ZED2i Camera displaying how tracer particles are stretched from the water surface to the canyon bed..... 143

List of Tables

Table 1: Summary table of image velocimetry variations *4*
Table 2: AXIS P1378-LE camera key specifications (Source: Axis.com, Accessed 15 Aug 2024) *35*
Table 3: Key ADCP specifications for the different models used in the Castor River (Sontek, n.d.; Teledyne Marine, 2006, 2023; USGS, n.d.) *38*
Table 4: Stereolabs ZED2i camera specifications (Source: Stereolabs.com, Accessed 15 Aug 2024) *38*
Table 5: ACTi A310 Camera Specifications (ACTi Corporation, n.d.) *44*
Table 6: Tracer particles tested and results for various criteria employed *49*
Table 7: ADCP data used to normalize velocity difference plots. Discharge was taken from either the ADCP or gauge station. Gauge station discharge is denoted with a bracketed G next to the value. Wetted Area was taken from RIVeR and Mean velocity was found by dividing the discharge by wetted area. Alpha was found using the plot previously shown in 3.3.2.4.1 Determination of Alpha. Average Surface Velocity was computed by dividing the mean velocity by the average surface velocity. *71*
Table 8: Mean absolute errors (MAE) of surface velocities between methods for March 18th, 2022 Survey *75*
Table 9: Mean Absolute Error (MAE) of the surface velocity differences between methods for March 21st, 2022 survey *79*
Table 10: Mean Absolute Error (MAE) of surface velocity differences between methods for surface velocity comparisons *83*
Table 11: Mean absolute error (MAE) of the surface velocity differences of the camera comparisons for the May 5th, 2022 survey *87*
Table 12: Easting and Northing Velocity Differences between varying PIVLab median frames *88*
Table 13: Mean absolute error (MAE) of the surface velocity differences between methods for the May 5th, 2023 survey *91*
Table 14: Sensitivity analysis of the maximum allowable distance between two points to be used for a velocity comparison between the left and right bank cameras. Mean absolute error being one of the two ways used to evaluate the thresholds *94*
Table 15: Sensitivity analysis of the maximum allowable distance between a camera surface velocity vector and the closest ADCP near-surface velocity measurement looking at both single ping ADCP and 5 ping boxcar average ADCP data *95*
Table 16: Mean absolute error of the surface velocity differences between methods for the March 6th, 2024 survey *101*
Table 17: Mean absolute errors (MAE) of the surface velocity differences between methods for the May 15th, 2024 survey *105*
Table 18: Mean Absolute Error (m/s) in velocity difference for May 15th drone videos *111*
Table 19: Mean Absolute Error (m/s) between ADCP Transects *114*
Table 20: Mean Absolute Error (m/s) between ADCP Transects without outliers shown in Figure 77 ..... *115*
Table 21: Difference (m/s) between near-surface FlowTracker2 velocity magnitudes vs ADCP (Top 2 bins) velocity magnitudes *116*
Table 22: Summary of Relative Error between Combined Camera Discharge and ADCP Discharge *117*
Table 23: Summary of MAE of velocity differences between fixed cameras and ADCP data for all survey dates *118*
Table 24: Estimated single camera LSPIV Discharge from May 15th, 2024 Drone Videos *126*
Table 25: Comparison of best single camera discharge (m^3/s) and combined camera discharge (m^3/s) to the ADCP (m^3/s) *129*
Table 26: Difference between ADCP discharge and gauge station discharge *129*
Table 27: Percent Difference Comparison of Multi-Camera LSPIV, Gauge station discharge, and ADCP discharge *130*
Table 28: Discharge (m^3/s) from each LSPIV setup and absolute percent difference to the ADCP for each camera *131*
Table 29: Comparison of methods in computation of single camera discharge (m^3/s) from May 5th 2023 survey *135*

List of Equations

Equation 1: Lucas-Kanade Equation *15*
Equation 2: Camera intrinsic parameters matrix *20*
Equation 3: Ground Sampling Distance *24*
Equation 4: 3D Orthorectification matrix *26*
Equation 5: 2D Orthorectification *27*
Equation 6: Black Canyon model discharge scaling equation *41*
Equation 7: Distortion correction equation used by RIVeR (Patalano et al., 2017) *55*
Equation 8: Distance between two points *62*
Equation 9: Velocity magnitude difference equation *63*
Equation 10: Distance equation in 3-dimensions *63*
Equation 11: Rotation Equations *64*
Equation 12: Difference between actual coordinates and rotated coordinates broken into x and y components *64*
Equation 13: Rotation equations where all y-values = 0 ..... *65*
Equation 14: WinRiver discharge interpolation method (Teledyne RD Instruments, 2021) *66*
Equation 15: Standard error of the mean *114*

Symbols and Abbreviations

ADCP – Acoustic Doppler Current Profiler

ADV – Acoustic Doppler Velocimeter

ECCC – Environment and Climate Change Canada

EDF – Électricité de France

DCC – Direct Cross Correlation

DFT – Direct Fourier Transform

FOV – Field of View

GCPs – Ground Control Points

GSD – Ground Sampling Distance

IA/IW – Interrogation Area/Interrogation Window

IMU – Inertial Measurement Unit

LiDAR – Light Detection and Ranging

LSPIV – Large Scale Particle Image Velocimetry

MAE – Mean Absolute Error

MAPE – Mean Absolute Percentage Error

OTV – Optical Tracking Velocimetry

PIV – Particle Image Velocimetry

POE – Power-Over-Ethernet

PTV – Particle Tracking Velocimetry

RIVeR – Rectification of Image Velocimetry Results

RMSE – Root Mean Square Error

ROI – Region of Interest

RPi – Raspberry Pi

SfM – Structure for Motion

STIV – Space Time Image Velocimetry

TIR-IV – Thermal Infrared Image Velocimetry

USGS – United States Geological Survey

UAVs – Unmanned Aerial Vehicle

WSC – Water Survey of Canada

1.0 Introduction

Hydrometric monitoring is crucial in water resources engineering, particularly in Canada with it's abundance of available freshwater. It is vital for flood monitoring and forecasting and water resources management to protect public infrastructure and safety. Discharge measurements are a routine task of hydrometric monitoring, essential for maintaining rating curves used for discharge estimation from water levels. Additionally, as climate change continues to have a greater impact on watersheds throughout Canada, accurate discharge measurements are required to help model the changing climate as well as influence policymaking.

Conventional discharge measurements have been proven to be effective and have allowed for extensive stream gauging networks to be established throughout Canada and other countries. Environment and Climate Change Canada (ECCC) operates a real-time monitoring network with over 2100 operational sites (Figure 1) with data that is publicly available on their website (Environment and Climate Change Canada, 2022a). Additionally, many conservation authorities in Ontario have their own smaller gauging networks with publicly available data (e.g., https://trcagauging.ca/, https://mvc.on.ca/water-levels/). Most discharge measurements are presently made with direct contact methods using velocimetry instruments such as acoustic Doppler current profilers (ADCPs), acoustic Doppler velocimeters (ADVs), and conventional propeller current meters. While these measurement methods are generally reliable, they can be very labour intensive and can be quite expensive. Additionally, most methods require the operator to work in or around the river, and there are scenarios where this may not be possible or safe, so other (non-contact) methods may be better suited for accurate discharge measurements. Emerging technologies have led to the development of effective innovative non-contact methods to help fill the gap left by conventional methods. Image velocimetry is one such non-contact method.

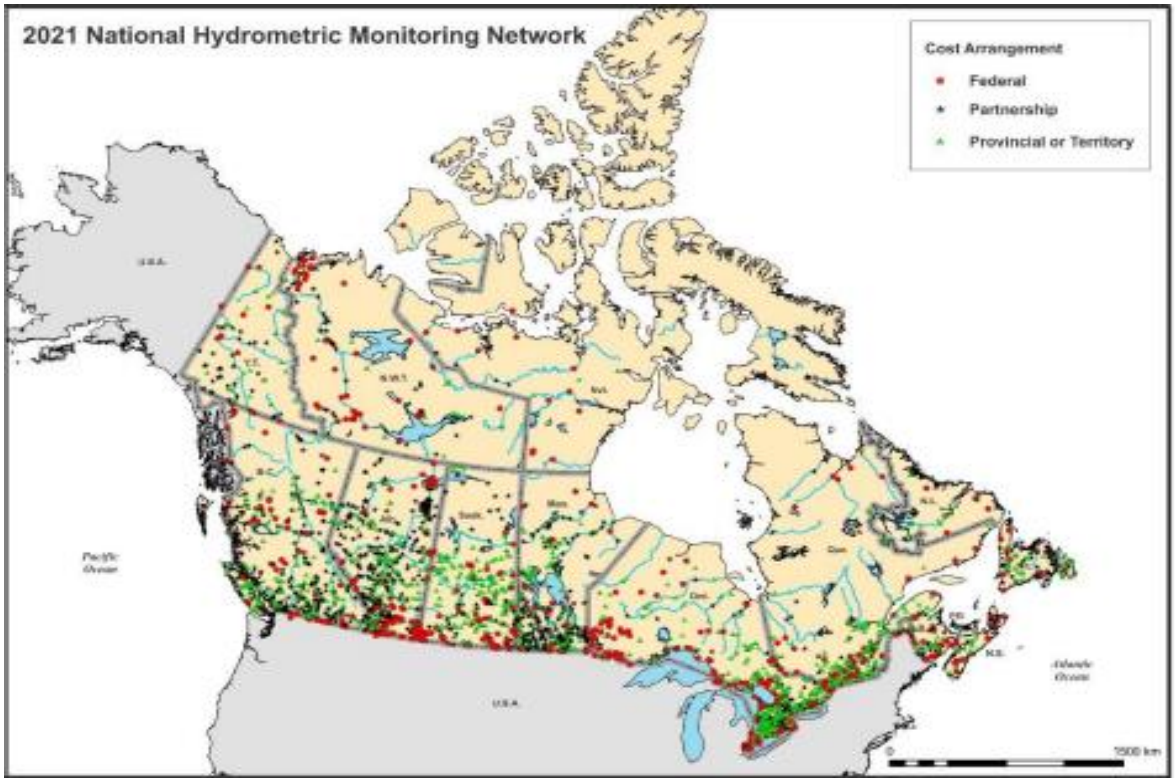

Figure 1: Water Survey of Canada (WSC) Hydrometric Monitoring Network Map (Environment and Climate Change Canada, 2022b)

Remote sensing and non-contact approaches have given engineers and researchers the ability to manage water resources in new ways and in larger-scales than previously before – both spatially and temporally. For example, Light Detection and Ranging (LiDAR) uses light in the form of pulsed lasers to measure distance from an aerial vehicle such as an unmanned aerial vehicle (UAV) to a target object. Bathymetric LiDAR can be used to reconstruct channel bathymetry, while topographic LiDAR can reconstruct surrounding floodplains. This data can be used to create river models to assist in understanding large channels and watersheds with high resolution and accuracy (B. Li et al., 2021). Meanwhile, advancements in commercial drone technology and optical camera technology in terms of product quality and lowered cost has led to techniques like Structure-from-Motion (SfM) and image velocimetry. SfM is a photogrammetric technique where information is extracted from overlapping images for mapping purposes. A moving camera records video to reconstruct a 3-dimensional model of the area imaged by matching coordinates between image frames to stitch them together. It has been successfully used as a low-cost system to create high resolution digital elevation models (DEMs) and for measuring bathymetry in

shallow clear water channels (Westoby et al., 2012; Zhang et al., 2022). Similarly, image velocimetry is a non-intrusive technique used for smaller-scale stream gauging while still operating at a larger spatial and temporal scale than conventional stream gauging techniques. With fixed cameras, discharge can be captured over extended periods of time compared to conventional methods where a hydrometric technologist must be on site. Spatially, image velocimetry can capture surface velocity for the entirety of the channel in the field of view (FOV), rather than a single cross-section which is typically how a conventional method is taken. It was adapted to the field from lab experiments in the late 1990's (Fujita et al., 1998). Since then, it has become a popular research area in water resources engineering with the number of annual papers published increasing from 2 in 2000 to nearly 200 in 2020 (Jolley et al., 2021). Image velocimetry has been used both for surface velocity and discharge estimations. Several different image velocimetry techniques have been developed, as summarized in Table 1.(Fujita et al., 2007; Jolley et al., 2021; Li et al., 2019; Muste et al., 2008; Tauro et al., 2018).

This thesis explores one of the emerging non-contact surface image velocimetry techniques that has been developed in the past couple decades; Large Scale Particle Image Velocimetry (LSPIV). In particular, this thesis examines how different camera angles and set ups at a field site affect the derived surface velocity distribution, and how to best optimize a multi-camera image velocimetry system in order to improve the accuracy of LSPIV.

1.1 Image Velocimetry Techniques

Since Image Velocimetry was first introduced in the 1990's it has been adapted into several different variations, some of which are summarized in Table 1.

Table 1: Summary table of image velocimetry variations

Image Velocimetry Subcategory	Description
Particle Tracking Velocimetry (PTV)/Large-Scale PTV (Adrian, 1991)	Tracks individual particles through a Lagrangian frame of reference by locating the centroid of each particle in subsequent image frames to determine the trajectory of each particle. Requires less surface texture compared to PIV.
Particle Image Velocimetry (PIV)/Large-Scale PIV (Fujita et al., 1998)	Uses cross-correlation algorithms to determine the most likely displacement of surface particles between successive image frames within individual interrogation areas to calculate instantaneous surface velocity flow fields. This method requires tracer particles to cover a sufficient portion of the river.
Space Time Image Velocimetry (STIV) (Fujita et al., 2007)	Creates space-time images (STIs) from change in brightness variation over time following a user defined search line. Each search line resolves an average velocity of that line. Requires colour variation along the surface as the water surfaces moves and only produces streamwise velocities.
Thermal Infrared LSPIV (TIR-IV) (Eltner, Mader, et al., 2021)	Utilizes differences in water surface-air surface temperatures in tandem with conventional PIV processing.
Optical Flow Tracking Velocimetry (OTV) (Tauro et al., 2018)	Uses the Lucas-Kanade algorithm for feature detection and trajectory-based filters to determine the most likely displacement of particles. Length, angle and maximum number of trajectories are all user defined parameters.

This thesis focuses on PIV/LSPIV. Initially developed for lab experiments, it was eventually adapted for field work (Fujita et al., 1998). Individual image frames are extracted from videos where each frame is further subdivided into interrogation areas (IA). Then using cross-correlation algorithms, tracer particles or texture variations on the water surface are tracked through IAs between image frames to determine the most likely displacement of the water surface to resolve a 2-dimensional flow field.

Environmental conditions like wind, inconsistent surface texture and sunlight/glare can make setting up LSPIV field sites very challenging as different locations are very unique and they generally do not have the idealized controlled conditions of laboratory experiments.

One key challenge in LSPIV is finding a suitable location for fixed cameras. A NADIR view of the river is ideal, but bridges are not always available where needed and in some cases the bridges may be too low for a camera to capture the full width of the river in the field of view (FOV), which is necessary in order to see ground control points (GCPs) to rectify images and to compute discharge of a full cross-section. One solution to this challenge is through the use of unmanned aerial vehicles (UAVs) for capturing NADIR videos; however, there are still locations where foliage or public infrastructure such as power lines can obstruct the FOV, and negatively impact results. Cameras can also be mounted on channel banks at oblique angles; however, as an object gets further away from a camera lens the pixel size of that object changes resulting in less detail. Therefore, the far shore of the channel could yield lower accuracy surface velocimetry results than the near shore.

This study assesses the implementation of a second camera on the opposite shore and combines the results of the two to optimize and increase accuracy of LSPIV in the field.

1.1.1 Stereoscopic Image Velocimetry

Stereoscopic image velocimetry techniques have been developed to use two cameras to generate three-dimensional (3D) surfaces for image velocimetry, although there has been significantly less research than single camera techniques. Stereoscopic image velocimetry could possibly obtain surface velocity in 3D by using multiple cameras focused on the same area of interest. Using epipolar geometry and known real-world coordinates the image coordinates

between the cameras can be matched and a three-dimensional surface can be reconstructed. The most current research to date has been able to reconstruct a 3D point cloud and project that point cloud onto a 2D surface to obtain surface velocities (W. Li et al., 2019). In addition to the multi-camera LSPIV system, this thesis also documents an attempt in the present research to develop Stereoscopic-LSPIV in both field and lab settings.

1.2 Problem Statement

Conventional discharge measurement techniques have proven to be effective. In Canada's National Hydrometric Program (Water Survey of Canada), hydroacoustic instruments are used for the majority of discharge measurements, with over 90% of measurements obtained using ADCPs and ADVs (Personal Communication, Elizabeth Jamieson, Environment and Climate Change Canada, 2024). However, there are scenarios where non-contact methods may be a more suitable choice. A drawback of conventional methods is they require site visits and an instrument to be placed in the flow field. In flashy streams such as concrete flood control channels the change in water levels can be so rapid that technologists are unable to get to the gauging location in time to obtain peak flows. Additionally, technologists typically oversee multiple locations resulting in prioritizing some locations over others. Field visits can be very time-consuming from driving to the location and setting up equipment (particularly with ADCP setup) before data collection.

High flows are also major safety risks to technologists. This removes the ability to use ADVs because wading measurements become hazardous. Even ADCP measurements may not be feasible in peak flows if velocities are too fast to be accessible by boat. ADCPs can be used in relatively high flows but are prone to error from waves, turbulence and moving channel beds.

The use of rating curves for continuous discharge monitoring also presents some key challenges, particularly for measuring high flows. Standard rating curves operate on a stage-discharge relationship. They are developed by hydrometric technologists taking several stage (water level) and discharge measurements to develop a relation curve. Then using sensors, such as a pressure sensor, water level is continuously measured, and the established rating curve is applied to estimate discharge. Inaccuracies in rating curves can occur at higher flows because hydrometric technologists are not always able to validate discharge in said scenarios which results

in the rating curve being extrapolated to estimate those flows. More inaccuracies can occur in rating curves when velocity profiles become more complex, for example in cases of backwater effect or partial ice cover. Additionally, establishing rating curves at new sites can be very expensive and time-consuming as hydrometric technologists must visit the site frequently at various flows to ensure an accurate rating curve is created.

Research has shown that image velocimetry can be a viable alternative for discharge monitoring in flood flows and at remote locations (Fujita & Kunita, 2011; Huang et al., 2018; Johnson & Cowen, 2016; Le Coz et al., 2010; W. Li et al., 2019). Another advantage of image velocimetry is videos do not have to be taken by trained technologists; any member of the public could take a video on their phone and send it off to be processed (Le Boursicaud et al., 2016). Lastly, a potential use case for image velocimetry is rapid rating curve development as fixed cameras could capture a range of flows over a smaller period of time than a hydrometric technologist (Bomhof et al., 2024).

There are challenges with image velocimetry techniques. As previously stated, an ideal setup would observe the water surface at a NADIR angle to obtain a uniform pixel size, however this is not always possible for permanent installations. Oblique camera angles result in a non-uniform pixel size distribution, and the pixels represent a larger area the further away from the camera they are. This has the potential to increase distortion as well as underestimate surface velocities near the far shore of the channel. A potential solution to this involves a multi-camera image velocimetry system with cameras installed on both banks. This solution is explored in detail throughout this thesis.

1.3 Objectives

The main objective for this thesis was to examine the surface velocity differences between four different camera setups through a field study to determine how camera angles can affect LSPIV measurements, to improve understanding of the process and optimize low-cost multi camera systems to be used as alternatives to conventional stream gauging techniques. Specifically, this research targets three key objectives.

1. Examine and quantify surface velocity differences in the field between four different camera set-ups; two synchronous oblique bridge cameras (one on either bank), one oblique view gaugehouse camera (elevated higher than the left bridge camera on the same bank, and synchronous with the bridge cameras) and a drone mounted camera.
2. Identify possible reasons for observed surface velocity differences between camera set ups.
3. Establish a method to combine surface velocity vector fields between synchronous optical cameras to both optimize image velocimetry performance for discharge monitoring at the field location. The intent is to develop a methodology that could be applied for surface velocimetry at other rivers and streams.

The research endeavour also included initial testing of multi-camera surface velocimetry setups in the laboratory, as well as an attempt to develop a procedure for stereoscopic surface velocimetry. These research activities will also be described in this thesis.

1.4 Contributions and Novelty of the Study

There has been some research involving optimal camera angles for fixed and mobile setups (Eltner et al., 2020; Perks, 2020). There are no studies that have examined the differences between multiple simultaneous or synchronous velocity fields computed from individual cameras stationed in different locations around the field of view (FOV).

This research enhances the understanding of how different parameters like camera angle and ground sampling distance (GSD) affect LSPIV accuracy compared to typically used techniques. This novel study compares surface velocity vectors spatially between cameras to investigate how to use multiple cameras to overcome known limitations to better measure surface velocity and estimate river discharge. The results from this study will enhance further research into LSPIV and assist researchers when attempting to establish LSPIV setups for stream gauging purposes.

1.5 Outline

This thesis document encompasses various chapters to better present the research and is briefly outlined in this section. Chapter 2 discusses previous literature related to both conventional discharge measurement methods and their uncertainty as well as various image velocimetry techniques. Chapter 3 details the methodology used for both the field study and laboratory experiments, including site setup, data collection, data validation and data processing methods. In Chapter 4, results from the research are presented and analyzed. Chapter 5 discusses the results and observations, as well as recommendations for further research. Chapter 6 concludes the study with a summary of the previous chapters. Lastly, the appendices contain figures illustrating results not presented in the main thesis and raw MATLAB code used for processing the data and other experimental data.

2.0 Literature Review

2.1 Discharge Measurements

Conventionally there are two main devices presently used for collecting discharge measurements: ADCPs and point velocity meters (such as mechanical current meters and ADVs). Both ADCPs and ADVs operate on the Doppler effect principle using acoustics. ADCPs operate with 3 or 4 transducers, sending out acoustic sound waves into the water column which reflect off suspended particles such as sediments and return to the receiver at a different frequency allowing for velocity to be determined through the water column (Figure 2). ADVs on the other hand measure the velocity in a specified (single) sampling volume, sending and receiving a sound signal via separate transducers (at a specific location and depth in the river). These devices each have their own unique method of deployment. ADCPs are typically deployed using a moving boat, such as a manned boat, tethered boat or remote-controlled boat (Environment and Climate Change Canada, 2021). ADVs are handheld devices that require hydrometric technologists to hold the device while wading in the water.

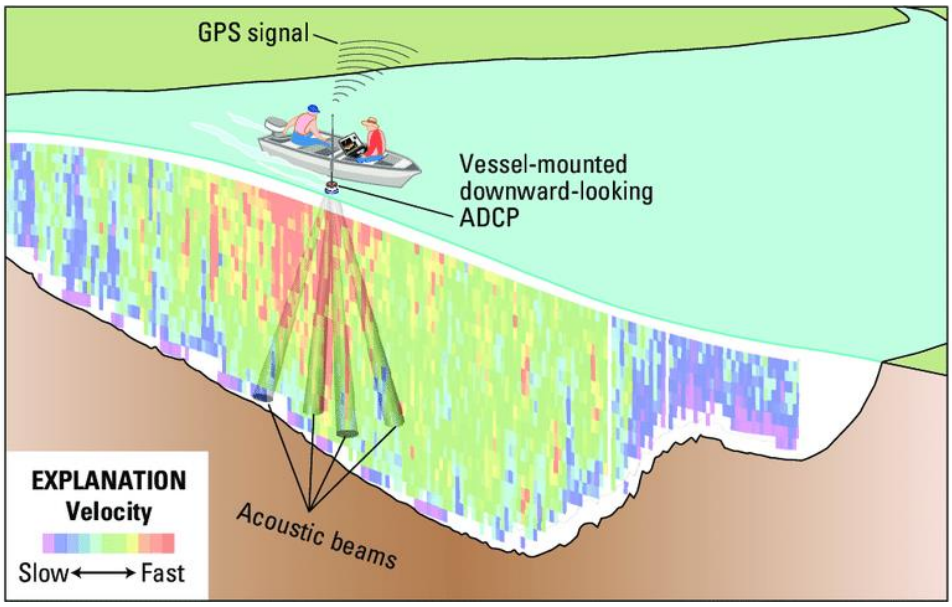

Figure 2: Illustration displaying ADCP Operation (D. Mueller et al., 2013)

These acoustic discharge measurement methods have some key advantages over previous methods such as mechanical current meters. ADCPs are capable of obtaining velocity at a much higher temporal and spatial resolution in significantly less time, they can obtain velocity measurements in wide channels at significant depths and have several deployment options such as cableway or boat. Additionally, they have other functions such as bathymetric reconstruction. Over recent decades the use of ADCPs and ADVs in hydrology has become incredibly common across the world (Aberle et al., 2017). Data from the World Meteorological Organization (WMO) shows that ADCP measurements increased by 11% from 2009 to 2014 (Le Coz, 2017). In 2014, the USGS (United States Geological Survey) performed over 37,000 ADCP measurements (31% of all discharge measurements that year) (Boldt & Oberg, 2015), the Électricitéde France (EDF) used ADCPs for 58% of their stream gauge measurements that year (Despax et al., 2016) and in Canada, ECCC performs over 90% of all discharge measurements with hydroacoustic instruments (ADCP and ADV) (Personal communication, Elizabeth Jamieson, Environment and Climate Change Canada, 2024).

Acoustic discharge methods are not without their limitations. They are expensive devices, can be time-consuming to calibrate prior to a survey, dangerous for hydrometric technologists in high flow conditions and there are unmeasurable areas in a water column (due to blanking and

side lobe interference). These unmeasurable zones include near the water surface, channel bed and channel banks. ADCPs struggle to measure near the surface for two reasons. The first is due to the transducer being submerged to a certain depth depending on the make and model of ADCP. The second is caused by the blanking zone. The blanking zone is the distance between the transducer face to the edge of the first measurement cell that is required to avoid vibrations caused by the signal transmission (D. Mueller et al., 2007; Muste et al., 2010) resulting in missing velocity data along the surface of a measurement area. Generally, the area near the streambed that cannot be measured is between 6-10% of the water depth (Gordon, 1989). Side lobes reflecting off the bed have greater signal strength than the main beam backscattered within the water column at the same range, which negatively biases near-bed velocity measurements (Gordon, 1989). ADCPs are capable of measuring discharge in streams ranging from depths of 0.5-60m (Despax et al., 2019), but they are unable to measure in anything shallower than that, which limits the use of ADCPs both in shallow streams and on shallow banks. Velocity must be extrapolated in these zones leading to uncertainties in the discharge. Despax et al., 2019, examined ADCP uncertainty using an ANOVA test[1] and found that the uncertainty for a single transect is ±6.9% while with 6 repeat transects, they found an uncertainty of ±5.7%. ADCP setup can also be time intensive due to systems tests such as compass calibration and moving bed tests. In high flows, ADCP deployment may not be feasible due to operator risks or the inability to deploy a moving boat. Additionally, in non-homogeneous conditions errors in velocity measurement can occur.

Rating curves are used to continuously estimate discharge. Rating curves are created by determining the stage-discharge relationship of the river. By measuring discharge at several different stages with ADCPs or ADVs, the points can be plotted, and a curve can be created to approximate flow for various stages in the river (Figure 3). Establishing a rating curve is site specific, requiring an extensive amount of time and manpower to ensure an accurate curve due to measurements being taken over an extended period of time. Often in high flows, hydroacoustic measurements are not possible due to safety risks. Additionally, in flashy channels

1 – An ANOVA or analysis of variance test is a statistical test used to analyze the difference between the means of two of more groups

or in remote locations it may not be possible to get to the station in time to obtain a discharge measurement at the peak of the high-water event. This results in extrapolating the rating curve

and can lead to significant errors in discharge as there is no way to validate these extrapolations (Johnson & Cowen, 2016). Furthermore, there can be cases of hysteresis[1], gaps in the curve where no validation measurements have been collected, backwater effects or partial ice cover that can cause errors in the derived discharge.

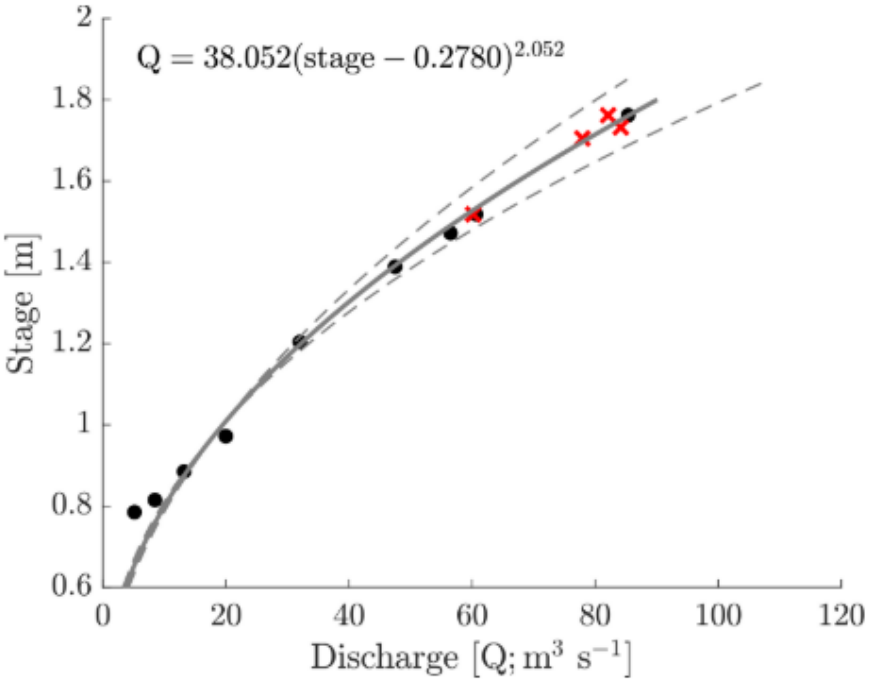

Figure 3: Rating Curve Example from Perks., 2020 KLT paper where the dashed lines represent a 95% confidence interval, the black circles represent fixed camera KLT-IV measurements, and the red crosses are UAV KLT-IV measurements

To fill this gap, innovative techniques should be used to estimate discharge. In the last few decades, remote sensing, non-contact approaches like image velocimetry techniques have become popular in the field of hydrometry and experimental hydraulics.

2.2 Image Velocimetry

Large Scale Particle Image Velocimetry (LSPIV) setups are comprised of cameras that can be setup along riverbanks, mounted on bridges or by using aerial vehicles such as drones or helicopters (Eltner, Bertalan, et al., 2021; Kinzel & Legleiter, 2019) that are focused on an area of interest of a riverine environment. Surface velocities can be extracted from videos. Then, with

1 – Hysteresis is the phenomenon where the value of a physical property lags behind the changes in the effect that is causing it

bathymetry data and the coefficient of average velocity to surface velocity (alpha) discharges can be computed.

Initially, particle image velocimetry was developed for hydraulic experiments in laboratories where tracer particles were used to visualize the flow (Aberle et al., 2017; Dal Sasso et al., 2020; Fujita et al., 1998) and an illumination source – typically a pulsed laser – was required to enhance the visibility of the particles (Aberle et al., 2017; Prasad et al., 1992). In the 1990s researchers adapted PIV to large scale surface flows in the field with a method known as large scale particle image velocimetry (LSPIV). Fujita et al., 1998 first developed LSPIV as an extension of PIV capable of covering surfaces up to 45,000m^2. It was tested for a number of applications including floodplain discharge measurements in the Yodo River in Japan. Results were within 3% of conventional methods. In 2003, Fujita processed flood videos from a moving helicopter finding reasonable results (Fujita & Hino, 2003). Fujita & Kunita (2011) further advanced the use of aerial vehicles in LSPIV by using a helicopter again to measure large flood flows in the Yodo River that compared well to the gauging data. Kim et al., 2008 produced a paper where a mobile LSPIV set-up was tested, and it was found in good agreement with USGS stream gauges. LSPIV has also been successfully applied to a real-time system where surface velocities were processed every few minutes (Hauet, Kruger, et al., 2008). It was found to have favourable measurements compared to the stream gauge, however one limitation noted was changing environmental conditions like wind, precipitation and sunlight.

LSPIV has been successfully applied in both low flows and flood flows. Meselhe et al., 2004 examined LSPIV in shallow flows using orifice-meter measurements to validate the surface velocities and found errors of 21% or less with the camera measurements. Another study employed the use of a UAV in low-flows and used Kanade-Lucas-Tomasi Image Velocimetry (KLT-IV), LSPIV and OTV and found all methods were within 0.05m/s of the ADCP measurements. Researchers in France have published multiple papers showing the success of LSPIV in high flow or flooding scenarios. One study looked at YouTube videos using LSPIV with success while also analyzing how image resolution can affect measurements and found a difference of no more than

5% between 240p and 1080p with a minimum of 50 image pairs (Le Boursicaud et al., 2016). Another study by Le Coz et al., (2010) used LSPIV for flash floods in the Mediterranean. LSPIV measurements were found to be within ±10% of ADCP measurements and within 20% of the rating curve. There have also been some studies on the use of LSPIV without the need for GCPs which could improve the feasibility of mobile systems. Tauro et al., 2014 used lasers pointed on the water surface to perform camera calibration and, a camera at a nadir angle.

LSPIV has been proven to be applicable to a wide range of flow scenarios. Nonetheless, other image velocimetry methods continue to be developed. Fujita et al., 2007 introduced space-time image velocimetry (STIV), a one-dimensional image velocimetry method that uses a space-time image created from the change in brightness in search lines that run parallel to the main flow direction so streamwise velocity can be obtained (Figure 4).

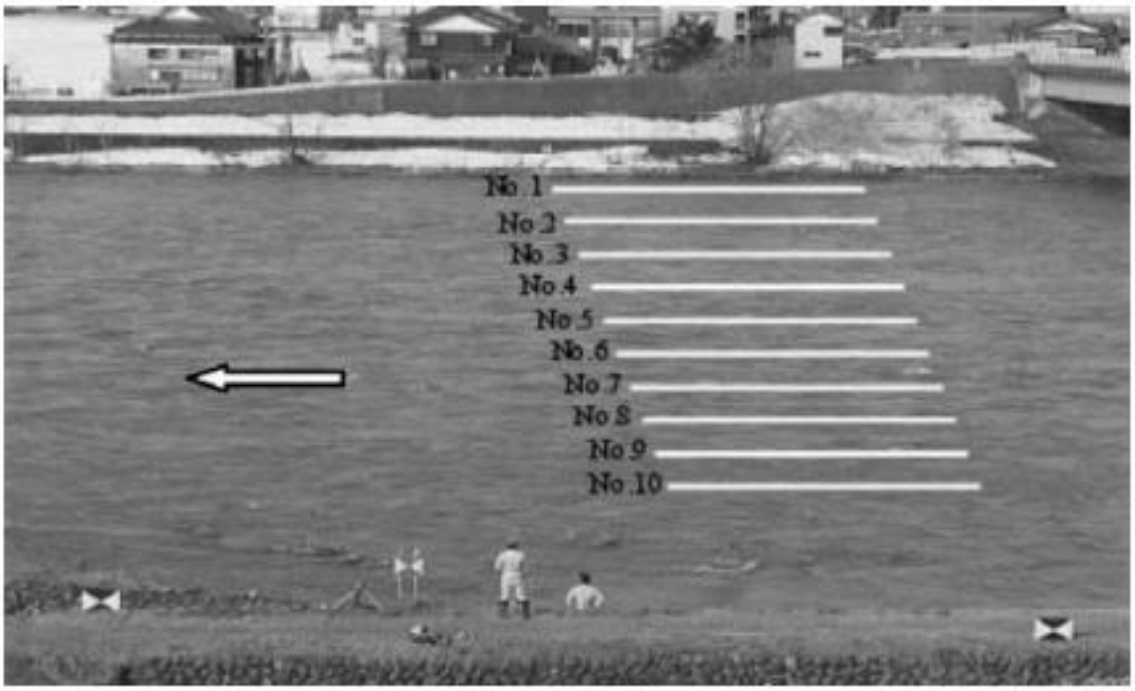

Figure 4: Example of STIV Processing of the Uono River (Fujita et al., 2007)

Tauro et al., 2018 developed Optical Tracking Velocimetry using the Lucas-Kanade optical flow algorithm to compute spatio-temporal derivatives of image intensity to determine surface velocity. An R^2 value of 0.83 was found compared to measurements obtained by a current meter despite the measurements recorded 3cm below the surface potentially impacting the R^2 value.

$$\nabla I(x,t) \cdot v + \frac{\partial I(x,t)}{\partial t} = 0$$

Equation 1: Lucas-Kanade Equation

Ansari et al., 2023 combined optical flow techniques with Convention Neural Networks (CNN) with an algorithm named RIVQNet. The study looked at several different CNNs with data from a lab experiment, the Castor River and the Salmon River in British Columbia. The method was evaluated with root mean square error (RMSE) and mean absolute percentage error (MAPE). In the lab experiment the best CNN used had a RMSE of 0.01m/s and a MAPE of 5.3% compared to an ADV. Low flow conditions at the Salmon River resulted in a 0.2m/s RMSE and 17.5% MAPE while in high flow conditions at the Castor resulted in RMSEs of 0.10-0.16m/s and MAPEs of 7.14-12.06%.

Schweitzer & Cowen, 2021 established an infrared image velocimetry method called infrared quantitative image velocimetry (IR-QIV) (Figure 5). The majority of natural flows have miniscule temperature differences between the air and the water surface caused by heat exchange so infrared cameras can be employed to track thermal patterns on the surface obtain instantaneous velocity measurements. ADCP and ADV measurements were compared with IR-QIV instantaneous velocity measurements at Sutter Slough River in California, USA with reasonable error being found (Schweitzer & Cowen, 2021)

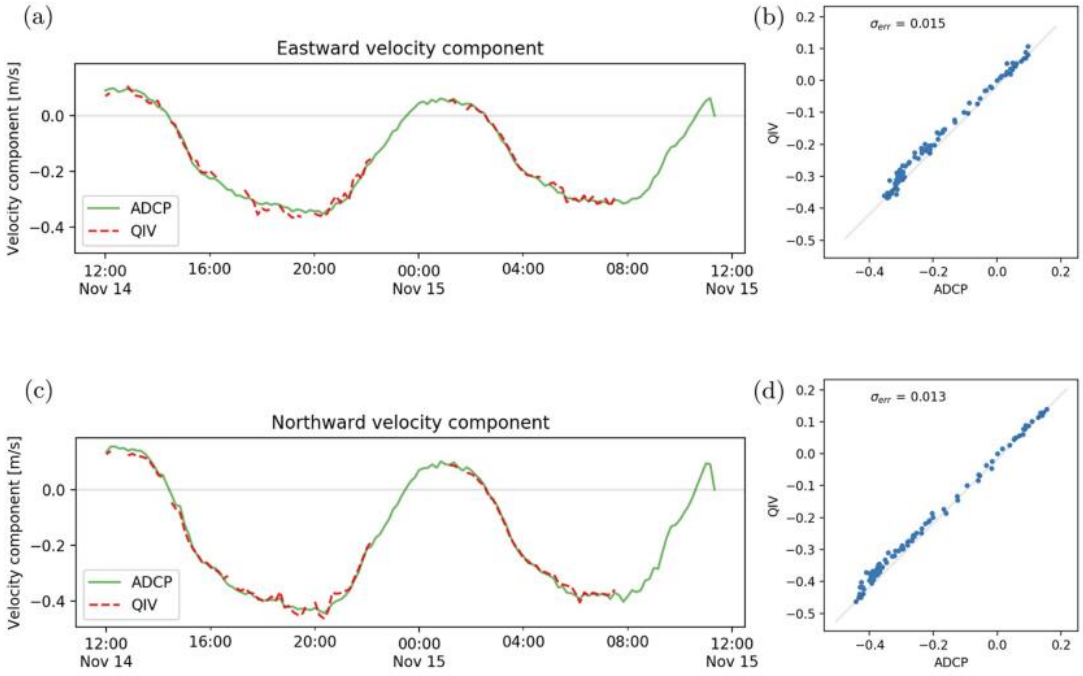

Figure 5: ADCP vs IR-QIV velocities over a 20hr period (Schweitzer & Cowen, 2021).

In addition to these new image velocimetry techniques, advances in unmanned aerial vehicles have led to researchers heavily relying on drones for image velocimetry research (Eltner et al., 2021; Kinzel & Legleiter, 2019; Pearce et al., 2020).

A significant challenge with all of these new image velocimetry methods is successfully replicating laboratory experiments in the field due to environmental conditions. Environmental conditions ranging from wind to sunlight (or lack thereof) can have a large impact on the image processing stage of image velocimetry. Additionally, as previously mentioned, another noteworthy challenge is the inability to always be collecting images at a nadir angle resulting in distorted views that have to be corrected during processing (Patalano et al., 2017). Despite these challenges, with advancements in camera technology (W. Li et al., 2019), LSPIV and other image velocimetry techniques have become a cost-effective method that has been successfully applied by both researchers (Ansari et al., 2018; Huang et al., 2018; Patalano et al., 2017) and some hydrometric monitoring agencies in a variety of different scenarios (Hauet, Creutin, et al., 2008; Le Coz et al., 2010).

2.2.3 Stereoscopic Image Velocimetry

In addition to previously mentioned image velocimetry techniques, one of the newest methods has the potential to resolve all three velocity components. Stereoscopic imagery uses multiple cameras focused on the same area of interest to reconstruct a 3-dimensional image by using epipolar geometry to match image points between the two cameras. The epipolar plane is formed by the object imaged and the optical centers of each camera so any image point from one camera has a matching point that is restricted on the epipolar line that intersects the epipolar plane and the other camera (W. Li et al., 2019). A minimum of 8 known image point pairs are required for stereo reconstruction (W. Li et al., 2019). Stereoscopic PIV has been applied previously in the medical field (Khodarahmi et al., 2010) and has been researched in coastal engineering to measure the water surface elevation of ocean waves (Benetazzo, 2006).

The first case of using stereoscopic imaging in hydrology was in 2016 when a stereoscopic imaging system was used to determine the bathymetry of a mountain stream (Ran et al., 2016). In a follow up study, Li et al., 2019, used a stereoscopic PIV set-up (Figure 6) to obtain discharge of the steep mountain stream by reconstructing the 3D surface and projecting the point cloud onto a 2D plane.

Figure 6: Stereo Imaging Configuration on the Longxi River where 1 and 2 are the cameras used, 3 is the solar panel used to power the system and 4 is a box where additional equipment is stored (W. Li et al., 2019)

Two-dimensional image velocimetry systems assume a uniform water surface slope which can result in substantial inaccuracies in steep slopes and mountainous channels due to complex topography. Introducing a second camera to make a system stereoscopic has shown the ability to resolve the complex topography effectively. Li et al., 2019 validated their system using an impeller flow meter and found an average difference in surface velocity of under 6%. A shortcoming of this study was errors of up to 0.2m with GCPs in the water with the stereo reconstruction, a significant value for a small mountain stream suggesting other methods may be better for obtaining bathymetry. More recently, a pre-built stereo camera was used to monitor streamflow (Hutley et al., 2023). A stereo camera was used to estimate water level based on the three-dimensionally generated point cloud created from the surface reconstruction. Those water level estimates were combined with the bathymetry in order to estimate discharge which was found to be with 5-15% of ADCP comparison measurements (Hutley et al., 2023). Despite these successful applications, it is important to note that neither were successful in obtaining three-dimensional velocity components. Li et al., 2019 projected their 3D reconstruction onto a horizontal plane. In Hutley et al., 2023 the cameras were individually processed using optical flow and averaged to get the channel's surface velocities.

2.2.4 Environmental Conditions

Environmental conditions are arguably the largest challenge when attempting to replicate laboratory experiments in field studies, as it is extremely difficult to predict or control conditions in the environment and that is no different with image velocimetry. According to Detert, 2021 there are five main sources of bias caused by the environment: sunlight reflections, whitewater, shadows, flow induced movement of vegetation and ground motion resulting in camera instability. Another environmental factor not mentioned by Detert, 2021 is wind, which can significantly alter surface velocity estimates depending on the magnitude relative to the flow. Additionally, natural tracers, or the lack thereof, can complicate the process of filtering between signal and noise (Detert, 2021).

Sunlight can have both positive and negative effects for image processing. Generally, poor or strong illumination can degrade image quality (Figure 7), however there are cases where sunlight can be beneficial as it can help with backscattering of the water surface (Muste et al.,

2008). Another important aspect to consider with lighting is that a homogeneous distribution of light intensity is very important (Kantoush et al., 2011; Muste et al., 2008), so wooded streams, vegetation along the banks or even bridges could cause variations in lighting affecting the image quality in portions of the image, making it more challenging to accurately track tracer particles.

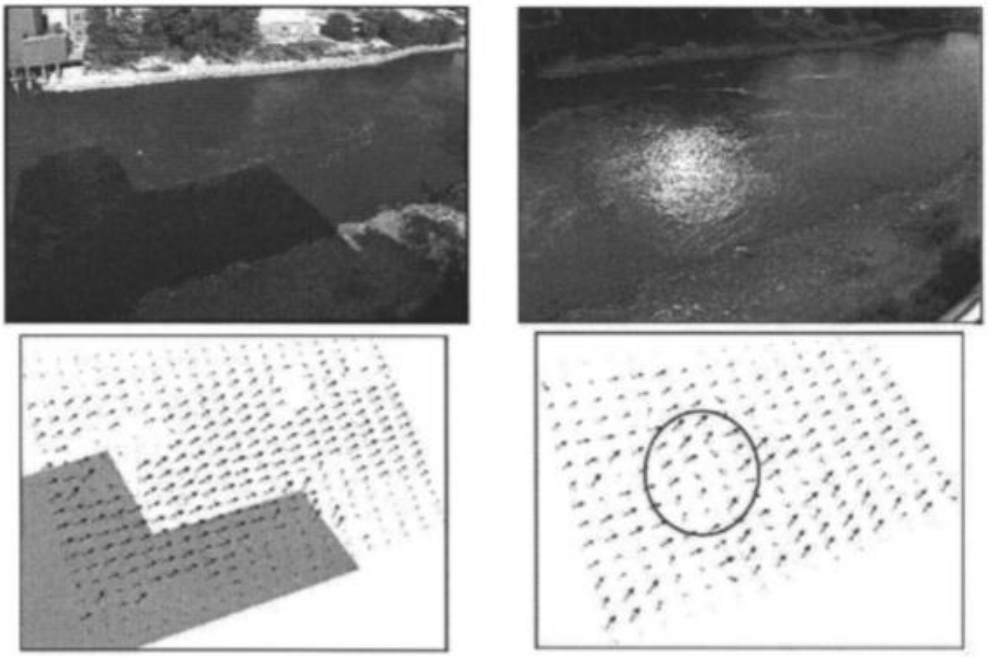

Figure 7: Effect of shadows and glare on surface velocity field (Hauet, Kruger, et al., 2008)

Wind has the largest effect on surface velocity estimates when approaching from the opposite direction of surface velocity in low flows (Le Coz et al., 2010) and the magnitude of the wind is significant in comparison to the discharge. It has been found that wind causes a 3% difference in surface velocity estimates on average up to a maximum of 8% (Peña-Haro et al., 2020). Biggs et al., 2021 recommends disregarding videos that are clearly impacted by wind shear. Some other important aspects to consider in Canada include rain, snow, fog and ice cover. Videos affected by these conditions should generally be disregarded due to a lack of research (Jolley et al., 2021). It is impossible to fully eliminate all environmental factors in the field, making it important to consider a site carefully when selecting a new location.

2.2.4.1 Tracer Particles

Tracer particles are required for any image velocimetry system. Natural tracers can be used, however in the absence of natural tracers, artificial particles should be used to seed the flow. Natural tracers can include ripples, floating objects or color differences on the water surface

(Fujita & Kunita, 2011). Artificial tracers can be any environmentally friendly material that is naturally buoyant (Muste et al., 2008). This includes but is not limited to woodchips, foam pellets, mulch, cornstarch chips, and rice crackers (Dal Sasso et al., 2020; Jodeau et al., 2008). There is a lot of research available showing how different types of artificial tracers have been used to produce accurate surface velocity results. For example, different types of tracers or fluorescent particles have been used to help enhance contrast and improve illumination respectively (Dal Sasso et al., 2020; Tauro et al., 2014), but these methods may be site dependent. It should be noted that use of artificial tracers consistently is not a viable option for continuous stream gauging. Seeding distribution is another key parameter to consider for tracer particles. It is recommended that 10-30% of the water surface is covered by tracers throughout image frames and is uniformly distributed (Meselhe et al., 2004). The absence of densely seeded surfaces can lead to velocity underestimates. More recent work by (Pizarro, Dal Sasso, & Manfreda, 2020) suggests choosing the optimal frames of a video through the use of a seeding distribution index (SDI). The SDI looks at tracer density and tracer dispersion to determine the best sequence of frames in a video to analyze. It was found that when using SDI, surface velocity error could be reduced by between 16.1 and 39% (Dal Sasso et al., 2021; Pizarro, Dal Sasso, Perks, et al., 2020).

2.2.6 Camera Characteristics

Another important aspect to be considered in image velocimetry is the camera itself. Cameras have varying intrinsic and extrinsic parameters that should be known when choosing a camera and must be known for camera calibration – a necessary step in image-preprocessing. Equation 2 shows the intrinsic parameters matrix denoted as K.

$$K = \begin{matrix} f_x & s & c_x \\ 0 & f_y & c_y \\ 0 & 0 & 1 \end{matrix}$$

Equation 2: Camera intrinsic parameters matrix

Where f_x and f_y are the focal length of the x and y directions in pixels, s is the skew coefficient which is non-zero if the image axes are not perpendicular, and c_x and c_y are the optical center of the camera in pixels. Focal length is the distance between the image sensor and camera

lens when the object is in focus (Figure 8). Smaller focal length means that more area can be captured, and as focal length increases the area becomes smaller, but the detail of said area improves.

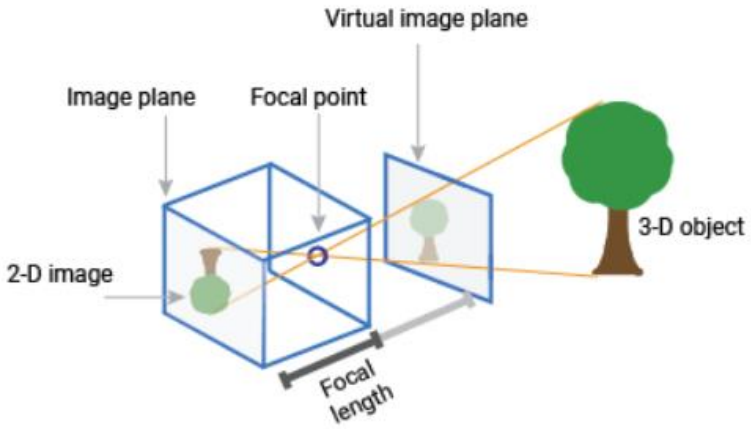

Figure 8: Typical pinhole camera model and explanation of focal length (Source: Mathworks.com, Accessed 15 Aug. 2024)

The extrinsic parameters are the rotation and translation of the camera. Lastly, camera weight is an additional parameter to possibly consider in order to minimize camera shake. Shaking can occur in fixed cameras due to factors such as wind or vehicles on bridges (Perks, 2020). This can impact results as the region of interest will shift between frames. In these cases, image stabilization must occur during image pre-processing to correct this. A number of methods exist for image stabilization, and some are built into image velocimetry processing toolboxes (Hydro Technology Institute Co., 2024; Legleiter & Kinzel, 2023). Typically, to reconstruct the frame without the shift, the initial frame is used as a reference frame and static features in the frame are selected and then searched for in subsequent frames to determine the shift between frames (Rodriguez-Padilla et al., 2020).

Camera calibration is an additional necessary step in pre-processing to remove lens distortion in the images that is often forgotten about or done poorly in field studies (Detert, 2021). Lens distortion occurs in cameras as both pincushion and barrel distortion. Pincushion distortion is when light rays bend more near the edges of a lens than at the center. Barrel distortion happens when the lens and image plane are not parallel with one another (Figure 9).

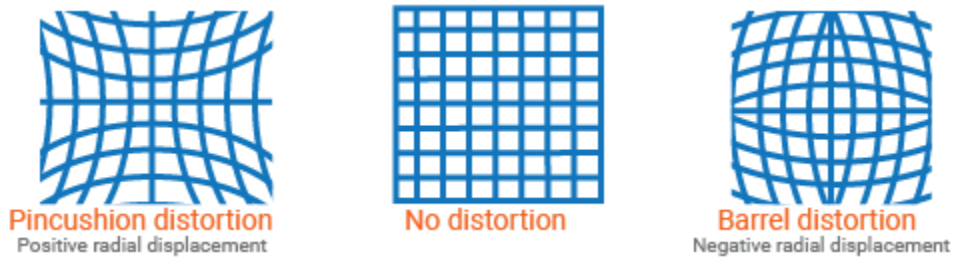

Figure 9: Different ways images are distorted radially (Source: Mathworks.com, Accessed 15 Aug. 2024)

These types of distortion introduce error into the results when not accounted for, so it is important to include this step. Lens distortion correction can be performed before or after image processing, however it is recommended that it is done before (Detert, 2021; WaMSTeC, 2021). Camera calibration is performed by taking images of a uniformly distributed chessboard with a known distance of the squares at various locations in the image plane. A minimum of 3 images is required, however Detert, 2021 recommends 20+ images to get accurate results. These images are then processed in tools such as the MATLAB camera calibration app (seen in Figure 10) to obtain the intrinsic parameters of the camera. Then using these intrinsic parameters from camera calibration, they can be applied to the image to remove the lens distortion.

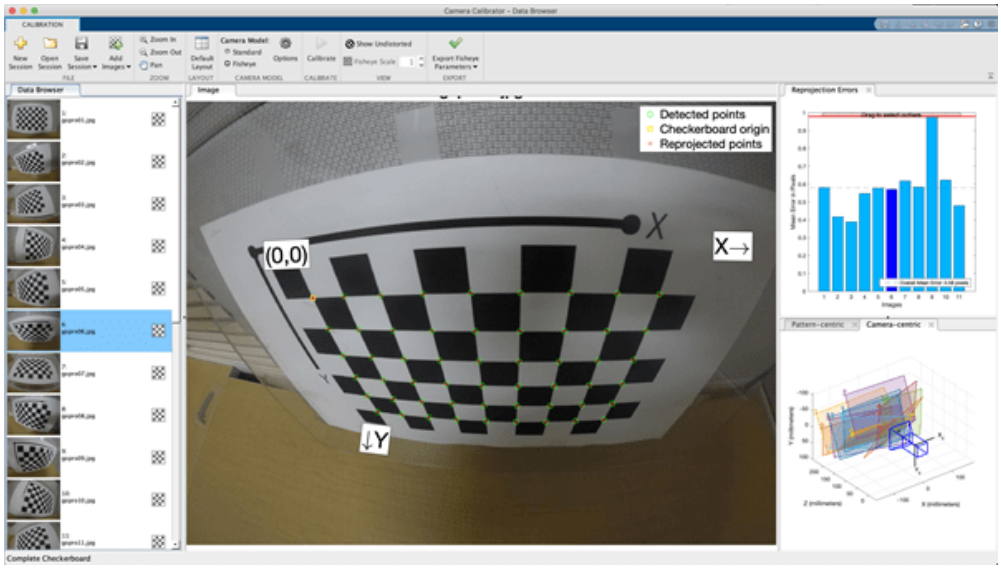

Figure 10: MATLAB single camera calibrator application GUI (Source: Mathworks.com, Accessed 15 Aug. 2024)

Additional camera parameters to consider are capture frames rates and image resolution. It is recommended that a minimum of 24 frames per second are used (WaMSTeC, 2021) however, cameras with a frequency as low as 5 Hz can produce results (Jolley et al., 2021). One challenge is having a consistent frame rate throughout the duration of the video. When using cameras that send data remotely, the data loggers that send the data may not always have enough power to do so. This can result in lost frames or incorrect timestamps (Detert, 2021; Jolley et al., 2021). Additionally, increasing frame rate also requires an increase in bandwidth; e.g., 1fps versus 30fps requires a 7x increase (Jolley et al., 2021). Loss of frames can cause errors in the analysis, so it is important to consider frame rate and whether to use a data logger or just store data on SD cards.

Lastly image resolution is something to consider. The minimum resolution required will vary depending on factors such as distance of the camera to the river. WaMSTeC, 2021 recommends a minimum resolution of 5 cm/pixel, however there is some research suggesting that image resolution is not the most important factor to consider in a camera. A 2016 study used LSPIV to process random videos found on YouTube (Le Boursicaud et al., 2016). The authors analyzed the videos using image resolutions ranging from 240 to 1080 pixels and found that the average streamwise velocity when analyzing over 50 image pairs produced a difference of less than 5% between methods (Figure 11), suggesting that LSPIV is not affected much by reductions in image resolution (Le Boursicaud et al., 2016). With 4k cameras being commercially available nowadays, having high image resolution is not a challenge but one thing to consider is higher resolution will result in higher storage requirements and longer processing time.

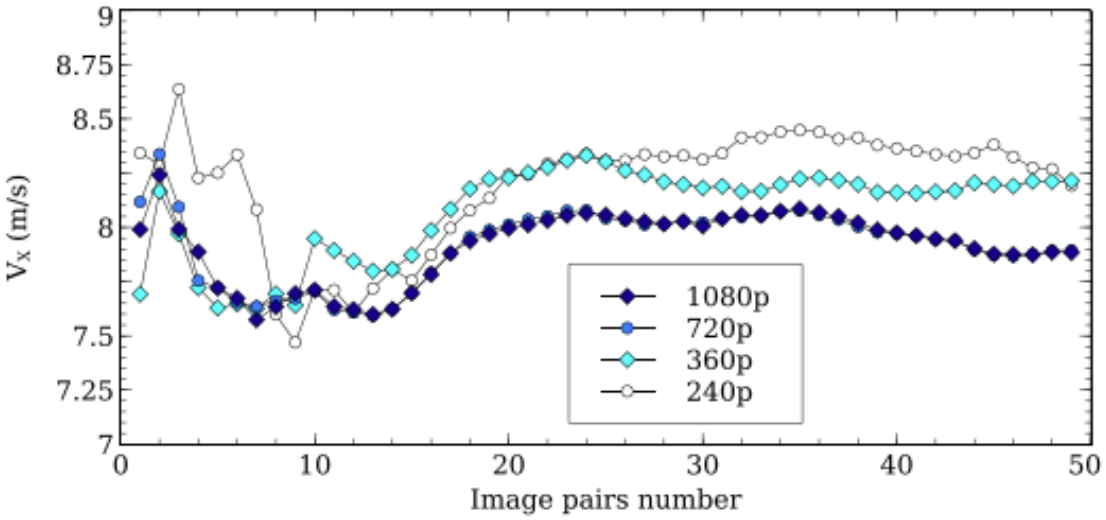

Figure 11: Analysis of the number of Image pairs versus longitudinal velocity at varying image resolutions (Le Boursicaud et al., 2016)

2.2.7 Image Rectification

Ground sampling distance (GSD) is the distance between the centroid of two adjacent pixels. In image velocimetry, if the features that are being tracked in the image processing are smaller than the GSD, those features will be poorly resolved. Estimating the GSD in advance can be important when establishing an image velocimetry site (Jolley et al., 2021). The equation for GSD can be seen below.

$$GSD = \frac{L\ x\ 200}{IwP}$$

Equation 3: Ground Sampling Distance

Where L is the length both vertically and horizontally and IwP is the image width given in pixels. In ideal conditions, cameras should be at a nadir angle with the water surface to ensure a uniform GSD throughout the images. As previously mentioned, one of the constraints of image velocimetry is that cameras cannot always be nadir to the water surface. Obstructions over a river can impact the accuracy of the surface velocity estimates when using UAVs and bridges are not always present or elevated high enough over the channel. When cameras are at an oblique angle, the GSD will be variable depending on the camera angle and distance from the camera sensor. This is demonstrated in Figure 12. Previous research has seen success with oblique camera angles of up to 57 degrees from nadir (Perks et al., 2020), while Eltner et al., 2020 suggest that an angle of more than 10 degrees in mobile cameras should be avoided.

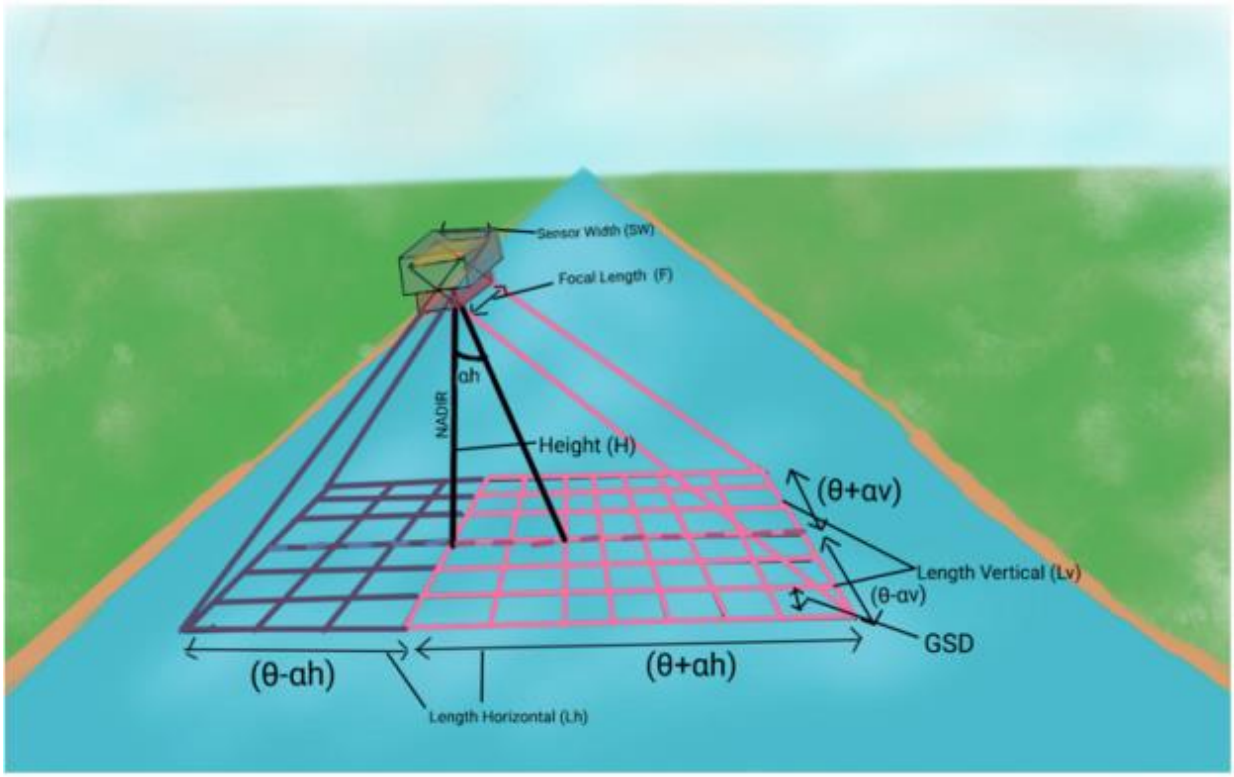

Figure 12: Diagram displaying how ground sampling distance (GSD) is affected by an oblique camera angle (Jolley et al., 2021)

Oblique views create distorted images requiring orthorectification during processing to obtain a nadir result. This will be discussed in a further subsection. It is also necessary to rectify nadir videos to define real-world distance and correct any distortion caused by the camera lens, however nadir videos can be processed by simply defining pixel size or with a known real-world distance between two points (Patalano et al., 2017). Images can be rectified either two-dimensionally or three-dimensionally. Rectification is performed by matching image coordinates to known real-world coordinates of ground-control-points (GCPs). GCPs should be easily identifiable fixed objects such as large rocks or trees, but they can also be manmade targets like the ones seen in Figure 13.

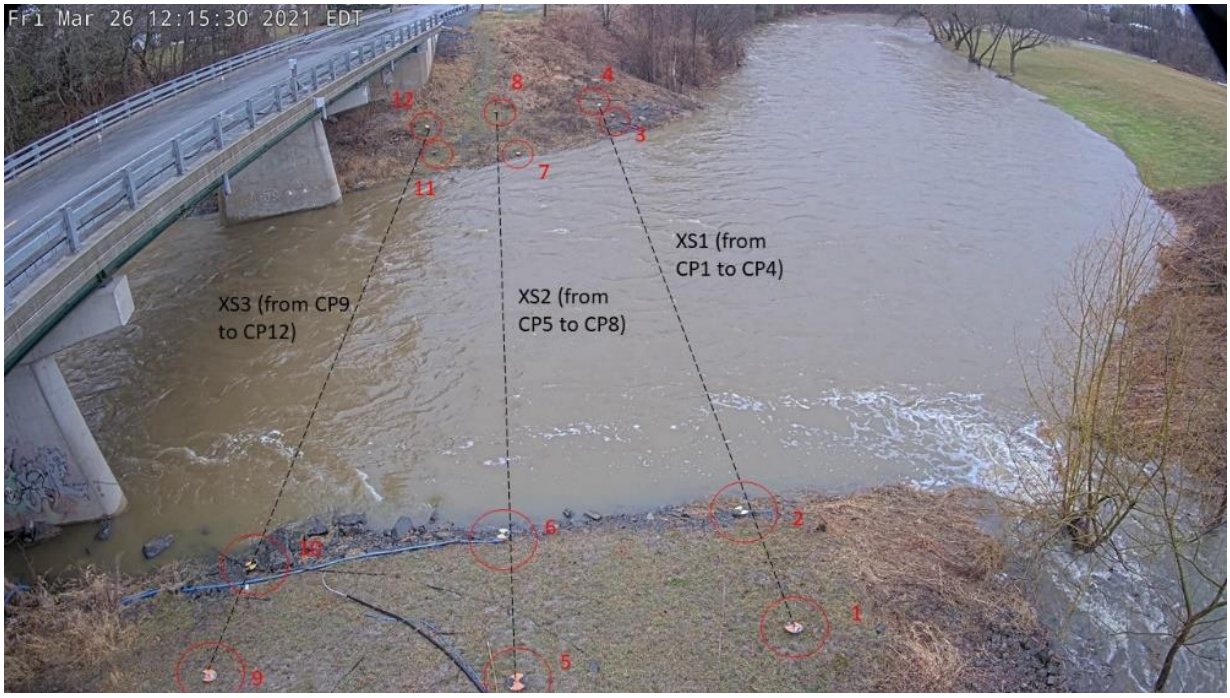

Figure 13: Castor River Ground Control Points Setup used for image rectification (Source: James Bomhof, National Hydrological Service, Environment and Climate Change Canada)

Four GCPs at water surface elevation are required for 2D orthorectification while a minimum of six are needed for 3D orthorectification (necessary for oblique cameras). Equation 4 illustrates how the image coordinates are matched with the known real-world coordinates.

$$\begin{pmatrix} \tilde{x} \\ \tilde{y} \\ \tilde{z} \end{pmatrix} = \begin{pmatrix} C_{11} & C_{12} & C_{13} & C_{14} \\ C_{21} & C_{22} & C_{23} & C_{24} \\ C_{31} & C_{32} & C_{33} & C_{34} \end{pmatrix} \begin{pmatrix} X_r \\ Y_r \\ Z_r \\ 1 \end{pmatrix},$$

Equation 4: 3D Orthorectification matrix

Where x, y and z are the image coordinates, X, Y, Z are the real-world Cartesian coordinates and the C's are the camera matrix representing the intrinsic and extrinsic parameters of the camera. In 2D orthorectification the water surface is assumed to be the plane that is being rectified so the z-coordinates are removed from the equation, and the camera matrix becomes the homography matrix seen in Equation 5 (Patalano et al., 2017).

$$\begin{pmatrix} X_p \\ Y_p \\ 1 \end{pmatrix} = \begin{pmatrix} H_{11} & H_{12} & H_{13} \\ H_{21} & H_{22} & H_{23} \\ H_{31} & H_{32} & 1 \end{pmatrix} \begin{pmatrix} X_r \\ Y_r \\ 1 \end{pmatrix}.$$

Equation 5: 2D Orthorectification matrix

Where the X_p and Y_p represent the image coordinates, X_r and Y_r represent the real-world coordinates and H is the homography matrix with 8 unknowns that is solved with 4 GCPs.

In Rectification of Image Velocimetry Results (RIVeR), an image processing software that will be discussed in detail further in later sections, the user inputs the distance between the 4 known GCPs and the least squares method is used to rectify the images (Patalano et al., 2017). If the GCPs are on approximately the same z-plane, then 2D image rectification is suitable. However, if the cameras are oblique and GCPs are at varying elevations then it is important to rectify the images using Equation 4. There are mixed opinions in the literature on how many GCPs are required for 3D rectification. The camera matrix has 12 unknowns so in theory can be solved with a minimum of 6 GCPs (Jolley et al., 2021; W. Li et al., 2019), however other research suggests that at least 10 GCPs with known 3D coordinates are needed (Fujita & Kunita, 2011; Le Boursicaud et al., 201). Regardless, increasing the number of GCPs should help increase the accuracy of orthorectification and allows for some redundancy in the system (Jolley et al., 2021).

2.2.8 Image Processing

This sub-section involves research revolving around selecting video length, choosing interrogation window sizes, the available software for image processing and available research into alpha – the coefficient used to obtain a depth averaged velocity from the measured surface velocity.

2.2.8.1 Pre-Processing

Image preprocessing can be used to enhance image features improving the chances of detecting valid velocity vectors. A common filter used is the Contrast Limited Adaptive Histogram Equalization (CLAHE) filter (Figure 14), which spreads out the intensity histogram to the full range operating in small areas of the image and then integrated using bilinear interpolation (Kumar et al., 2019; Patalano et al., 2017).

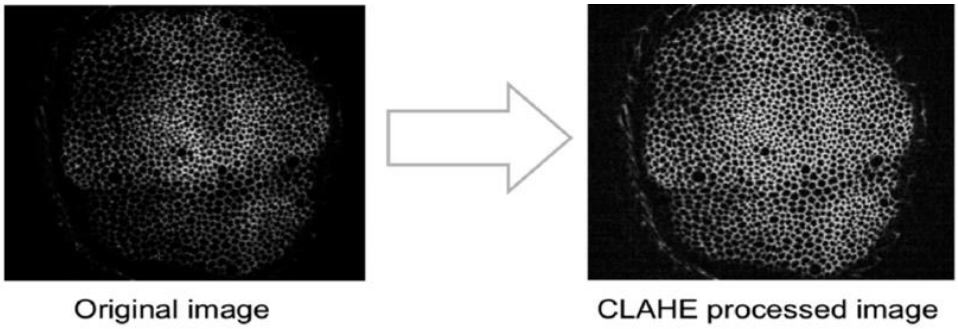

Figure 14: Example of CLAHE filtering (Kumar et al., 2019)

Intensity capping is another common pre-processing filter. It deals with the displacement of bright pixels that can control cross-correlation calculations within an interrogation window, which can potentially cause bias in the velocity vectors. Intensity capping puts a limit on grayscale intensity reducing the intensity values of bright spots that can overwhelm the cross-correlation algorithms (Shavit et al., 2007). A third popular filter is high-pass filtering. It is used to sharpen edges and remove light reflections in an image. The filter works by blurring the image using a low-pass filter and then subtracting that result from the original image to remove the low frequency background information (Thielicke, 2014).

2.2.8.2 Processing

The consensus of researchers is that video durations should be between 20-30 seconds so velocity variation can be seen; however, there is little research to support this claim. In fact, there are studies that have had success with videos as short as 5 seconds long (Patalano et al., 2021; Ran et al., 2016). Figure 15 shows work done by Patalano et al., 2021 where the author looked at how discharge varied with video duration. The results show that this is a very small variation in discharge estimates between 4 to 20 seconds of video suggesting that shorter videos should produce reasonable estimates.

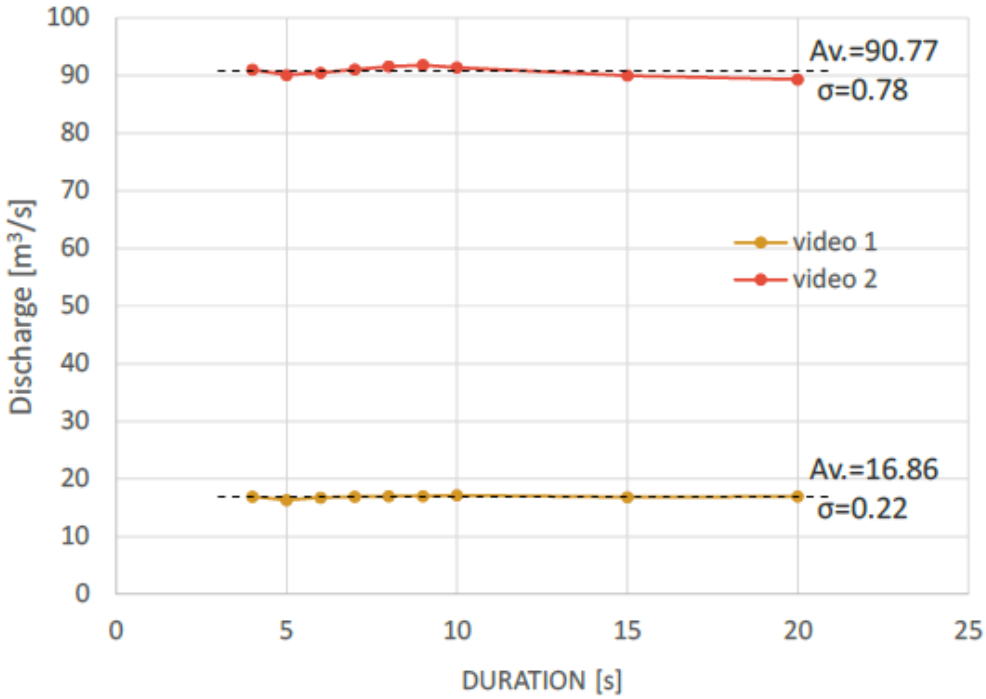

Figure 15: Analysis performed for ECCC displaying how varying video durations affect discharge estimates (Patalano, 2021)

Selecting the proper interrogation area (IA) size is another important consideration to be made. The interrogation area must be small enough to preserve the scale of interest of the flow but still large enough to include recognizable tracer patterns (Jolley et al., 2021). Tauro et al., 2018 suggests that a minimum of 4-5 tracer particles per interrogation area is ideal for well resolved velocity vectors to be obtained. Thielicke, 2014 also notes that a lot of research uses "extremely small" interrogation areas in the final image pass. This will increase the resolution of the vector results; however, it will also increase the noise and erroneous vectors (Thielicke, 2014) so it is suggested to keep interrogation areas "as large as possible".

In PIV analysis, there are several cross-correlation algorithms that can be used to obtain a vector field. These methods work by processing one IA and then searching neighboring IAs in successive frames to determine the most likely displacement of the tracer particles Figure 16.

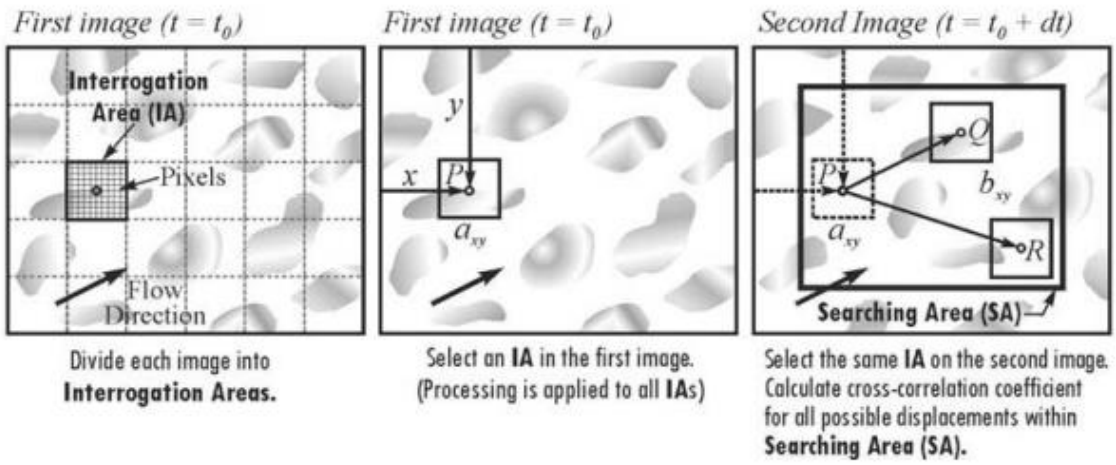

Figure 16: Diagram displaying how cross-correlation methods are used to determine particle displacement between image frames (Muste et al., 2008)

2.2.8.3 Alpha Determination

To get discharge once surface velocity is obtained, it must be multiplied by a velocity index, also known as alpha (α) to get the average velocity for the channel. A widely accepted value in literature is 0.85 (Le Coz et al., 2010). However, this is only acceptable if the channel follows a typical logarithmic velocity profile which is not the case in many occasions so using this generic value can lead to errors in discharge estimates. Factors such as wind or surface roughness can significantly alter the velocity index (Biggs et al., 2021). Hauet et al., 2018 found that for natural rivers less than 2m deep an alpha of 0.8 was sufficient while rivers over 2m deep and concrete channels, a value of 0.9 should be used. Based on literature, alpha should be site specific, with a typical range between 0.72 and 0.9 (Biggs et al., 2023; Hauet et al., 2018; Jodeau et al., 2008; Patalano et al., 2017). Biggs et al., 2023 suggest a number of potential approaches to determining an accurate alpha coefficient for a specific river. Alpha can be determined based on a site's log law profile or power law profile. Alpha also will usually vary at a site based on stage so a rating curve could also be developed to determine alpha (Biggs et al., 2023).

2.2.8.4 Available Image Velocimetry Software

This subsection briefly describes some of the different software packages that are available to obtain image velocimetry results.

RIVeR

Rectification of Image Velocimetry Results (RIVeR) is a free LSPIV application developed in MATLAB that has integrated PIVLab into it. PIVLab was developed by William Thielicke for PIV analysis. Frames are analyzed in PIVLab giving results in pixel scale, then the file is uploaded into RIVeR where it is orthorectified using GCPs to obtain surface velocity in SI units. It is also capable of estimating discharge of a cross-section with user-inputted bathymetry data and water level estimates (Jolley et al., 2021; Patalano et al., 2017).

Fudaa-LSPIV

Fudaa is another free software built by the Électricitéde France (EDF) using a java graphical user interface. Unlike RIVeR it orthorectifies the images first and then analyzes the images. Additionally, it can compute discharge for multiple cross-sections at the same time given user inputted bathymetry data and water level estimates (Jolley et al., 2021; Le Coz et al., 2010).

Hydro-STIV

Hydro-STIV is a STIV software developed in collaboration with Fujita. It is one of the only processing suites that has a cost associated with it as it is maintained by HydroSoken. In addition to the basic ability to measure discharge using STIV, it is capable of correcting for wind speed, and automatically detecting water level from images (Hydro Technology Institute Co., 2024)

KLT-IV

Kanade-Lucas-Tomasi Image Velocimetry is another recently developed user-friendly software that has a step-by-step workflow to obtain surface velocity vectors. It uses the Kanade-Lucas-Tomasi algorithm to search 30 iterations within an interrogation area to find the new location of each point. It does this until it reaches a convergence and ignores any results with errors of 1 pixel or higher (Jolley et al., 2021; Perks, 2020).

OTV

Lastly, Optical Tracking Velocimetry uses the Lucas-Kanade algorithm and trajectory-based filters to improve reliability of the velocities and can produce an average surface velocity estimation. Both vector direction and vector length are user-inputted, and the user can also determine trajectory quality (Jolley et al., 2021; Tauro et al., 2018).

3.0 Experimental Methods

This section details the equipment, methods and applications used to collect, process and analyze discharge in both field and laboratory settings. It first describes the field site, and the equipment used for each survey. Then the same is done for the laboratory experiment, Lastly, the different MATLAB scripts created and software used to analyze the videos was outlined.

3.1 Castor River

The Castor River is located near Ottawa, Ontario draining into the South Nation River near Casselman, Ontario with a total drainage area of 439km^2. The field site is located along a section of the river located in Russell, Ontario approximately 30 minutes outside of Ottawa (Figure 17). It is at Water Survey of Canada gauge station 02LB006, one of two Environment and Climate Change Canada (ECCC) hydrometric gauging sites along the Castor River. ECCC uses a rating curve to disseminate real time data using a pressure sensor that corresponds to a discharge validated by ADCP measurements. ECCC also operates station 02LB006 as an experimental methods site, with both a surface velocity radar (SVR) mounted on the bridge, and a fixed camera for image velocimetry mounted above the gaugehouse on the left bank (Figure 19 & 20).

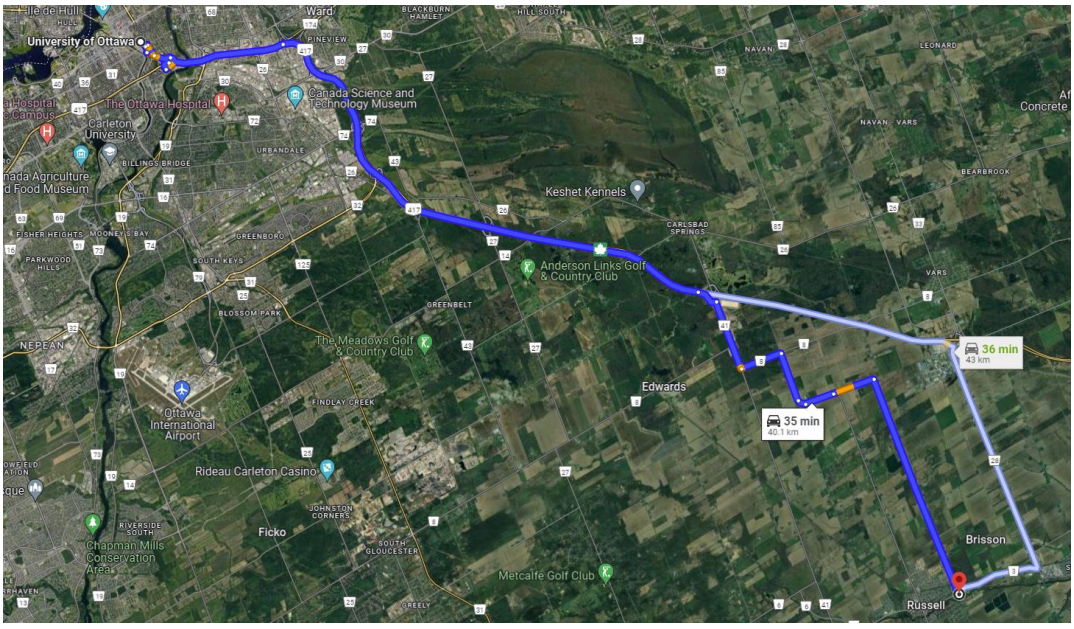

Figure 17: Google maps image showing fastest route from the University of Ottawa to the Castor River field site

The Castor River is a relatively small stream with low flows. Figure 18 displays the flow duration curve (FDC) at the gauging station using mean daily discharge values between 1968 and 2024. Discharge measures under 13m^3/s approximately 90% of the time and the slope of the curve suggests that high-flow events are driven primarily by precipitation and freshet.

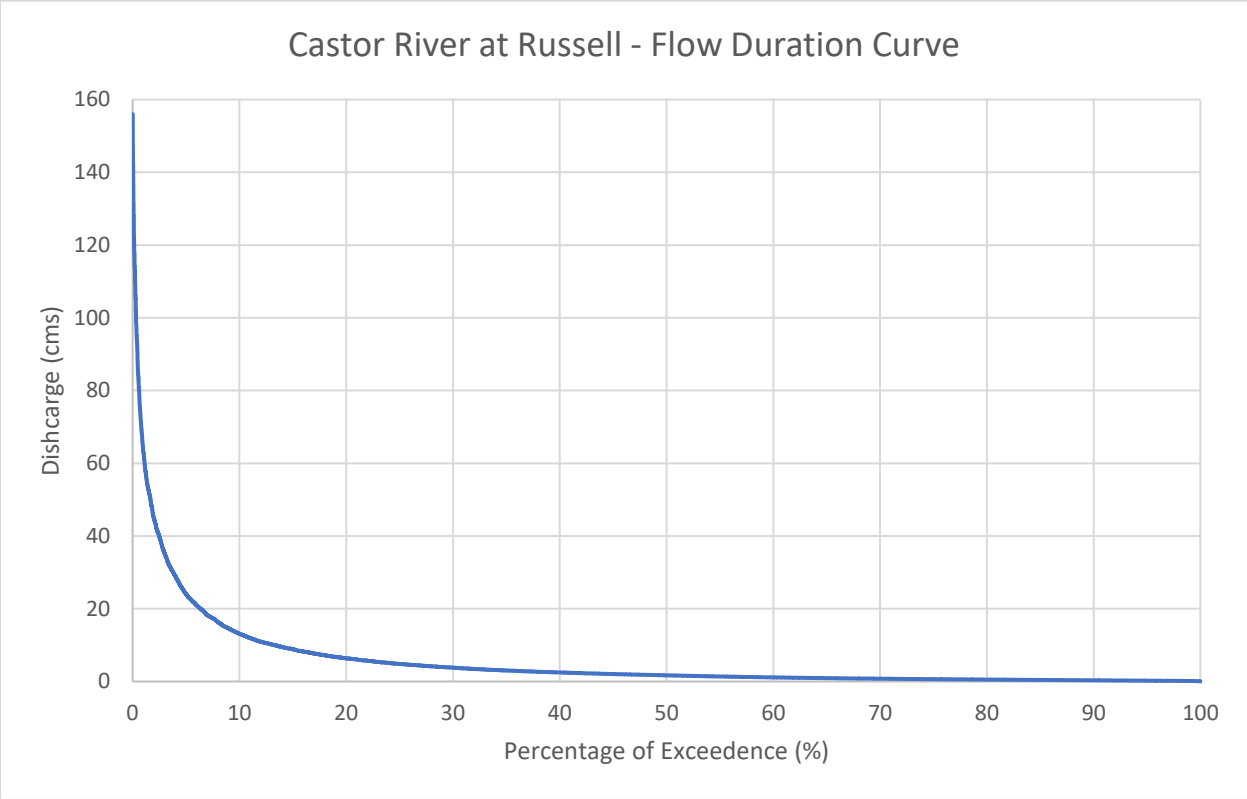

Figure 18: Castor River flow duration curve using average daily discharge values from the gauging station between 1968 and 2024

Upstream of the station, the river meanders for ~150m with a bedrock bed into a straight section where the pressure sensor is located with a stable bed composed of cobble and boulders. Downstream of the bridge seen in Figure 19 a concrete weir is present that is used as a control structure. Major ice jams occur here in the winter due to changes in slope which can affect the rating curve. Having the control structure is useful in maintaining a consistent relation between the stage and discharge. Furthermore, due to foam naturally generated from an upstream riffle, there are typically sufficient natural tracer particles along this stretch for LSPIV analysis.

Figure 19: Left) Bridge cameras installation Top Right) Left bank field of view Bottom Right) Right bank field of view

3.1.1 Data Collection

Two AXIS P1378-LE cameras were installed on either end of the bridge located at the downstream section of the site as shown in Figure 19. Additionally, there is a third AXIS P1378-LE that was installed by ECCC on top of the gaugehouse which can be seen in the background of Figure 19 with Figure 20 showing the FOV from the gaugehouse camera.

Figure 20: Field of view from the camera mounted on top of the gaugehouse

These cameras have an adjustable focal length with 4k image resolution and the ability to withstand cold winter temperatures. Additionally, they have a sun cover to reduce the impact of glare. For the cameras to see the full field of view, they had to be fully zoomed out resulting in a focal length of 3.9mm. Important camera specifications are detailed in Table 2.

Table 2: AXIS P1378-LE camera key specifications (Source: Axis.com, Accessed 15 Aug 2024)

Camera Specifications	
Focal Length	3.9mm – 10mm
Image Resolution	3840 x 2160 pixels
Operating Temperature	-40 to 60 ℃
Maximum frames per second (fps)	30

The three cameras are wired through ethernet cables to an ECCC camera board which is capable of handling up to 4 cameras. The system uses a Raspberry Pi (RPi) computer and a power over ethernet (POE) switch connected to a 12-volt battery for power that is generated using a solar panel on top of the gaugehouse. Each camera is connected to the camera board using ethernet cables that were installed along the bridge railing. Python scripts on the RPi are used to turn the cameras on and record synchronous videos that are saved to the RPi. Then using the cell modem, datalogger and antenna, videos are uploaded to an ECCC server where all the videos are stored. Additionally, the files are saved on the RPi for an extended period of time so if needed, videos can be retrieved manually. Figure 21 shows the camera board setup with individual parts labelled.

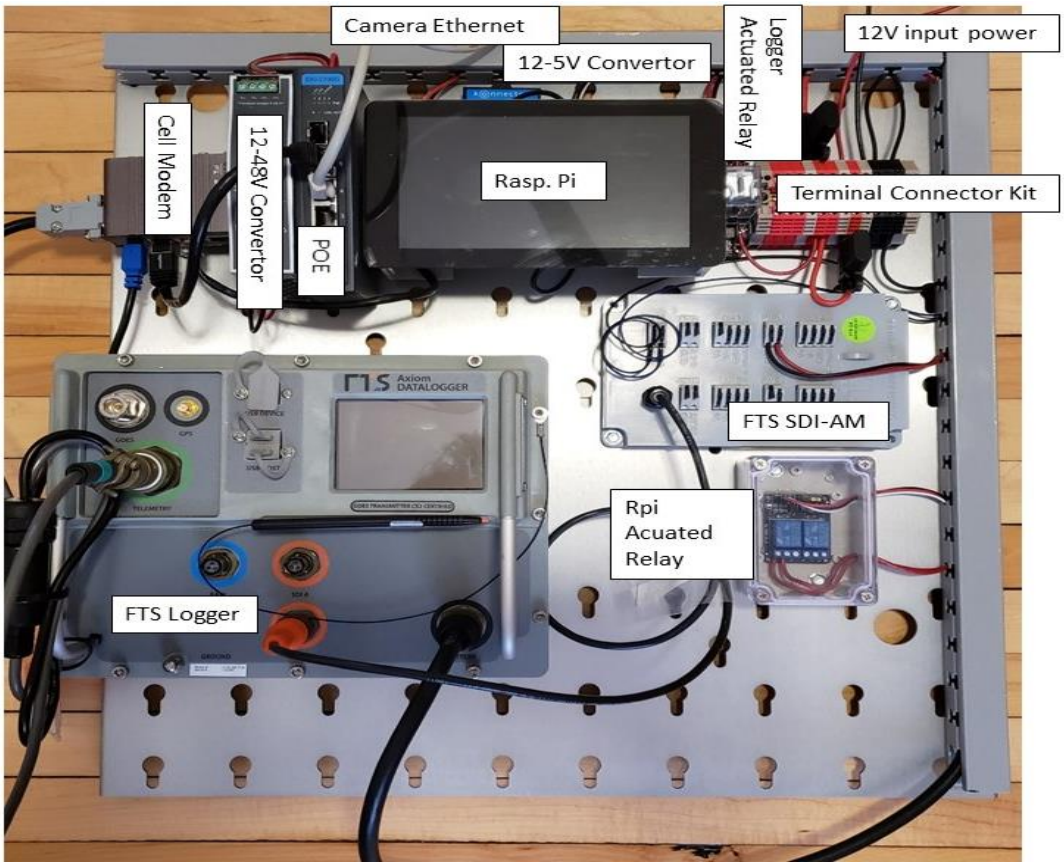

Figure 21: LSPIV camera board setup (Source: James Bomhof, National Hydrological Service, Environment and Climate Change Canada)

Typically, three 20 second videos were recorded per day, although frequency and duration of the videos were increased for field surveys and during high flow events such as freshet in the spring. Frequency was decreased to once per day during summer low flows and in the winter when ice cover was present and there was no water surface to track. A benefit of the setup was the frequency and duration of the cameras could be changed remotely through the RPi.

For orthorectification, a total of 12 GCPs were used to correct the oblique angles (Figure 22). Additionally, 3 cross-sections were established between the GCPs for discharge computation. ADCP transects were taken at cross-section 2 to validate the LSPIV results and real-time flow data.

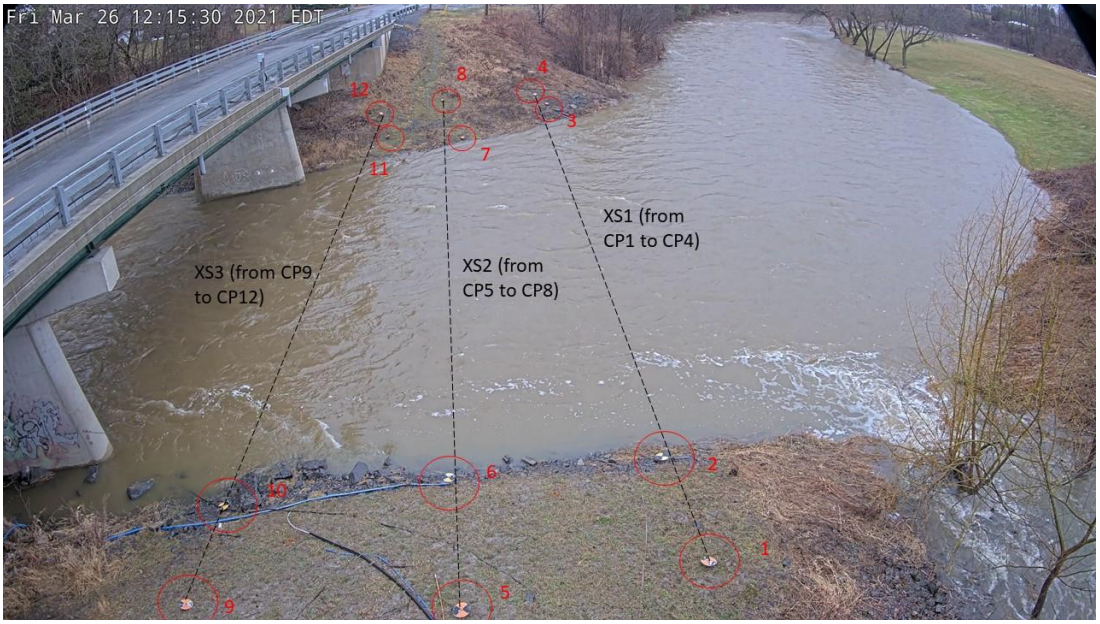

Figure 22: Ground Control Points and the corresponding surveyed cross-sections at the Castor River from the view of the Gaugehouse Camera. Flow is from right to left.

3.1.1.1.1 ADCP Specifications

Three different ADCP models were used during the surveys by moving boat deployment with a tagline. A Sontek M9 river surveyor was used on May 5th, 2023, and May 15th, 2024. A Teledyne RiverPro was used on April 8th, 2022, and a Teledyne StreamPro was used for March 21st, 2022, and March 6th, 2024. To compare to the surface velocimetry results from the LSPIV analysis the average of the top 2 ADCP bins were taken. It is also important to note that each of these models have varying specifications which could influence the results, particularly blanking distance and depth measurement. Blanking distance is a user-specified distance where velocities are not measured because the of disturbances caused by both the immersion of the ADCP and near-transducer error caused by ringing. These two specifications can change the depth of the top 2 velocity bins used resulting in some velocities being taken further from the surface than others. These specifications can be seen in Table 3. To try to ensure consistent results despite different ADCP models, the data was postprocessed using QRev version 4.36. Bottom track was the navigational reference used for all surveys except for the March 21st survey performed by ECCC where several warnings were issued by QRev when selecting the bottom track reference. Instead, the GGA navigational reference was used for the March 21st, 2022 survey. When choosing the fit for extrapolating discharge for unmeasurable zones, the automatic best fit selected by QRev was used to ensure consistency for all surveys.

Table 3: Key ADCP specifications for the different models used in the Castor River (Sontek, n.d.; Teledyne Marine, 2006, 2023; USGS, n.d.)

ADCP Model	Blanking Distance	Velocity Accuracy	Depth Range	Velocity Range
Teledyne RiverPro	10cm	±0.25%	0.54m to 100m	±9m/s
Teledyne StreamPro	3cm	±1%	0.1m to 6m	±5m/s
Sontek M9	5cm	±0.25%	0.06m to 40m	±20m/s

3.1.1.2 May 5th, 2023

This survey was conducted by the author and supervisors. In addition to the videos from the three Axis cameras, a stereoscopic camera system was used to collect videos from both banks for a minimum of 30 seconds as well as on top of the bridge near the middle. The aim was to record from a nadir angle on the bridge however the length of the tripod did not extend high enough to be able to see the entire width of the river, so the videos had to be recorded from an oblique angle.

The stereoscopic camera used was a Stereolabs ZED2i camera with a polarizer lens to reduce the impact of glare. Each of its camera's records at a maximum of 30fps with an image resolution of 1920 x 1080 pixels. A focal length of 2.1mm was used to ensure the full width of the river could be seen in the camera FOV. The optical centers of each camera are spaced 12cm apart and the cameras automatically correct for distortion with factory camera calibration. Furthermore, the system includes an inertial measurement unit (IMU), gyroscope, barometer and magnetometer. The key specifications can be seen in Table 4.

Table 4: Stereolabs ZED2i camera specifications (Source: Stereolabs.com, Accessed 15 Aug 2024)

Camera Specifications	
Focal Length	2.1mm
Image Resolution	1920 x 1080 pixels
Temperature Range	-40 to 125 ℃
Camera Spacing	12cm

Validation data for this survey was collected with a Sontek M9 ADCP. A zig zag survey was performed to get a wide spatial distribution across the FOV. The survey began slightly upstream of cross-section 1 on the left bank, it was then pulled diagonally downstream across the width of the river until it reached the right bank. It was pulled back and forth until ADCP data was obtained across all three cross-sections shown in Figure 22. Furthermore, four transects at cross-section 2 were collected to measure discharge (1 transect had to be discarded due to operator error).

Figure 23: Author and supervisors performing an ADCP zig zag survey from May 5th, 2023

3.1.1.3 May 15th 2024

This survey was also conducted by the author and supervisors. Fixed camera recording frequency was increased to every 20 minutes during this survey. Similarly to the May 5th, 2023 survey, a Sontek M9 ADCP was used to collect velocity data. A zig zag survey was performed to obtain near-surface data across the entire FOV, followed by 4 transects at cross-section 2. In addition to ADCP data, ten near-surface FlowTracker2 measurements were taken roughly evenly spaced along cross-section 2. These were later used to check for accuracy of ADCP data near the surface. Lastly, 6 drone videos were collected. Each video varied in both height and angle with respect to the water surface to examine how distance and angle affects surface velocimetry results.

3.1.1.1 ECCC Surveys

Other survey data was provided by ECCC staff for 5 additional surveys with discharge ranging between 5.77 & 57.38m^3/s – March 18th, March 21st, April 8th, and May 5th, 2022 as well as March 6th, 2024. ADCP data was collected during four of these surveys March 18th, March 21st, April 8th, 2022 and March 6th, 2024. The ADCP data collected on March 18th had velocity errors for unknown reasons and while the discharge seemed reasonable in comparison to the rated discharge, it was decided to disregard the data. A Teledyne RiverPro ADCP was used for April 8th while the Teledyne StreamPro was used for the other surveys (Table 3 displays key differences between these models). Drone videos were recorded on March 18th, and May 5th, 2022. Station cameras were recording at various frequencies depending on the survey so the videos with the closest timestamp to the ADCP or drone surveys were used as the comparison.

3.2 Black Canyon Laboratory Experiment

The purpose of the Black Canyon model experiment was to compare stereoscopic image velocimetry to conventional LSPIV in the laboratory and determine if a stereoscopic image system could produce more detailed results than a single camera setup. Permutations of the camera setup were considered by altering a few parameters for each test. Different oblique angles, horizontal separation between the cameras and the distance from the camera to the water surface were examined to determine how a camera's extrinsic properties may impact the stereo reconstruction of an image. This section discusses the creation of the model, equipment used in the study and the data collection processes.

3.2.1 Model Creation & Installation

The 3D printed Black Canyon Lab Model was created by Saber Ansari. A 2,227m reach of the canyon had previously been surveyed using multiple ADCPs and a Reson 7125 multibeam echosounder during both moderate flow (5500 m^3/s, June 2016) and low flow (2175 m^3/s, August 2016). An additional ADCP survey occurred in September 2009 at 1820 m^3/s (Venditti et al. 2014; Rennie et al. 2018). Mean flow is 2,730m^3/s (Rennie et al., 2018). Zig zag ADCP transects were taken at multiple sections of the reach. Boat passages with the multibeam echosounder enabled collection of the canyon bathymetry. The data collection procedures are described in Hurson et al., 2022, although that paper focuses on Alexandra Canyon downstream of Black Canyon. The

bathymetry data did not cover the upper portion of the canyon walls, thus the elevation data were extrapolated to the top of the canyon walls using Google Earth elevation data.

An 11 m long 3D model of the canyon was 3D-printed. The canyon DEM was used to create a SolidWorks model and then transferred to Civil 3D. The model was then split into eleven separate sections, each section was further divided into 20cm x 20cm x 5cm subsections where a STM file was created and printed. It is important to note that meandering sections of the Black Canyon had to undergo a straightening process in the building of the model in order to have a straight model in the flume. The 3D-printed pieces of the canyon surface were attached to one another using contact cement and the underlying support structure comprised of construction foam was attached using wood glue. Then they were installed into 1-meter-width aluminum boxes and assembled in the University of Ottawa hydraulics laboratory flume. The model used a length scale of 0.00494 or approximately 1:202 while the discharge was scaled with the following equation.

$$Q_t = {L_t}^{5/2}$$

Equation 6: Black Canyon model discharge scaling equation

Where Q_t is the discharge scale and L_t is the length scale. The model was scaled to be run in a flume with flows ranging from 3 to 15 litres per second, equivalent to Black Canyon flows of 1,750m^3/s to 8,745m^3/s which is a typical range of flow that would be seen in the canyon.

During installation, a problem occurred that resulted in an improper setup of the model. This resulted in the model having a positive gradient throughout. To resolve this, point gauge measurements were taken along the thalweg of the channel to determine if sections could be removed to produce a negative slope. The final section of the model was removed to achieve this. Unfortunately, the errors made it so that the model was no longer an accurate representation of the Black Canyon and was instead used just as a generic canyon model with complex flow fields (Figure 24).

Figure 24: Upstream end of the canyon model facing downstream

3.2.2 Data Collection

The section of interest in the model that was chosen was between 6 and 6.75m in the x-direction (streamwise). The section was chosen based on video collected by Ansari et al., 2018 who used LSPIV to estimate the surface boil velocity in the ROI (Figure 25).

Figure 25: Left) Region of Interest (ROI) in the Black Canyon (Ansari et al., 2018) Right) NADIR view of ROI in lab model

The experiment was performed over an extended period of time resulting in data being collected on different days. The flume did not have a flow meter so flow would be based on water level of the section of interest. To get proper ADV measurements the model had to be run near-bank full conditions. To replicate flow conditions between runs, markings were applied at

the upstream and downstream sections of the model on both left and right banks to where the desired water level should be. Additionally, the flow valve was marked to ensure it was opened to the same flow for each run.

In the field of view cross sections were marked every 10cm between 6.15m and 6.55m in the x-direction (the last two cross-sections are shown in Figure 25) to facilitate comparison of velocity measurements obtained from the ADV and the image velocimetry results. A total of 16 GCPs were setup in the section with 8 below the water surface and 8 more along the banks with 4 on either side. These can be seen in Figure 26.

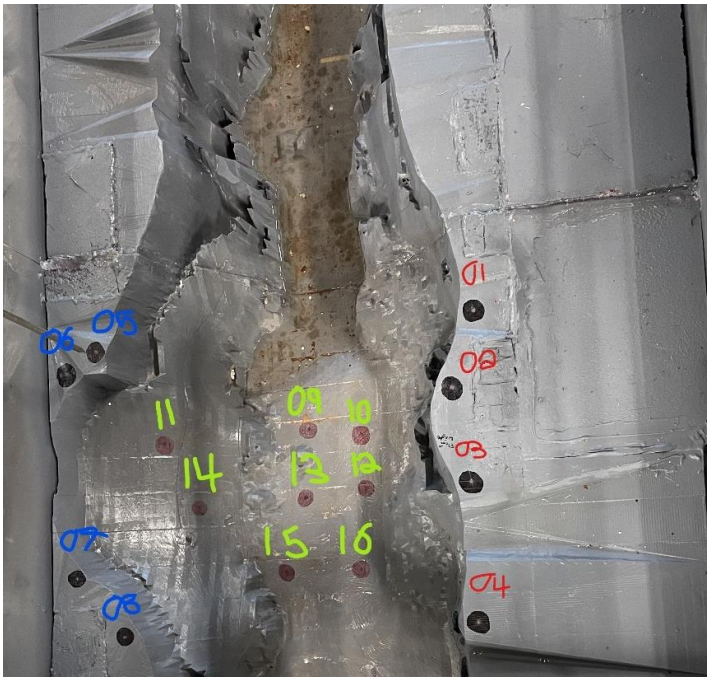

Figure 26: Ground Control Points in the section of interest for the canyon model

3.2.2.1 Equipment

Three separate cameras were fixed above the Black Canyon model. Two Acti A310 cameras with an image resolution of 2688 x 1520 pixels, and a focal length of 2.8mm with wide angle lenses (Table 5). They were fixed on an adjustable mount custom built in-house that is shown in Figure 27. The mount was adjustable along the y-axis, and x-axis. Additionally, the cameras can be rotated at their base to alter the angles of the camera. The cameras were connected to an ethernet switch using ethernet cables and a laptop was connected to the switch to access the camera interfaces. The other camera used for video collection was the Stereolabs ZED2i

stereoscopic camera (also shown in Figure 27); key specifications were previously detailed in Table 4. The camera was mounted to an adjustable tripod and connected directly to a laptop for video collection.

Table 5: ACTi A310 Camera Specifications (ACTi Corporation, n.d.)

Acti A310 Camera Specifications	
Image Resolution	2688 x 1520 pixels
Focal Length	2.8mm
Frames per second	30fps

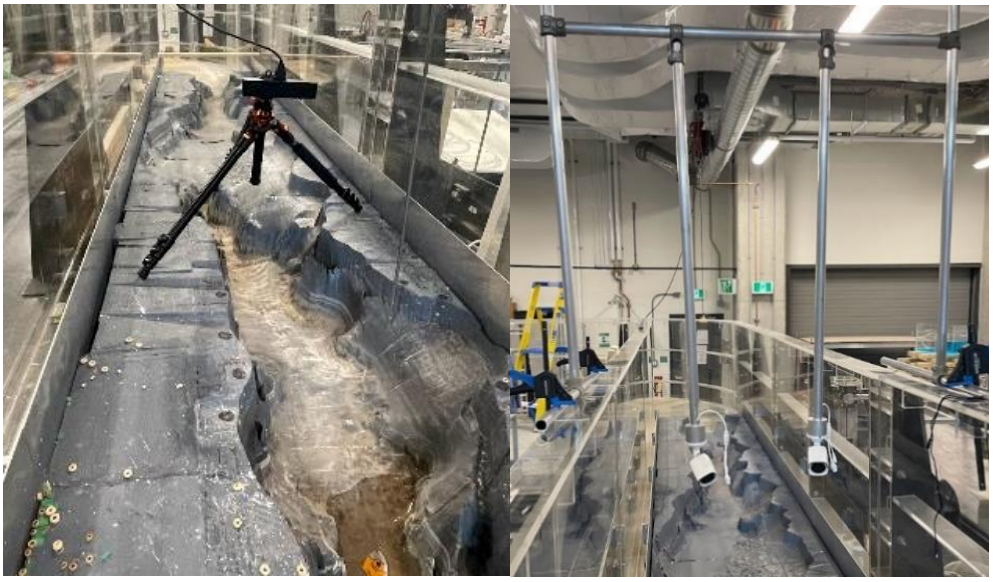

Figure 27: Camera Setups for the canyon model. Left) Stereolabs 2i camera on an adjustable tripod. Right) Acti A310 cameras on adjustable mount

A Vectrino sidelooker ADV probe was used to obtain velocity measurements near the surface and for full cross-sections. The probe was a four-beam configuration with the intersection point being 5cm from the central transducer where the sampling volume occurs. An example of the sidelooker probe can be seen on the left of Figure 28. For depth and water surface elevation measurements a point gauge was used for both streamwise and cross-stream measurements. Lastly, it was decided to use cheerios as tracer particles which will be discussed in more detail later in this section.

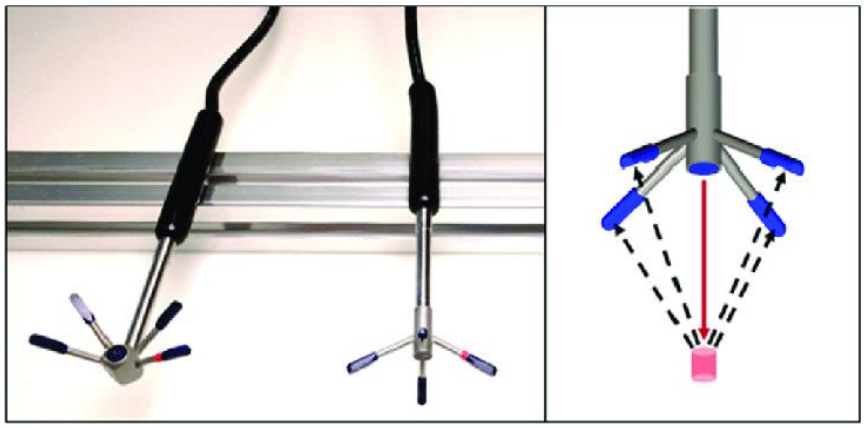

Figure 28: Sidelooker and downlooker ADV probes where the right side displays the location of where the four beams intersect to obtain velocities. This is known as the sampling volume.

3.2.2.2 Video Collection

Before each lab session the Acti cameras were manually time synced, as they frequently had errors where the times of each camera would fall out of sync. A total of 20 videos were collected from each Acti camera. The starting height used was 38cm above the water surface (Note: The height was chosen based on a ruler marked on the mount and was 70cm from the base of the mount). Videos were recorded with the two cameras placed on either side of the channel centreline, at 5 different horizontal spacings. At camera separations of 20cm, 30cm, and 40cm, videos were recorded from nadir. At 50cm and 60cm apart the cameras were pointed towards the center of the canyon model at an oblique angle to replicate the field site setup. Videos were recorded for a minimum of 30 seconds with tracer particles in the FOV. After recording all 5 videos at 38cm above the water surface the height was increased by 10cm and the process was repeated for a total of 4 heights – 38cm, 48cm, 58cm, and 68cm.

The ZED2i was attached to the tripod and setup with a NADIR view of the canyon model. The camera was setup at a similar height to the Acti cameras, however, it was a challenge to obtain the exact height and there was a difference of up to 5cm in height between the two camera setups. For each height of the Acti videos at a separation of 20cm, one video was also recorded with the ZED2i camera for a minimum duration of 30 seconds. Additionally, two more videos were taken with the ZED2i camera separate of the Acti configurations. These were taken at 60 and 70cm above the water surface with a duration of at least 30 seconds.

3.2.2.3 ADV Velocity Measurements

A sidelooker Vectrino ADV probe was used to collect velocity measurements. A benefit of sidelooker probes is that only the lower two beams need to be below the water to obtain cross-stream and streamwise velocities so the probe can get very close to the water surface allowing for comparison to image velocimetry results. The ADV was mounted overtop of the model with a scale on the y-axis and z-axis. Near-surface measurements were taken at 5 different cross-sections spaced every 10 centimeters in the section of interest between 6.15m and 6.55m along the x-direction. For each cross-section, measurements were collected with 2cm spacing between each measurement across the y-axis. Additionally, two full velocity sections were collected at 6.15m and 6.45m. Each cross-section was split into five different vertical profiles, starting at the center of each cross-section followed by two more vertical profiles on either side. The number of intervals and spacing for each interval collected was dependent on water depth. Data was more densely collected near the surface and near the channel bed with less density in the middle of the vertical.

At 6.15m, 15 points were collected in the center, 5 in the center left vertical, 3 points near the left bank, 5 points in the right center profile and 5 points near the right bank. At 6.45m, 16 points were collected in the center profile, 10 points were collected in the center right profile, 3 near the right bank due to shallow depths near the canyon wall. 16 points were collected in the center left profile and 8 points collected near the left bank.

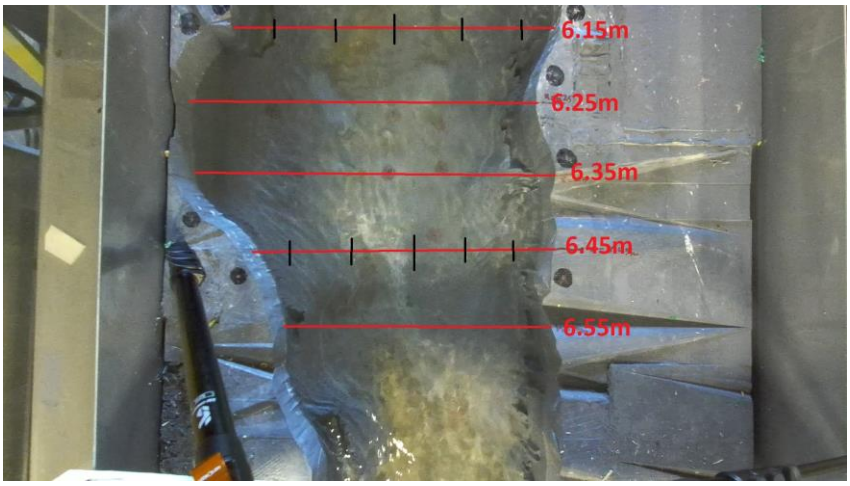

Figure 29: Approximate locations of the ADV sampling, where the black ticks represent the location of each vertical profile sampled and the red lines indicate the cross-section. Spacings of 2cm were used for the near surface measurements which were performed at all red lines.

The beam with the red label (displayed in Figure 28) was always oriented downstream. Thus, it was not possible to measure within 5cm of the right bank as the sample volume is 5cm from the probe tip. Consequently, measured velocity data were extrapolated to obtain the full cross-section.

3.2.3.5 Tracer Particles

Extensive testing was done to determine the best particles to use for seeding the water surface. When testing the variety of tracer particles examined, the following factors were considered.

- Pixel Size – The ideal tracer particles should be > 1 pixel and somewhere between 2-5 pixels per particle (Jolley et al., 2021). With varying camera heights this becomes a challenge without using different particles for each camera height.
- Pixel Shape – A uniform particle shape – i.e. circle or square – is ideal due to the complex flow of the canyon model. Vorticity effects from the flow can cause particle rotation that is more pronounced in non-uniform shapes.
- Pixel Colour – The colour of the pixels should be the same and they should contrast the colour of what they are floating in so the PIV algorithms can clearly distinguish where the water surface is.
- Pixel Separation – Pixels should ideally be spaced out and not clumped together so the water surface is still visible.
- Buoyancy – Since the PIV algorithms track the surface of the water, it is important that all of the particles are buoyant and remain above the surface.
- Cost – Due to the number of tests, and the duration of each test, a large number of tracer particles is required. This makes the cost of particles an important factor that must be considered.

The first particles considered were small green Styrofoam pellets approximately 2-3mm in diameter which fit the necessary pixel size based on the initial camera height. However, when seeding the water with these particles they conglomerated and floated through the center of the canyon model. This could have potentially been solved with the use of a surfactant, but a

surfactant would change the water surface tension, and thus may influence the flow behaviour. A company called Cospheric that specializes in manufacturing small PIV particles considered next. They offered a good selection of fluorescent PIV particles, with a couple options that were near the size needed for the canyon model. The constraint in this case became the cost, with small quantities of particles costing anywhere between $100- $500, which was not feasible for the number of tests to be conducted. Next, green rectangular confetti was tested, and because they were rectangular strands, they needed to be ripped up. This was done by hand, but it was not possible to create uniform square pieces. The water was seeded in a test run with these particles but because they were non-uniform rectangular pieces they rotated due to the complexity and vorticity of the flow. After further searching, a square confetti was found and tested, but it was insufficiently buoyant with a considerable amount of them becoming entrained in the water as they moved downstream. Sequins were tried but similarly to the square confetti not all of them stayed on the surface as they travelled downstream. Mini soft pom poms were tried but also lacked buoyancy. Glitter was tested, but the cameras were unable to see the glitter likely due to light reflections on the glitter making them invisible to the cameras. Lastly, cheerios were tested. They did not get stuck together nearly as much as other particles tested, they contrasted very well with the grey colour of the canyon model, were all buoyant and the circular shape of the cheerios is ideal as a tracer. The only con of the cheerios was they were larger than the ideal size at around 8-12 pixels per tracer. However, since they were closest to meeting all criteria, they were selected for the testing. Table 6 summarizes the particles tested and how they scored against the criteria used.

Table 6: Tracer particles tested and results for various criteria employed

Tracer Particle	Pixel Size (~Diameter)	Pixel Shape	Pixel Separation	Pixel Colour	Buoyancy	Cost
Styrofoam Pellets	In the ideal range (10mm)	Circular & Uniform	Sticks together	Contrasted model colour	Remains on the surface	Low Cost
Cospheric Particles	Smaller than ideal range (1.4mm)	Circular & Uniform	Never tested	Contrasted model colour	Never tested	Very high cost
Rectangular Confetti	Larger than ideal range	Non-Uniform	Moderate clumping	Contrasted model colour	Remains on surface	Moderate Cost
Square Confetti	Larger than ideal range (30mm)	Uniform	No clumping	Contrasted model colour	Mixed buoyancy	Moderate Cost
Sequins	In the ideal range (10mm)	Circular & Uniform	No clumping	Contrasted model colour	Mixed buoyancy	Low Cost
Mini pompoms	In the ideal range (5mm)	Circular & Uniform	No clumping	Contrasted model colour	Not buoyant	Low Cost
Glitter	Smaller than ideal range (<1mm)	Circular & Uniform	No clumping	Invisible to cameras	Mixed buoyancy	Low cost
Cheerios	Larger than ideal range (20mm)	Circular & Uniform	Minor clumping	Contrasted model colour	Remains on surface	Low cost

When seeding the flow upstream of the section the majority of tracers would remain in the middle of the flow or move towards the left bank. As the right bank widens at the embayment, tracer particles were not travelling into it due to the flow pattern and higher flows being present elsewhere. There was also recirculating flow in the embayment. This resulted in tracers requiring extra time to exit the embayment and move further downstream. An additional consequence was some tracers got stuck along the right bank. Due to this, along the right bank of the model additional tracers were added before recording the videos. Only when tracers moved out of the embayment the left bank began to start seeding the flow and the video recording began.

3.3 Multi-Camera LSPIV Processing

After data collection, the next step was image processing. The following sections detail the use of the Rectification of Image Velocimetry Results (RIVeR) software and the MATLAB scripts that were written to process collected data (Figure 30).

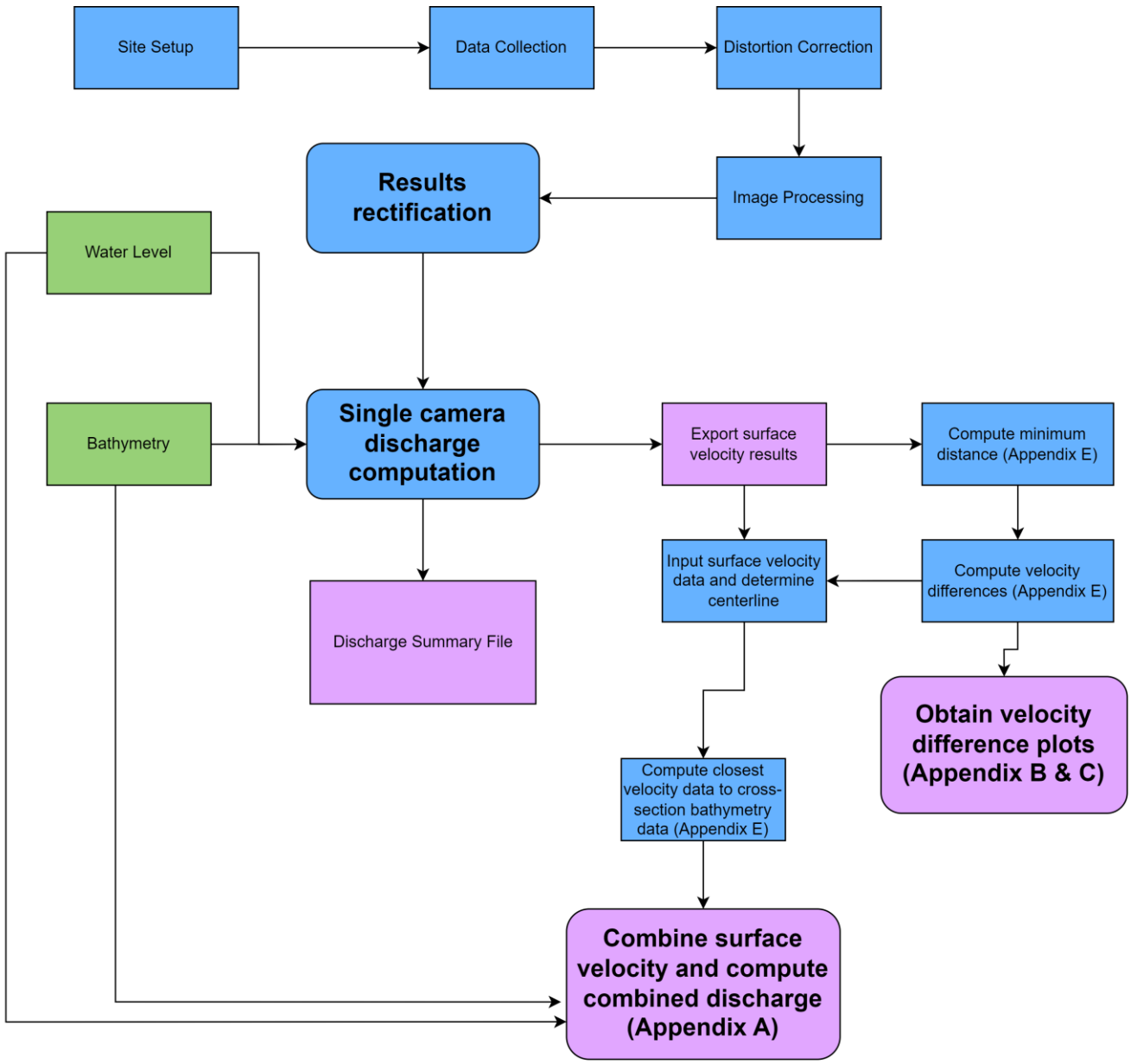

Figure 30: Multi-Camera LSPIV Workflow Diagram

3.3.1 Camera Calibration

As previously mentioned in the literature review, the majority of cameras have image distortion, particularly on the edges where the light rays will cause objects to bend. It is recommended that the distortion is corrected prior to image processing, and to do lens distortion correction several of the camera's intrinsic parameters must be known. Some camera manufacturers will do the camera calibration in the factory and make the results available for users (e.g., the Stereolabs camera that was used), however in many cases the calibration must be done by the user.

Both the Acti A310 camera and the AXIS P1378-LE cameras were calibrated in the lab with the AXIS calibration being performed by ECCC staff. AXIS camera calibration was performed using Agisoft Lens while the ACTi cameras were performed using the MATLAB stereo camera calibrator app. The principle for both is the same. The intrinsic parameters that camera calibration solves for are the focal lengths (f_x and f_y), the camera's optical center (c_x and c_y), the radial distortion factors (denoted as k_1,… k_n where n can equal up to 5 but typically defaults to 3), tangential distortion factors (p_1 and p_2) and the camera skew.

The AXIS cameras were calibrated in the ECCC warehouse with the lens fully zoomed out similar to typical field conditions. Additionally, AXIS camera have the ability to remove distortion prior to video recording. This feature was used for the gaugehouse camera, however it could not be used for the bridge cameras because the FOV became smaller resulting in a loss of visibility of some GCPs. For that reason, the bridge cameras had to be calibrated manually. For the ACTi camera calibration, a large checkerboard was placed in the flume and moved around the 2 cameras' fields of view to obtain a minimum of 20 image pairs. Figure 31 shows an example of what the calibration checkerboard looked like in a camera's FOV and demonstrates how distortion occurs as the straight outside edge of the checkerboard appears to be bending in the image. For every image pair the following criteria were attempted to be met.

- Checkerboard should be at least one-third the size of the total image.
- Checkboard should not be more than a 45-degree angle between the camera and image plane.

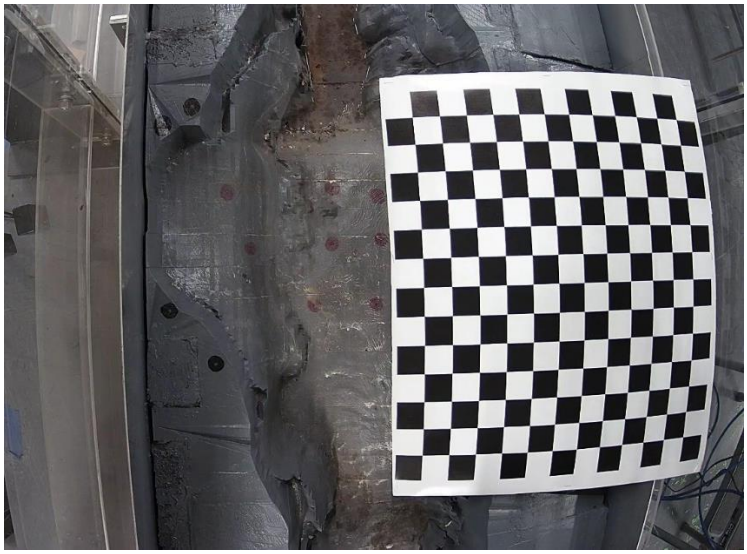

Figure 31: Calibration checkerboard sitting in laboratory flume

It is a challenge to meet these criteria when working with stereoscopic imagery particularly in a non-nadir system. When the cameras are both at oblique angles to the water surface, keeping the checkerboard at less than a 45-degree angle to the camera plane is difficult (Figure 32).

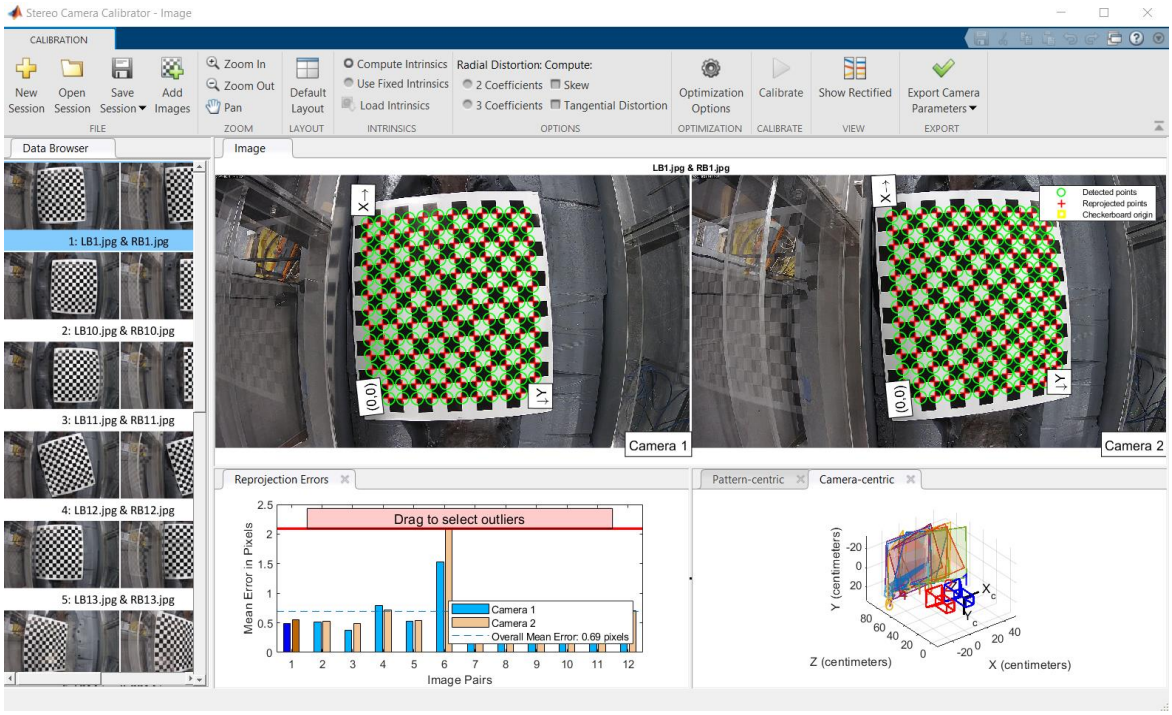

Figure 32: MATLAB Stereoscopic camera calibrator app

After calibration is performed, the app displays the error for each image pair as seen in the bottom left of Figure 32, where outliers can then be removed and the dataset reprocessed. Any high error pairs were removed during this study. Acceptable errors were deemed to be 1 pixel or less. Once satisfied with the levels of error in the dataset, the intrinsic parameters were applied to the images to remove the lens distortion as shown in Figure 33.

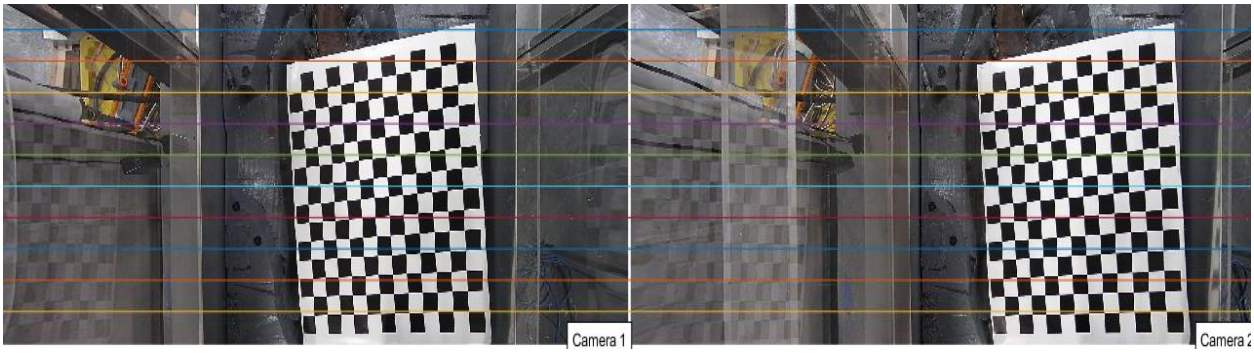

Figure 33: Distortion corrected image pair in MATLAB

3.3.2 Rectification of Image Velocimetry Results (RIVeR)

RIVeR is an application built through MATLAB by Patalano et al., 2017 for the purpose of LSPIV processing and orthorectification. It was chosen for multiple reasons. It has a very simple user-friendly workflow with PIVLab embedded in the application, it is free to use and had been previously tested by ECCC. The following sections break down each step of RIVeR as illustrated in Figure 34.

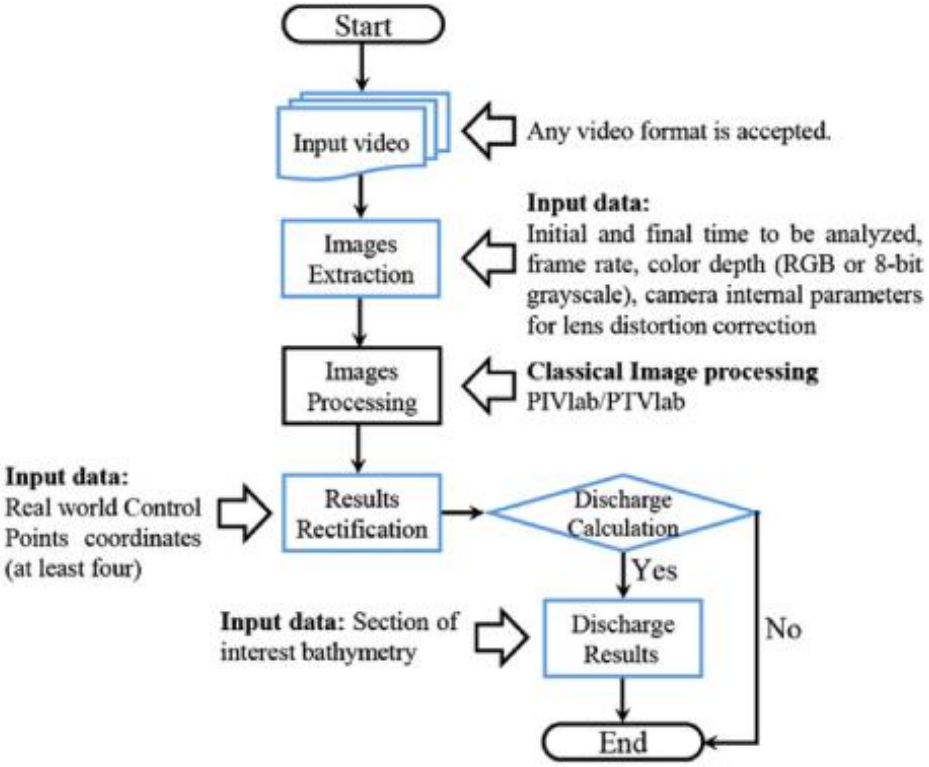

Figure 34: RIVeR flowchart (Patalano et al., 2017)

3.3.2.1 Video Input & Image Extraction

The first step was to convert the video formats of the AXIS cameras. These cameras recorded videos with a .mkv codec and while most video formats work in RIVeR, .mkv is not one of them. A multimedia framework called ffmpeg was used to convert the video codecs to mp4. A simple batch file was setup with the following code to perform this task for all videos at the same time.

for /r %%i in (.mkv) do ffmpeg -n -i %%i -codec copy %%~ni.mp4*

The resulting mp4 files were then loaded individually into RIVeR and image extraction was performed. Figure 35 shows what the image extraction window looks like. The step specifies if consecutive frames are used or every other frame and so on. A step size of 1 indicates consecutive frames while a step size of 2 would be every other frame extracted. The time range allows for a smaller video size to be extracted, reducing processing costs. The image resolution can be reduced, and the images can be made grayscale, both to reduce processing time. In this study five

seconds of each video were extracted, the image resolution was kept at 3840 x 2160 pixels, and they were left in colour. Additionally, lens distortion was corrected in this step. The intrinsic camera parameters determined by camera calibration were inputted into RIVeR and lens distortion was removed using Equation 7.

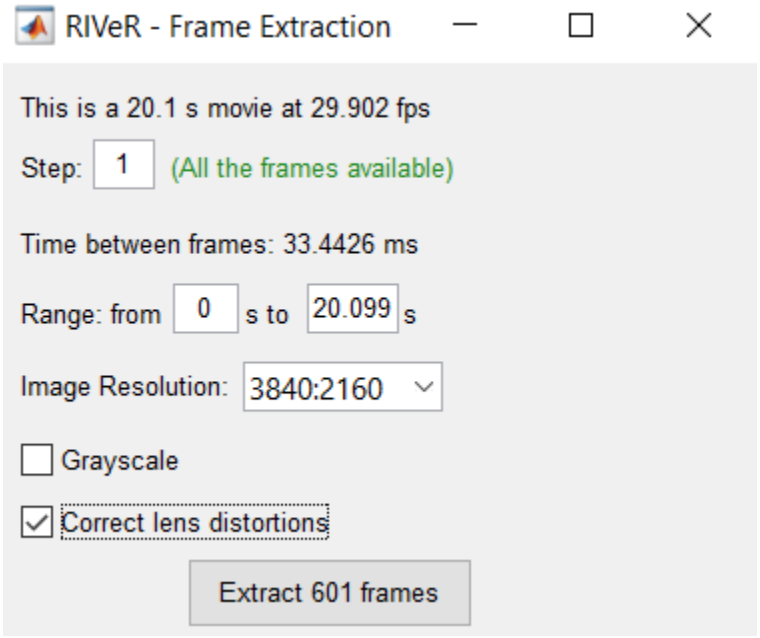

Figure 35: Image extraction window in RIVeR from an AXIS camera recording of the Castor River

$$\begin{pmatrix} X_p \\ Y_p \\ 1 \end{pmatrix} = KK \begin{pmatrix} X_d \\ Y_d \\ 1 \end{pmatrix}, \quad \text{where } KK = \begin{pmatrix} fcx & alpha0*fcx & ccx \\ 0 & fcy & ccy \\ 0 & 0 & 1 \end{pmatrix},$$

Equation 7: Distortion correction equation used by RIVeR (Patalano et al., 2017)

Where X_p and Y_p are the corrected pixels, X_d and Y_d are the distorted pixels, and KK represents the cameras intrinsic parameters matrix. With the extraction window completed, the frames were then extracted and saved on the desktop.

3.3.2.1 PIVLab

Following the workflow in Figure 34, the next step is image processing. The image processing is done using PIVLab developed by (Thielicke, 2014). After loading the images, the first step was to select the ROI and apply masks to the banks, so the algorithm does not search for velocity vectors outside of the wetted perimeter. The ROI is a user-defined box, and the software only analyzes displacement inside of the ROI. Masks were defined in one frame and then applied to the series of images. Figure 36 demonstrates what the typical ROI and masks looked like for this study. A CLAHE filter was applied for pre-processing as shown in Figure 37. This filter was used to enhance the images to be better able to detect velocity vectors.

PIVLab includes three different correlation algorithms: direct cross-correlation (DCC), direct Fourier transform (FFT) and ensemble correlation. The ensemble correlation is used when tracer particles are lacking in density (Thielicke & Sonntag, 2021), which was not the case in this study. Both DCC and FFT were tested, with FFT producing less spurious vectors. FFT is what typically delivers the best results (Thielicke, 2014). FFT uses a multiple pass approach where the interrogation windows become smaller with each pass. It is recommended that the first pass has a large interrogation window because it will give a better signal-to-noise ratio, but smaller passes will give a higher vector resolution (Thielicke, 2014). A 2-pass FFT algorithm was used in this study with the interrogation areas ranging between 32 to 128 pixels depending on the tracer particles and velocity.

Figure 36: User-defined region of interest with masked banks for a left bank video at the Castor River

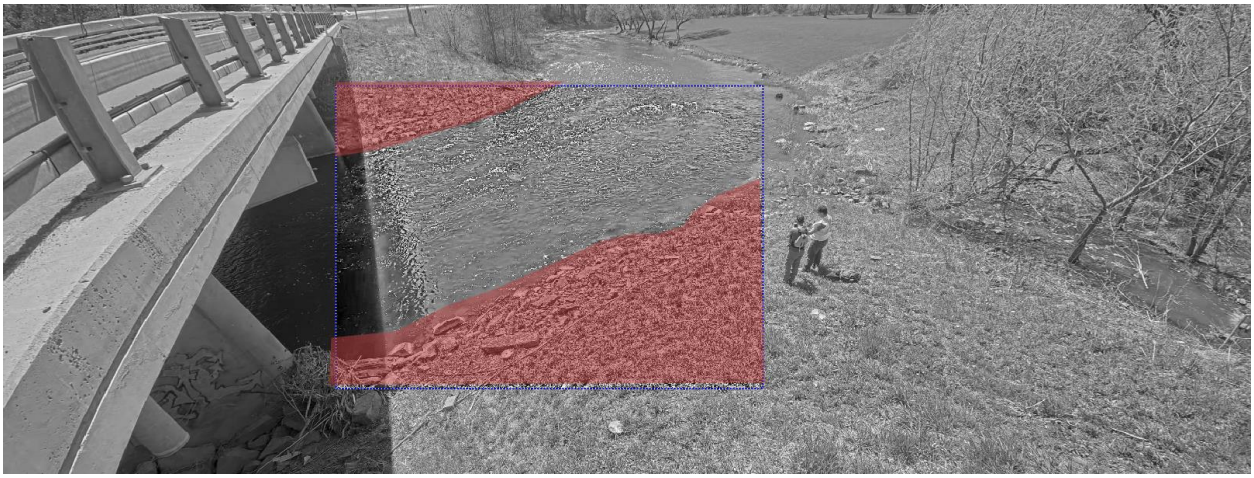

Figure 37: Example of an image frame with the CLAHE pre-processing filter applied

After all image pairs have been processed, the median velocity field is calculated and appended to the end of the time-series. Velocity filters were also applied. Due to the number of videos processed the post processing filtering was kept simple. Both a standard deviation and local median filter were applied to every dataset. The local median filter considers velocity fluctuation within a 3x3 area around a single vector. The default value of 3 was used for the local median filter while the default value of 8 was used for the standard deviation filter. Additionally, the option to interpolate any missing data after removing outliers was applied so there were no gaps in the data.

3.3.2.3 Image Rectification

PIVLab results are presented in units of pixels per frame so the dataset must be orthorectified to obtain results in m/s. A spreadsheet containing the image coordinates as well as the real-world coordinates is imported into RIVeR and the GCPs are defined on the image as seen in Figure 37 to confirm coordinate accuracy. As mentioned, in the literature review, only six GCPs are needed for 3D image rectification (W. Li et al., 2019), and there are 12 GCPs at the Castor River both for increased accuracy in the image rectification (Jolley et al., 2021), but also for redundancies. In some videos not all GCPs were able to be used. An example is shown in Figure 37 where GCP11 was not used as it was submerged below the water surface. There are several videos where GCPs are either submerged beneath the water surface, hidden behind vegetation, glare or not in the FOV in the case of some drone videos. Next, the water level and the region of interest were defined. The water level was defined based on the gauge station water level at the

closest recorded time to the video timestamp, and RIVeR assumed that the elevation was the same as the defined water level. The ROI coordinates were defined by importing the real-world easting and northing coordinates (GCP2, GCP3, GCP10 and GCP11 were the four corners used).

Figure 38: Imported ground control points marked on an image of the Castor River

Finally, the timestep between frames was defined in milliseconds. This can be user-defined however RIVeR also determines it automatically during image extraction. Results are given as a magnitude or as a vector field shown in Figure 39 with the velocity in the same units as the defined coordinate system. The mean surface velocity vector fields were then exported from RIVeR as four separate excel sheets (Easting, Northing, Easting velocity, and Northing velocity). The method to analyze and compare the surface velocity fields between cameras will be explained further in 3.4 Matlab Processing, while the next section will detail how RIVeR computes discharge of a cross-section.

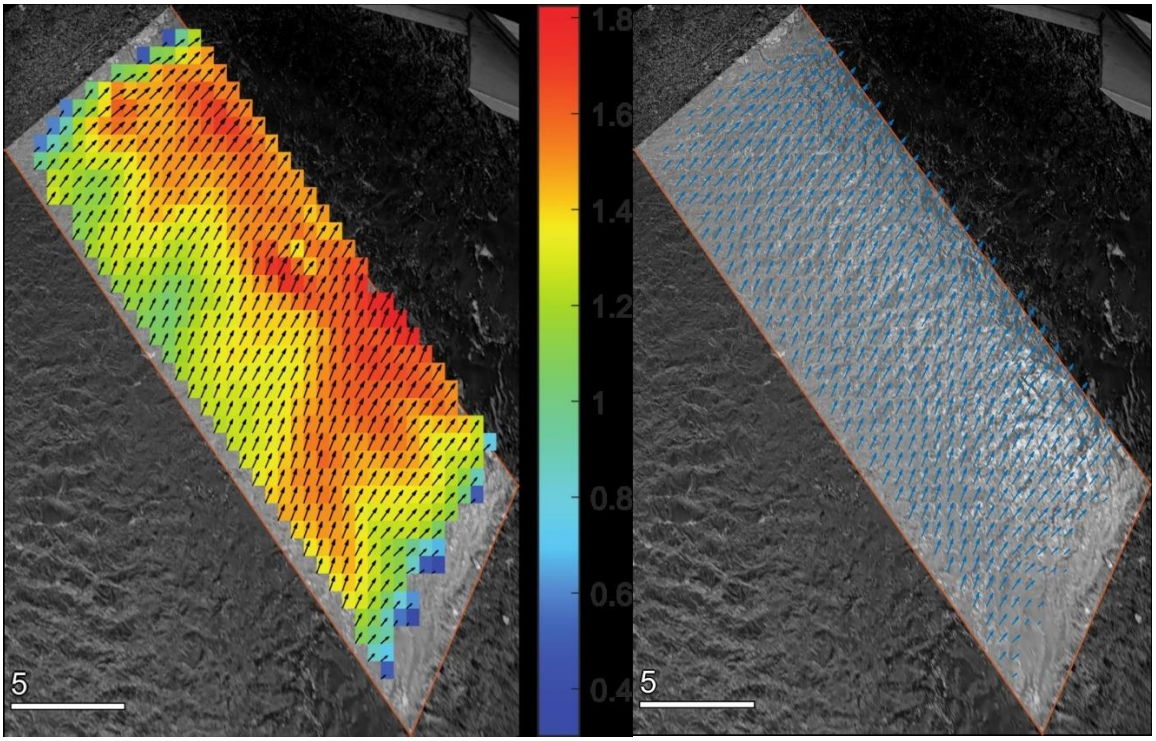

Figure 39: Left) Median magnitude field of a video at the Castor River produced in RIVeR. Right) Median vector field from the same Castor River video processed through RIVeR. The scale bar unit is in meters.

3.3.2.4 Discharge Computation

Discharge at a cross-section can be determined using bathymetry data and water level. As previously shown in Figure 22, the Castor River was setup with 3 cross-sections and bathymetry data was taken at all of them. However, only cross-section 2 was used in this study.

The first step was to define the cross-section. The cross-section could be defined by the coordinates of the start and end of the cross-section whether in pixel coordinates or the real-world coordinates, or it could be defined by manually defining a line from the left to right bank on either the original image or the orthorectified image. Selecting the cross-section accurately did end up being somewhat challenging due to likely error in the orthorectification on the far shore. The cross-section should start and end at the control points, however when entering the real-world coordinates of those points, they did not always show up on the image where the control points were supposed to be. In some cases, the lines were moved before finalizing the cross-section in an effort to match them more accurately to the bathymetry data.

After defining a cross-section, AreaComp2 is used, a separately developed tool that is embedded in RIVeR. AreaComp2 is a tool developed by USGS to analyze ADCP data and obtain a relationship between channel area and stage (Figure 40) (Lant & Mueller, 2012). Adapted for LSPIV, the bathymetry file can be inputted, and the water level is defined. Then a surface coefficient (alpha) can be applied – how the surface coefficient was calculated will be discussed in the following section. Additionally, the number of verticals can be defined in RIVeR's main window. It is recommended that 20 to 25 verticals be used when computing discharge (Environment and Climate Change Canada, 2021); in this study, each cross-section met the minimum of 20 verticals. There are two methods available to compute discharge: mean-section or mid-section method. ECCC guidelines state the mid-section method should be used (Environment and Climate Change Canada, 2021). RIVeR then computes discharge by interpolating the velocity data along the cross-section linearly. If there is no data along a portion of the transect then it is considered null (Patalano et al., 2017). Figure 38 shows the GUI of AreaComp2 while Figure 41 shows the discharge split into verticals across the cross-section.

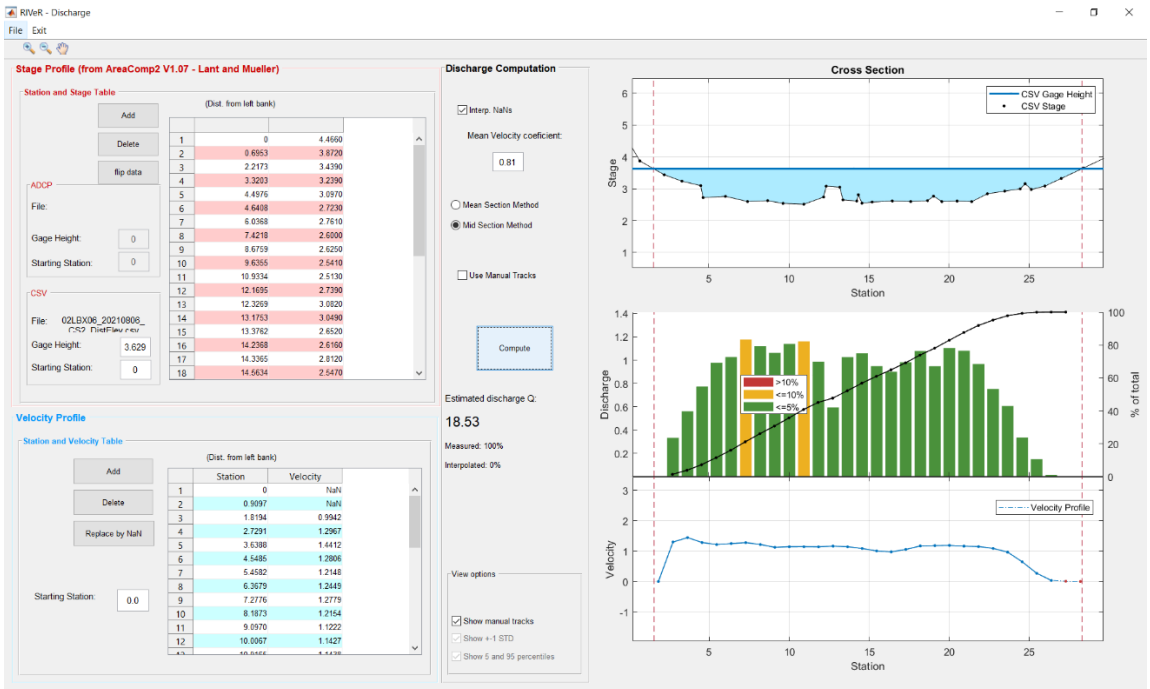

Figure 40: AreaComp2 GUI after determining discharge of a cross-section

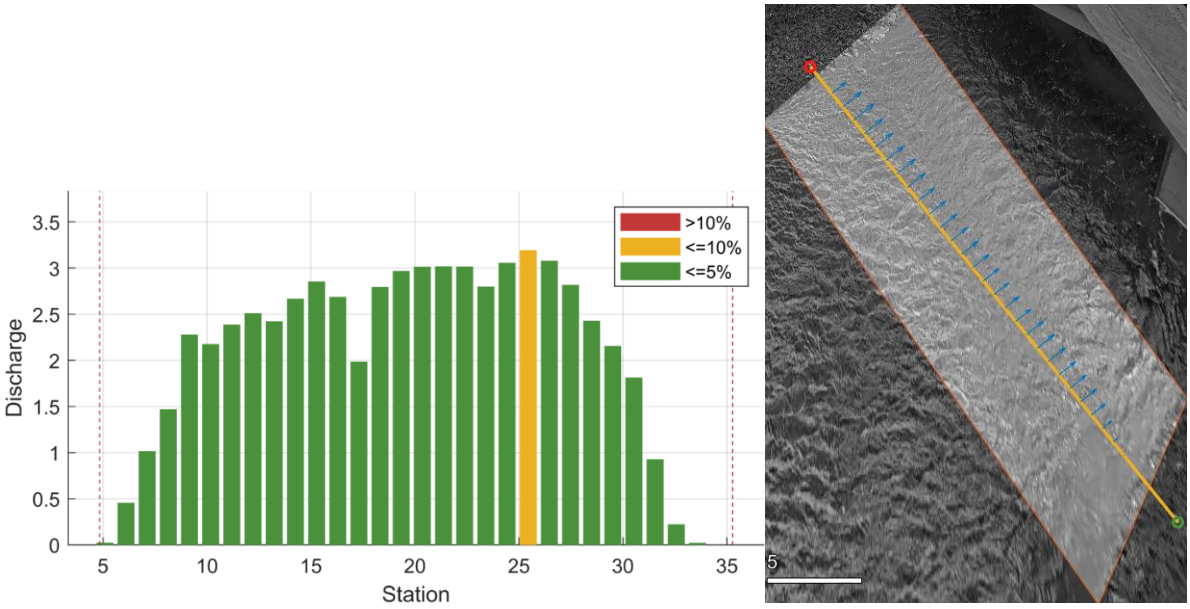

Figure 41: Left) Discharge at the cross-section broken up into verticals. The colour scale represents the percentage of discharge contained in each panel. Right) Verticals shown as velocity vectors on the rectified median image

3.3.2.4.1 Determination of Alpha

Work on determining a site-specific alpha value at the Castor River has been done by James Bomhoff at ECCC. Alpha was found using both a power-law fit, and a constant no-slip fit for a diverse range of flows and plotted against discharge as shown in Figure 42. Power, logarithmic and linear trendlines were all added, and alpha was calculated using each trendline equation. In the end, the linear trendline was chosen because both the power and logarithmic equations resulted in some alpha values that were too low compared to literature values.

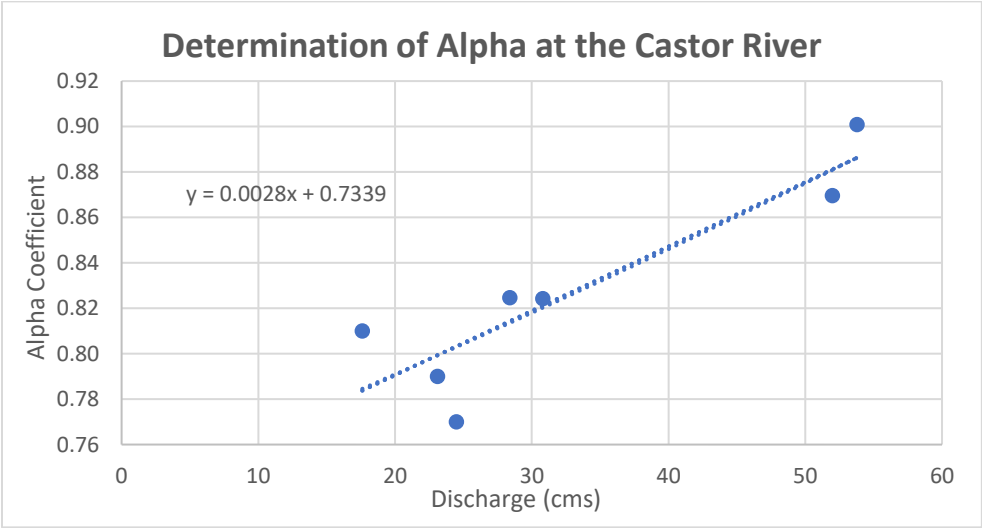

Figure 42: Discharge vs Alpha at the Castor River from several surveys

3.4 Matlab Processing

This section goes through the different detailed MATLAB scripts that were written to process the collected data. Additional smaller, less complex scripts, as well as the code for these scripts can be found in the appendices.

3.4.1 Velocity Difference Code

Unfortunately, despite using the same regions of interest for every camera in a survey the velocity fields do not completely line up with each other, making it a less than straightforward process to compare the vectors between the different measurements. A code was developed to spatially compute the closest vectors between the different methods that were used to compute surface velocity.

The code was setup to be able to compare all methods of LSPIV (Cameras) and validation (ADCPs) to one another. The process of comparing methods was very similar for most methods but to compare all of them at once it was easier to include all methods in one script. The script loops through the x and y coordinates of both methods computing the distances between methods with the following equation.

$$Distance = \sqrt{(x_2 - x_1)^2 + (y_2 - y_1)^2}$$

Equation 8: Distance between two points

When the minimum distance was found between two points, the cell locations were stored and the minimum distance for the next point of one of the cameras was searched for. These minimum distances were stored in a new matrix, as well as the cell numbers for those minimum distances which were then used to calculate the velocity differences. If the distances in the matrix were under a certain threshold – 0.5m for camera comparisons or 1.0m when compared to the ADCP survey – then the velocity differences would be calculated with the u and v-vectors being compared separately and then the magnitude of these differences was determined with the following equation.

$$Velocity\ Difference\ Magnitude = \sqrt{(u_{diff})^2 + (v_{diff})^2}$$

Equation 9: Velocity magnitude difference equation

As stated, these differences were found for all comparison methods, they were then plotted using the surf plot function in MATLAB. In addition to these plots, the mean absolute error (MAE) was found for each comparison method. The velocity differences were determined using both the actual differences as well as normalized differences. To normalize the plots the difference magnitudes were divided by the average surface velocity for the survey. The average surface velocity was found by dividing the wetted area by either the ADCP discharge or gauge station discharge if there was no ADCP data available. Then dividing by the alpha determined in section 3.3.2.4.1 Determination of Alpha the average surface velocity was calculated.

Furthermore, this script was used to create scatterplots comparing the difference magnitude of each point to the distance between that point and the camera for surveys with ADCP data. The distance from each point to the camera was calculated with the following equation.

$$Distance = \sqrt{(x_2 - x_1)^2 + (y_2 - y_1)^2 + (z_2 - z_1)^2}$$

Equation 10: Distance equation in 3-dimensions

The elevation of the surface velocity vectors was assumed to be the water surface elevation for this equation.

The difference between the camera velocity and the ADCP velocity was also grouped based on velocity. The classifications were based on standard deviation from the ADCP velocity magnitude where the lowest level was the average velocity of the ADCP minus 2 times the standard deviations, the second level was average minus the standard deviation, the third was the average and the fourth was the average plus the standard deviation. The distance between the velocity vector and the camera vs the difference magnitude was then plotted and examined for possible trends.

3.4.2 Distance Made Good Code

Many of the surveys were taken by Water Survey of Canada (WSC), and two of those surveys did not have GPS data collection. To plot the ADCP data spatially against the camera's surface velocity for those 2 surveys, the ADCP data had to be converted into real-world coordinates.

Distance made good is the straight-line distance between the starting point of the transect and current location of the ADCP (Mueller et al., 2013). The distances away from the bank for both the start and end point of the survey were noted. Knowing these distances, the water level and the bathymetry data, it was possible to estimate where in the cross-section the water level intersected with the bathymetric survey and determine the distance from the control point to beginning of the ADCP survey.

With all this information, it was possible to rotate the cross-section from an x & y coordinate system into Easting and Northing data that could be plotted on the same axes as the camera surface velocity data. A script was written to loop through values of theta to find the angle with the minimum difference between the real-world coordinates and the camera coordinates of the control points that were used in RIVeR. A loop was used to check theta values for each control point with the following rotation equations:

$$x = x'cos\theta - y'sin\theta$$

$$y = y'cos\theta + x'sin\theta$$

Equation 11: Rotation Equations

Where x and y are the real-world coordinates, x' & y' are the arbitrary coordinate system and θ is the angle required to rotate x' & y' to match the real-world x & y coordinates. To confirm the correct rotation angle, the difference between the actual real-world coordinates and rotated real-world coordinates can be calculated for both the easting and northing components.

$$diffEasting = x - E$$

$$diffNorthing = y - N$$

Equation 12: Difference between actual coordinates and rotated coordinates broken into x and y components

In this case the arbitrary coordinate system was the distance made good, and because it is a straight line, the y-coordinates could be assumed to be zero resulting in the following new equations:

$$x = x'cos\theta$$

$$y = x'sin\theta$$

Equation 13: Rotation equations where all y-values = 0

A for loop was used to run through angles between [0, 2π] and then calculate the difference in easting and northing between the rotated points and the actual points using the GCPs as the known real-world coordinates. The proper rotation angle will be the theta value that results in a difference of zero between the points. Once that angle is found the x and y value given from Equation 13 is added to the Easting and Northing of the GCP to get the new coordinate. Then the distance made good values could all be rotated and translated based on the GCP to obtain the estimated easting and northing coordinates of the transect. For April 8th, the transects were converted based on the left bank GCP while the March 6th survey used the right bank GCP. This was done because in both cases it was easier to estimate the first point on the transect this way based on the water levels and known bathymetry data for the survey. For each survey three transects were used.

3.4.3 ADCP Variance Code

This script was written to compare variation in ADCP transects for the survey performed on May 15th, 2024. It is essentially the same process as the velocity difference code, but in this case ADCP transects are compared to each other. The distance between points in transects is calculated and looped through to find the minimum distance between those two points. Then if those two points are under the maximum distance threshold of 0.5m then the u and v-vector velocity differences are calculated between them. This was done until all four transects had been compared to one another. Then the MAE was calculated, and a boxplot was produced in MATLAB to determine if there were any significant outliers in the comparisons. Once they were detected, the outliers were removed, and average differences were calculated again and compared to the expected error of the mean.

3.4.4 Discharge Optimization Code

This final script was used to optimize the LSPIV setup by combining surface velocity results from two cameras. The same bathymetry data used in RIVeR was loaded into the script where a loop was run to filter bathymetry data above the water surface for each survey simply by checking if the elevation data was higher or lower than the water surface. Once the out-of-water points were filtered out, a "centerline" was established for each survey and the velocities were only kept if they were on the closer half of the centerline relative to each camera. Then loops were used to find the minimum distance between each bathymetry coordinate and the velocity vectors. The closest velocity vector was then assumed to be the same at that bathymetry coordinate and assigned those coordinates in the cross-section. This was done for either the gaugehouse or left bank camera (depending on which yielded better single camera LSPIV results, except in the case of April 8th, 2022 where the gaugehouse camera was overestimating discharge) and the right bank camera. The next step was to combine the streamwise velocities from each camera into a single matrix. The midsection method was used to determine discharge. Using the surface velocities, discharge per panel was calculated with the area of each panel and then discharge was summed in excel. Lastly, this calculated discharge was multiplied by alpha to obtain the section discharge. Some panels near the banks did not have a velocity associated with them, in these cases the discharge was calculated using the following equation, the same approach used to estimate edge discharges in the unmeasured edge portions of an ADCP discharge measurement.

$$Q = CV_m L d_m$$

Equation 14: WinRiver discharge interpolation method (Teledyne RD Instruments, 2021)

Where, C is a coefficient based on the channel shape. 0.3535 was used as a triangular shape was assumed. V_m is the velocity at the last measured location, d_m is the depth at the last measured location and L is the distance from the last measured location to the bank.

3.5 Stereoscopic LSPIV Processing

This section goes through the workflow of the stereoscopic LSPIV process undertaken in this study shown in Figure 43.

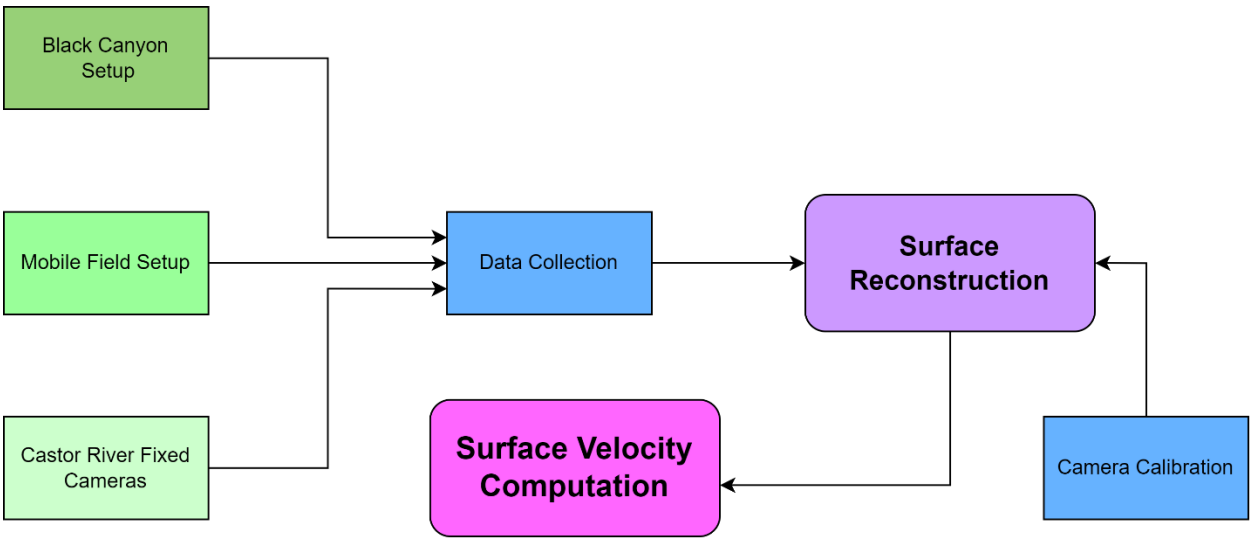

Figure 43: Stereoscopic LSPIV Workflow Diagram

3.5.1 Surface Reconstruction

The first step in image processing for stereoscopic LSPIV is reconstructing the 3D surface from the two cameras. The next sections go over the various software and methods used to attempt this process.

3.5.1.1 Pix4DMapper

Pix4DMapper is a structure from motion program that has the capability to stich a large quantity of images together into one image creating a 3-dimensional model of an area of interest. It was attempted with both lab images and field site images to create a 3D image using one image from each camera. However, it was determined the software was only capable of processing a single camera and required a larger number of images with more overlap than what the lab setup was capable of. It is a software that should be used for photogrammetry only.

3.5.1.2 Agisoft Metashape

Agisoft Metashape was tested using a similar methodology of stitching one image from each camera together to create a 3D point cloud of the canyon model. Images were loaded into the application and the intrinsic parameters found in camera calibration were specified. Then the photos were aligned using 3 translation components and 3 Euler rotation angles (Agisoft Metashape User Manual Professional Edition, Version 2.1, 2024). Aligning the photos defines

where the cameras are located and the angles of the cameras relative to the object being imaged. Then a point cloud can be built using all of these parameters, and depth maps are calculated for the overlapping image pairs. The quality of the point cloud was able to be adjusted to choose between detail versus time-costs with higher quality point clouds producing more points in the result. Then a 3D model, mesh, or DEM can be built based on that point cloud.

3.5.1.3 Stereolabs Depth Viewer

The Stereolabs ZED2i stereo camera that was also tested reconstructed the point clouds without the need for any calibration as the camera is already calibrated by Stereolabs and the camera positions relative to each other are fixed so there was also no need to align the images.

Stereolabs provides a GUI called “Depth Viewer” where the video file can be opened and viewed in multiple ways. The cameras can be viewed in 2D side-by-side or one at a time, and a live reconstructed point cloud can be seen as shown in Figure 44 or a depth image can be seen where the depth is the distance between the origin of the camera and the point in the image. Both point clouds and depth images were exported from this camera and processed in RIVeR.

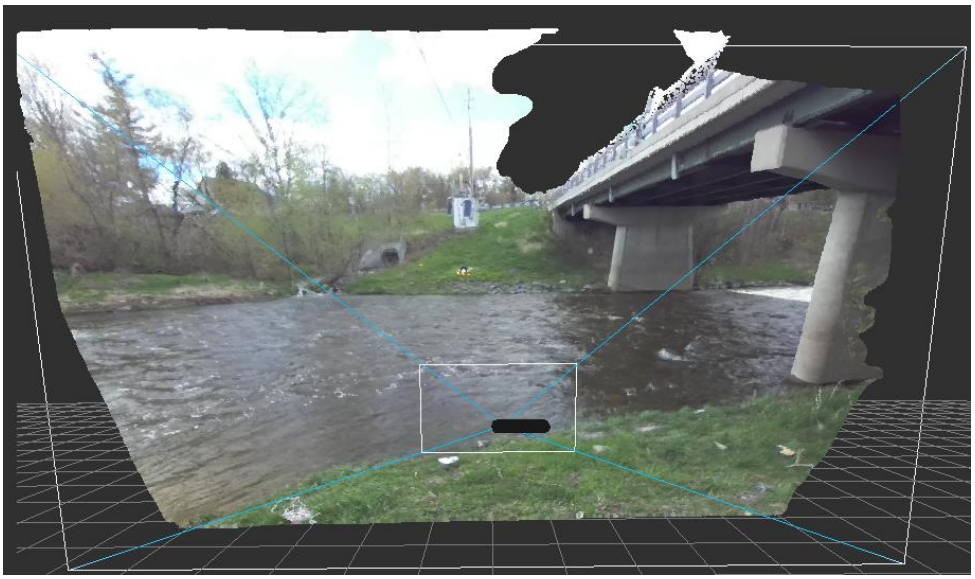

Figure 44: Reconstructed point cloud from the Stereolabs camera at the Castor River. The black object represents the camera location along the right bank

3.5.2 Standard Image Velocimetry Processing

Once the stereo surface is reconstructed for a set of image frames then they can be processed like any other image velocimetry dataset. Additional information in this section details a code that was used to convert point clouds into images because the .ply format is not accepted in RIVeR.

3.5.2.1 Point Cloud to Image Code

This code was designed to convert the 3D point clouds into a compatible image format so RIVeR could process the point clouds. The open3d library was used for data handling and visualization. The script sets the directory containing the .ply files and sorts them in ascending order by filename. Then a non-visible visualization window with a 1920 x 1080 image resolution takes view control for later camera adjustments. The point cloud data is loaded into a variable and added to the visualizer window so that the field of view can be adjusted, zoomed in and then updated in the visualizer. It takes depth and color buffers from the point cloud and converts the image from BGR to RGB. Then it crops a region of the image based on user-defined coordinates. Then the modified point cloud is converted to open3d image objects and saved as .png image files. The script runs through all point clouds in the directory and once they have all been converted, the visualization window is closed.

4.0 Results

This section details the results from the Castor River for both the multi-camera study and stereoscopic image velocimetry work as well as the stereoscopic image velocimetry results from the Black Canyon laboratory set-up.

4.1 Multi-Camera LSPIV

4.1.1 Castor River Field Site

The following subsections break down the results by each survey date followed by a section summarizing all of the results. Each survey has the following results: water surface velocity vector plots, velocity difference maps between methods, normalized velocity difference maps between methods and mean absolute errors (MAE) for each method. Additionally, for surveys with ADCP data, scatterplots showing distance to each camera vs velocity difference to the ADCP were created. Cross-section plots were created comparing discharge and velocity across the Castor River with all different methods used, this includes the discharge from combining results of multiple cameras. The flow direction for all plots is from the bottom left to the top right of the plot. Additionally, it should be noted that a full spatial comparison between cameras was not always possible. In some velocity difference plots white space is present indicating no comparisons were made in that section of the river.

Other results include a sensitivity analysis on the maximum distance threshold between surface velocity vectors for computing velocity differences. ADCP variance as well as near-surface FlowTracker vs ADCP measurements between transects were looked at for the May 15th, 2024 survey. While analyzing results in PIVlab, it was noticed some frames had zero velocity vectors. An analysis was performed to see how velocity values compared if those frames were included or disregarded in the median frame.

The velocity differences were normalized across the different datasets using the average surface velocities from each survey (Table 7). The average surface velocity was found by first dividing the discharge (ADCP or gauge station data) by the wetted area of the cross-section given in RIVeR to obtain a mean velocity. Then the mean velocity was divided by the alpha coefficient giving the average surface velocity. These values were validated by comparing them to the near-surface velocity measurements from the cameras.

On May 15th 2024 both ADCP and Flowtracker2 data were collected. The near-surface ADCP velocity data compared favourably to the FlowTracker2 near-surface velocity data, suggesting the top two bin ADCP data yielded good estimates of the surface velocity. The ADCP data were then interpolated onto a uniform grid to obtain equally spatially distributed near-surface velocity. With this method the average surface velocity was found to be 0.5480m/s, as compared to 0.5539 m/s (Table 7), a difference of 0.0059m/s. so the average surface velocity seen in the table was deemed to be valid for normalizing the velocity difference plots.

Table 7: ADCP data used to normalize velocity difference plots. Discharge was taken from either the ADCP or gauge station. Gauge station discharge is denoted with a bracketed G next to the value. Wetted Area was taken from RIVeR and Mean velocity was found by dividing the discharge by wetted area. Alpha was found using the plot previously shown in 3.3.2.4.1 Determination of Alpha. Average Surface Velocity was computed by dividing the mean velocity by the average surface velocity.

Date	Discharge (m^3/s)	Wetted Area (m^2)	Mean velocity (m/s)	Alpha	Average Surface Velocity (m/s)
March 18th, 2022	32.44 (G)	33.82	0.9592	0.8247	1.1631
March 21st, 2022	55.50	42.44	1.3521	0.8946	1.5114
April 8th, 2022	53.80	36.58	1.5472	0.8924	1.7337
May 5th, 2022	5.77 (G)	13.66	0.4224	0.7501	0.5631
May 5th, 2023	25.10	21.27	1.2206	0.8066	1.5133
March 6th, 2024	23.30	22.57	1.0877	0.8023	1.3557
May 15th, 2024	5.29	13.01	0.4149	0.7490	0.5539

4.1.1.2 March 18th, 2022

This survey was performed by ECCC hydrometric technologists. In addition to the fixed bridge and station cameras, ADCP data and drone videos were collected. As previously mentioned in 3.1.1.1 ECCC Surveys, the ADCP data had erroneous velocities, so the data was discarded and the camera surface velocity measurements were compared to the gauge station discharge.

Velocity Differences

Figure 45 shows the normalized velocity differences between all three cameras and Figure 46 shows the comparison between a drone recording and the bridge cameras. All plots quite clearly show that the large differences in velocity are near the banks while the velocities compare well in the center of the river. The gaugehouse camera compared to the left bank camera shows very similar velocities which is logical considering they are on the same bank. Figure 47 gives some explanation as to why there is some difference near the right bank between these cameras. The left bank camera incorrectly estimates the direction of the vector in the area resulting in a larger difference to the gaugehouse camera.

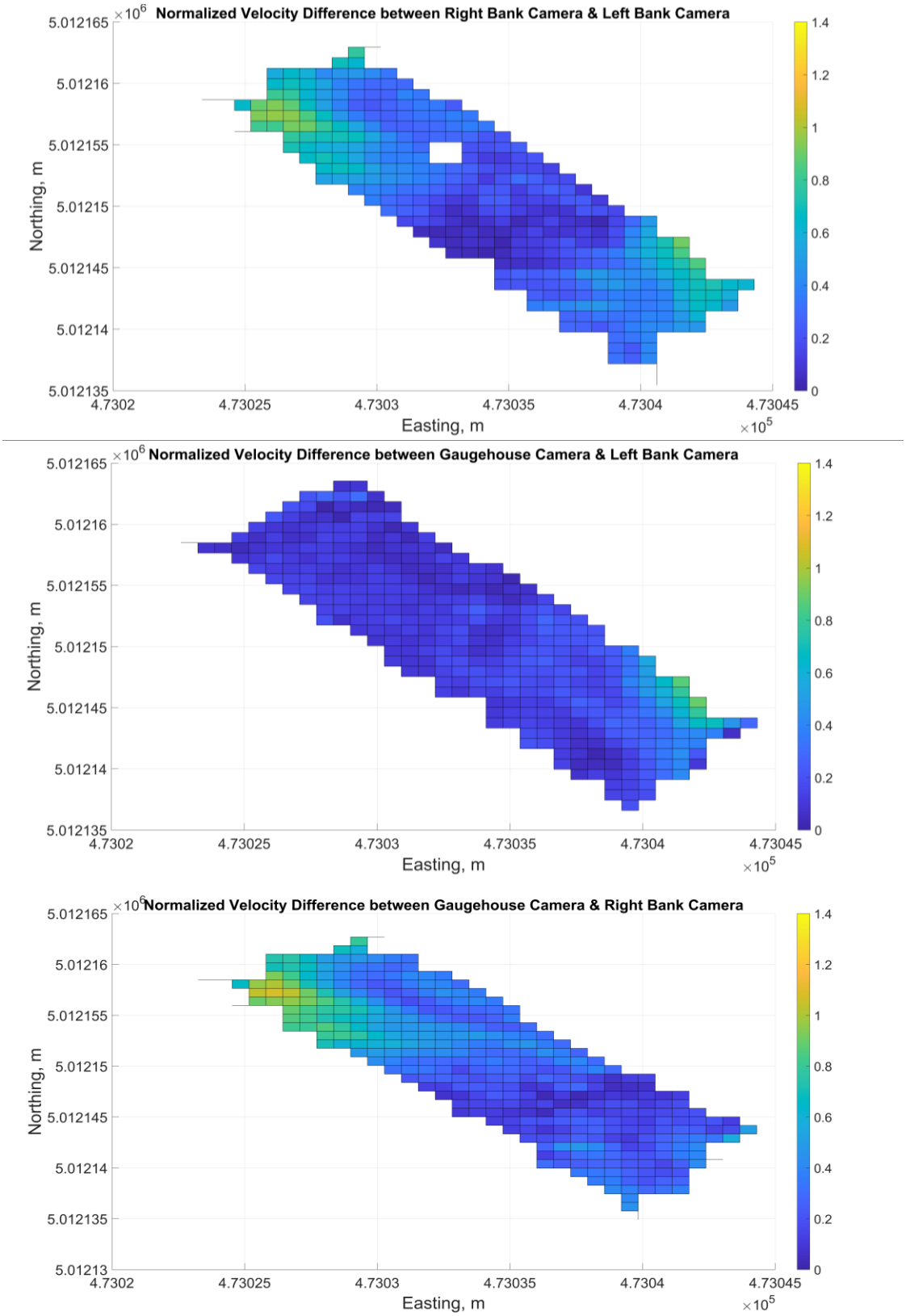

Figure 45: Normalized velocity differences between Top) Left and right bank cameras Middle) Gaugehouse camera and right bank camera Bottom) Gaugehouse camera and left bank camera

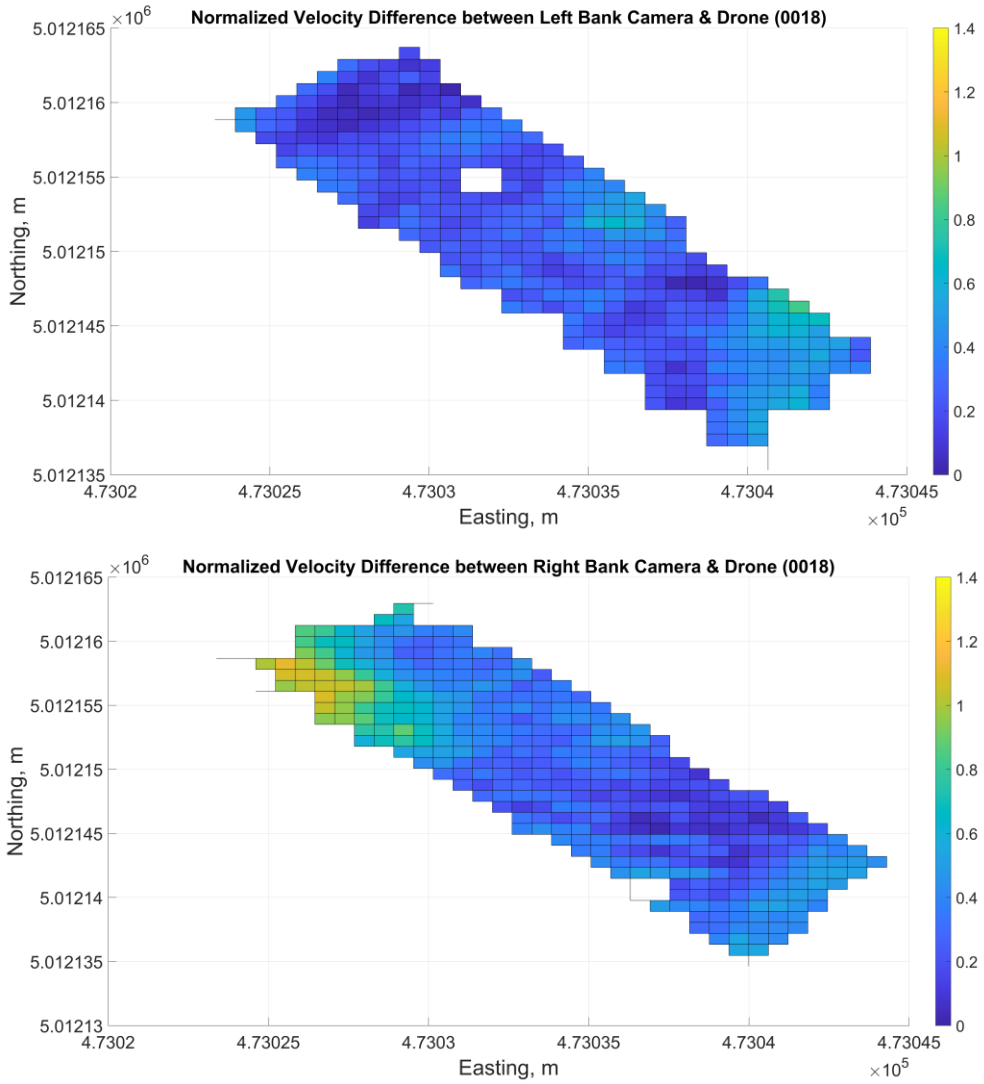

Figure 46: Normalized velocity differences between Top) Drone (DJI0018) and left bank camera Bottom) Drone (DJI0018) and right bank camera

Table 8 shows the mean absolute errors between methods. They are expected based on the velocity differences in Figure 45 and Figure 46 where the bridge cameras have the largest differences between each other, the right bank camera had significant differences on the left bank compared to the drone and the gaugehouse camera. The left bank camera compared quite closely to both the drone and the gaugehouse camera (Figure 47) with some small differences on the right bank.

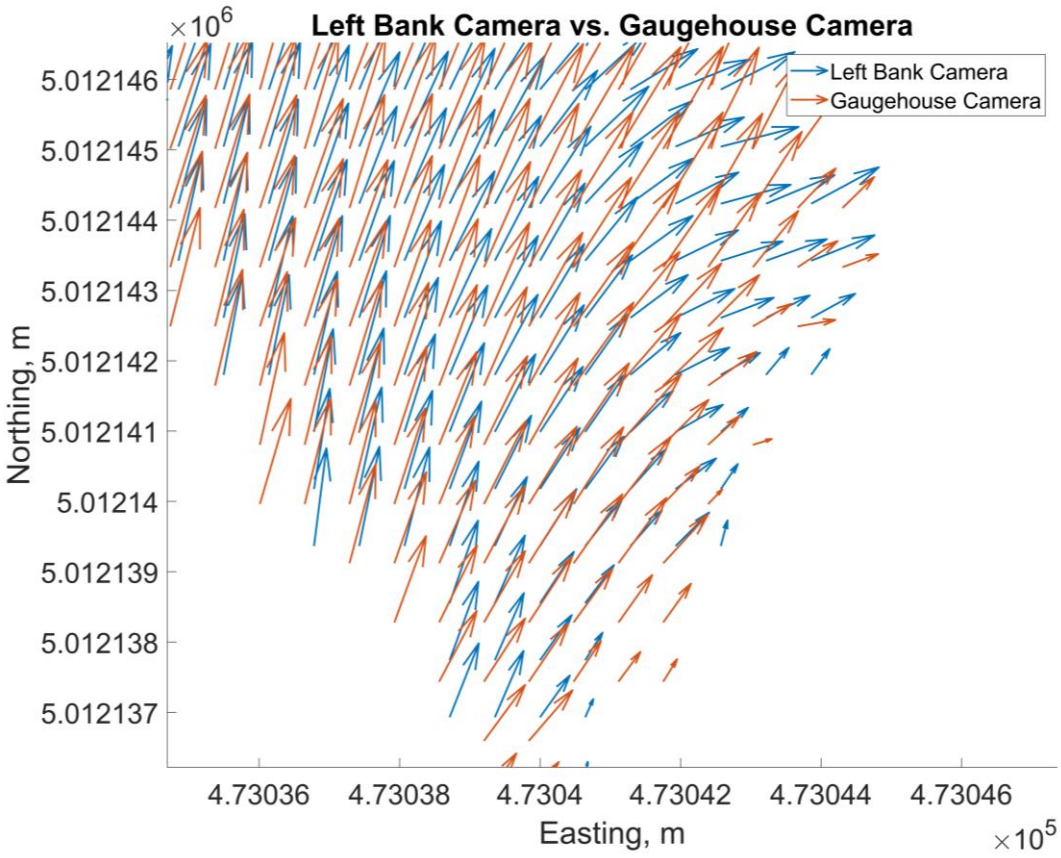

Figure 47: Left bank camera vs gaugehouse camera vector plot zoomed into the right bank for March 18th, 2022 survey

Table 8: Mean absolute errors (MAE) of surface velocities between methods for March 18th, 2022 Survey

Comparison	Normalized Differences (unitless)	Mean Absolute Error (m/s)
Left Bank vs Right Bank Camera	0.3733	0.431
Gaugehouse vs Right Bank Camera	0.3628	0.4219
Gaugehouse vs Left Bank Camera	0.1893	0.2202
Drone vs Right Bank Camera	0.3985	0.4634
Drone vs Left Bank Camera	0.2954	0.3436

4.1.1.3 March 21st, 2022

Velocity Differences

These plots (Figure 48) followed a similar trend to the previous survey where the substantial differences in velocity were found near the banks. This survey also demonstrated the challenges of environmental conditions and how obstructions in the FOV (power lines) can affect surface velocity estimates.

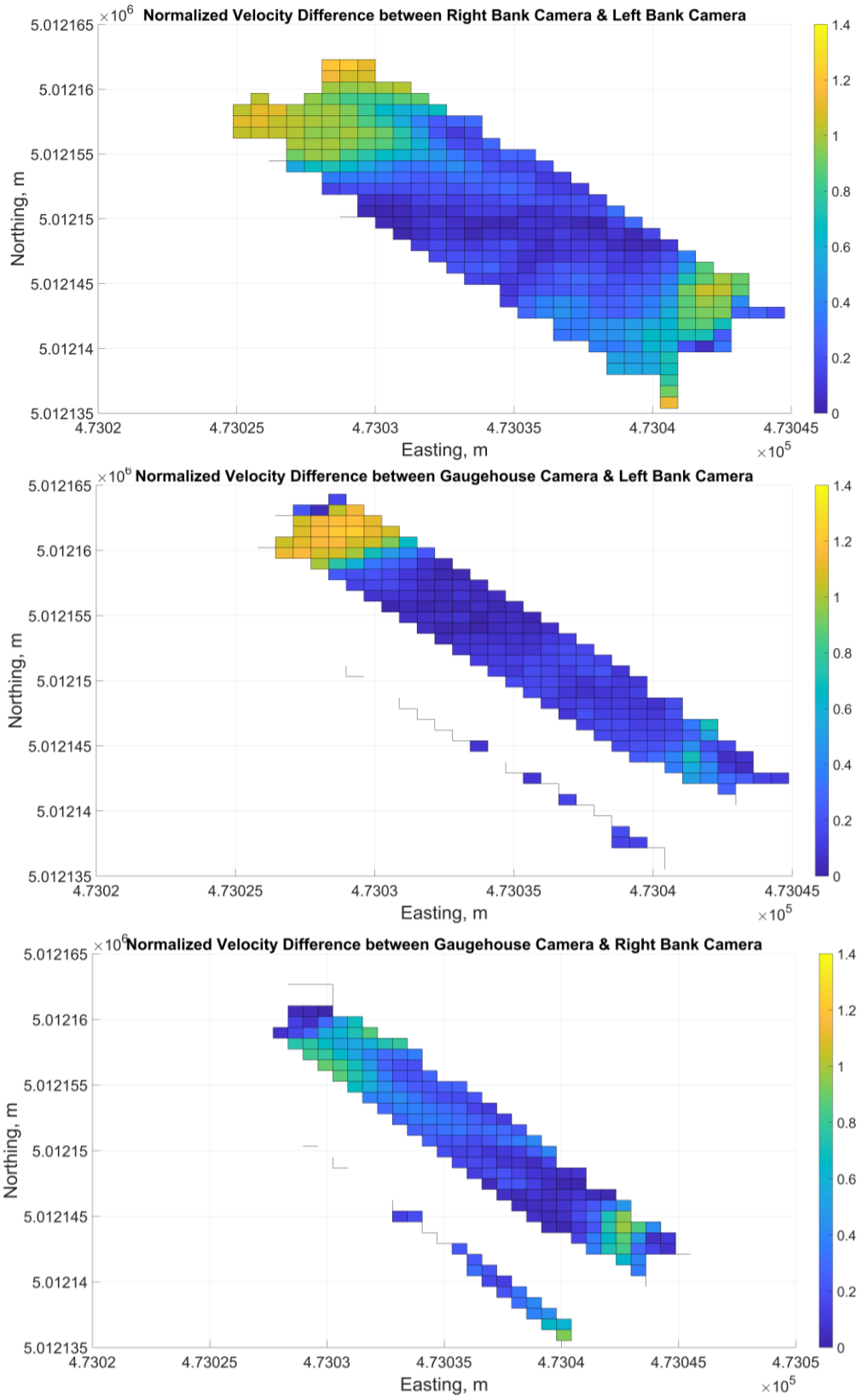

Figure 48: Normalized velocity difference plots Top) Left bank vs right bank camera Middle) Gaugehouse vs right bank camera Bottom) Gaugehouse vs left bank camera

The vector plot in Figure 49 shows how surface texture impacted the surface velocity results on the left bank of the river. Both the gaugehouse camera and the right bank camera had a patch of extremely low biased estimates due to a smooth surface caused by changes in glare throughout the video. Additionally, the tag line in the video affected the velocity estimates of the gaugehouse camera so that section was masked out of the images, hence why there are missing gaugehouse estimates in the plots near the upstream section of the river. The high differences between the gaugehouse camera and left bank camera along the left bank were likely attributed to the glare that changes throughout the video.

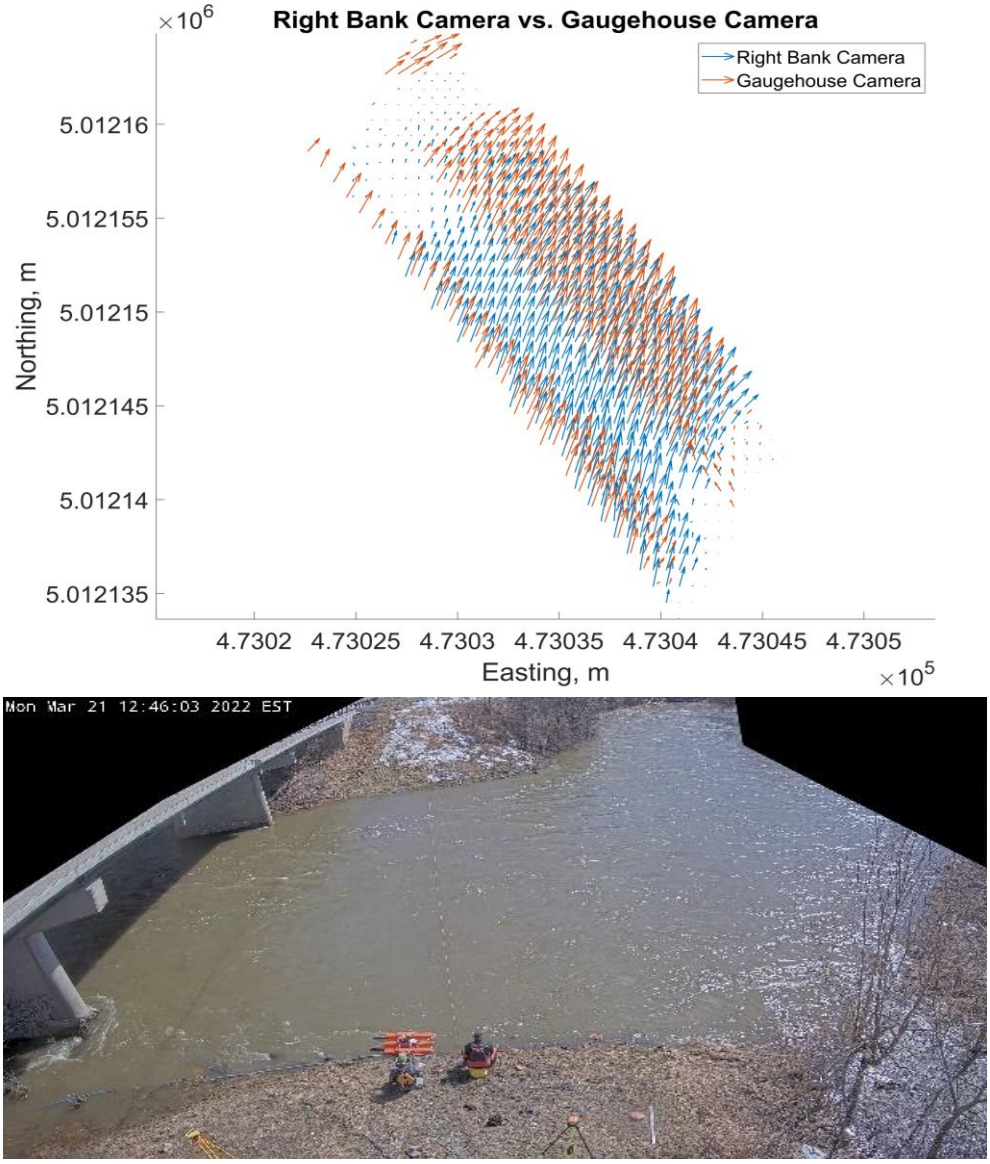

Figure 49: Top) Right bank vs Gaugehouse camera vector plot Bottom) Frame showing glare from sunlight that impacted the surface texture near the left bank

Figure 50 shows how the ADCP varies from the camera surface velocities. The ADCP data collected for this survey were only transects limiting spatial coverage, but they show the same trend where the cameras estimate lower velocities near the far shore. Table 9 shows the MAE for all comparisons. Due to the glare causing low estimates near the left bank it was difficult to compare the camera errors but the differences with the ADCP data were very high, 0.5691m/s and 0.3950m/s for the right bank and left bank, respectively. This further reinforces the finding that the cameras cannot accurately estimate the far shore surface velocity.

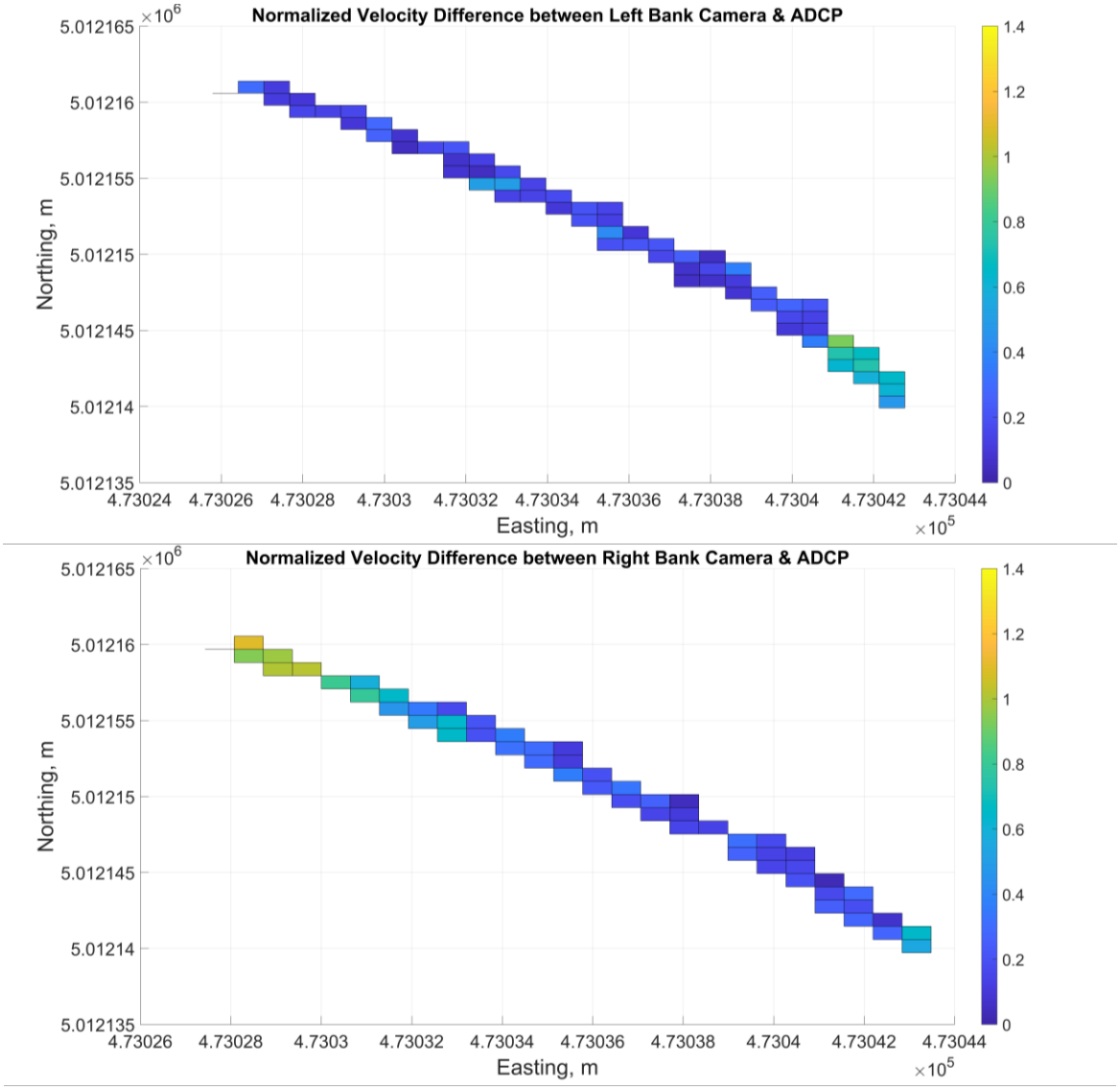

Figure 50: ADCP versus camera velocity differences Top) Left bank camera comparison Bottom) Right bank camera comparison

Table 9: Mean Absolute Error (MAE) of the surface velocity differences between methods for March 21st, 2022 survey

Comparisons	Normalized Differences (unitless)	Absolute (m/s)
RB vs LB	0.4435	0.6703
RB vs ADCP	0.3766	0.5691
LB vs ADCP	0.2614	0.3950
Gaugehouse vs RB	0.3016	0.4558
Gaugehouse vs LB	0.2692	0.4068
Gaugehouse vs ADCP	0.3601	0.5442

Distance Plots

The scatterplots in Figure 51 shows a trend where once the surface velocity vectors reach a distance of 30+m away from the camera the error begins to increase at a substantial rate approximately linearly. The gaugehouse camera scatterplot shows larger errors closer to the camera due to the poor surface texture on the near shore.

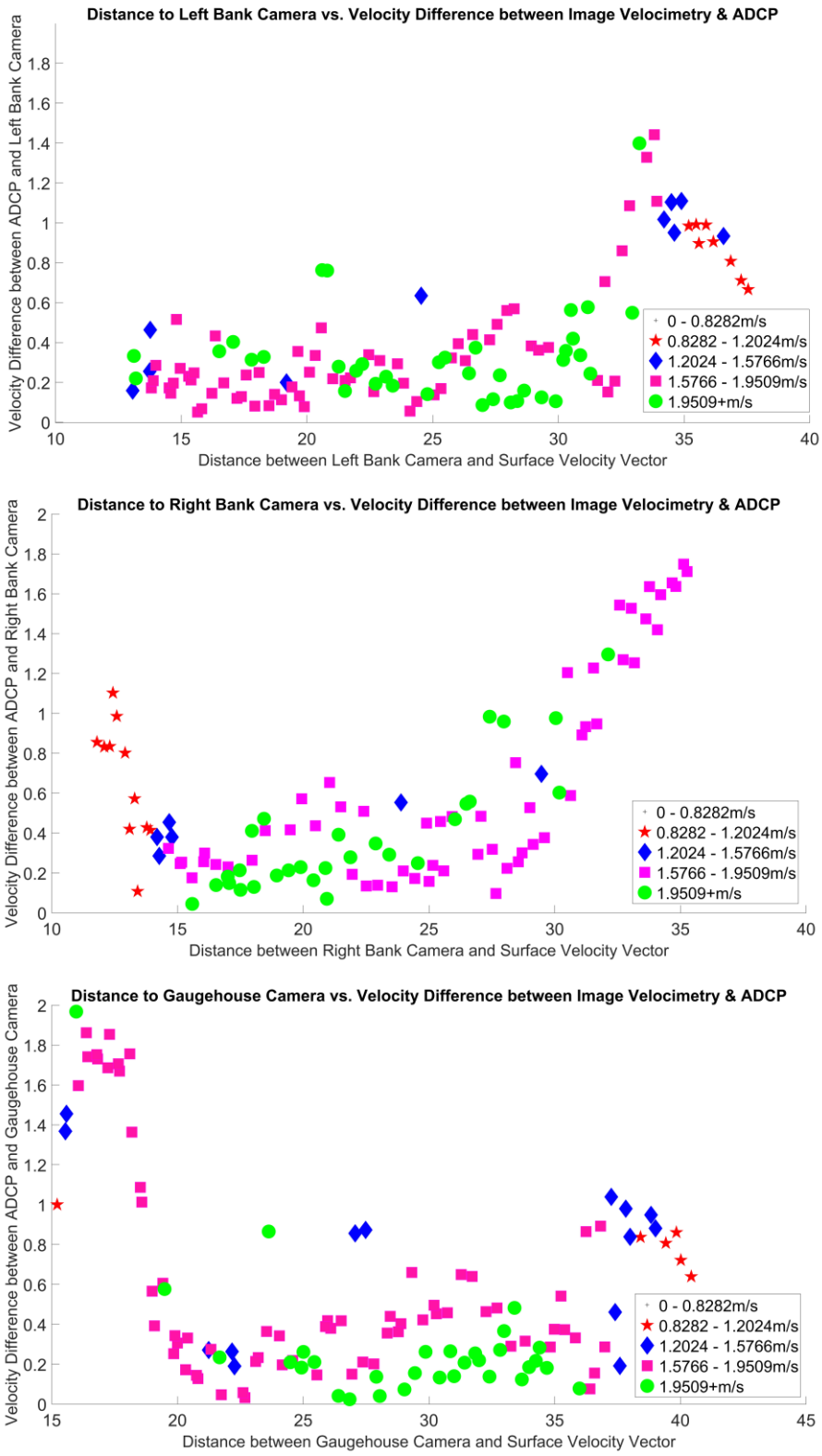

Figure 51: Distance versus velocity difference to the ADCP scatterplots Top) Left bank camera Middle) Right bank camera Bottom) Gaugehouse Camera

4.1.1.4 April 8th, 2022

Velocity Differences

Figure 52 illustrates that the largest differences between cameras are on the banks. This survey shows smaller differences relative to other surveys but still substantial differences throughout the ROI.

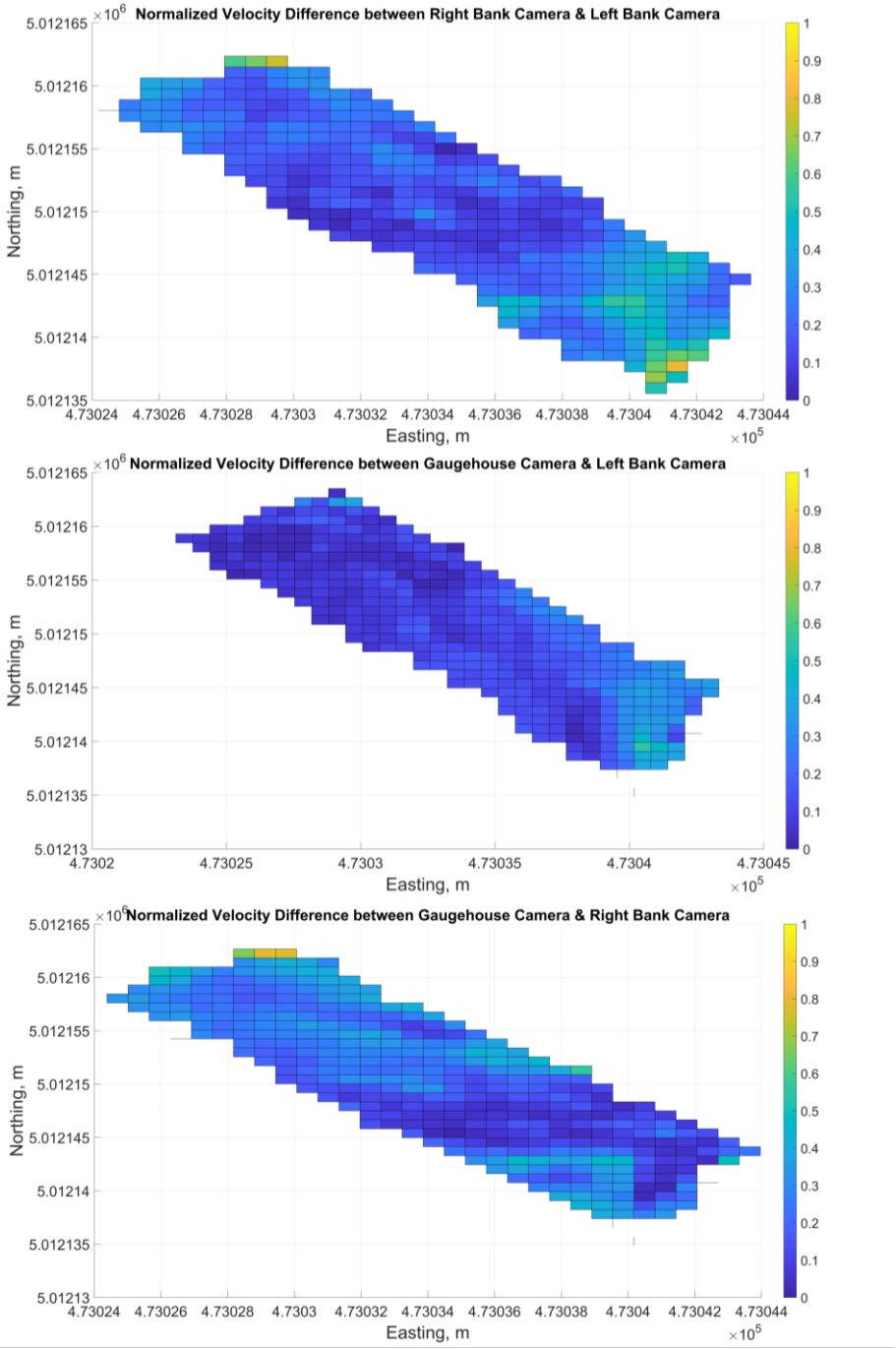

Figure 52: Normalized velocity differences Top) Left bank versus right bank cameras Middle) Gaugehouse camera versus left bank camera Bottom) Gaugehouse camera versus right bank camera

Figure 53 shows vector plots comparing the right bank camera to the cameras on the left bank. The vector directions were in the direction of flow, however, a difference in magnitude near the banks was evident.

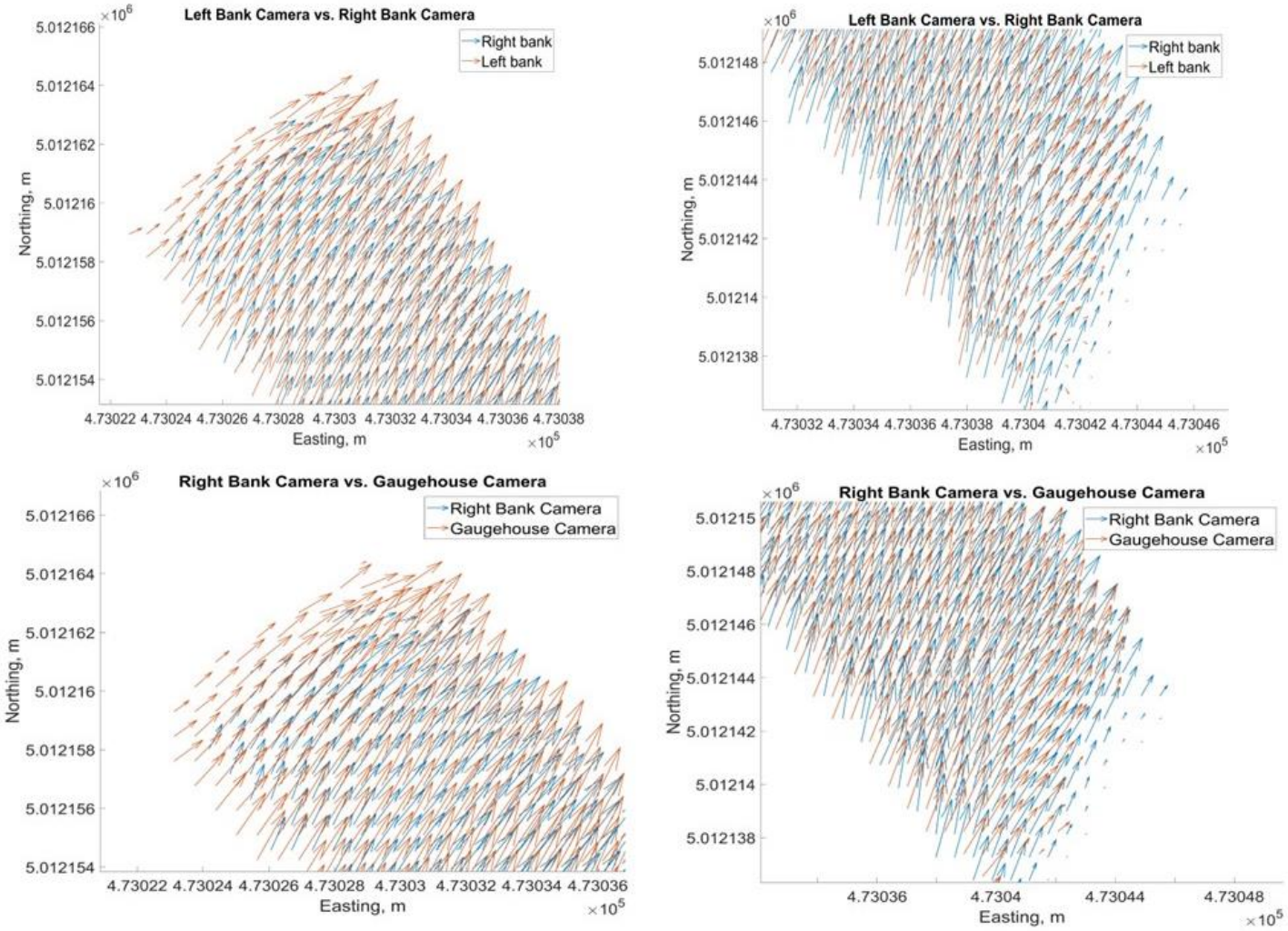

Figure 53: Zoomed in vector plots displaying the surface velocity differences near the banks for the April 8th, 2022 survey: Left) Zoomed into left bank. Right) Zoomed into right bank

Velocity differences compared to the ADCP measurements appeared to be more randomized and less substantial near the banks (Figure 54). This could have been caused by errors when using distance made good of the ADCP data to obtain real-world coordinates, however it is most likely that these larger differences were due to the single ping ADCP data being used in this survey. Mean absolute errors between the methods (Table 10) showed substantial surface velocity differences compared to the ADCP measurements and the other cameras.

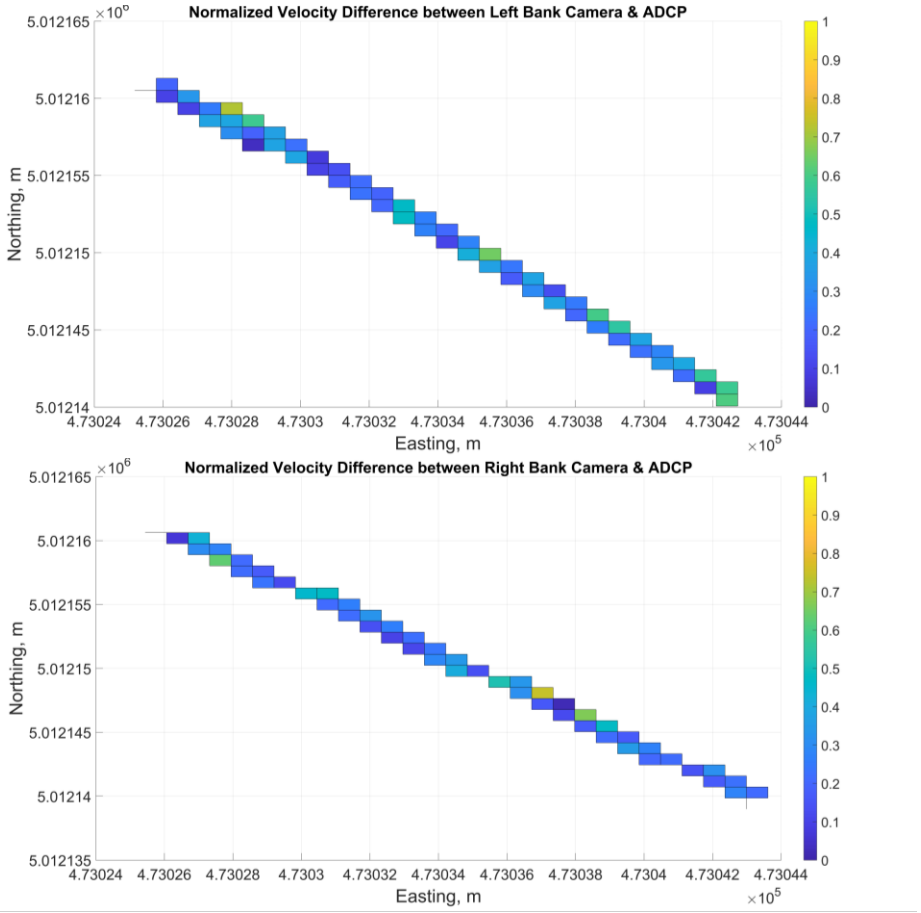

Figure 54: ADCP versus camera velocity differences Top) Left bank vs ADCP Bottom) Right bank vs ADCP

Table 10: Mean Absolute Error (MAE) of surface velocity differences between methods for surface velocity comparisons

Comparisons	Normalized Differences (unitless)	Mean Absolute Error (m/s)
RB vs LB	0.2394	0.4150
RB vs ADCP	0.2634	0.4566
LB vs ADCP	0.3225	0.5591
Gaugehouse vs RB	0.2428	0.4209
Gaugehouse vs LB	0.1464	0.2538
Gaugehouse vs ADCP	0.2928	0.5077

Distance Plots

The scatterplots (Figure 55) do not show any clear or noticeable trends for this survey. This is to be expected when looking at the ADCP differences between the cameras as the velocity differences have no consistent trends throughout the plots and the significant differences are somewhat sporadic.

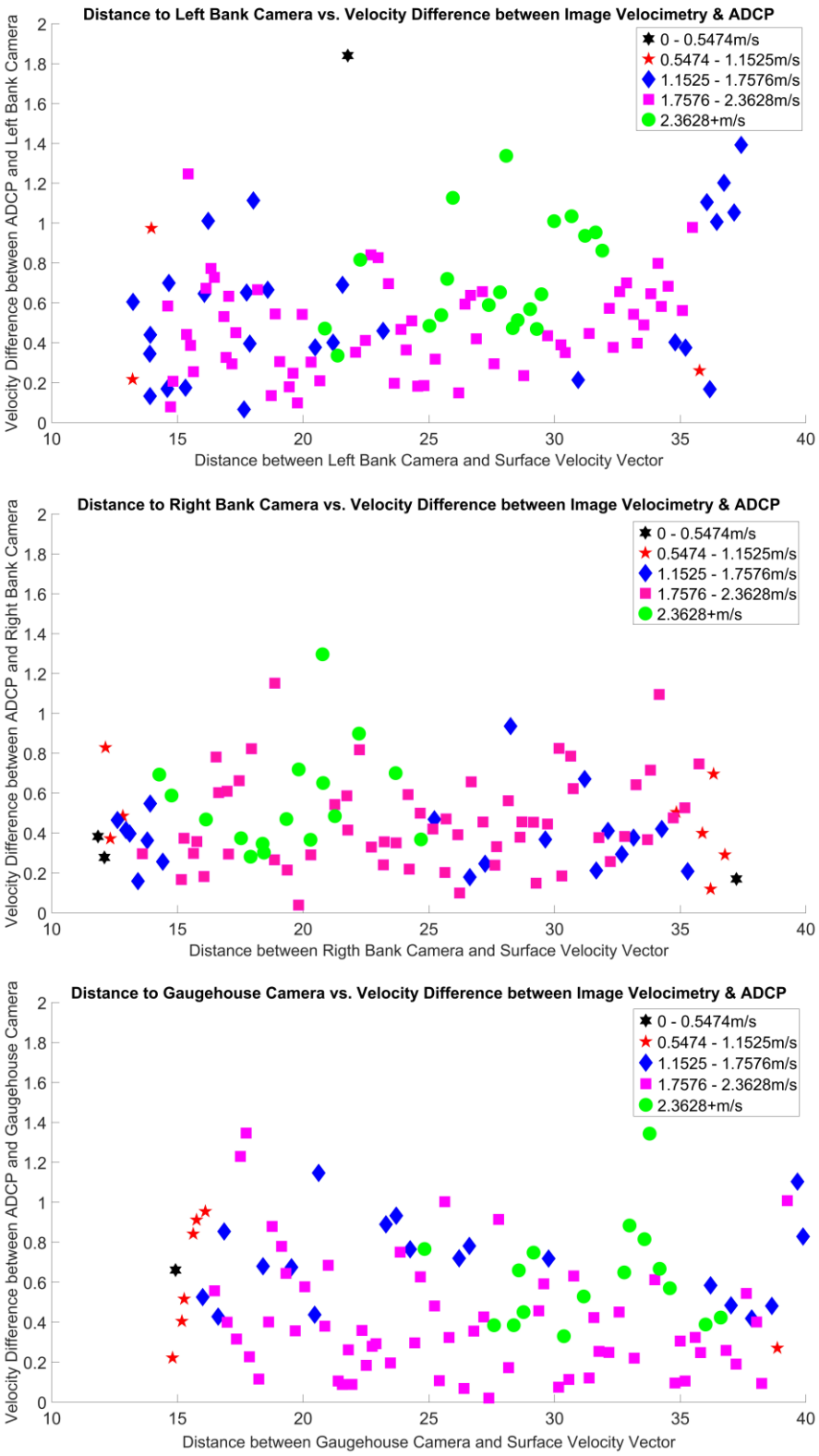

Figure 55: Distance to camera versus velocity differences to ADCP Top) Left bank camera Middle) Right bank camera Bottom) Gaugehouse camera

4.1.1.5 May 5th, 2022

Flow data was collected on this day using a FlowTracker2, however it was done outside of the camera's field of view and so gauge station data was used as a comparison instead. Additionally, drone footage was collected for this survey.

Velocity Differences

Once again, this survey demonstrated that surface velocity estimates near the far banks were poor. (Figure 56).

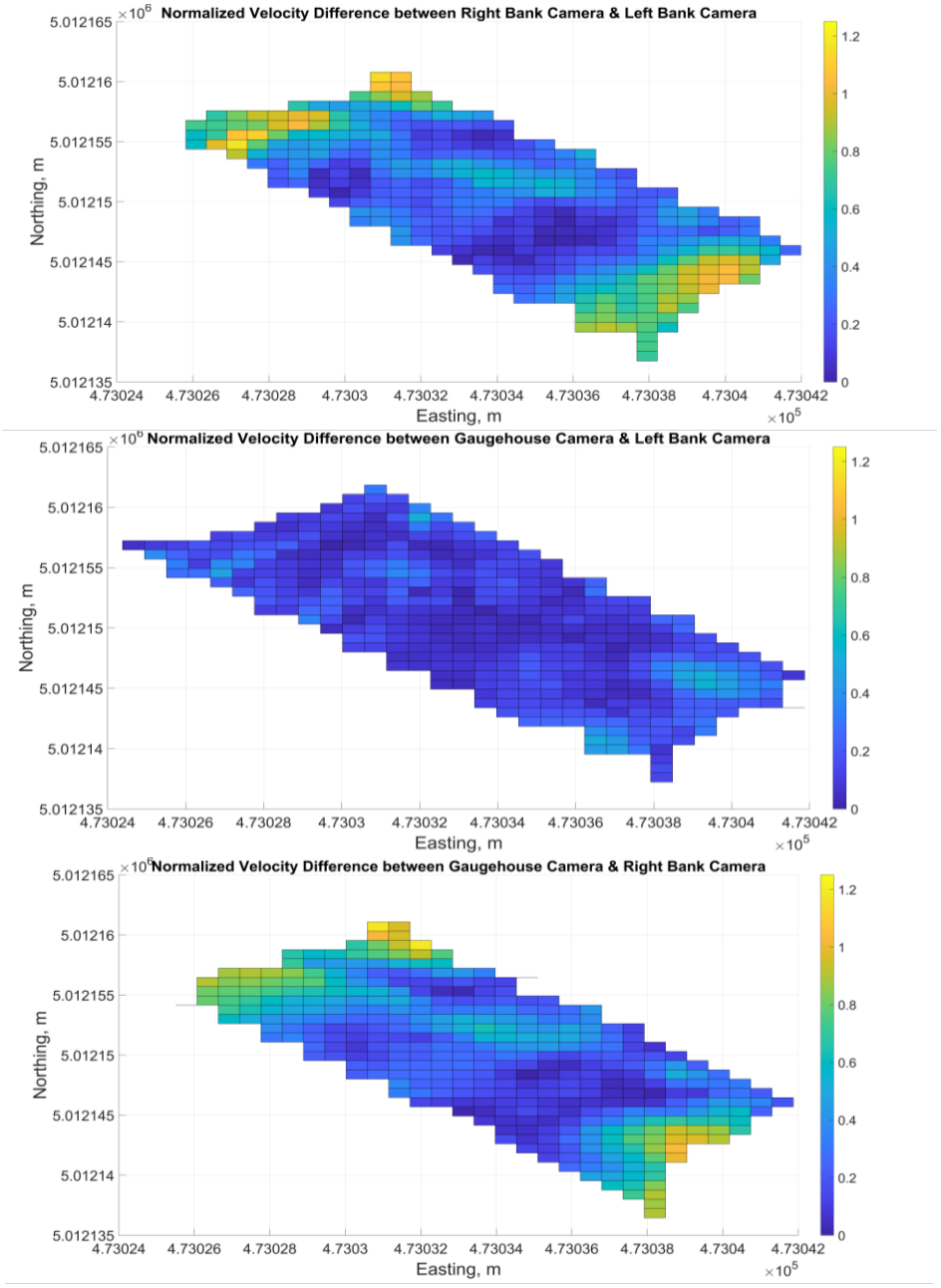

Figure 56: Normalized velocity differences Top) Right vs left bank camera Middle) Gaugehouse vs left bank camera Bottom) Gaugehouse vs right bank camera

When analyzing the drone measurements (Figure 57), results were unexpected with underestimates near the banks. This may have been caused by the power lines that run over the ROI causing interference with the surface velocity measurements of the drone. When included, they caused noticeable problems in PIVLab with large erroneous vectors running cross-stream (parallel to the power lines). The power lines were thus masked out to improve accuracy of the drone measurements.

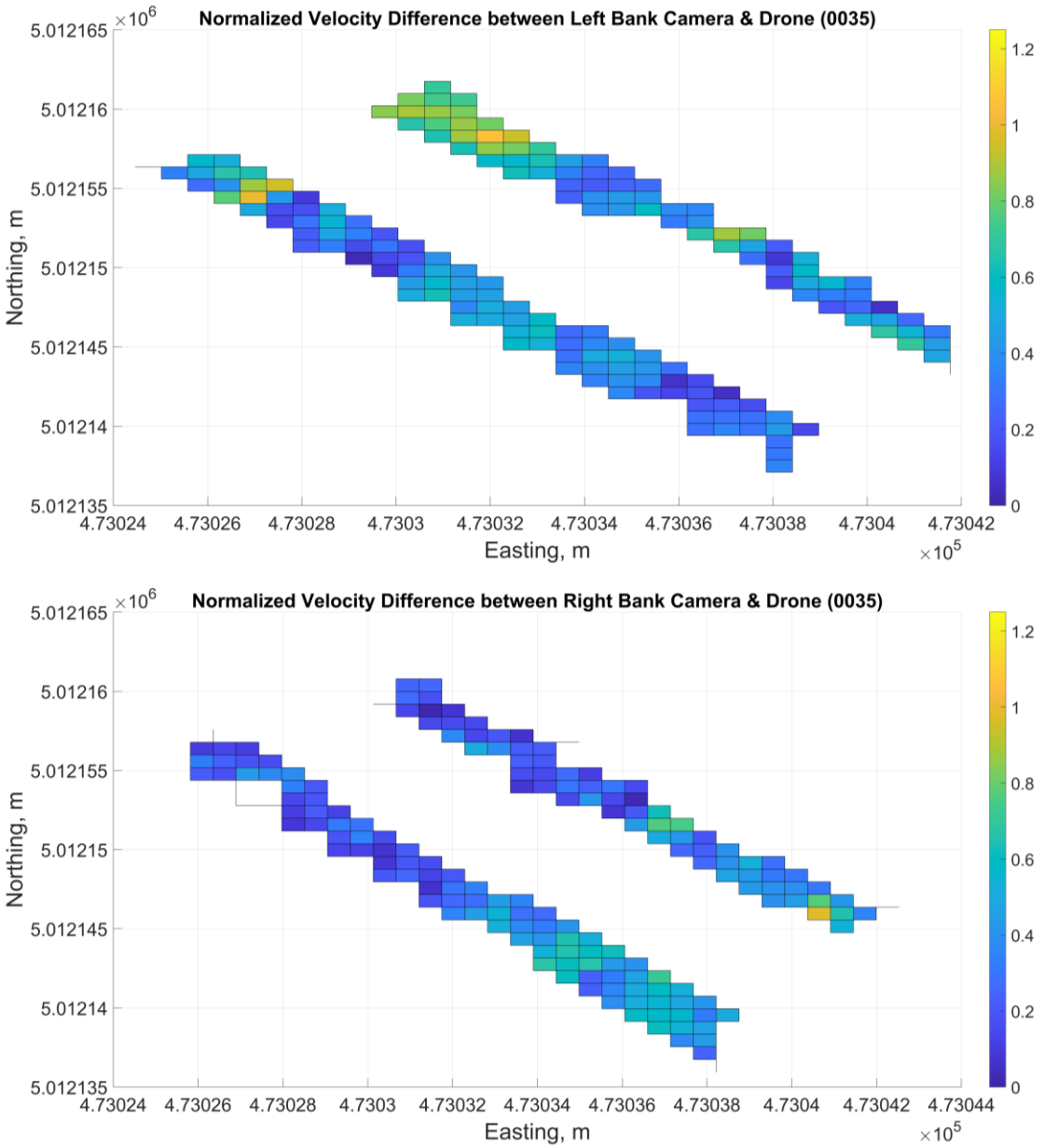

Figure 57: Velocity difference plots comparing drone camera to fixed cameras Top) Left bank camera vs Drone Bottom) Right bank camera vs Drone

The mean absolute errors (Table 11) between all methods were substantially lower than previous surveys, however this is likely due to the low flow. When looking at the normalized differences the error was much higher across all methods than any previous surveys. This indicated that the cameras may have performed worse at this low flow.

Table 11: Mean absolute error (MAE) of the surface velocity differences of the camera comparisons for the May 5th, 2022 survey

Comparisons	Normalized Differences (unitless)	Mean Absolute Error (m/s)
RB vs LB	0.4265	0.2402
Gaugehouse vs Right Bank	0.3997	0.2251
Gaugehouse vs Left Bank	0.1496	0.0843
Drone vs RB	0.3318	0.1868
Drone vs LB	0.4406	0.2481
Drone vs Gaugehouse	0.4495	0.2531

Missing PIV Data Analysis

When verifying surface vector results in PIVLab, it was noted that some frames had empty vector fields. An example of what the empty vector field looks like can be seen in Figure 58. An analysis was done to see whether the missing frames had a significant impact on the results. The median frame was calculated in PIVLab with and without the frames with missing data. Then both PIVLab sessions were processed in RIVeR. The surface velocity results were exported and compared by taking the differences in the streamwise and cross-stream velocities.

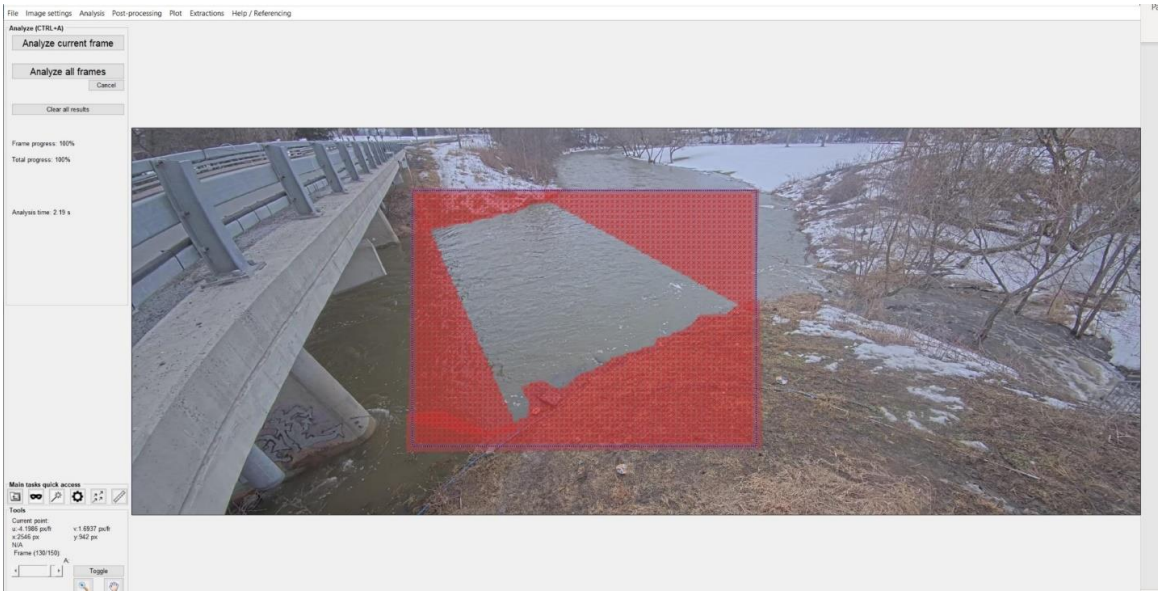

Figure 58: Example of Empty PIV vector field in PIVLab where the blue box represents the area being processed and the red indicates areas that have been masked out

As seen in Table 12 the differences between the two datasets produced negligible changes in average velocity. Since this difference has no significant impact, it was decided that empty frames would be acceptable for all surveys, and it would not be necessary to inspect results of individual frames. This resulted in a significant reduction in processing time.

Table 12: Easting and Northing Velocity Differences between varying PIVLab median frames

	Easting Velocity Difference	**Northing Velocity Difference**
Average Velocity Difference (m/s)	0.0007	0.0035
Maximum Velocity Difference (m/s)	0.0081	0.0191

4.1.1.6 May 5th, 2023

This survey was done by the author and supervisors. The GCPs and camera locations were surveyed, and ADCP data was collected: both a zig zag survey and transects of cross-section 2 were performed.

Velocity Differences

Figure 59 shows a continued trend with the most substantial surface velocity differences occurring near the banks indicated reduced accuracy in the image velocimetry estimates as the distance from the camera increased. Additionally, the left bank camera had poor estimates near the right bank compared to the gaugehouse camera suggesting that the higher elevation of the gaugehouse camera is preferred as it results in less of an oblique angle.

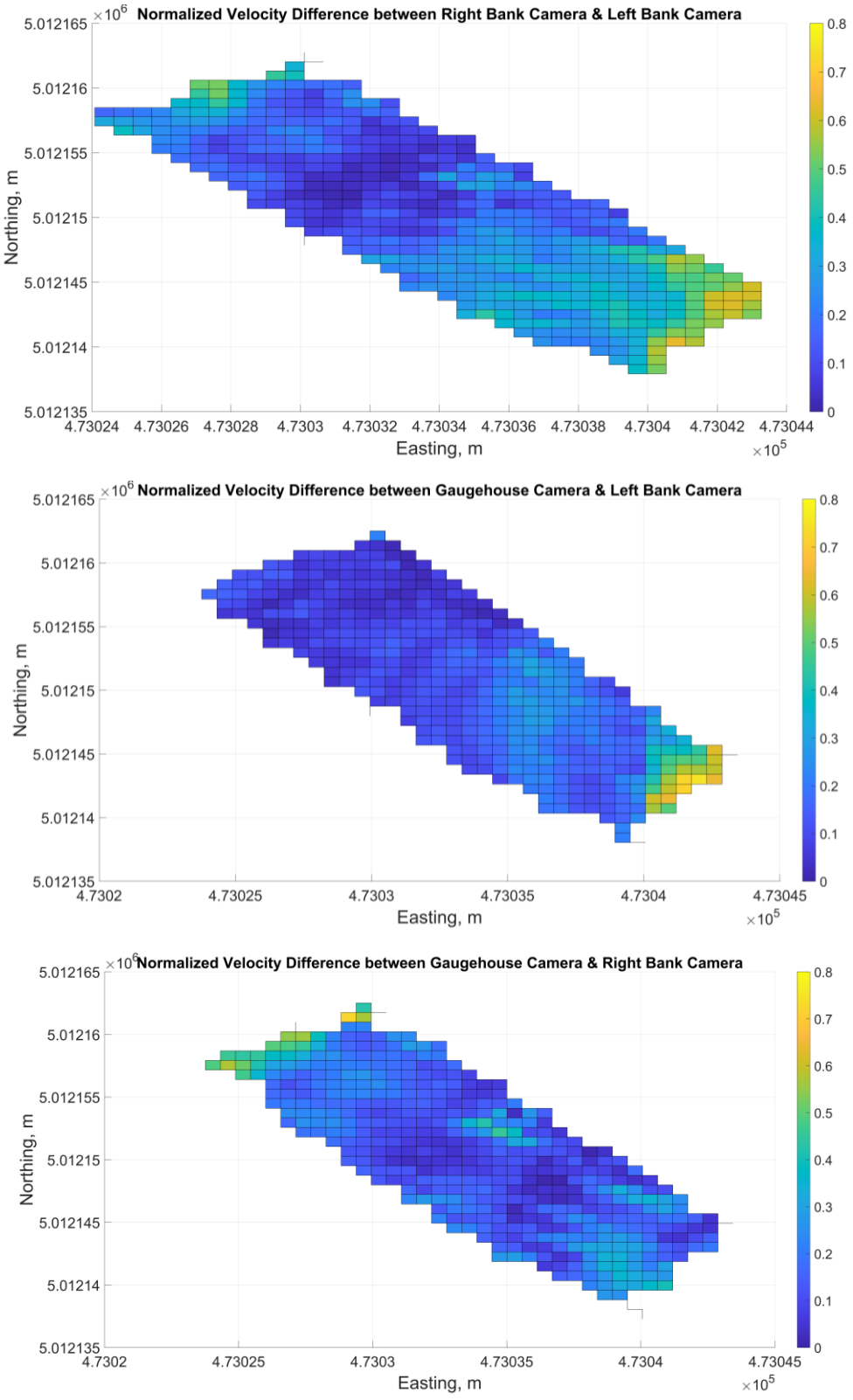

Figure 59: Normalized velocity difference plots Top) Left bank vs right bank camera Middle) Gaugehouse vs left bank camera Bottom) Gaugehouse vs right bank camera

Figure 60 shows the comparison between the cameras and the ADCP measurements. A 5-ping boxcar average was used when processing the ADCP data. Once again, the ADCP measurements verify the cameras' inability to accurately estimate surface velocities on the far shores.

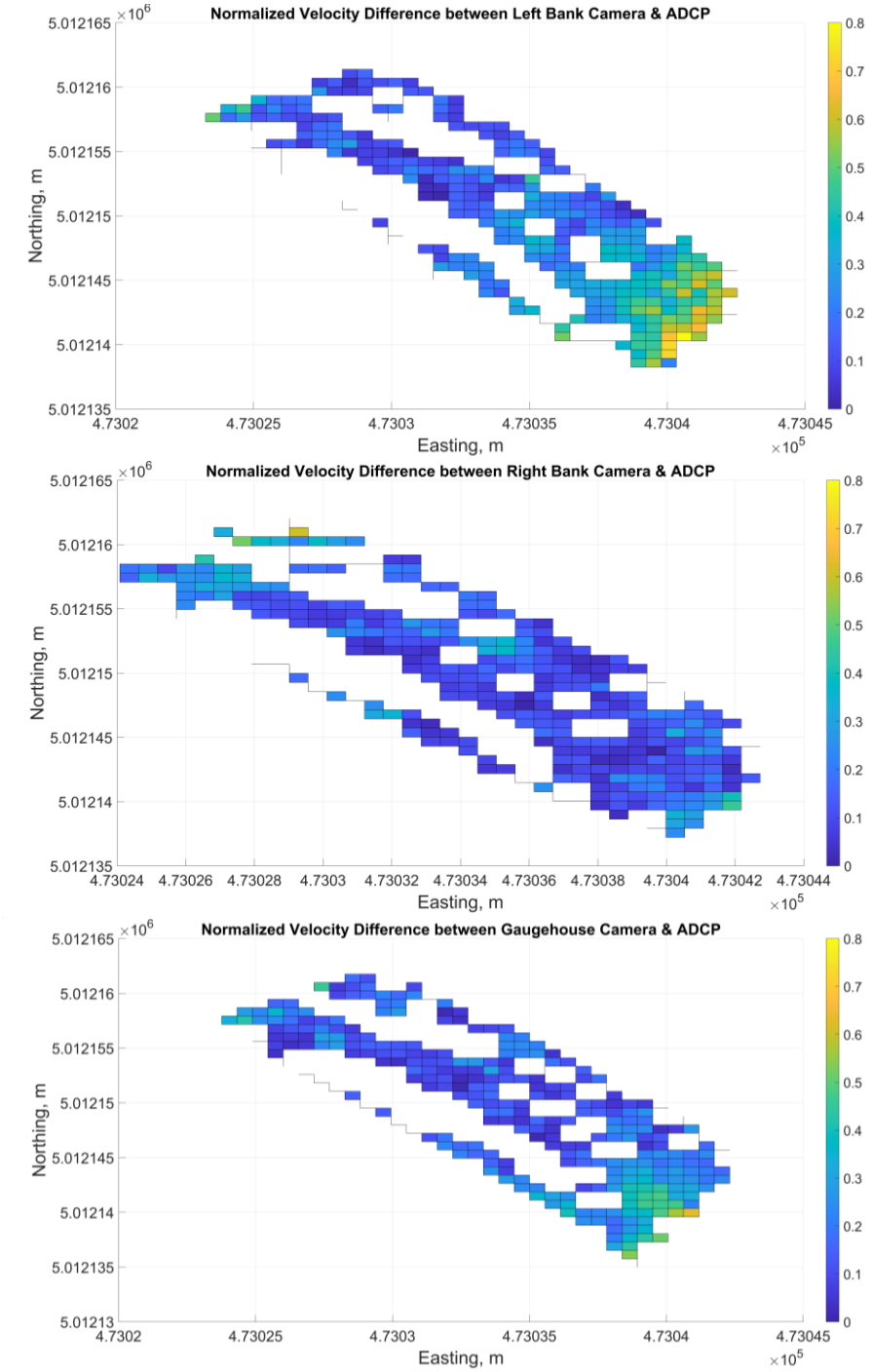

Figure 60: ADCP versus camera comparisons Top) Left bank camera versus ADCP Middle) Right bank camera versus ADCP Bottom) Gaugehouse camera versus ADCP

The mean absolute errors for this survey are shown in Table 13. The error was reasonably consistent between all comparisons. The left and right bank had the highest error between cameras at 0.3523m/s. This makes sense based on the velocity difference plots as they had the largest quantity of significant differences in the near-bank regions. The ADCP compared to the left bank cameras have the 2nd and 3rd largest errors which again makes sense as they have major differences along the right bank of the river in the surface velocity difference plots.

Table 13: Mean absolute error (MAE) of the surface velocity differences between methods for the May 5th, 2023 survey

Comparisons	Normalized Differences (unitless)	Mean Absolute Error (m/s)
RB vs LB	0.2329	0.3523
RB vs ADCP	0.1584	0.2397
LB vs ADCP	0.2492	0.3771
Gaugehouse vs RB	0.1788	0.2706
Gaugehouse vs LB	0.1646	0.2491
Gaugehouse vs ADCP	0.1856	0.2809

Distance vs Velocity Differences Scatterplots

The scatterplots (Figure 61) did not show much of a trend until the distance to the cameras is greater than around 30m for the bridge cameras and 35m for the gaugehouse camera and then an approximately logarithmic relationship starts to appear. These results demonstrate the velocity difference compared to the ADCP starts to increase the further the camera is from the water surface, suggesting distance should be limited for oblique cameras or the angle should be reduced.

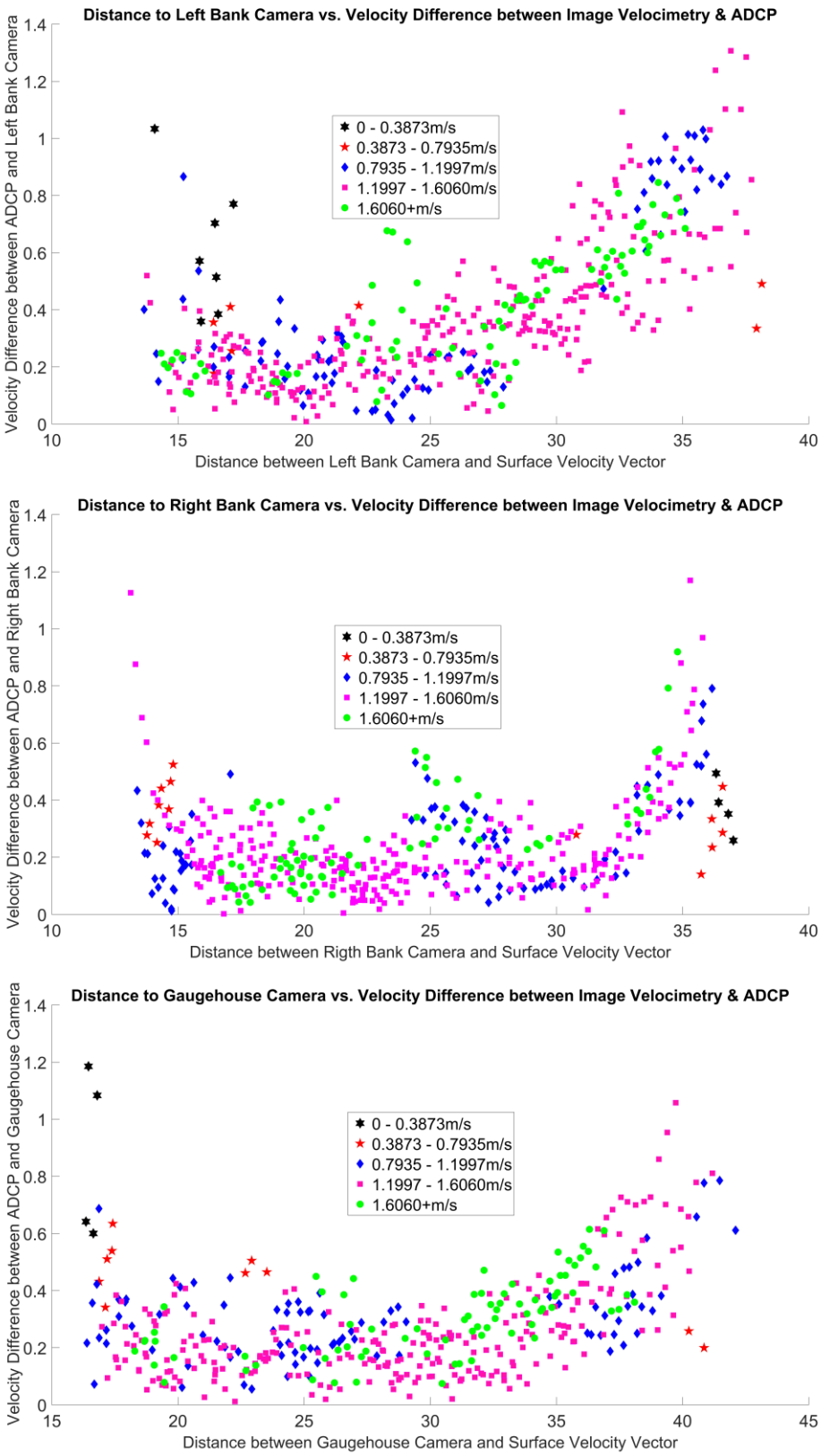

Figure 61: Distance vs Velocity Differences to the ADCP Scatterplots for May 5th, 2023 Top) Left bank camera Middle) Right bank camera Bottom) Gaugehouse camera

4.1.1.6.1 Maximum Distance Sensitivity Analysis

As previously mentioned in the analysis, surface velocity vectors were being compared between methods by finding the closest point between two methods. A sensitivity analysis was done looking at two parameters; the maximum distance allowed between 2 points, and the difference in results when using single ping ADCP data vs 5 ping boxcar average ADCP data. This was done to see what distance threshold gave a dense spatial comparison between methods while also ensuring that the distance between the points was not inducing unnecessary error in the results.

Table 14 and Figure 62 shows the mean absolute error and the velocity differences between the left and right bank cameras for various distances, respectively. The MAE for the cameras is the highest at a maximum distance of 0.25m with a value of 0.5494m/s. This can likely be attributed to the small amount of velocity differences that are calculated at this maximum threshold seen in the velocity difference plots. The top left plot in Figure 62 displays velocity differences on the left bank and a small few on the right bank but lacks any spatial comparison inwards from the banks towards the center of the Castor River. As the maximum distance threshold increases, a downward trend in MAE error is shown and the spatial distribution of velocity differences increases. Once a maximum distance of 0.6m the downward trend in MAE stops and begins to increase again slightly suggesting that some error might be attributed by comparing velocity vectors that are too far apart. Furthermore, when looking at the velocity difference plots there is little to no difference in the spatial availability of velocity comparison measurements between 0.5m and 1.0m maximum distance. For these reasons it was determined that 0.5m was the best choice for the maximum allowable distance between two velocity points.

Table 14: Sensitivity analysis of the maximum allowable distance between two points to be used for a velocity comparison between the left and right bank cameras. Mean absolute error being one of the two ways used to evaluate the thresholds

Maximum Distance (m)	Right Bank vs. Left Bank Camera MAE
0.25	0.5494
0.3	0.4625
0.4	0.3465
0.5	0.3426
0.6	0.3426
0.75	0.3486
1.0	0.3516

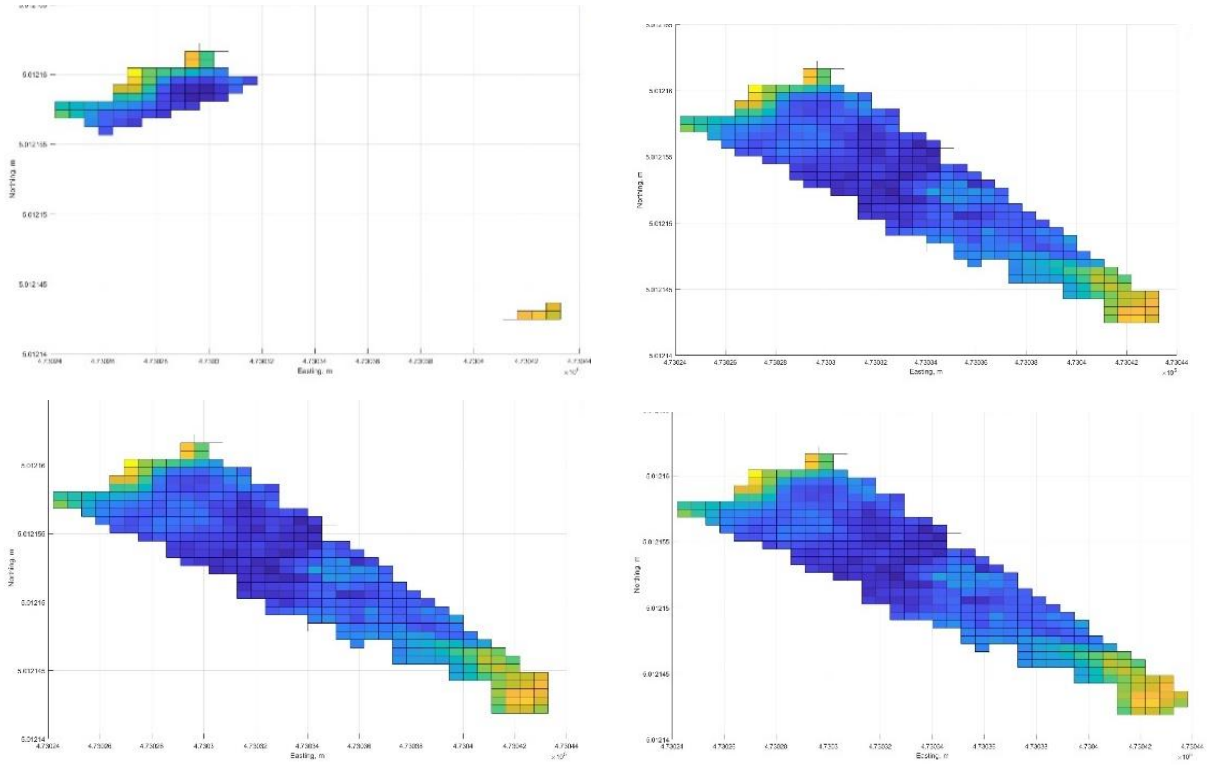

Figure 62: Velocity difference plots between left and right bank cameras with varying sensitivities Top Left) 0.25m maximum distance threshold Top Right) 0.5m maximum distance threshold Bottom Left) 0.75m maximum distance threshold Bottom Right) 1.0m maximum distance threshold

Table 15, Figure 63, and Figure 64 displays the mean absolute error for the cameras compared to both the single ping and 5-ping boxcar averaged ADCP data as well as the velocity differences between the ADCP near-surface measurements and the right bank camera surface velocities. When comparing the single ping and 5-ping boxcar average data, the results of the analysis show that the single ping does in fact produce more velocity comparisons. On the other hand, as shown in the velocity difference plots it also increases the variance in the velocity comparisons and it can be seen that there is less consistency with some sporadic velocity differences in the single ping plots shown in Figure 63. This is also demonstrated in the MAE comparison between boxcar and single ping. The single ping data error is on average, approximately 10cm/s higher than the boxcar averaged data. This is likely due to errors in the single ping ADCP data. For these reasons the boxcar average ADCP data was chosen over the single ping data. However, some of the ADCP surveys done by ECCC had to be processed in alternative ways so some single ping ADCP data was used in the study. It was concluded that the most appropriate maximum distance threshold to be used would be 1.0m for the boxcar averaged ADCP data as it gave the maximum number of velocity comparisons while maintaining a similar level of mean absolute error as the smaller maximum distance thresholds that were tested.

Table 15: Sensitivity analysis of the maximum allowable distance between a camera surface velocity vector and the closest ADCP near-surface velocity measurement looking at both single ping ADCP and 5 ping boxcar average ADCP data

Maximum Distance (m)	Right Bank Camera vs. ADCP MAE		Left Bank Camera vs. ADCP MAE	
	Boxcar	*Single Ping*	*Boxcar*	*Single Ping*
0.25	0.2498	0.3392	0.3652	0.4513
0.50	0.2527	0.3519	0.3865	0.4776
0.75	0.2476	0.3490	0.3808	0.4639
1.0	0.2425	0.3538	0.3836	0.4670

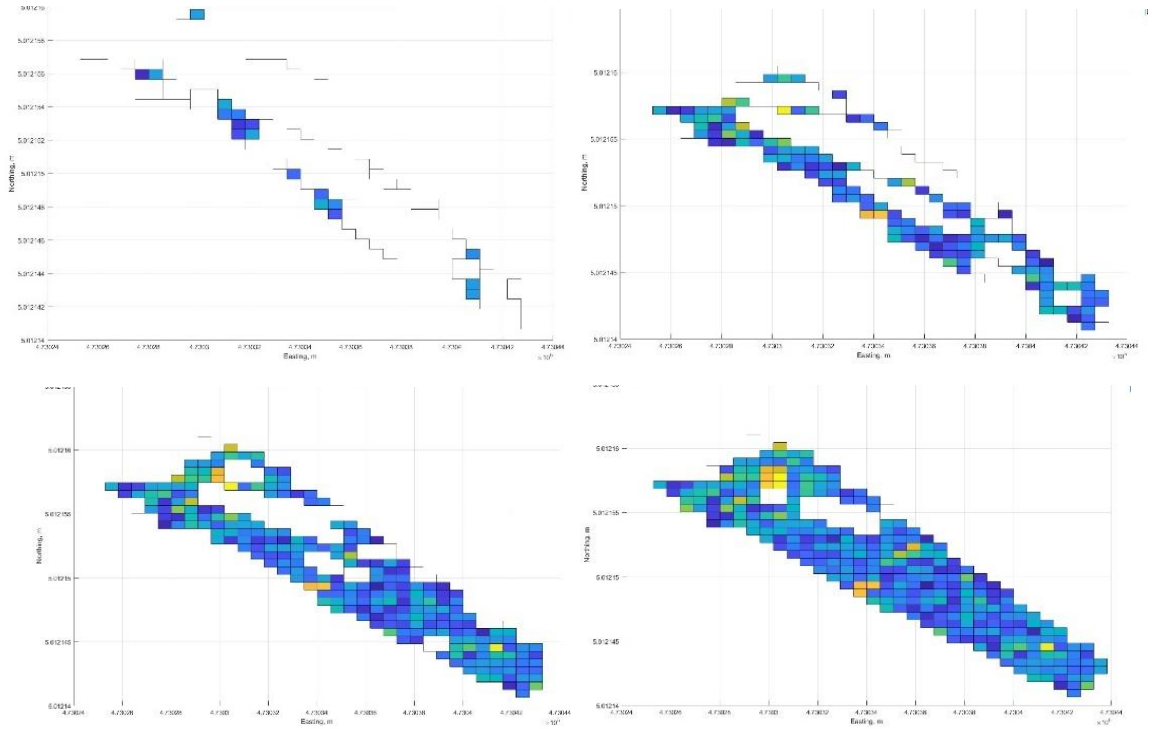

Figure 63: Velocity difference plots between right bank camera and single ping ADCP data Top Left) 0.25m maximum distance threshold Top Right) 0.5m maximum distance threshold Bottom Left) 0.75m maximum distance threshold Bottom Right) 1.0m maximum distance threshold

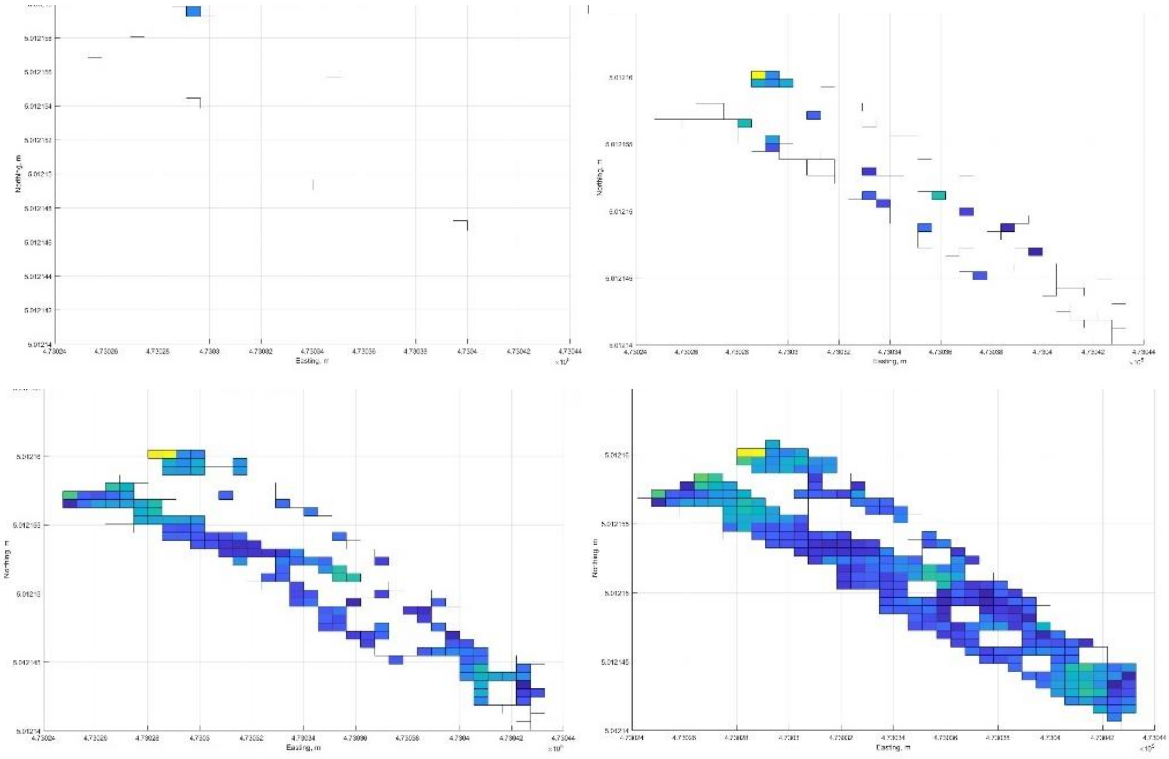

Figure 64: Velocity difference plots between left bank camera and 5-ping boxcar average ADCP data Top Left) 0.25m maximum distance threshold Top Right) 0.5m maximum distance threshold Bottom Left) 0.75m maximum distance threshold Bottom Right) 1.0m maximum distance threshold

4.1.1.7 March 6th, 2024

Velocity Differences

The velocity differences for this survey follow less of a trend (Figure 65), this is likely due to a lack of surface texture that affected the estimates of the left bank camera. Figure 66 (Top) compares the left and right bank camera velocity vector field. The lack of sunlight resulted in inadequate tracer particles along the surface on the left bank (shown in Figure 66 (Bottom)) causing extremely underestimated velocity estimates; because of this it is difficult to analyze the velocity differences near the left bank with the left bank camera. Looking at the left versus right bank camera, the expected trend of significant differences near the banks can be seen along the right bank. With the gaugehouse and right bank camera the largest differences are seen near both banks.

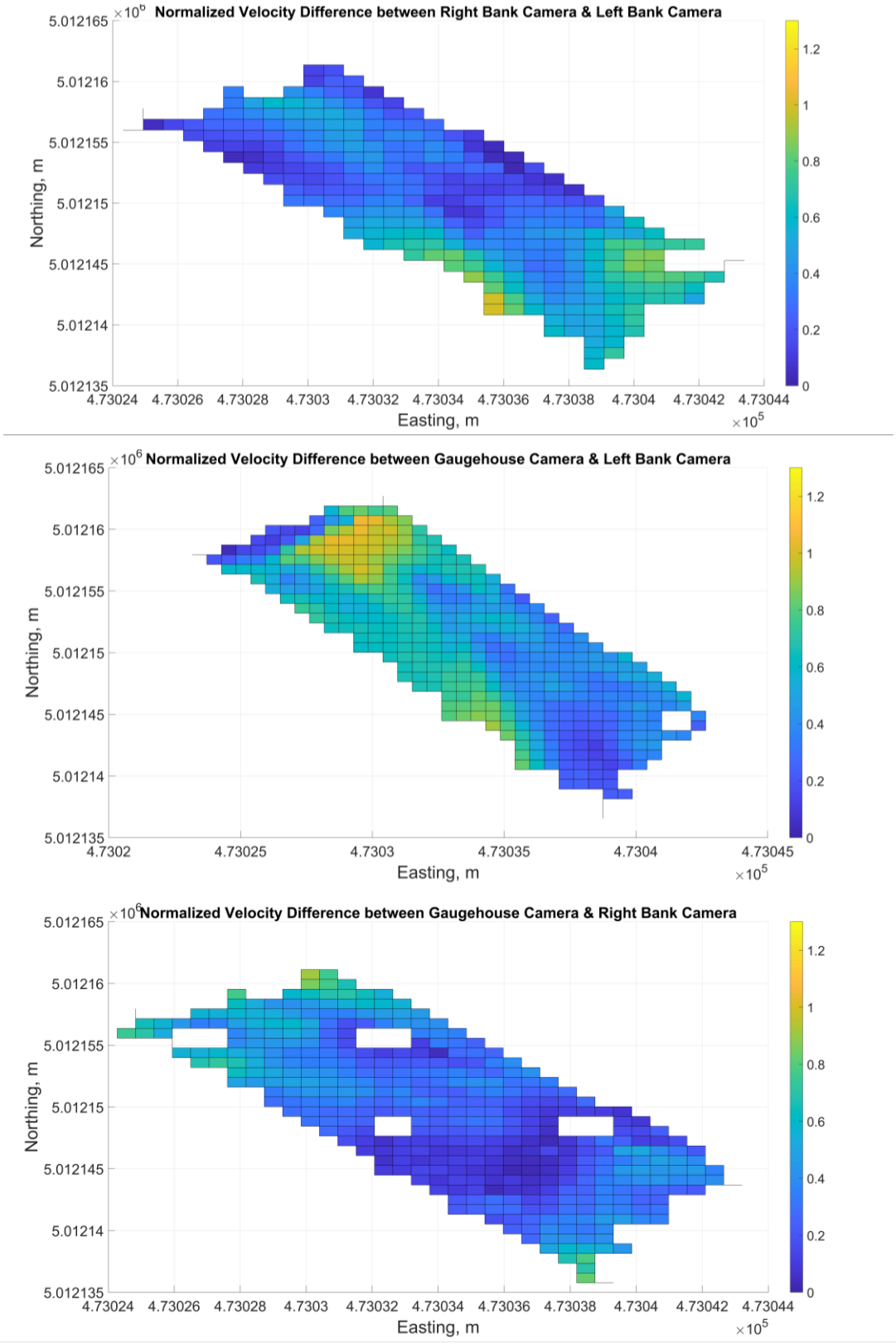

Figure 65: Normalized velocity differences between cameras for March 6th, 2024 survey Top) Right bank vs left bank camera Middle) Gaugehouse vs right bank camera Bottom) Gaugehouse vs left bank camera

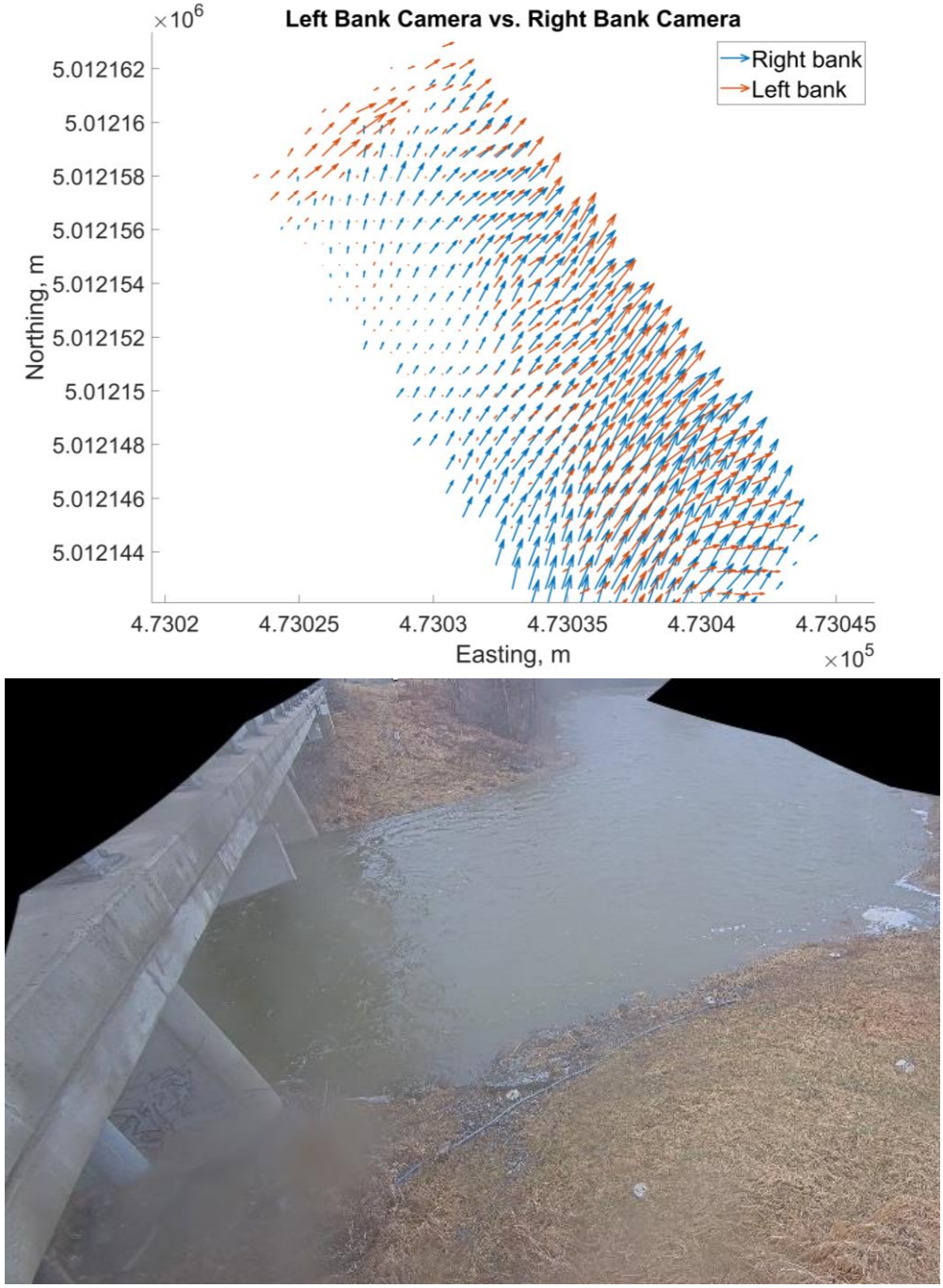

Figure 66: Top) Left bank vs right bank camera vector plot zoomed in towards left bank. Bottom) Frame from left bank camera showing lack of surface texture along the left bank caused by glare

Comparing the right bank camera to the ADCP shows significant differences from the center of the channel through to the left bank (Figure 67). The gaugehouse camera shows moderate differences, which is somewhat unexpected however when looking at discharge comparisons which will be discussed later in the results, the gaugehouse camera performed very well in comparison to the ADCP discharge which could be an explanation for this plot. The left bank comparison plot was not included here due to the lack of tracer particles influencing the results but can be found in Appendix C – Normalized Velocity Difference Plots.

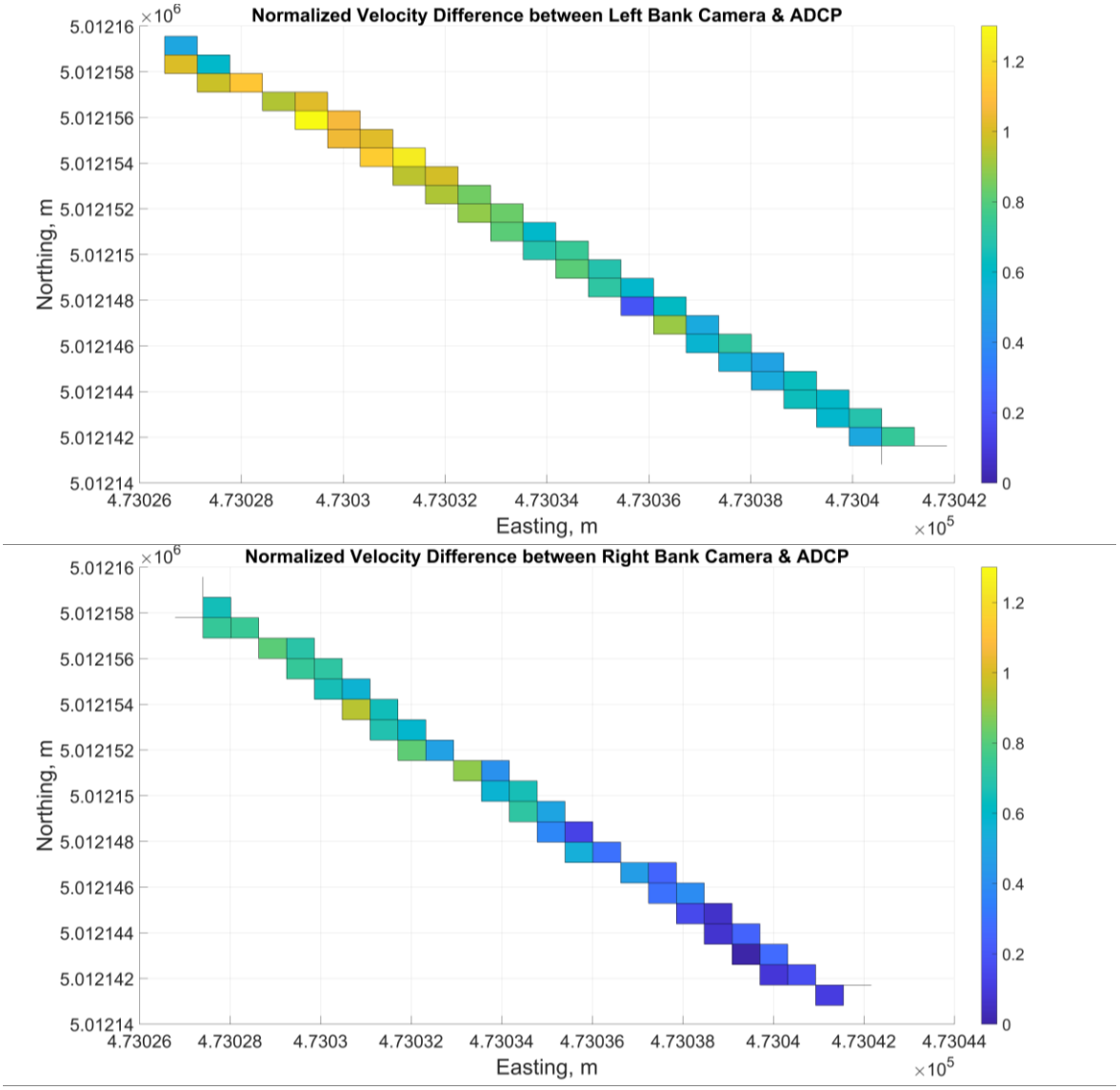

Figure 67: Camera surface velocity differences compared to the ADCP Top) Right bank camera vs ADCP Bottom) Gaugehouse camera vs ADCP

The mean absolute errors (Table 16) were much higher than other surveys but should be disregarded when comparing the left bank camera due to erroneous velocity estimates. The right bank has a very high level of error compared to the ADCP, even when normalized and compared to the other surveys. It is possible that the surface texture also affected the right bank camera's measurements in that area as the vector plot does seem to suggest the camera was affected by the same patch of poor surface texture that the left bank camera had issues with.

Table 16: Mean absolute error of the surface velocity differences between methods for the March 6th, 2024 survey

Comparisons	Normalized Differences (unitless)	Mean Absolute Error (m/s)
RB vs LB	0.3924	0.5320
RB vs ADCP	0.4682	0.6348
LB vs ADCP	0.7688	1.0423
Gaugehouse vs RB	0.3269	0.4432
Gaugehouse vs LB	0.5099	0.6913
Gaugehouse vs ADCP	0.3270	0.4434

Distance Plots

The left bank distance scatterplot was not included in this section because of the inadequate tracer particles near the left bank causing a bias in the results, but it can be found in the Appendix E – Other Plots & MATLAB Scripts. The scatterplots (Figure 68) were as expected based on the velocity differences to the ADCP data. The gaugehouse camera did not indicate any relationship between the distance to the camera and the velocity difference. The right bank camera on the other hand, had an approximately linear upwards trend through nearly the entire plot. It likely starts earlier due to the velocity underestimates seen in the vector plot but followed a similar trend to other surveys where the distance from the camera does influence the velocity estimates.

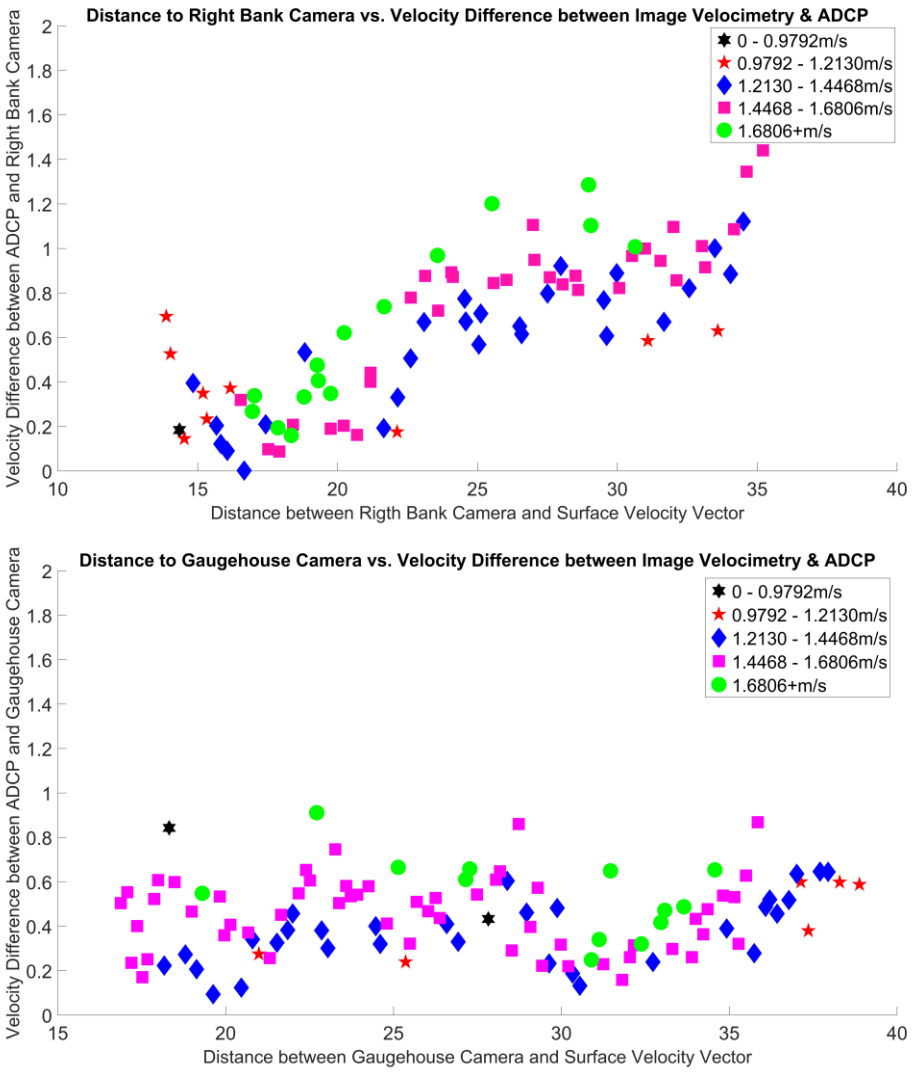

Figure 68: Distance to the camera versus velocity difference compared to the ADCP for March 6th, 2024 Top) Gaugehouse camera vs ADCP Bottom) Right bank camera vs ADCP

4.1.1.8 May 15th, 2024

ADCP and FlowTracker2 data were taken for this survey. Additionally, drone footage was collected at multiple angles and heights for comparison.

Velocity Differences

The velocity differences for the fixed cameras for this survey followed the same trend that other surveys exhibited (Figure 69 and Figure 70). The cameras underestimated the surface velocities on the far shore compared to the ADCP measurements.

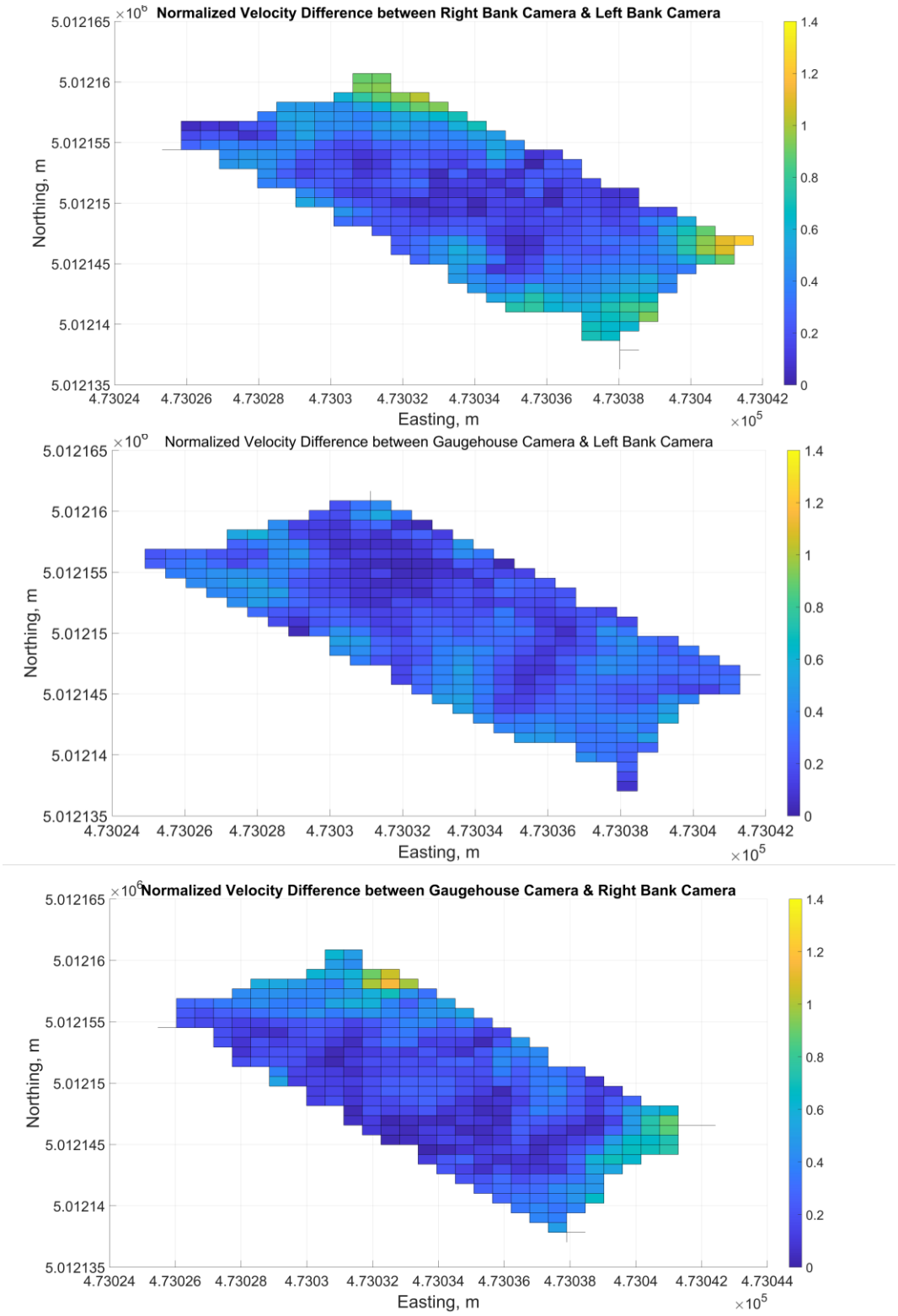

Figure 69: Surface velocity differences between cameras Top) Left bank vs right bank camera Middle) Gaugehouse vs left bank camera Bottom) Gaugehouse vs right bank camera

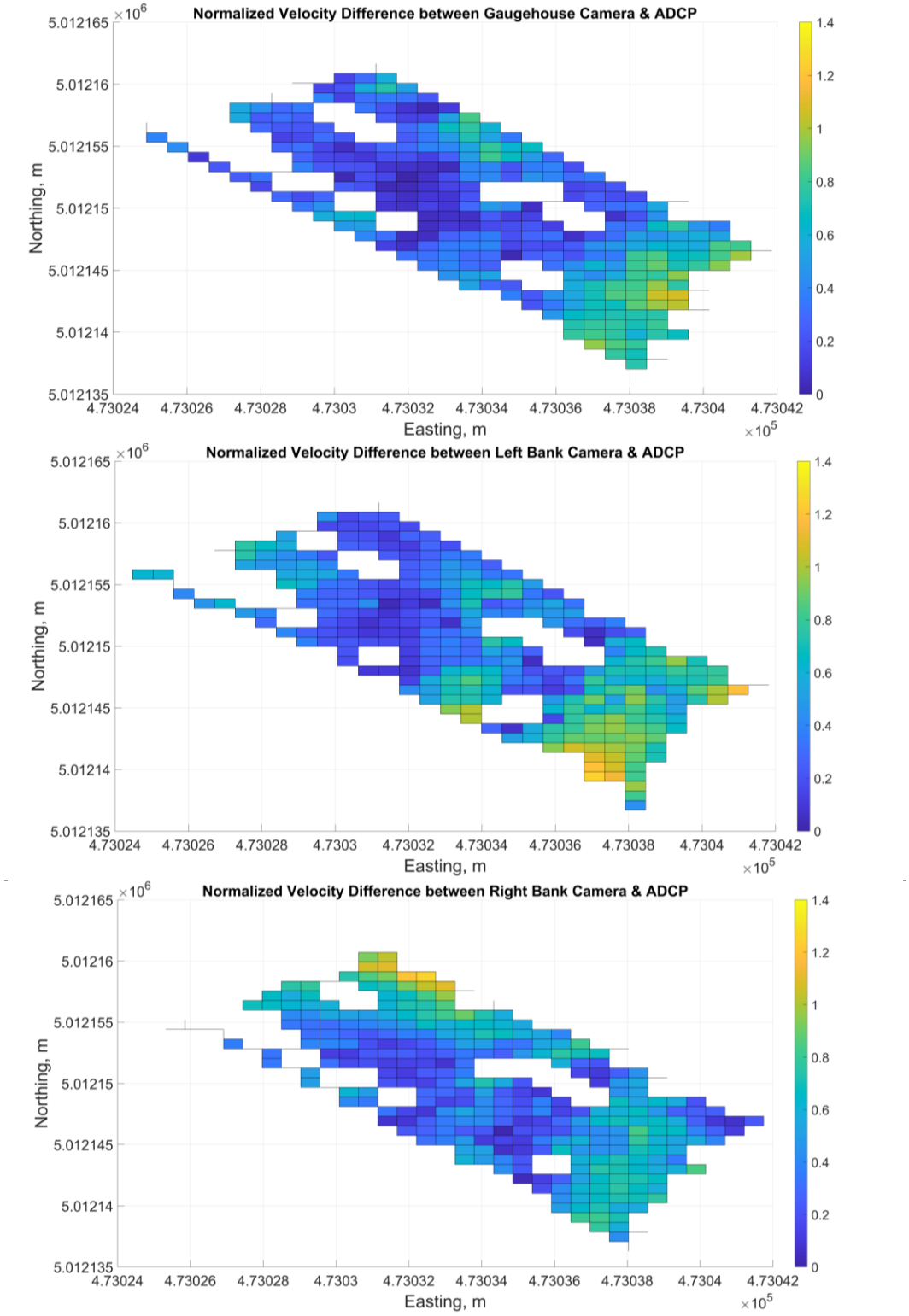

Figure 70: Surface velocity differences between cameras and ADCP measurements Top) Gaugehouse camera vs ADCP Middle) Left bank camera vs ADCP Bottom) Right bank camera vs ADCP

The mean absolute error in Table 17 showed a relatively low absolute error across all comparison methods but when normalized they were similar to the other surveys. The largest errors were the left and right bank cameras compared to the ADCP measurements. The differences were not all very large but because a zig zag survey was performed there were more data points to compare to.

Table 17: Mean absolute errors (MAE) of the surface velocity differences between methods for the May 15th, 2024 survey

Comparisons	Normalized Differences (unitless)	Mean Absolute Error (m/s)
RB vs LB	0.3880	0.2149
RB vs ADCP	0.4817	0.2763
LB vs ADCP	0.4772	0.2672
Gaugehouse vs RB	0.3080	0.1706
Gaugehouse vs LB	0.2669	0.1478
Gaugehouse vs ADCP	0.4018	0.2488

Drone Measurements

Several drone videos were taken during this survey at varying heights and angles to analyze how a camera's extrinsic parameters might affect the results. The drone was first flown at a nadir angle, and in an effort to avoid the overhead power lines the ROI was smaller than the subsequent videos. The angles were altered slightly for each subsequent video and the height/distance to the water surface was adjusted in a way that resulted in the full ROI being in the camera FOV.

The drone and ADCP showed small differences suggesting that the nadir view does help with estimating surface velocity. The right bank is also in good agreement with the drone while the left bank camera had some substantial differences near the right bank from the left bank camera which underestimated the velocities (Figure 71).

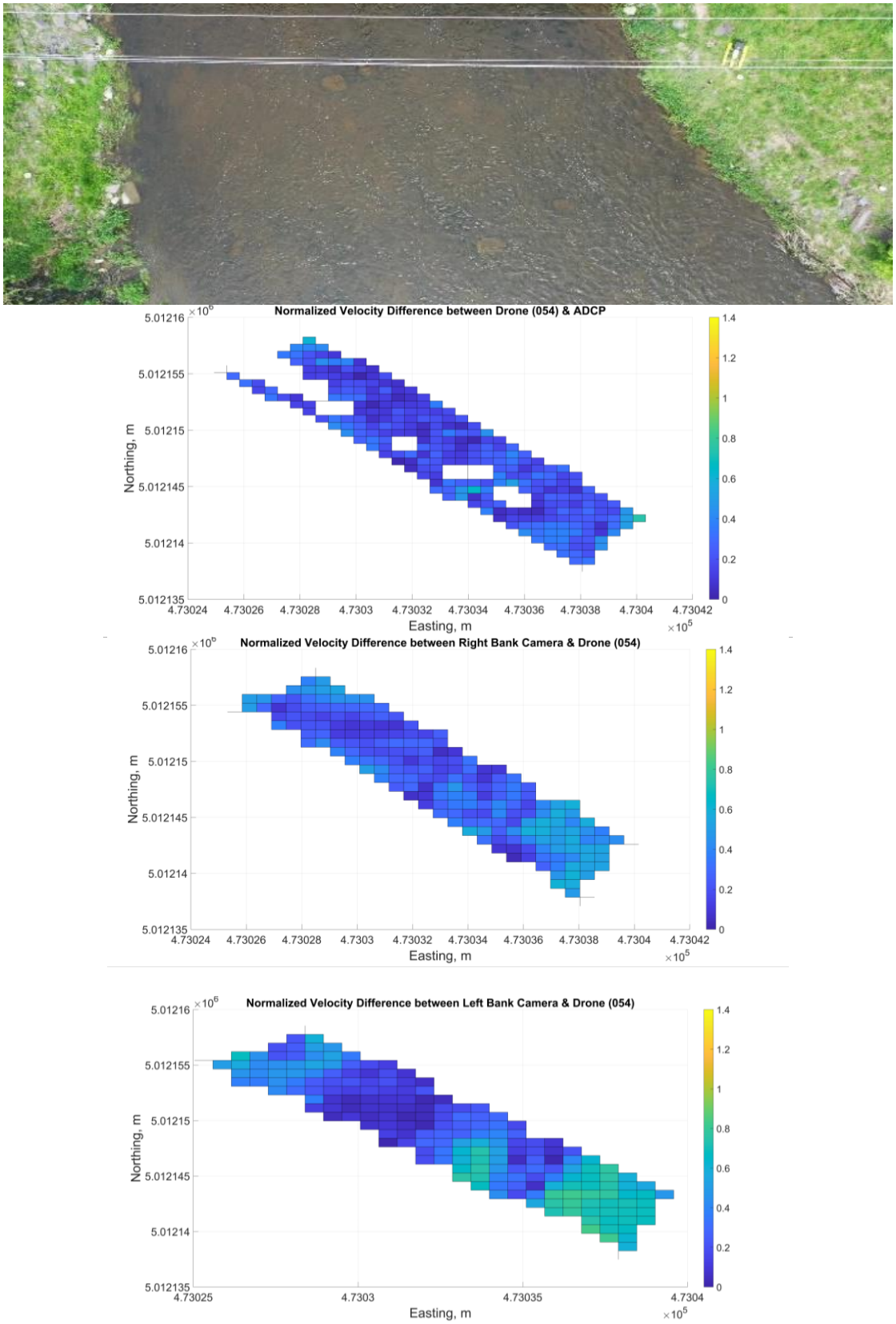

Figure 71: Velocity differences for DJI054 Top) Frame showing FOV from drone Top Middle) Drone vs ADCP Bottom Middle) Drone vs right bank camera Bottom) Drone vs left bank camera

The following video (DJI055) also performed strongly when compared to the ADCP. Both the bridge cameras had substantial differences near the opposite banks of both cameras, attributed to the vector directions of the surface velocity vectors near the banks pointing cross-stream rather than in the actual direction of flow (Figure 72). These velocity differences can be seen in Figure 73.

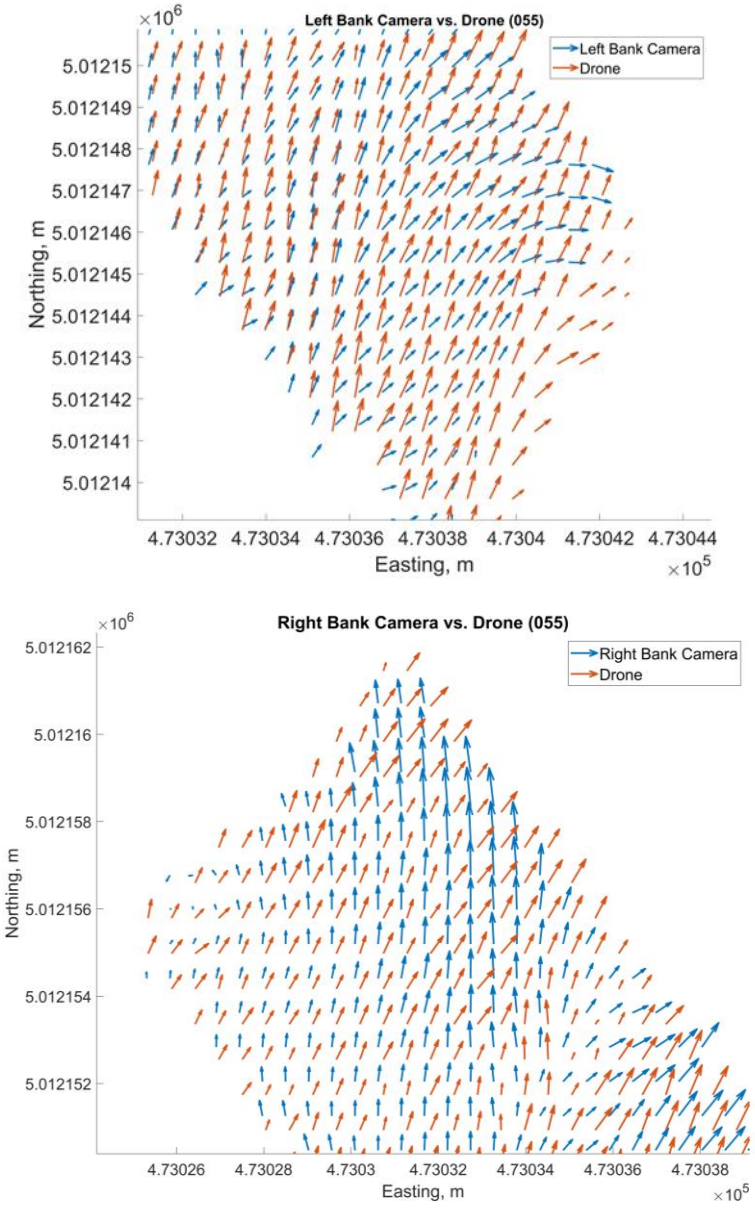

Figure 72: Zoomed in velocity vector plots showing near-bank surface velocity estimates between bridge cameras and drone estimates Top) Left bank camera zoomed in on the right bank Bottom) Right bank camera zoomed in on left bank

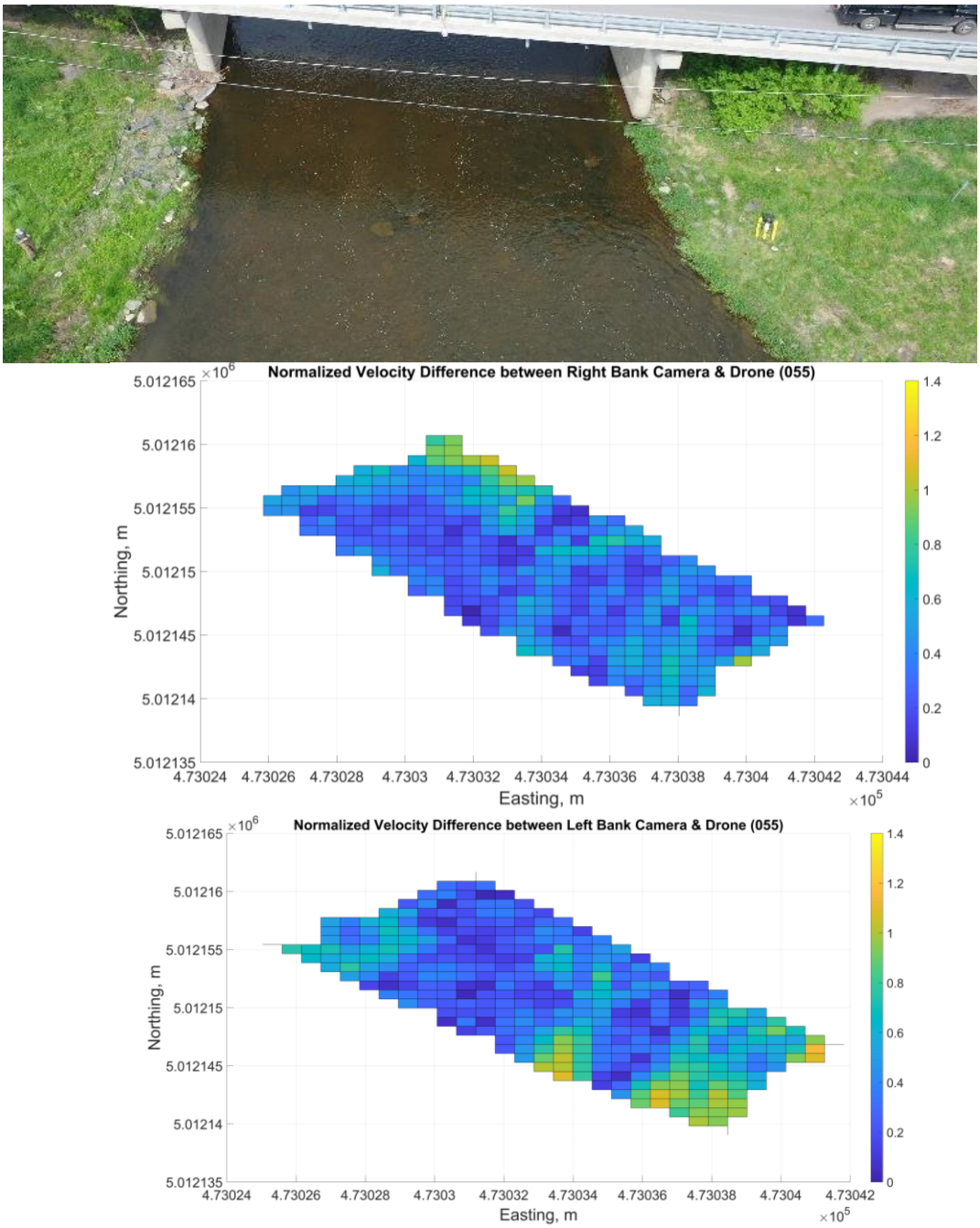

Figure 73: Velocity differences for DJI055 Top) Frame showing FOV from drone Middle) Drone vs right bank camera Bottom) Drone vs left bank camera

DJI057 (Figure 74) had good comparison with the ADCP. The right bank camera also performed similarly to the drone with the largest differences near the left bank. The left bank camera resulted in substantial differences due to the drone overestimating discharge and poorly estimating direction of flow near the right bank.

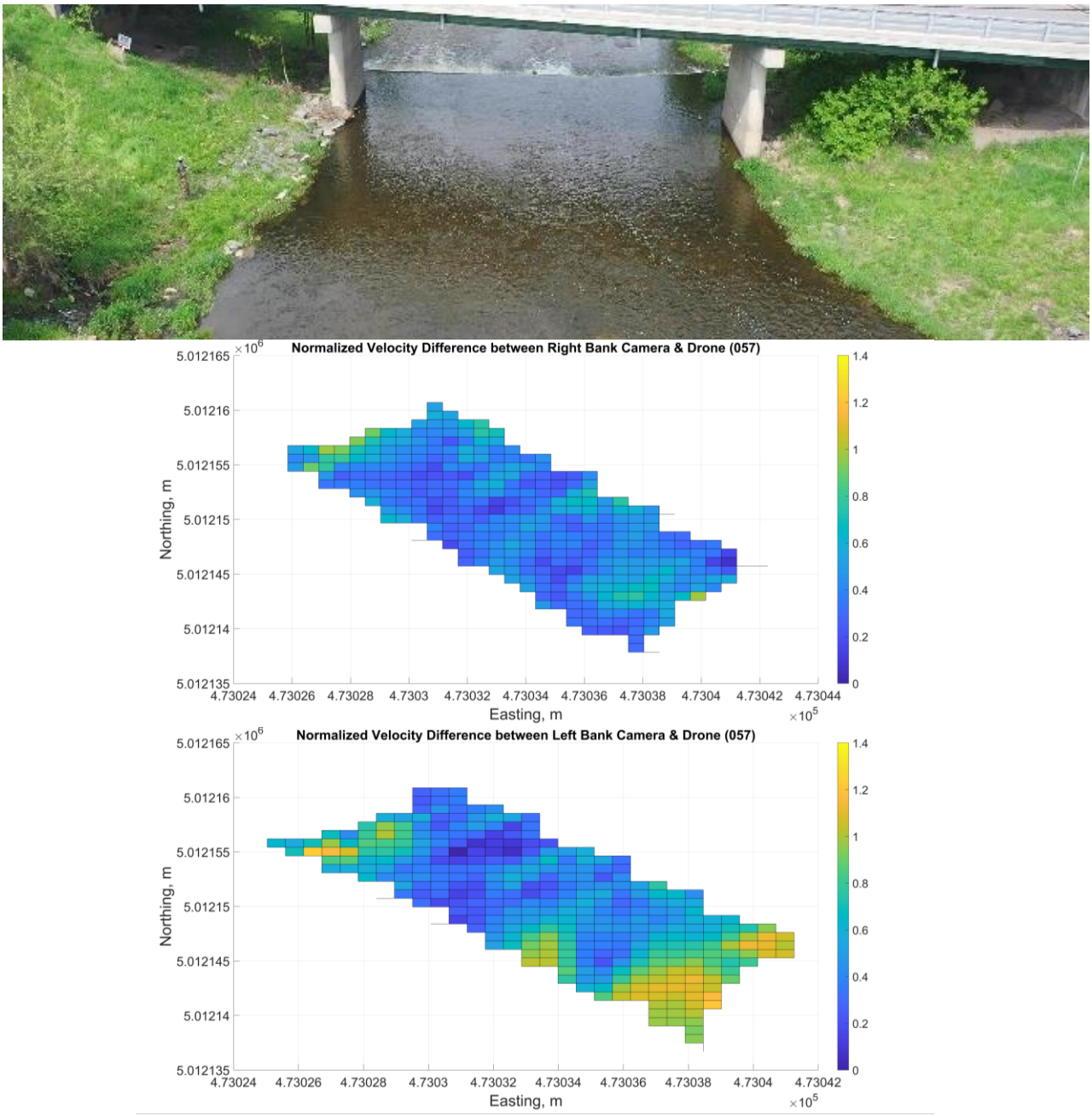

Figure 74: Velocity differences for DJI057 Top) Frame showing FOV from drone Middle) Drone vs right bank camera Bottom) Drone vs left bank camera

Lastly, DJI058 shows some large sporadic differences across all plots (Figure 75). The ADCP had a few large differences, more so than previous videos. The bridge cameras had some substantial differences but were somewhat random as opposed to being near the banks.

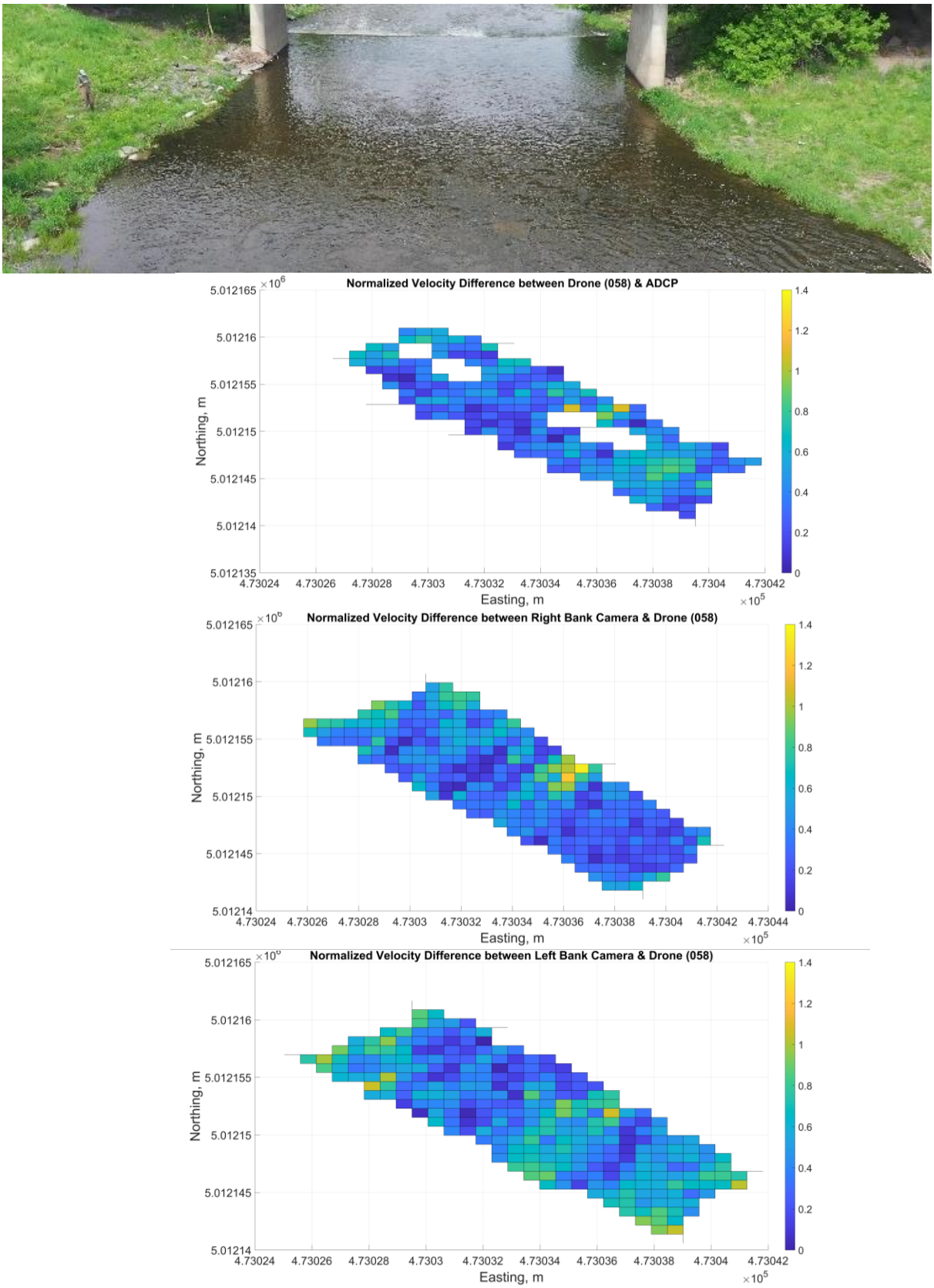

Figure 75: Velocity differences for DJI058 Top) Frame showing FOV from drone Top Middle) Drone vs ADCP Bottom Middle) Drone vs right bank camera Bottom) Drone vs left bank camera

Table 18 displays the MAE for each drone video compared to the other cameras and the ADCP measurements. Overall, errors were consistent across all videos but there were some outliers, particularly, DJI057. The left bank camera compared to the drone had a MAE of 0.3244m/s, nearly 0.05m/s higher than the second highest error. As previously mentioned, this was likely because this drone video overestimated discharge while the left bank camera underestimated resulting in a bigger discrepancy between the two cameras. DJI058 also had higher errors than average. This was also likely caused by having a higher discharge estimate than the fixed cameras. Compared to the average errors for all six drone videos, most of the errors from each drone video did not deviate far from that average.

Table 18: Mean Absolute Error (m/s) in velocity difference for May 15th drone videos

Drone Filename (DJI_00xx)	Mean Absolute Error	Drone vs RB	Drone vs LB	Drone vs Gaugehouse	Drone vs ADCP
54	Normalized	0.3374	0.3660	0.2888	0.2554
	Absolute	0.1869	0.2027	0.1600	0.1679
55	Normalized	0.4015	0.4497	0.3504	0.2230
	Absolute	0.2224	0.2491	0.1941	0.1291
56	Normalized	0.4275	0.3698	0.3865	0.3297
	Absolute	0.2368	0.2048	0.1706	0.1826
57	Normalized	0.4433	0.5856	0.4257	0.3667
	Absolute	0.2456	0.3244	0.2358	0.2031
58	Normalized	0.4183	0.5015	0.3765	0.4123
	Absolute	0.2317	0.2778	0.2085	0.2284
59	Normalized	0.3484	0.3462	0.3457	0.4592
	Absolute	0.1930	0.1918	0.1915	0.2543
Average	**Normalized**	**0.4056**	**0.4545**	**0.3656**	**0.3174**
	Absolute	**0.2194**	**0.2418**	**0.1934**	**0.1942**

Distance Plots

Fixed Cameras

Figure 76 examines the velocity differences compared to the distance from the camera. All three cameras showed a similar trend. The errors were moderately high the closer to the camera the velocity vector was and then an increase in error occurred as the distance became greater similar to some other surveys.

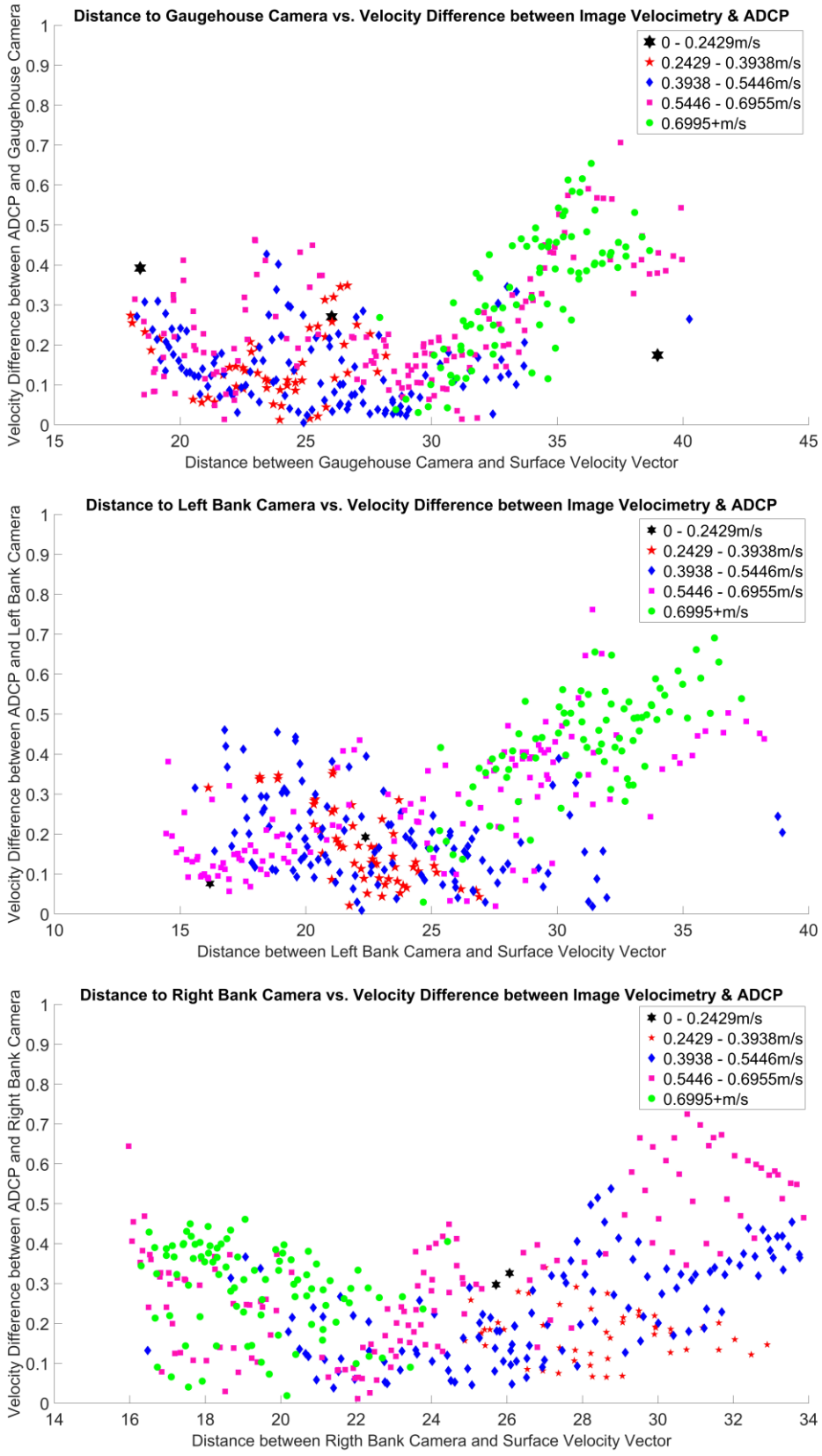

Figure 76: Distance to camera versus velocity differences to ADCP: Top) Gaugehouse camera. Middle) Left bank camera. Bottom) Right bank camera

Drone Videos

Figure 77 displays the distance compared to the velocity difference scatterplots for all surveys taken that day combined into a single plot. Neither this plot nor any of the individual plots that can be found in Appendix E – Other Plots & MATLAB Scripts showed any sort of distinguishable trend, this is perhaps because the drone was flown near the center of the channel, so distance did not affect the GSD or pixel size distribution throughout the channel as much as the fixed cameras.

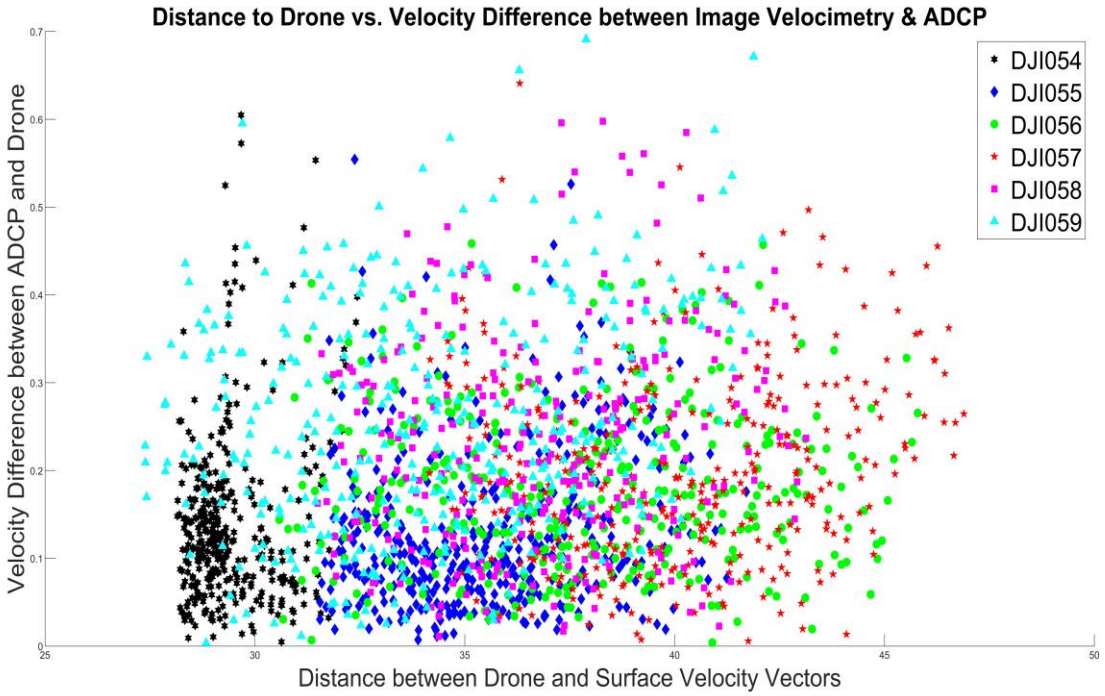

Figure 77: All surveys combined distance to drone versus surface velocity differences plot between drone image velocimetry and ADCP

ADCP Variance

ADCP variance between transects was determined for this survey to ensure that the ADCP validation measurements used in this study did not deviate significantly between each ADCP transect. As previously explained, the closest velocity values within 1.0m or less between transects were compared. The MAE was then found for each transect comparison and then averaged as seen in Table 19. The average MAE for the entire cross-section survey performed was 11.85cm/s or 0.1185m/s.

Table 19: Mean Absolute Error (m/s) between ADCP Transects

Transect 1 vs 2	0.0665
Transect 1 vs 3	0.0831
Transect 1 vs 4	0.1253
Transect 2 vs 3	0.1444
Transect 2 vs 4	0.1495
Transect 3 vs 4	0.1423
Average MAE	0.1185

To determine if this level of variance was acceptable, the standard error of the mean was found using the following equation:

$$Standard\ Error\ of\ the\ mean = \frac{\sigma}{\sqrt{n}}$$

Equation 15: Standard error of the mean

Where σ is the variance and n is the number of samples. This data was boxcar averaged over five single pings and the top two bins were used giving an n of ten. ADCP variance for a single ping and one bin has been shown to be 0.30m/s (Rennie and Church, 2010) so the expected error was 0.095m/s or 9.5cm/s. This gave an extra variance of 2.35cm/s than what was expected which was relatively small with the average surface velocity being 0.5539m/s. Additionally, there were a couple outliers (Figure 78). When these outliers were removed the average MAE was be reduced to below the standard error of the mean (Table 20).

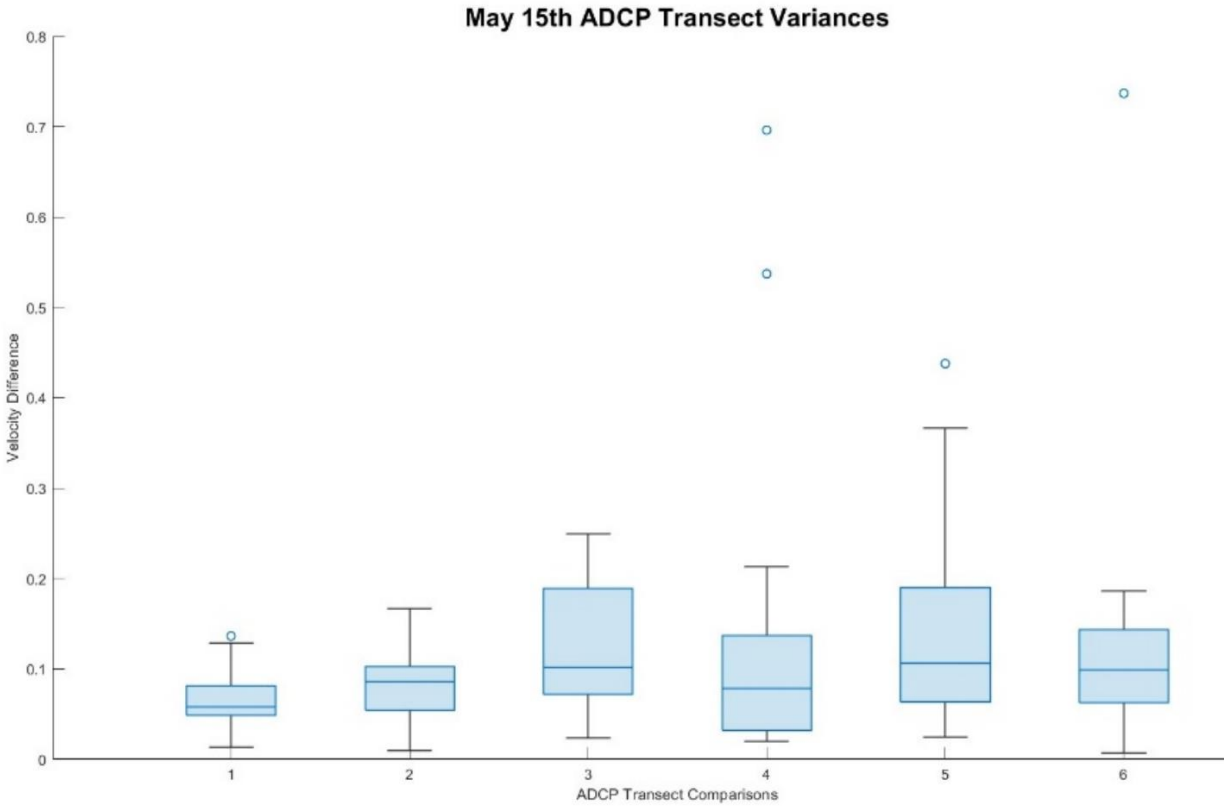

Figure 78: Boxplot of ADCP variance between transects

Table 20: Mean Absolute Error (m/s) between ADCP Transects without outliers shown in Figure 77

Transect 1 vs 2	0.0624
Transect 1 vs 3	0.0831
Transect 1 vs 4	0.1253
Transect 2 vs 3	0.0769
Transect 2 vs 4	0.1273
Transect 3 vs 4	0.0928
Average MAE	0.0946

ADCP vs Near-surface FlowTracker

For the May 15th survey, ten near-surface FlowTracker2 points were taken along cross-section 2. These were then compared to the top two bins of the ADCP data by taking the difference in velocity magnitude between the closest points spatially, instead of comparing the east and north velocity vectors to one another first and then taking the difference as was done for the rest of the comparisons. The velocity magnitude had to be compared because the FlowTracker2 points were taken as close to parallel with the flow as possible so the velocity vectors from the FlowTracker2 were not necessarily in an easting and northing direction.

All ten FlowTracker2 points were compared to each measured ADCP transect as well as the zig zag survey that was performed. Then the average difference for each survey comparison was calculated as seen in Table 21. The results show a small difference between the two methods making it reasonable to state that the top two bins of the ADCP surveys were a valid comparison measurement.

Table 21: Difference (m/s) between near-surface FlowTracker2 velocity magnitudes vs ADCP (Top 2 bins) velocity magnitudes

FlowTracker2 Measurements	Transect 1	Transect 2	Transect 3	Transect 4	Zig Zag Survey
Point 1	-0.0421	0.1388	0.1240	0.0612	0.0421
Point 2	0.1330	0.1785	0.0754	0.0312	0.0754
Point 3	-0.0490	0.0255	-0.0597	-0.0551	-0.1192
Point 4	0.1423	0.1900	0.1625	0.0139	0.1561
Point 5	0.2322	0.2528	0.0812	0.1792	0.2537
Point 6	-0.1256	-0.0344	-0.1883	0.0530	-0.0860
Point 7	0.0335	-0.0353	-0.0459	-0.2159	-0.0503
Point 8	-0.1098	0.0321	-0.0300	-0.0236	-0.0284
Point 9	-0.0536	0.0596	0.0081	0.0036	0.0081
Point 10	-0.0228	-0.0298	-0.0437	0.0029	-0.0486
Average Difference	0.0138	0.0778	0.0084	0.0050	0.0203

4.1.1.9 Combined Discharge Results

This section summarizes combining results from multiple cameras and how these compare to the ADCP discharge (Table 22). The largest percent differences in discharge were found in both a low flow and a high flow survey but percent differences were fairly consistent across all surveys. Overall, the average absolute percent difference across all surveys was 8.19% suggesting good agreement with the ADCP measurements. These results will be further compared to the individual camera results in the discussion.

Table 22: Summary of Relative Error between Combined Camera Discharge and ADCP Discharge

Survey Date	March 6th, 2024	May 15th, 2024	April 8th, 2022	March 21st, 2022	May 5th, 2023
ADCP Q	23.30	5.29	53.80	55.50	25.10
Combined Q	22.09	4.57	59.85	58.10	23.54
Error (m^3/s)	-1.21	-0.72	6.05	2.60	-1.56
Percent difference	-5.19%	-13.61%	11.25%	4.68%	-6.22%
Absolute Average % difference	8.19%				

4.1.1.10 Summary of Surveys

The majority of the data shows the same trend. The cameras are capable of accurately estimating surface velocities, however that accuracy was typically diminished near the far shore. Comparing the cameras along the left bank the velocity differences generally showed that the gaugehouse camera performed slightly better than the left bank camera when measuring the far shore. The velocity magnitudes of the left bank cameras near the right bank were typically lower than the right bank camera, and the vector directions were not accurate with respect to the actual direction of flow as they were oriented more cross-stream than they should be. The same can be said for the right bank camera measuring near the left bank in comparison to the left bank cameras. Additionally, some of the results demonstrated the importance of tracer particles and how a lack of them can result in low velocity estimates. As seen in Table 23, the highest levels of

normalized error, ignoring the outliers, occurred when comparing the cameras that are on opposite banks, followed by the comparisons to the ADCP measurements.

Table 23: Summary of MAE of velocity differences between fixed cameras and ADCP data for all survey dates

Survey Date	Mean Absolute Error	RB vs LB	RB vs ADCP	LB vs ADCP	Gaugehouse vs RB	Gaugehouse vs LB	Gaugehouse vs ADCP
May 15th, 2024	Normalized Differences (unitless)	0.3880	0.4817	0.4772	0.3080	0.2669	0.4018
	Absolute (m/s)	0.2149	0.2763	0.2672	0.1706	0.1478	0.2488
March 18th, 2022	Normalized Differences (unitless)	0.3733	N/A	N/A	0.3628	0.1893	N/A
	Absolute (m/s)	0.4310	N/A	N/A	0.4219	0.2202	N/A
May 5th 2022	Normalized Differences (unitless)	0.4265	N/A	N/A	0.3997	0.1496	N/A
	Absolute (m/s)	0.2402	N/A	N/A	0.2251	0.0843	N/A
March 21st 2022	Normalized Differences (unitless)	0.4435	0.3766	0.2614	0.3016	0.2692	0.3601
	Absolute (m/s)	0.6703	0.5691	0.3950	0.4558	0.4068	0.5442
April 8th, 2022	Normalized Differences (unitless)	0.2394	0.2634	0.3225	0.2428	0.1464	0.2928
	Absolute (m/s)	0.4150	0.4566	0.5591	0.4209	0.2538	0.5077
March 6th, 2024	Normalized Differences (unitless)	0.3924	0.4682	0.7688	0.3269	0.5099	0.327
	Absolute (m/s)	0.5320	0.6348	1.0423	0.4432	0.6913	0.4434
May 5th, 2023	Normalized Differences (unitless)	0.2329	0.1584	0.2492	0.1788	0.1646	0.1856
	Absolute (m/s)	0.3523	0.2397	0.3771	0.2706	0.2491	0.2809

4.2 Stereoscopic Image Velocimetry Results

Unfortunately, no promising surface velocity results were produced with the stereoscopic setups. This section will detail the efforts that were made and what results were able to be generated from them.

4.2.1 Castor River Field Site

For the field site, only the Stereolabs ZED2i camera was used. Data was collected from both banks and on the bridge during the May 5th, 2023 survey. The Stereolabs camera was excellent at reconstructing a 3D surface and gave both a distance image measuring distance between the object and camera (Stereolabs refers to them as depth images, shown in Figure 79 as well as a 3D point cloud of the river (Figure 80).

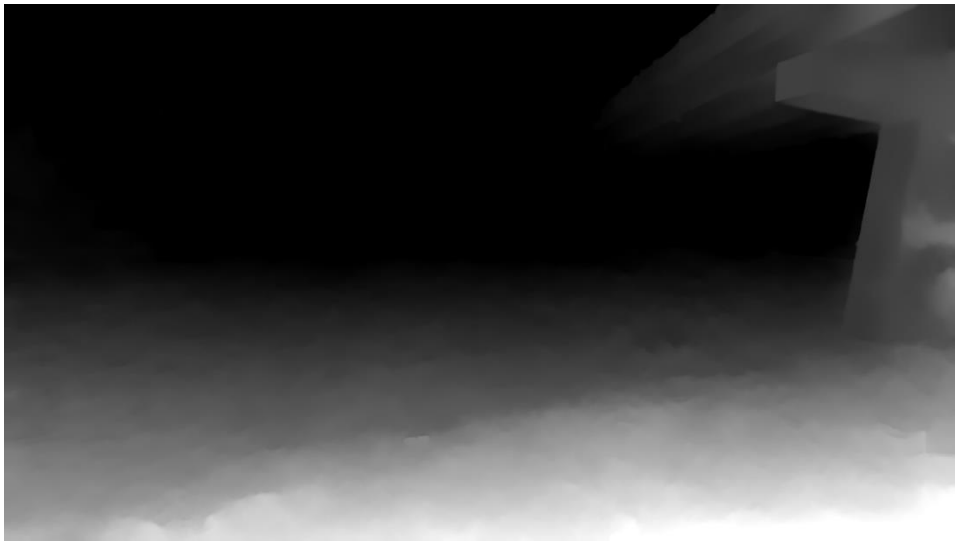

Figure 79: Depth image of the Castor River taken on the right bank

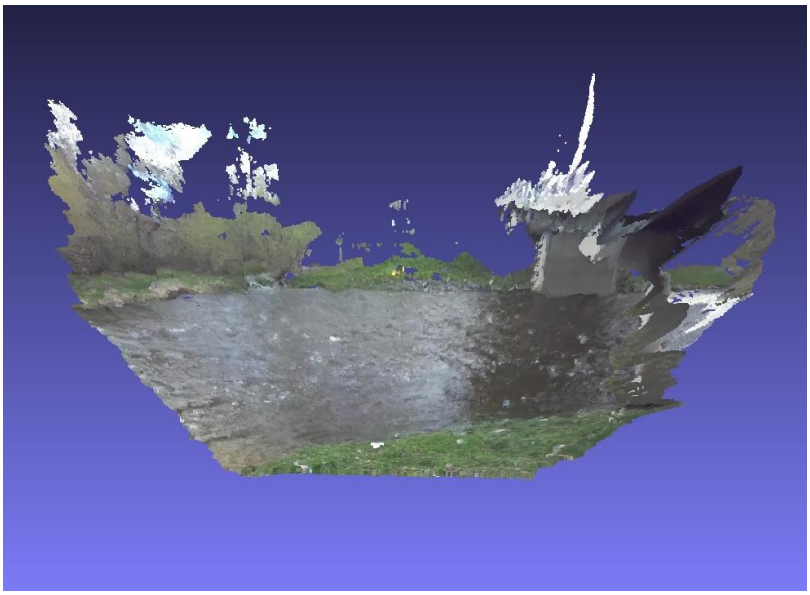

Figure 80: Snapshot of reconstructed point cloud of the Castor River collected from the right bank

The depth images were processed using RIVeR but were poorly resolved. It was determined that this was because the depth images were measuring the distance between the camera and the water surface. Since the camera was fixed there was minimal change in depth to the water surface with the moving surface being the only variable. The point clouds appeared to be an accurate representation of the river, however, RIVeR is only able to handle image and video codecs so there was no way to process the point clouds without first converting them to an image format. The point clouds were converted to .png files using the code described in 3.5.2.1 Point Cloud to Image Code. They were all rotated to obtain a nadir view as seen in Figure 81. Point

clouds had to exported from the Stereolabs application manually, so a test using ten point clouds was performed to ensure that the method was first working before exporting a large quantity of them which would have been very time consuming. Unfortunately, the results were very poor as shown in Figure 82. Both the vector magnitudes and directions are incorrect. The vector directions were extremely random, and the magnitude showed some extreme overestimates.

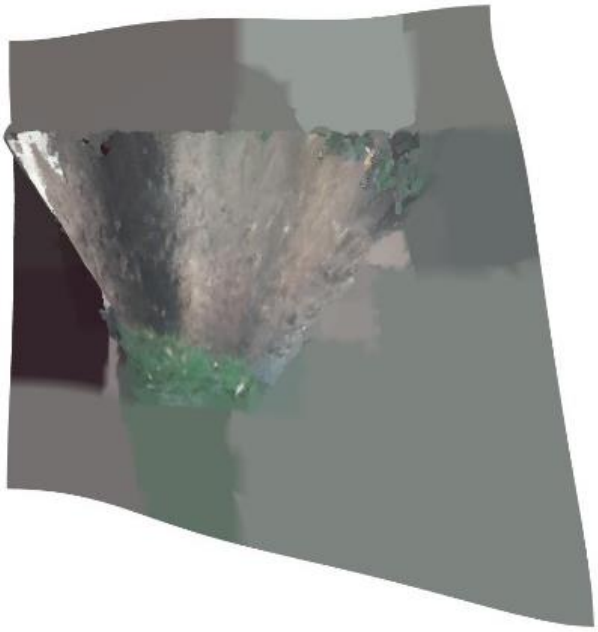

Figure 81: .png nadir image of the Castor River taken from the right bank video converted from .ply

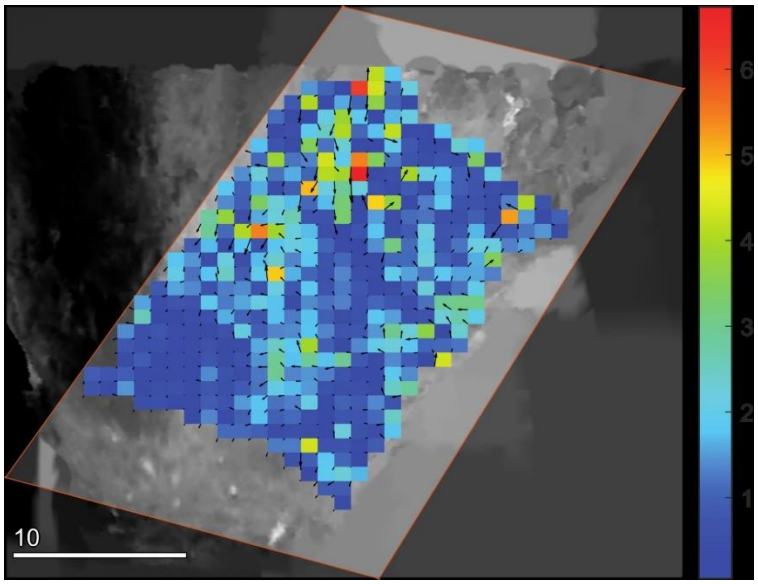

Figure 82: RIVeR median frame from converted point clouds test

4.2.2 Black Canyon Lab Model

Both Pix4D and Agisoft Metashape were tested for the lab setup. Pix4D proved to be unsuitable as it was only able to use multiple images from a single camera and not two separate cameras. Agisoft Metashape initially produced reasonable results with a dry canyon model. The reconstructed point cloud generated a high number of matching points and while there were some gaps in the reconstruction it was enough to obtain an accurate 3D model. However, when the model had flow running through, the water surface could not be reconstructed resulting in a point cloud with just the canyon floodplains. The cameras were adjusted and placed closer together to allow for more overlap between images but even with them side-by-side the water surface could not be reproduced.

Additionally, the Stereolabs camera was used in the lab. The surface is very well constructed, however, it could not differentiate between the water surface and the channel bed as shown in Figure 83 where the tracers particles are stretched from the surface to the bed. This suggests that the water is too clear to identify the water surface.

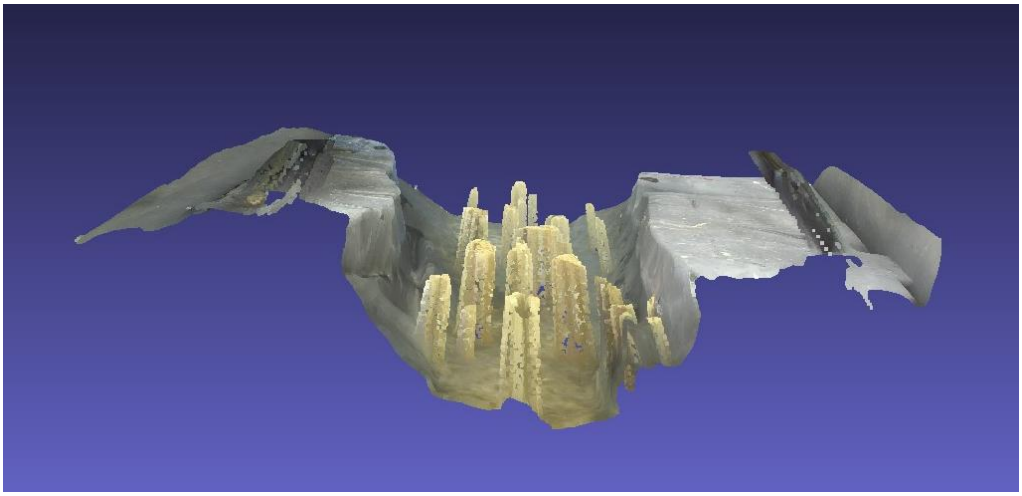

Figure 83: Surface reconstruction of the canyon lab model

A total of ten nadir point clouds (Figure 84) were converted to images and processed in RIVeR (Figure 85). Due to the lack of good tracer densities, the ensemble correlation was used and produced reasonable results compared to ADV surface measurements shown in Figure 86.

Figure 84: Nadir view of canyon reconstructed point cloud converted to image file

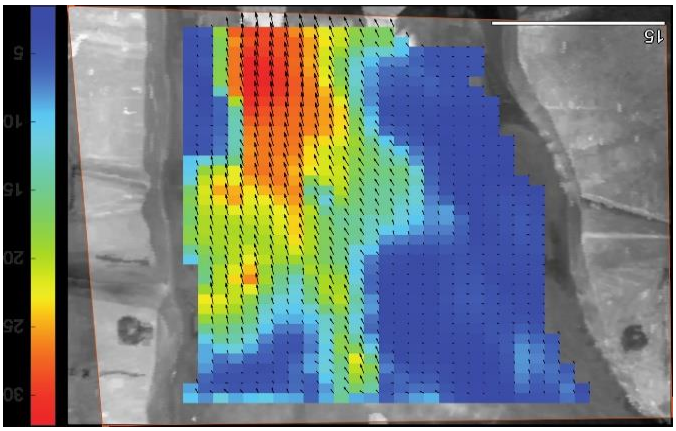

Figure 85: Median frame of point cloud image files processed in RIVeR

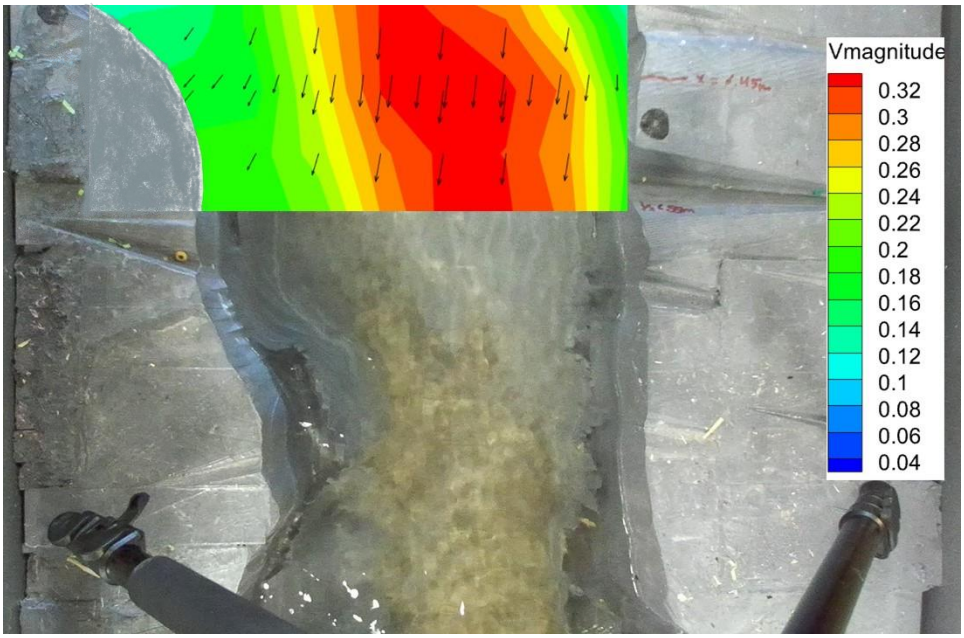

Figure 86: Near-surface ADV data overlayed on Black Canyon

5.0 Discussion

5.1 Multi-Camera LSPIV

Far Bank Velocity Estimates

Figure 87 shows the vector fields for the May 5th, 2023 survey for the left and right bank camera zoomed in on each bank. Both plots show that the cameras underestimate the velocities on the far shore when compared to the other camera. There are two likely explanations for this reduced accuracy; the first is that as the distance to the camera increases the object imaged/pixel size increases. A limiting factor with processing oblique videos through RIVeR is that the image processing is done prior to orthorectification. This leads to interrogation areas having non-uniform real world distances across the images which likely results in error in the far shore.

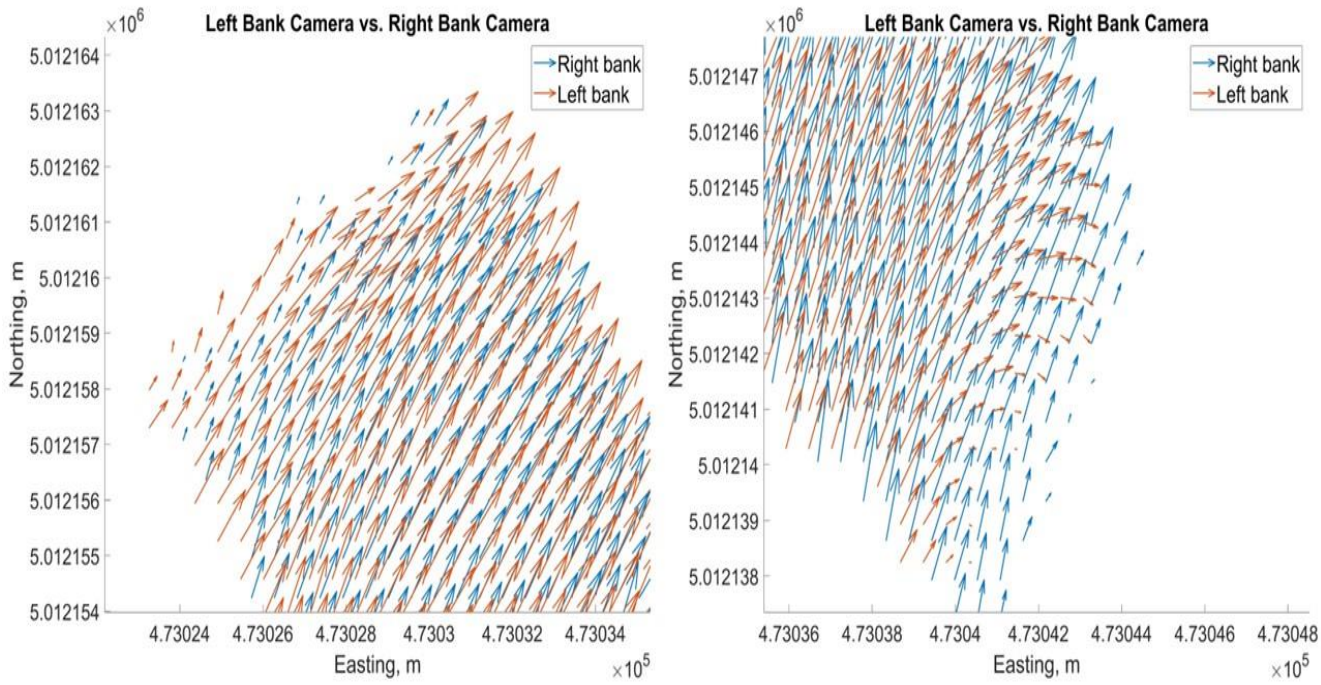

Figure 87: May 5th, 2023 left bank vs right bank camera vector plot. Left) Zoomed in on the left bank Right) Zoomed in on the right bank

Secondly, they show an inability in estimating the velocity direction on the far shores. This is due to a combination of both the distance from the camera but also the oblique angle of the cameras. Figure 88 shows a vector plot comparison between the left bank and gaugehouse camera near the right bank. The left bank camera is substantially worse at estimating the direction than the gaugehouse camera. This is likely because the gaugehouse camera is at a less oblique angle to the water surface than the bank cameras resulting in different GSDs than the left bank camera.

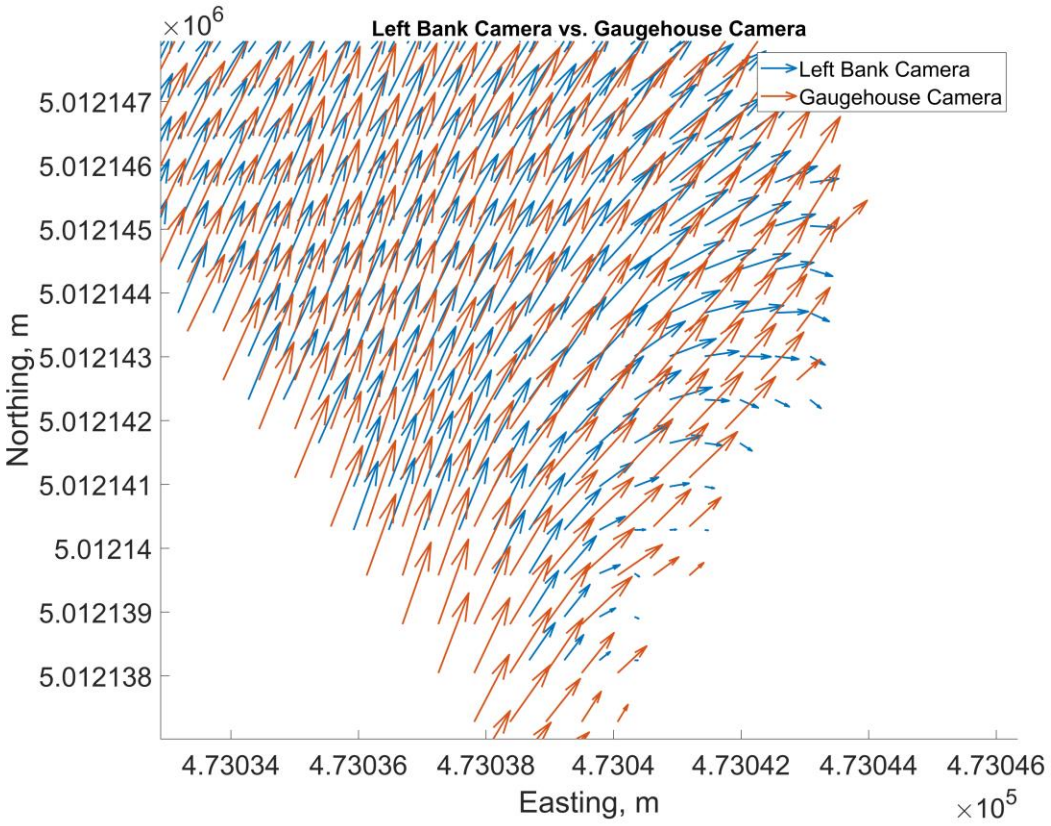

Figure 88: May 5th, 2023 left bank vs gaugehouse camera zoomed in on the right bank

Figure 89 shows even after distortion correction, some distortion is still present in the images. The red lines dictate roughly what the expected image would look like after distortion was removed, so it was evident that there is still some error present post distortion correction. The gaugehouse camera had distortion removed from the camera through the AXIS camera interface so the recorded videos were undistorted and did not need to be corrected in RIVeR. This could not have been done with the bridge cameras as it resulted in too much area in the ROI

being lost so it had to be done post-recording. A third potential reason is that the bending of the far shore vectors, could have been caused by environmental factors. It is possible that the sunglight caused glare, shadows or even resulted in the camera not being able to see tracer particles in that patch of the water surface. This could be why the gaugehouse camera better estimated the surface velocities as it was mounted at a higher elevation and therefore a less oblique angle. Lastly, the overlap of vectors appears to show that there may be a range limitation when considering the same region of interest between two cameras.

Figure 89: Distortion still affecting images post-distortion correction in the left bank camera

Another likely cause of the errors on the opposite banks could be attributed to orthorectification resulting ROIs with the same coordinates having different image coordinates. In RIVeR the images were interrogated post orthorectification to determine accuracy of GCP coordinates. It was noted that when interrogating GCP coordinates on the far shore of each camera the error was as great as 5m while the near shore showed differences of 0.5m or less typically. It is important to note that when working in the Cartesian coordinate system the decimals cannot be seen – most likely because RIVeR is only scripted to read a certain number of significant digits so some of the differences in coordinates could be attributed to this, however, it still demonstrates that there is increased error on the far shore that affected the accuracy of the image velocimetry results.

Drone Videos

During the May 15th, 2024 survey, a drone was flown overhead of the Castor River and six videos were recorded. The first video was taken from nadir and each subsequent video became a greater angle away from nadir than the previous. Based on previous research into the use of UAVs for LSPIV (Pearce et al., 2020; Perks, 2020) it was expected that more oblique views would have reduced accuracy in the discharge estimates, but as seen previously in Table 18 the nadir view did not produce the best results. This is further reinforced with the results in Table 24. The nadir video (DJI_054) had the second lowest discharge estimate while DJI_058 was the closest estimate to the ADCP data with a difference of -0.95%% suggesting that environmental conditions may be a more important factor to consider rather camera angles when employing LSPIV. Figure 90 shows a still frame from each drone video, and it is of the author's opinion that the major difference between videos is how the sunlight reflects or casts shadows on the water surface. The more accurate estimates appear to have a darker water surface in the area of the cross-section caused by the sunlight and shadows caused by the bridge while the less accurate estimates have a much brighter water surface potentially affecting the ability of PIVLab to track surface displacement.

Table 24: Estimated single camera LSPIV Discharge from May 15th, 2024 Drone Videos

Drone Filename	DJI_054	DJI_055	DJI_056	DJI_057	DJI_058	DJI_059
Discharge (m^3/s)	3.93	4.44	3.76	5.79	5.24	4.11
Error (m^3/s)	-1.36	-0.85	-1.53	0.50	-0.05	-1.18
% Difference	-25.71%	-16.07%	-28.92%	9.45%	-0.95%	-22.31%

Figure 90: Individual Camera Frames from May 15th, 2024 Survey. Top Left) DJI_054 Top Right) DJI_055 Middle Left) DJI_056 Middle Right) DJI_057 Bottom Left) DJI_058 Bottom Right) DJI_059

The May 5th, 2022 survey also examined the effects of distance of the camera from the water surface on the accuracy of surface velocity estimates. There were two videos taken at significantly different heights. One was taken just above the bridge while a second video was recorded from a significantly higher elevation (100m+). Power lines caused some interference in the processing in both cases and a discharge at the cross-section 2 could not be calculated but there was a large discrepancy between the velocities with the video recorded at the higher elevation having lower estimates compared to the other video which had more expected measurements based on the discharge from the rating curve (Figure 91). It is likely that the higher elevation resulted in lower estimates due to the GSD being higher caused by the difference in

elevation. Based on these observations, when using UAVs for LSPIV the drone should be flying at an elevation where the full width of the river can be seen but there it is unnecessary to record from any higher.

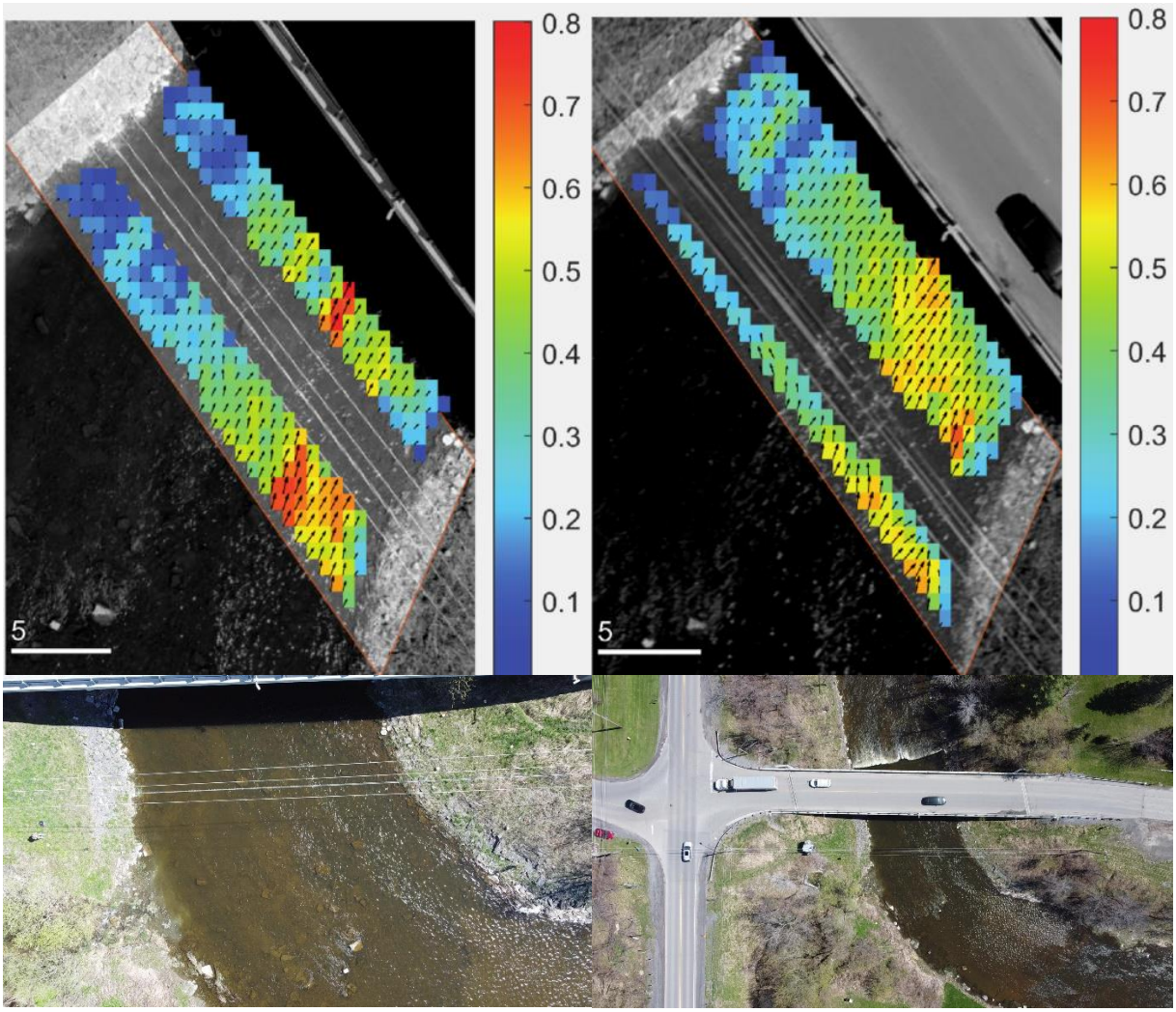

Figure 91: May 5th drone median velocity comparisons extracted from RIVeR where the top left is associated with the bottom left frame and the top right is associated with the bottom right frame. The velocity results near the power lines have been excluded.

Multi-Camera LSPIV

Combining the near half of two cameras resulted in a more accurate discharge estimate in all but one of the surveys compared to the best single camera estimates. Table 25 shows the discharge from the ADCP, best single camera estimate, combined camera estimates and the percent differences of the LSPIV estimates. Improvements in the four surveys ranged from 1.57% to 8.24% while the April 8th survey resulted in a decline of 8.24%. The decline in accuracy for the

April 8th survey was due to the MATLAB code yielding higher single camera estimates than RIVeR. This is explained further in RIVeR versus MATLAB Discharge. Additionally, the underestimates on May 15th, 2024 can likely be attributed to low flows generally being poorly resolved using image velocimetry.

Table 25: Comparison of best single camera discharge (m^3/s) and combined camera discharge (m^3/s) to the ADCP (m^3/s)

Survey Date	ADCP Discharge	Best single camera Discharge	Best single camera % difference	Combined Camera Discharge	Combined camera % difference
March 21st, 2022	55.57	52.03	-6.25%	58.10	4.68%
April 8th, 2022	53.80	55.42	3.01%	59.85	11.25%
May 5th, 2023	25.10	22.2	-11.55%	23.54	-6.22%
March 6th, 2024	23.30	20.17	-13.43%	22.09	-5.19%
May 15th, 2024	5.29	4.44	-16.07%	4.57	-13.61%

Table 26 was included to show that even the rating curve can still vary from ADCP discharge. The rating curve for the surveys performed at the Castor were as great as 16.81%, however, in some of these surveys the gauge station discharge was taken at the same as the start time of the video while the ADCP discharge was taken at another time in the day. The most extreme case of this was seen on March 6th, where the ADCP survey was performed two hours after the video was recorded.

Table 26: Difference between ADCP discharge and gauge station discharge

Survey Date	Average ADCP Discharge (m^3/s)	Gauge Station Discharge (m^3/s)	Percent Difference
March 21st, 2022	55.5	55.57	0.13%
April 8th, 2022	53.8	53.91	0.20%
May 5th, 2023	25.1	20.88	-16.81%
March 6th, 2024	23.3	22.03	-5.45%
May 15th, 2024	5.29	4.85	-8.32%

Table 27 compares the percent difference of both the combined camera discharge and rated discharge from the gauge station to the ADCP discharge as well as the combined camera percent difference to the rated discharge. March 6th and the May 15th surveys had two of the larger differences between the multi-camera LSPIV and the ADCP, however when compared to the rated discharge the differences were much smaller. As mentioned in the previous paragraph,

this is very likely caused by the video and the ADCP surveys being performed at different times. March 6th the ADCP survey was performed two hours prior to the video and the discharge dropped significantly over that time. A suspected reason for the larger differences on May 5th is because that survey was not performed by ECCC. When ECCC performs their surveys if the ADCP and gauge station differ significantly then a correction to the rating curve (or shift) may be applied. Since, this survey was done by the University of Ottawa no correction factor was applied which could attribute to the larger difference. This presents another potential use case where rather than requiring a field visit to validate a rating curve, LSPIV could be used and could be done with enough accuracy to shift the curve properly. Especially in cases where calibration measurements cannot be performed such as high flows that are typically extrapolated on a rating curve.

Table 27: Percent Difference Comparison of Multi-Camera LSPIV, Gauge station discharge, and ADCP discharge

Survey Date	Combined Camera % Difference from ADCP	Gauge Station % Difference from ADCP	Combined Camera % Difference from the Gauge Station
March 21st, 2022	4.68%	0.13%	4.55%
April 8th, 2022	11.25%	0.20%	11.02%
May 5th, 2023	-6.22%	-16.81%	12.74%
March 6th, 2024	-5.19%	-5.45%	0.27%
May 15th, 2024	-13.61%	-8.32%	-5.77%
Average Absolute Difference	8.19%	6.18%	6.87%

March 6th the multi-camera LSPIV compared extremely well suggesting that had the ADCP survey been performed closer to the time the video was recorded the multi-camera LSPIV would have been in good agreement. On average, the multi-camera LSPIV had a percent difference of 8.19% to the ADCP and when compared to the rated discharge had even closer agreement with an average of 6.87%. Table 28 shows some sort of relationship is present between the error for the individual camera of the 2 cameras combined so while there is still significant improvement the results of the combined LSPIV are highly dependent on both of the single cameras used in

that combination. On average, the combined camera method to the ADCP did just as well as the gauge station did.

Looking at the LSPIV results one more time in Table 28, it shows how the combination of cameras improved the estimates in two of the surveys and stayed consistent in the estimates for the other three. The improvement from the best single camera estimate was already discussed. Additionally, there is very large improvement over the 2nd best single cameras. The combined percent difference is an improvement of between 1.84% to 27.81% over the 2nd best single camera estimate (not including April 8th) demonstrating how beneficial a two-camera system can be.

Table 28: Discharge (m^3/s) from each LSPIV setup and absolute percent difference to the ADCP for each camera

Survey Date	ADCP Discharge	Gaugehouse Camera Discharge	Left Bank Camera Discharge	Right Bank Camera Discharge	Combined Camera Discharge	Gaugehouse Camera % Difference	Left Bank Camera % Difference	Right Bank Camera % Difference	Combined Camera % Difference
March 21st, 2022	55.5	52.03	51.83	41.62	58.10	-6.25%	-6.61%	-25.01%	4.68%
April 8th, 2022	53.8	59.89	51.77	55.42	59.85	11.32%	-3.77%	3.01%	11.25%
May 5th, 2023	25.1	22.2	18.53	19.45	23.54	-11.55%	-26.18%	-22.51%	-6.22%
March 6th, 2024	23.3	20.17	8.93	15.61	22.09	-13.43%	-61.67%	-33.00%	-5.19%
May 15th, 2024	5.29	4.44	3.5	4.01	4.57	-16.07%	-33.84%	-24.20%	-13.61%

Cross-Section Plots

This section examines the surface velocities across the section from both the cameras (computed using MATLAB code) and ADCP (Figure 92) where the start of the section (x = 0m) is considered GCP05 – the upper ground control point on the left bank. These plots were created using the code that was used to obtain the combined camera discharge, and therefore the combined camera series' overlap two other series in each plot because those were the velocities used in the combination. The general trend of the single camera surface velocities exhibited was like the surface velocity difference plots. Near the banks the opposite camera underestimated surface velocities. This resulted in sharp declines in velocities as the far-bank was approached when compared to the ADCP and the near-bank camera (i.e. on the right bank the right bank camera had a more gradual decline in comparison to the left bank or gaugehouse camera). This differs from a typical velocity profile where a gradual decline is expected. The combined camera method showed a more expected surface velocity profile and the velocities near the banks do not decline to the same degree of the single cameras which appeared to be the largest differences in the single camera comparisons. This resulted in a more consistent surface velocity profile across the cross-section and therefore improved discharge estimates. Based on the plots it was also gleaned that the far-bank camera may not be able to estimate velocities as far as the other camera can estimate the near-shore. For example, the April 8th survey showed that last data point available for both the left bank and gaugehouse camera was nearly 1.5m apart from the right bank camera. This meant that more interpolation was required for the single camera discharge estimates resulting in increased uncertainty. Lastly, the ADCP data was more difficult to compare due to the noise from the instrument but in general it compared well to the combined camera for both surveys shown in Figure 92 and Figure 93. April 8th in particular showed excellent comparison, this may have been influenced by the five-point moving average used to reduce the noise of the single-ping data while the March 21st and May 15th surveys had more fluctuation in the ADCP data but still compared excellently to the combined camera method.

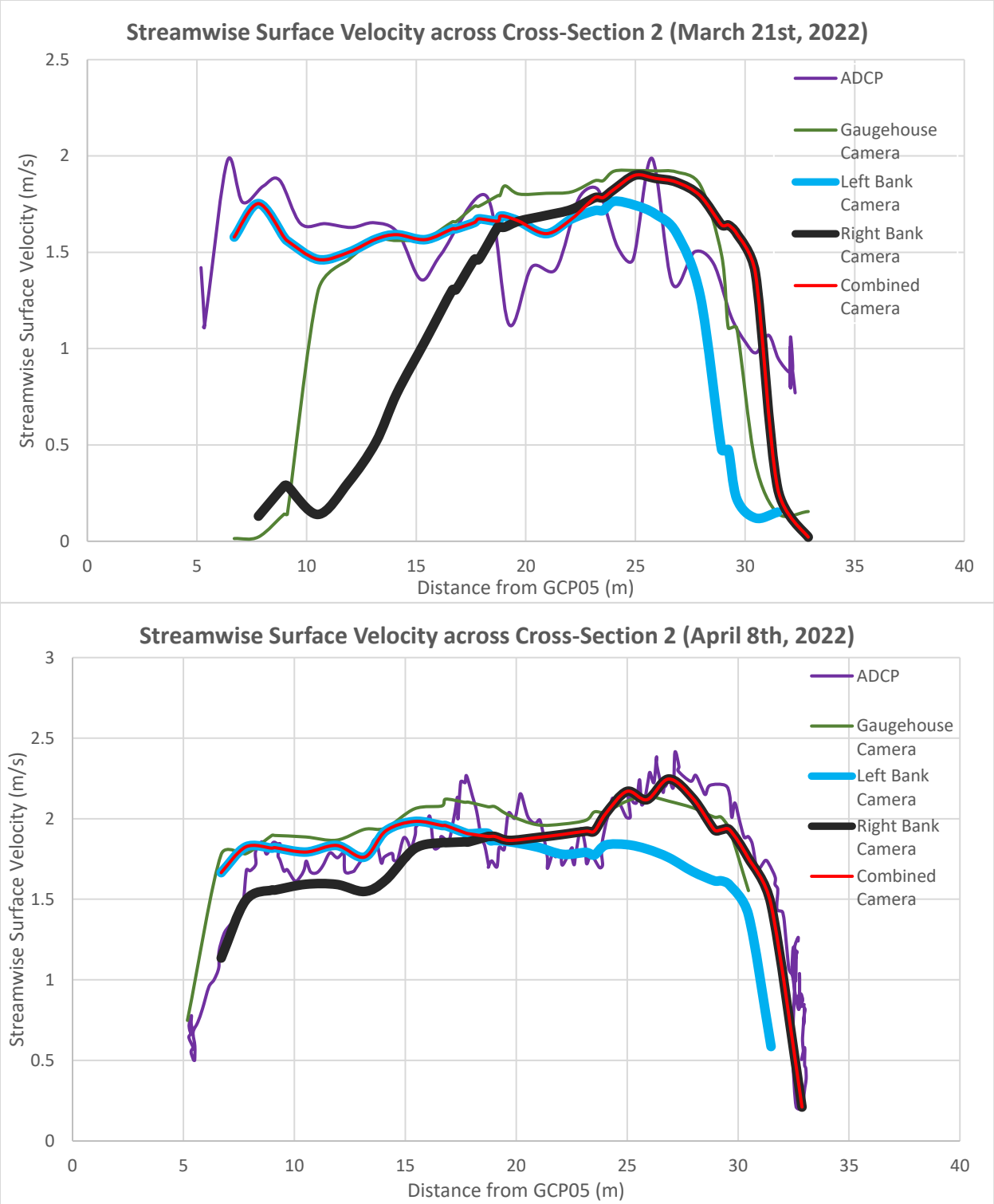

Figure 92: Streamwise surface velocity plots across cross-section 2 for March 21st and April 8th, 2022 surveys where x=0m is the location of the upper ground control point (GCP05) on the left bank of the channel. Note that the ADCP data from April 8th was plotted using a five-point moving average while the other surveys used a five-ping boxcar average to reduce noise.

Figure 93 shows the surface velocities across the section for the May 15th, 2024 survey. In addition to the trends discussed in the previous paragraph this survey showed a section of velocities in the middle of the channel that may had been affected by poor surface texture that was not previously observed in the videos or images. All three cameras appeared to underestimate the surface velocities in this section compared to the ADCP which had estimates of 0.3m/s higher than any of the cameras. Based on the plot it appears that this may be the reason the discharge was still underestimated. This is a potential drawback of the multi-camera method because if none of the cameras can make accurate estimates in sections due to environmental factors then the discharge estimate will not improve when combined.

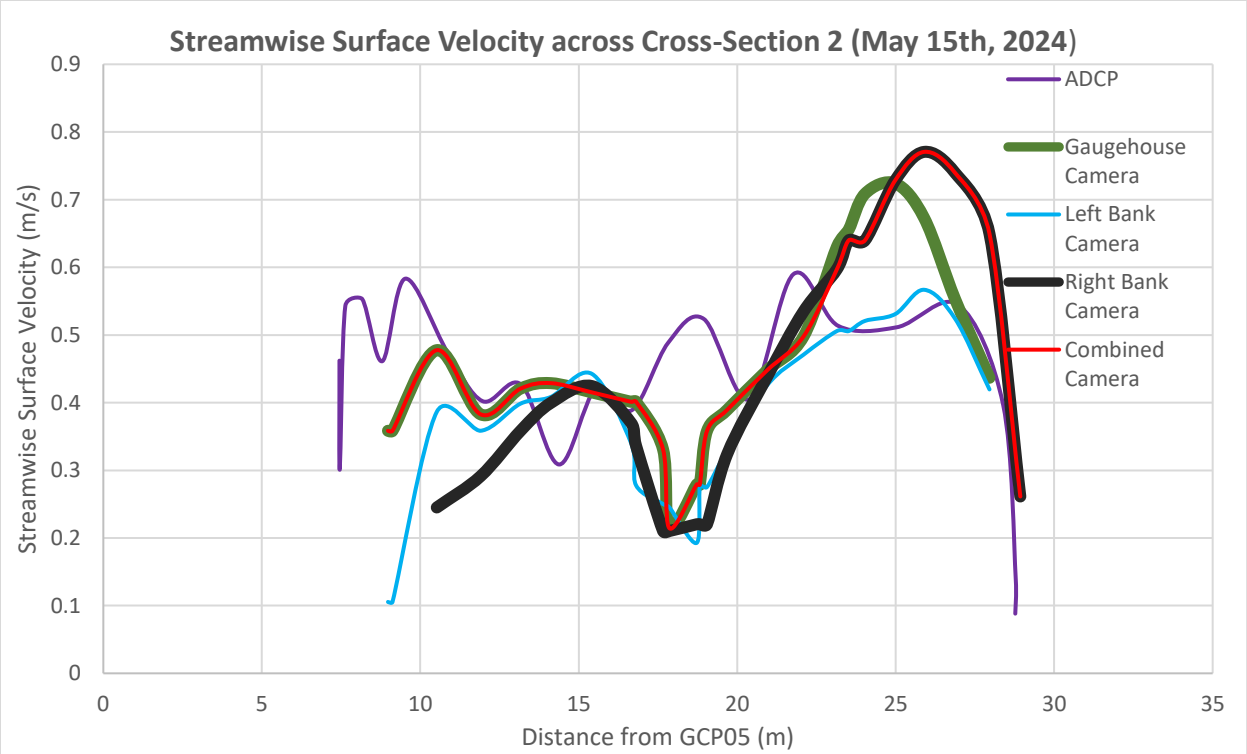

Figure 93: Streamwise surface velocity plots across cross-section 2 for May 15th, 2024 survey where x=0m is the location of the upper ground control point (GCP05) on the left bank of the channel. Note that the ADCP data from April 8th was plotted using a five-point moving average while the other surveys used a five-ping boxcar average to reduce noise.

RIVeR versus MATLAB Discharge

An observation made when computing the combined camera discharge was the results from the single camera computed in MATLAB differed from what RIVeR computed. A test was performed to examine the magnitude of these differences by computing all three single camera discharges for the May 5th, 2023 survey. Table 29 displays the computed discharges from both methods and the differences between them. Both the gaugehouse and left bank camera had slightly higher estimates using MATLAB while the right bank camera underestimated by over $3m^3/s$. Additionally, this was also the case for the April 8th, 2022 survey and the reason that the combined results were much higher than the ADCP. The single camera estimates in MATLAB were over $4m^3/s$ and $2m^3/s$ higher for the left and right bank camera respectively, compared to the estimates in RIVeR. The most plausible explanation for these differences is the way that velocity vectors were snapped to the cross-section line. RIVeR interpolated data along the cross-section based on the surface velocity field provided, likely using several points for each discharge panel to find the average velocities around the cross-section whereas the MATLAB method tookthe closest point available, sometimes even using the same vector twice.

Table 29: Comparison of methods in computation of single camera discharge (m^3/s) from May 5th 2023 survey

Method	Gaugehouse Camera	Left Bank Camera	Right Bank Camera
MATLAB	23.69	20.42	16.38
RIVeR	22.20	18.53	19.45
Difference	1.49	1.89	3.07

Environmental Conditions

Environmental conditions were partially discussed when talking about the drone videos, however it can be discussed further as more observations were made with the fixed cameras. The importance of surface texture cannot be overstated. As previously discussed in the literature, surface texture as well as environmental factors like sunlight play a key role in the success of LSPIV. While for the majority of this study, the environmental conditions were adequate, on two occasions poor surface texture affected the accuracy of the LSPIV and will be discussed here. The March 21st, 2022 survey and the March 6th, 2024 survey both had patches in the ROI where surface velocity was biased extremely low due to poor surface texture.

Figure 94 and Figure 95 displays the median vector plots comparing the poor LSPIV results to the ADCP and the right bank camera, respectively which are the results that would be expected with good surface texture. They also display the approximate area of the poor surface texture. In the March 21st, 2022 video a smooth surface texture with a lack of visible tracers can be seen on and off in the highlighted area whereas further away from the camera many tracer particles are visible moving downstream. In this instance, some tracers do move through the highlighted area during the video but not enough resulting in a patch of low bias vectors. A possible reason for the smooth patch is glare from the sun affecting the camera's FOV. Both other cameras are not affected by this smooth patch suggesting the angle of the camera and position of the sun in relation to one another caused the smooth patch.

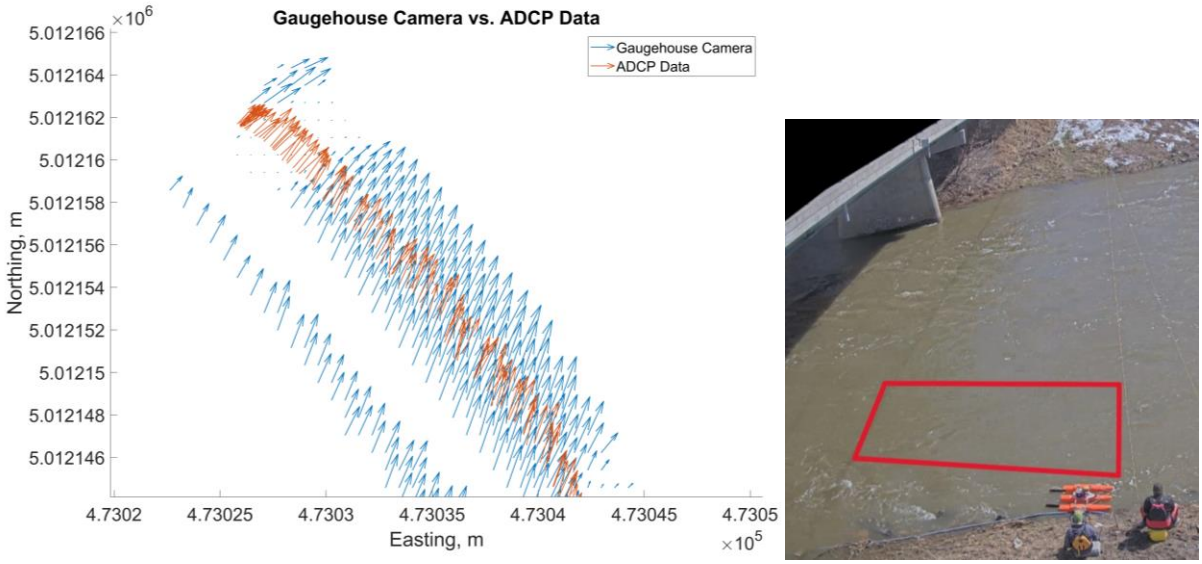

Figure 94: Results of poor surface texture from March 21st, 2022 survey. A) Vector plot comparing ADCP to the gaugehouse camera B) Field of view from camera with red box highlighting approximate area of poor surface texture

In the March 6th, 2024 survey the highlighted area is a larger area in the ROI. The vectors from the left bank camera are smaller in magnitude than the right bank camera which is already underestimating the actual velocity. The weather during this survey was much cloudier and possibly during a period of rain as there appear to be raindrops on the camera. Although the conditions are different it also seems to be some sort of glare caused by the sunlight or lack thereof.

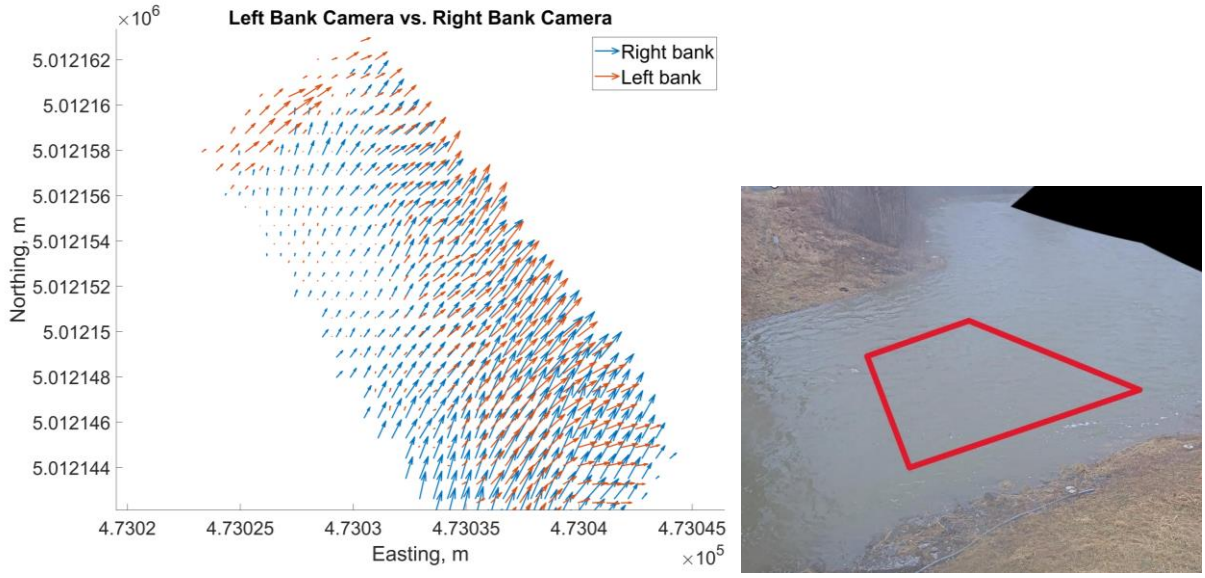

Figure 95: Result of poor surface texture from March 6th, 2024 survey. A) Vector plot zoomed in on the left bank comparing right bank camera to the left bank camera B) Field of view from camera with red box highlighting approximate area of poor surface texture

Both of these cases demonstrate the importance of proper environmental conditions for LSPIV analysis. Without adequate tracer particles, surface velocity estimates will always be underestimated. Unfortunately, it is not possible to always predict ideal conditions for image velocimetry, but this is something that could be looked at during site installations to determine how different camera angles and the patterns of sunlight may affect the camera's FOV. Additionally, it could help determine the best preset time in permanent installations to record videos. These environmental drawbacks also demonstrate how having multiple cameras installed can benefit. In both cases, when one camera was negatively impacted by the environment the other two cameras were still able to provide reasonable velocity estimates. In these cases when the problem is occurring on the near shore it would make it difficult to combine two cameras but if the problem is occurring for one of the cameras on the far-shore then this would also be another reason to have multiple cameras on site for LSPIV.

Distance Plots

Figure 96 shows the distance versus velocity difference plots for all of the surveys performed – minus the gaugehouse camera from the March 21st, 2022 survey and the left bank camera from the March 6th, 2024 survey due to the patches of missing surface texture. Both the left bank and right bank camera appear to follow a systematic trend where as distance from the camera increases the velocity difference between the surface velocity vector and ADCP increases. This was to be expected based on the change in GSD as the distance away from the camera increases. An explanation for why there are also high errors close to the camera could be explained because the ADCP is unable to measure as close to the banks as the cameras so in the code when searching for velocity vectors up to one meter away these ADCP vectors could be further towards the middle of the river. The gaugehouse camera does not show the same upwards trend with distance. It is not clear why the trend with distance is not evident with this camera, but it could have to do with the camera being at a higher elevation and therefore an angle closer to nadir; however, more analysis would be required to confirm this hypothesis. Lastly, when looking at the drone videos there is no trend between distance and error. This further reinforces the fact that environmental factors are more important for drone imagery than how close to a nadir angle the drone is recording from.

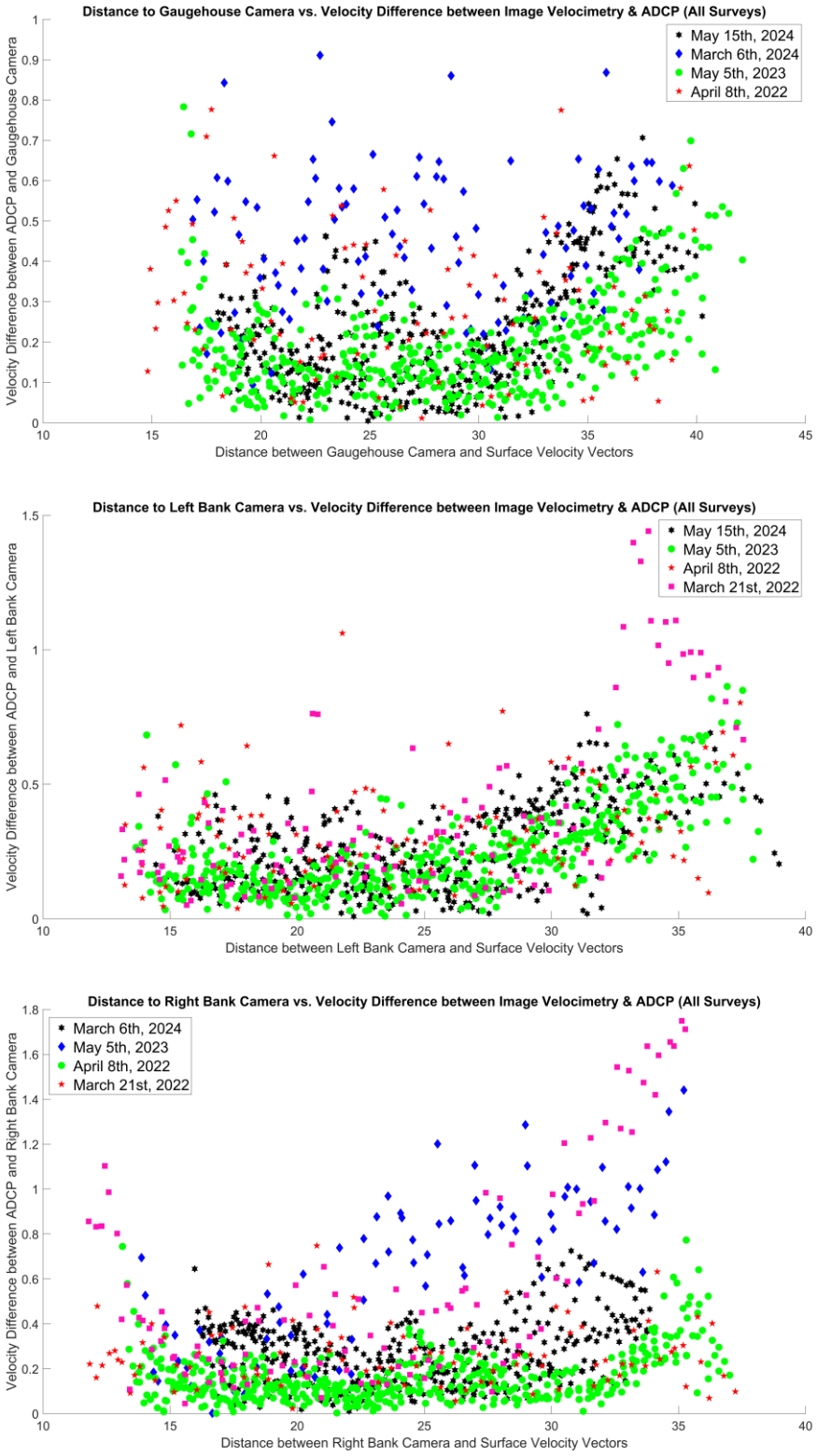

Figure 96: Distance to the camera versus velocity differences to the ADCP with all surveys combined Top) Gaugehouse camera Middle) Left bank camera Bottom) Right bank camera

Sources of Uncertainty

For one, as just mentioned, there is a discrepancy between the point velocity locations in the combined camera versus the single camera suggesting that RIVeR found the velocity positions in a different manner than what was used in the MATLAB code for searching for nearest velocity vectors.

There is some uncertainty that can be associated with the ADCP measurements and the various types of ADCPs used in the surveys. While the May 15th survey did confirm that ADCP measurements were similar to the near-surface measurements taken by the FlowTracker2, this was not done for all surveys and could have had higher differences particularly on the high flow days. Additionally, there were a few different ADCPs used and all of them have different blanking zones which also could have affected the difference between the top 2 ADCP bins and the surface in terms of velocity.

There is also some uncertainty when looking at velocity differences between the cameras and the ADCP near the banks because the ADCPs cannot measure near them. Since the code searched for a maximum of distance of 1.0m between the camera vectors and the ADCP vectors it is possible that the near-bank camera velocity vectors were compared to the ADCP vectors closer to the middle of the channel, thereby increasing the error in those locations.

Using single ping ADCP data in some surveys rather than boxcar averaged ADCP data also contributed to the uncertainty. Single ping data was used for several of the surveys done by ECCC. The standard error of the mean was found to be 0.095m/s so it was expected that the surveys done with single ping ADCP data would have a higher velocity difference of at least 0.095m/s when compared to the MAE of the surveys where a boxcar average was used.

Environmental conditions were also previously discussed but wind was not quantified during the study which would contribute to the uncertainty of the results. For example, it was noted that during the May 15th survey wind was travelling upstream. It is possible in these cases that wind travelling upstream caused lower surface velocity estimates.

Limitations

In theory, this method should be scalable for a diverse range of reaches. However, in general, it poses the same limitations as conventional image velocimetry systems. Not all sites have the capacity to mount cameras on both banks. Bridges are not always available, and even in some cases where they are available, they may not be at the necessary elevation to be able to see the full ROI. Channel width also affects the required elevation of a camera where increasing width of a channel will require the camera to be installed at higher elevation. As demonstrated in this study, the severity of the camera angle relative to the water surface has an effect on surface velocity estimates in addition to the distance from the camera with the higher elevated gaugehouse camera typically having the most accurate discharge estimates of the three cameras used.

Environmental conditions will always be a limitation with image-based methods as surface texture and appropriate sunlight are key to achieving accurate image velocimetry results. This is extremely challenging to predict regardless of research done prior to installing an image velocimetry system. If environmental conditions affect the near shore velocity estimates of a camera in multi-camera LSPIV then it negates the purpose of this method.

Lastly, the success of multi-camera LSPIV is based on the success of the single-camera velocity estimates. As discussed previously, the best multi-camera LSPIV surveys correlated with the best single-camera estimates. While the accuracy of the single camera declines with distance, there are still inaccuracies when compared to the ADCP in the near shore.

Integration into ECCC hydrometric network

Integration into the ECCC hydrometric network should be straightforward as long as the location is ideal for image velocimetry. ECCC already operates several image velocimetry sites with one camera. Existing procedures for installation already exist and modifying them would be easy. This method is intended to supplement conventional hydroacoustic measurements and not be used as a real-time replacement. As such, it would only require cell service in order for videos to be sent to an ECCC server. Even at remote locations, it could be possible to implement, although it would require technologists to collect the videos when conducting visits but would allow for verification of the real-time data over periods where site visits were not conducted. Additionally,

ECCC is currently in the process of approving STIV as an alternative method when hydroacoustic instruments cannot be conducted (Bomhof et al., 2024) so it is plausible that this could also become an approved method in the future.

5.2 Stereoscopic Image Velocimetry

Reconstruction of the surface was a key challenge in this study. Obtaining a detailed 3D point cloud proved impossible in Agisoft and other attempted methods. This seems to be caused by the software being unable to identify the water surface resulting in the banks of the canyon model being reconstructed but none of the water surface. In W. Li et al., 2019 the water surface had lots of surface texture and whitewater, which could explain why they were successful in their reconstruction (Figure 97). Clear water may not give enough detail for the software to be able to identify locations and match coordinates.

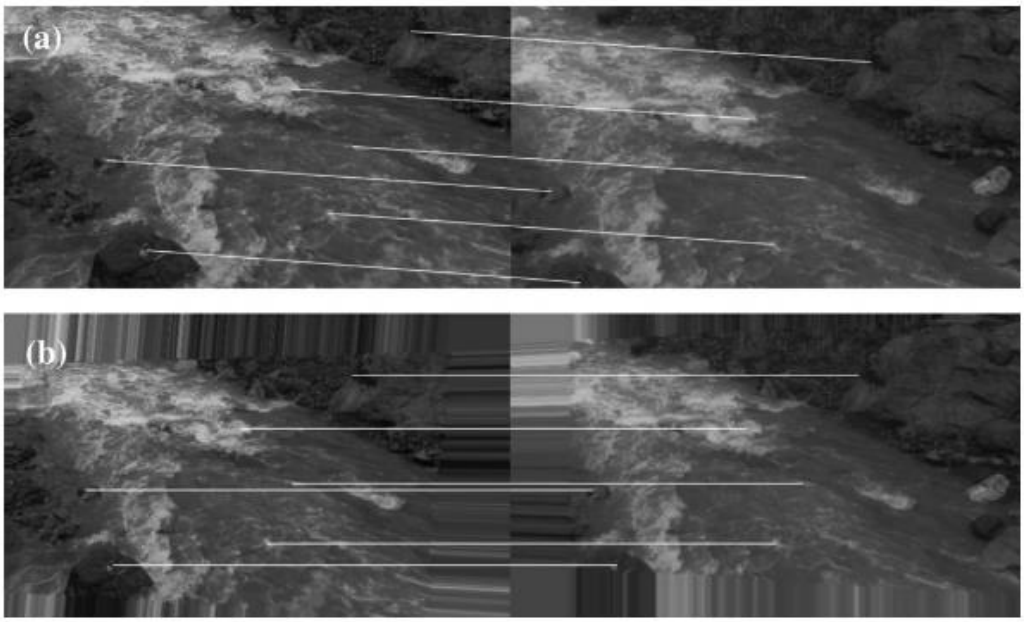

Figure 97: Image pairs of the original stereo image (Top) and the rectified pair (Bottom) from Li et al., 2019

Surface reconstruction was also attempted using Castor River footage using Agisoft Metashape and while there was some surface texture, the results were still disappointing. In this case, it could be because the cameras were located on opposite ends of the bridge approximately 40m apart from one another. In successful cases of stereoscopic reconstruction, the cameras are located next to each other. As the cameras spread further apart it is possible that the coordinate matching between images has reduced accuracy.

Surface reconstruction was successful with the Stereolabs camera in both the field and lab. However, in the lab, the tracer particles were stretched between the water surface and the bed as seen in Figure 98. Due to the clear water, the algorithm used for stitching images seemed to identify the water surface only when and where tracer particles were present. At the Castor, the surface reconstruction appeared to be very accurate as previously shown in Figure 80. This further reinforces that surface texture should be well distributed throughout the image to obtain an accurate point cloud.

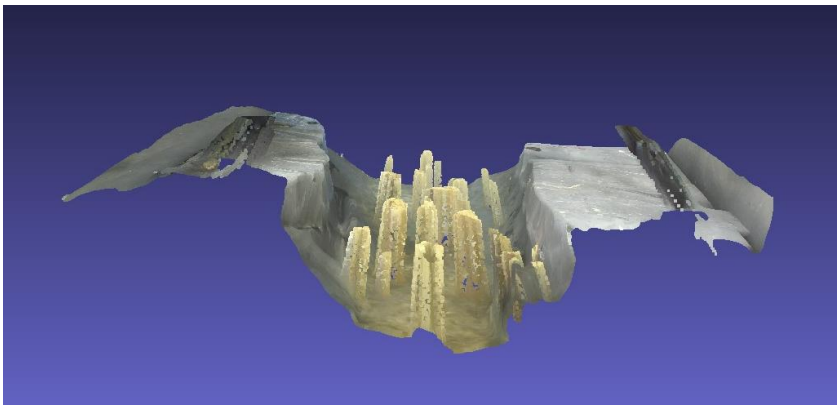

Figure 98: Reconstructed 3D Point Cloud of the Canyon Model created with the Stereolabs ZED2i Camera displaying how tracer particles are stretched from the water surface to the canyon bed

Even with the successful reconstruction of the water surface, the bigger challenge comes with obtaining velocities from these reconstructed point clouds. There does not appear to be any software capable of extracting velocities from a 3D point cloud without first projecting it onto a 2-dimensional surface as was done in Li et al., 2019. This incorporates the z-velocity into the x and y-vectors but does not allow for the determination of the z-velocity component which could be beneficial in canyons, hydraulic jumps or other scenarios where the water surface sees large changes in elevation. Hypothetically, a possible alternative to extracting all three velocities would be to project the reconstructed point cloud and extract the 2D velocity field, then do the same thing with a single camera and compare the differences between the velocity fields. Because the stereo camera setup requires two cameras in close proximity, the fundamental problem examined in this study with less accurate estimates on the far shores means a stereo setup on one bank may still have the same accuracy issues as a single camera. A camera such as the Stereolabs one used in this study is lightweight and could likely be mounted to a commercial drone with the right

setup. However, with the Stereolabs camera a cable connected to a laptop is required for recording. There may be other affordable lightweight systems available, however it is possible that further advancements are needed in this technology first.

5.4 Future Work & Recommendations

5.4.1 Recommendations for Multi-Camera Systems

For multi-camera LSPIV, there are several advancements that could be made for future work. Integrating this method of combining discharge into RIVeR could be very helpful in simplifying the workflow of using two cameras to obtain discharge. Having a user interface that allows the user to split the discharge allocation between cameras based on their observations would make it a very simple process.

Before implementing this method into software, more locations should be surveyed with different morphologies and flow characteristics than the Castor River (e.g., river width, bed morphology, flow rates, etc.). It would also be beneficial to study a river reach that is not located near a bend where a more uniform velocity profile would be expected in a straight section. It would also be beneficial to test various camera angles where possible. Lastly, establishing a cross-section with more uniform panels could also be helpful. There are also several recommendations based on this study for future research.

- Image rectification is an important step in image processing and results show that the far shore was not rectified as accurately. To reduce rectification errors, as many GCPs as possible should be surveyed.
- Surface texture and sunlight are major factors when selecting an image velocimetry site. It is important that the cameras can see adequate surface texture distributed along the water surface. When instrumenting a site, testing multiple camera locations could be beneficial to determine how to best see surface texture and how sunlight affects the camera.

5.4.2 Recommendations for Stereoscopic Image Velocimetry Systems

Future work with stereoscopic image velocimetry should consider that surface texture and colour are necessary for the surface reconstruction. Without them the matching algorithms are not able to match points between image pairs. Additionally, the cameras must be in in close

contact with one another (essentially next to each other) otherwise the same issue arises with point matching between image pairs. Lastly, at the moment it does not appear possible to extract the z-velocity vectors from a 3D point cloud, so for stereo LSPIV to work the point cloud would first have to be projected onto a 2D surface.

6.0 Conclusion

Hydrometric monitoring is vital in the Canadian landscape for flood monitoring, climate change modelling, maintaining the water balance and so much more. Discharge measurements are an essential part of hydrometric monitoring to ensure that established rating curves remain accurate over time. Conventional methods have been proving to work well but can sometimes be time consuming and the instruments used tend to be quite expensive. In high flow scenarios, these conventional methods pose safety risks to hydrometric technologists that operate them. Additionally, in flashy rivers such as concrete channels, or in remote locations (which is a common occurrence in Canada), the water level may rise and fall so quickly that hydrometric technologists are unable to get to the field site in time to measure the peak discharge. An alternative to conventional methods in these situations is image velocimetry.

This study looked at both multi-camera and stereoscopic LSPIV. The aim for the stereoscopic LSPIV was to obtain a working method that produced reasonable results. For the multi-camera LSPIV the goal was to identify where and why accuracy was diminished in the single camera setups and to combine discharge between two cameras to improve LSPIV estimates.

Stereoscopic LSPIV proved extremely difficult. Surface reconstruction with the two individual Acti cameras failed in the canyon model with Agisoft and the python code. Agisoft was able to recreate a point cloud however it was missing a very significant number of points and only reconstructed the canyon model walls accurately. The suspected reason for this was the clear water in the model so the algorithm used in Agisoft was not capable of distinguishing and matching points between the image pairs. With the ZED stereo camera the reconstruction in the model was better and did result in a fully developed 3D point cloud, however the tracers were stretched from the water surface down to the canyon bed as shown in Figure 83 suggesting that even the proprietary algorithm used here could not completely distinguish between the surface

and the bed due to the clear water. The AXIS cameras in the field failed to yield any point clouds, likely due to the large distance between each camera. The stereo camera successfully generated well-constructed points cloud like the one shown in Figure 80. Once the surface reconstruction was completed, several different methods of extracting the data were attempted. There is no software available to extract surface velocities from the point clouds, so they were changed to .png image files using a code that rotated them to a nadir view. These were processed in RIVeR with very poor results. Figure 82 showed the median surface velocity vectors for one of the videos and how the vector direction was extremely sporadic, and the vector magnitudes were in no agreement whatsoever with the ADCP data.

Seven different surveys were conducted at the Castor River encompassing a wide range of flow conditions at the site. Six of these surveys collected ADCP data, although March 18th, 2022 had an error in the data and was not used for comparison. May 5th, 2022 had no ADCP data taken however it was included as there was drone footage recorded. All of the videos taken – both fixed and drone – were processed in RIVeR and compared to the ADCP data. The velocity difference plots showed that the largest differences were typically near the far shore of the cameras while the center of the river had more similar velocity estimates. Additionally, when analyzing the vector plots, it was easy to see erroneous vectors near the far shore where typically the vector direction was skewed towards the bank rather than in the direction of flow and the vector magnitude was underestimated. There were also cases of poor surface texture in two cases – the March 6th, 2024 left bank camera and the March 21st, 2022 gaugehouse camera – resulting in velocity underestimates near 0m/s. Environmental conditions appeared to be the factor in both cases. Overall, the average difference between discharge estimates of the cameras and the ADCP for all 5 surveys with ADCP data were 11.73%, 26.41%, and 21.55% for the gaugehouse camera, left bank camera and right bank camera, respectively. It should be noted that removing the March 6th, 2024 left bank camera with the large missing patch of data reduced the average error for the left bank camera to 17.60%.

Drone videos were recorded March 18th, 2022, May 5th, 2022 and May 15th, 2024. March 18th and May 5th could only be compared to the fixed cameras as there was no validation data. Both of these surveys showed the largest differences to the fixed cameras was near the far shore

of each camera. On May 15th, 2024 several videos were recorded to determine optimal drone positioning. The results showed that it was not in fact the closest videos to nadir that produced the best results but instead an angle closer to 45 degrees to the river, which yielded a percent difference in discharge of -0.95%, suggesting that environmental conditions and how they affect the camera are a greater factor than having the camera at or close to a nadir view.

Lastly, for each survey a "centerline" was established to take the velocity vectors from approximately half of each camera and combine them in an attempt to improve the discharge estimates. It was found that this did in fact improve accuracy of the estimates with an average difference of 8.19% across all five surveys compared to the ADCP resulting in improvements in LSPIV estimates. The estimates were as close as 4.77% different to the ADCP while the furthest estimate was -13.61% but still showed improvement over the best single camera estimates. Overall, this method also compared extremely well to the rated discharge with an average difference of 6.87%.

There were several key findings from this study. For both LSPIV and the stereoscopic surface reconstruction surface texture is extremely important to get accurate results. Accuracy of surface velocity estimates typically show a diminishing trend the further from the camera the vectors are. Lastly, multi-camera LSPIV has demonstrated to be a promising solution in cases where cameras cannot be mounted directly in the middle of the river. Further work should be performed at alternative rivers to examine if this method is suitable for a wide range of morphologic conditions. Multi-camera LSPIV shows to be a valuable novel contribution to stream gauging. However, "LSPIV should not be construed as the magic instrument" (Muste et al. 2008), rather it should be used as an alternative in scenarios where conventional methods are challenged such as flash floods or remote rivers.

References

Aberle, J., Rennie, C., Admiraal, D., & Muste, M. (2017). *Experimental Hydraulics: Methods, Instrumentation, Data Processing and Management* (Vol. 2:).

ACTi Corporation. (n.d.). *A310*. Https://Www.Acti.Com/Product/A310?Tab=specifications.

Adrian, R. (1991). Particle-Imaging Techniques For Experimental Fluid-Mechanics. *Annual Review of Fluid Mechanics*, *23*(1), 261–304. https://doi.org/10.1146/annurev.fluid.23.1.261

Agisoft Metashape User Manual Professional Edition, Version 2.1. (2024).

Ansari, S., Rennie, C. D., Jamieson, E. C., Seidou, O., & Clark, S. P. (2023). RivQNet: Deep Learning Based River Discharge Estimation Using Close-Range Water Surface Imagery. *Water Resources Research*, *59*(2). https://doi.org/10.1029/2021WR031841

Ansari, S., Rennie, C. D., Venditti, J. G., Kwoll, E., & Fairweather, K. (2018). Shore-based monitoring of flow dynamics in a steep bedrock canyon river. *E3S Web of Conferences*, *40*. https://doi.org/10.1051/e3sconf/20184006025

Benetazzo, A. (2006). Measurements of short water waves using stereo matched image sequences. *Coastal Engineering*, *53*(12), 1013–1032. https://doi.org/10.1016/j.coastaleng.2006.06.012

Biggs, H., Doyle, M., McDonald, M., Smart, G., Holwerda, N., & Ede, M. (2021). *River discharge from surface velocity measurements A field guide for selecting alpha*.

Biggs, H., Smart, G., Doyle, M., Eickelberg, N., Aberle, J., Randall, M., & Detert, M. (2023). Surface Velocity to Depth-Averaged Velocity—A Review of Methods to Estimate Alpha and Remaining Challenges. In *Water (Switzerland)* (Vol. 15, Issue 21). Multidisciplinary Digital Publishing Institute (MDPI). https://doi.org/10.3390/w15213711

Boldt, J. A., & Oberg, K. A. (2015). Validation of Streamflow Measurements Made with M9 and RiverRay Acoustic Doppler Current Profilers. *Journal of Hydraulic Engineering*, *142*(2). https://doi.org/10.1061/(asce)hy.1943-7900.0001087

Bomhof, J., Aitken, M., Bedard, O., Bertrand, C., Bishop, Z., Carter, T., Elliot, D., Flemming, V., Garner, M., Goulet, A., Jamieson, E., Lipton, J., Mallany-Stanley, A., Maurier, M., Paul, C., Redmond, R., Schwarz, J., Sinclair, L., Wahl, B., & Willenburg, R. (2024). *Image Velocimetry Discharge measurement methods and its potential use in Water Survey of Canada operations Project Assessment Report*.

Dal Sasso, S. F., Pizarro, A., & Manfreda, S. (2020). Metrics for the quantification of seeding characteristics to enhance image velocimetry performance in rivers. *Remote Sensing*, *12*(11). https://doi.org/10.3390/rs12111789

Dal Sasso, S. F., Pizarro, A., Pearce, S., Maddock, I., & Manfreda, S. (2021). Increasing LSPIV performances by exploiting the seeding distribution index at different spatial scales. *Journal of Hydrology*, *598*. https://doi.org/10.1016/j.jhydrol.2021.126438

Despax, A., Favre, A. C., Belleville, A., Hauet, A., Le Coz, J., Dramais, G., & Blanquart, B. (2016). Field inter-laboratory experiments versus propagation methods for quantifying uncertainty in discharge measurements using the velocity-area method. *River Flow - Proceedings of the International*

Conference on Fluvial Hydraulics, RIVER FLOW 2016, 671–678. https://doi.org/10.1201/9781315644479-106

Despax, A., Le Coz, J., Hauet, A., Mueller, D. S., Engel, F. L., Blanquart, B., Renard, B., & Oberg, K. A. (2019). Decomposition of Uncertainty Sources in Acoustic Doppler Current Profiler Streamflow Measurements Using Repeated Measures Experiments. *Water Resources Research*, *55*(9), 7520–7540. https://doi.org/10.1029/2019WR025296

Detert, M. (2021). How to Avoid and Correct Biased Riverine Surface Image Velocimetry. In *Water Resources Research* (Vol. 57, Issue 2). Blackwell Publishing Ltd. https://doi.org/10.1029/2020WR027833

Eltner, A., Bertalan, L., Grundmann, J., Perks, M. T., & Lotsari, E. (2021). Hydro-morphological mapping of river reaches using videos captured with UAS. *Earth Surface Processes and Landforms*, *46*(14), 2773–2787. https://doi.org/10.1002/esp.5205

Eltner, A., Mader, D., Szopos, N., Nagy, B., Grundmann, J., & Bertalan, L. (2021). Using thermal and RGB UAV imagery to measure surface flow velocities of rivers. *International Archives of the Photogrammetry, Remote Sensing and Spatial Information Sciences - ISPRS Archives*, *43*(B2-2021), 717–722. https://doi.org/10.5194/isprs-archives-XLIII-B2-2021-717-2021

Eltner, A., Sardemann, H., & Grundmann, J. (2020). Technical Note: Flow velocity and discharge measurement in rivers using terrestrial and unmanned-aerial-vehicle imagery. *Hydrology and Earth System Sciences*, *24*(3), 1429–1445. https://doi.org/10.5194/hess-24-1429-2020

Environment and Climate Change Canada. (2021). *Measuring Discharge with Acoustic Doppler Current Profilers from a Moving Boat Version adapted for Water Survey of Canada Based on Techniques and Methods 3-A22, U.S. Geological Survey*. http://pubs.water.usgs.gov/tm3a22

Environment and Climate Change Canada. (2022a). *Canada Water Act Annual Report to Parliament 2021 to 2022*.

Environment and Climate Change Canada. (2022b). *Canada Water Act Annual Report to Parliament 2021 to 2022*.

Fujita, I., & Hino. (2003). Unseeded and Seeded PIV Measurements of River Flows Videotaped from a Helicopter. In *Journal of Visualization* (Vol. 6, Issue 3).

Fujita, I., & Kunita, Y. (2011). Application of aerial LSPIV to the 2002 flood of the Yodo River using a helicopter mounted high density video camera. *Journal of Hydro-Environment Research*, *5*(4), 323–331. https://doi.org/10.1016/j.jher.2011.05.003

Fujita, I., Muste, M., & Kruger, A. (1998). Large-scale particle image velocimetry for flow analysis in hydraulic engineering applications. *Hydraulic Research*.

Fujita, I., Watanabe, H., & Tsubaki, R. (2007). Development of a non-intrusive and efficient flow monitoring technique: The space-time image velocimetry (STIV). *International Journal of River Basin Management*, *5*(2), 105–114. https://doi.org/10.1080/15715124.2007.9635310

Gordon, R. L. (1989). Acoustic Measurement of River Discharge. *Journal of Hydraulic Engineering*, *115*(7).

Hauet, A., Creutin, J. D., & Belleudy, P. (2008). Sensitivity study of large-scale particle image velocimetry measurement of river discharge using numerical simulation. *Journal of Hydrology*, *349*(1–2), 178–190. https://doi.org/10.1016/j.jhydrol.2007.10.062

Hauet, A., Kruger, A., Krajewski, W. F., Bradley, A., Asce, A. M., Muste, M., Creutin, J.-D., & Wilson, M. (2008). Experimental System for Real-Time Discharge Estimation Using an Image-Based Method. *Hydrologic Engineering*, *13*(2), 105–110. https://doi.org/10.1061/ASCE1084-0699200813:2105

Hauet, A., Morlot, T., & Daubagnan, L. (2018). Velocity profile and depth-averaged to surface velocity in natural streams: A review over alarge sample of rivers. *E3S Web of Conferences*, *40*. https://doi.org/10.1051/e3sconf/20184006015

Huang, W. C., Young, C. C., & Liu, W. C. (2018). Application of an automated discharge imaging system and LSPIV during typhoon events in Taiwan. *Water (Switzerland)*, *10*(3). https://doi.org/10.3390/w10030280

Hutley, N. R., Beecroft, R., Wagenaar, D., Soutar, J., Edwards, B., Deering, N., Grinham, A., & Albert, S. (2023). Adaptively monitoring streamflow using a stereo computer vision system. *Hydrology and Earth System Sciences*, *27*(10), 2051–2073. https://doi.org/10.5194/hess-27-2051-2023

Hydro Technology Institute Co., Ltd. (2024). *Hydro-STIV Operation Manual*.

Jodeau, M., Hauet, A., Paquier, A., Le Coz, J., & Dramais, G. (2008). Application and evaluation of LS-PIV technique for the monitoring of river surface velocities in high flow conditions. *Flow Measurement and Instrumentation*, *19*(2), 117–127. https://doi.org/10.1016/j.flowmeasinst.2007.11.004

Johnson, E. D., & Cowen, E. A. (2016). Remote monitoring of volumetric discharge employing bathymetry determined from surface turbulence metrics. *Water Resources Research*, *52*(3), 2178–2193. https://doi.org/10.1002/2015WR017736

Jolley, M. J., Russell, A. J., Quinn, P. F., & Perks, M. T. (2021). Considerations When Applying Large-Scale PIV and PTV for Determining River Flow Velocity. *Frontiers in Water*, *3*. https://doi.org/10.3389/frwa.2021.709269

Kantoush, S. A., Schleiss, A. J., Sumi, T., & Murasaki, M. (2011). LSPIV implementation for environmental flow in various laboratory and field cases. *Journal of Hydro-Environment Research*, *5*(4), 263–276. https://doi.org/10.1016/j.jher.2011.07.002

Khodarahmi, I., Shakeri, M., Sharp, K., & Amini, A. (2010). Using PIV to determine relative pressures in a stenotic phantom under steady flow based on the pressure-poisson equation. *32nd Annual International Conference of the IEEE EMBS*.

Kim, Y., Muste, M., Hauet, A., Krajewski, W. F., Kruger, A., & Bradley, A. (2008). Stream discharge using mobile large-scale particle image velocimetry: A proof of concept. *Water Resources Research*, *44*(9). https://doi.org/10.1029/2006WR005441

Kinzel, P. J., & Legleiter, C. J. (2019). sUAS-based remote sensing of river discharge using thermal particle image velocimetry and bathymetric lidar. *Remote Sensing*, *11*(19). https://doi.org/10.3390/rs11192317

Kumar, T., Bhushan, S., & Jangra, S. (2019). A brief review of image quality enhancement techniques based multi-modal biometric fusion systems. *Communications in Computer and Information Science*, *955*, 407–423. https://doi.org/10.1007/978-981-13-3140-4_37

Lant, J., & Mueller, D. (2012). *Stage Area Rating Application-AreaComp2*.

Le Boursicaud, R., Pénard, L., Hauet, A., Thollet, F., & Le Coz, J. (2016). Gauging extreme floods on YouTube: Application of LSPIV to home movies for the post-event determination of stream discharges. *Hydrological Processes*, *30*(1), 90–105. https://doi.org/10.1002/hyp.10532

Le Coz, J. (2017). *Quantifying discharges and fluxes of matters in rivers*.

Le Coz, J., Hauet, A., Pierrefeu, G., Dramais, G., & Camenen, B. (2010). Performance of image-based velocimetry (LSPIV) applied to flash-flood discharge measurements in Mediterranean rivers. *Journal of Hydrology*, *394*(1–2), 42–52. https://doi.org/10.1016/j.jhydrol.2010.05.049

Legleiter, C. J., & Kinzel, P. J. (2023). The Toolbox for River Velocimetry using Images from Aircraft (TRiVIA). *River Research and Applications*, *39*(8), 1457–1468. https://doi.org/10.1002/rra.4147

Li, B., Hou, J., Li, D., Yang, D., Han, H., Bi, X., Wang, X., Hinkelmann, R., & Xia, J. (2021). Application of LiDAR UAV for High-Resolution Flood Modelling. *Water Resources Management*, *35*(5), 1433–1447. https://doi.org/10.1007/s11269-021-02783-w

Li, W., Liao, Q., & Ran, Q. (2019). Stereo-imaging LSPIV (SI-LSPIV) for 3D water surface reconstruction and discharge measurement in mountain river flows. *Journal of Hydrology*, *578*. https://doi.org/10.1016/j.jhydrol.2019.124099

Meselhe, E. A., Peeva, ; T, & Muste, M. (2004). Large Scale Particle Image Velocimetry for Low Velocity and Shallow Water Flows. *Hydraulic Engineering*, *130*(9), 937–940. https://doi.org/10.1061/ASCE0733-94292004130:9937

Mueller, D. S., Abad, J. D., Carlos, ;, García, M., Gartner, J. W., García, M. H., & Oberg, K. A. (2007). Errors in Acoustic Doppler Profiler Velocity Measurements Caused by Flow Disturbance. *Journal of Hydraulic Engineering*, *133*(12). https://doi.org/10.1061/ASCE0733-94292007133:121411

Mueller, D., Wagner, C., Rehmel, M., Oberg, K., & Rainville, F. (2013). Measuring discharge with acoustic Doppler current profilers from a moving boat. In *Applications of Hydraulics*. https://www.researchgate.net/publication/284587353

Muste, M., Fujita, I., & Hauet, A. (2008). Large-scale particle image velocimetry for measurements in riverine environments. *Water Resources Research*, *46*(4). https://doi.org/10.1029/2008WR006950

Muste, M., Kim, D., & González-Castro, J. A. (2010). Near-Transducer Errors in ADCP Measurements: Experimental Findings. *Journal of Hydraulic Engineering*, *136*(5). https://doi.org/10.1061/ASCEHY.1943-7900.0000173

Patalano, A. (2021). *Evaluation Report*.

Patalano, A., García, C. M., & Rodríguez, A. (2017). Rectification of Image Velocity Results (RIVeR): A simple and user-friendly toolbox for large scale water surface Particle Image Velocimetry (PIV) and

Particle Tracking Velocimetry (PTV). *Computers and Geosciences*, *109*, 323–330. https://doi.org/10.1016/j.cageo.2017.07.009

Pearce, S., Ljubicic, R., Peña-Haro, S., Perks, M., Tauro, F., Pizarro, A., Dal Sasso, S. F., Strelnikova, D., Grimaldi, S., Maddock, I., Paulus, G., Plavšic, J., Prodanovic, D., & Manfreda, S. (2020). An evaluation of image velocimetry techniques under low flow conditions and high seeding densities using unmanned aerial systems. *Remote Sensing*, *12*(2). https://doi.org/10.3390/rs12020232

Peña-Haro, S., Lüthi, B., Lukes, R., & Carrel, M. (2020). Wind Effect on image-based river surface velocity measurements. *EGU General Assembly 2020*.

Perks, M. T. (2020). KLT-IV v1.0: Image velocimetry software for use with fixed and mobile platforms. *Geoscientific Model Development*, *13*(12), 6111–6130. https://doi.org/10.5194/gmd-13-6111-2020

Perks, M. T., Fortunato Dal Sasso, S., Hauet, A., Jamieson, E., Le Coz, J., Pearce, S., Peña-Haro, S., Pizarro, A., Strelnikova, D., Tauro, F., Bomhof, J., Grimaldi, S., Goulet, A., Hortobágyi, B., Jodeau, M., Käfer, S., Ljubičić, R., Maddock, I., Mayr, P., … Manfreda, S. (2020). Towards harmonisation of image velocimetry techniques for river surface velocity observations. *Earth System Science Data*, *12*(3), 1545–1559. https://doi.org/10.5194/essd-12-1545-2020

Pizarro, A., Dal Sasso, S. F., & Manfreda, S. (2020). Refining image-velocimetry performances for streamflow monitoring: Seeding metrics to errors minimization. *Hydrological Processes*, *34*(25), 5167–5175. https://doi.org/10.1002/hyp.13919

Pizarro, A., Dal Sasso, S. F., Perks, M. T., & Manfreda, S. (2020). Identifying the optimal spatial distribution of tracers for optical sensing of stream surface flow. *Hydrology and Earth System Sciences*, *24*(11), 5173–5185. https://doi.org/10.5194/hess-24-5173-2020

Prasad, A. K., Adrian, R. J., Landreth, C. C., & Offutt, P. W. (1992). Experiments in Fluids Effect of resolution on the speed and accuracy of particle image velocimetry interrogation *. In *Experiments in Fluids* (Vol. 13).

Ran, Q. H., Li, W., Liao, Q., Tang, H. L., & Wang, M. Y. (2016). Application of an automated LSPIV system in a mountainous stream for continuous flood flow measurements. *Hydrological Processes*, *30*(17), 3014–3029. https://doi.org/10.1002/hyp.10836

Rennie, C. D., Church, M., & Venditti, J. G. (2018). Rock Control of River Geometry: The Fraser Canyons. *Journal of Geophysical Research: Earth Surface*, *123*(8), 1860–1878. https://doi.org/10.1029/2017JF004458

Rodriguez-Padilla, I., Castelle, B., Marieu, V., & Morichon, D. (2020). A simple and efficient image stabilization method for coastal monitoring video systems. *Remote Sensing*, *12*(1). https://doi.org/10.3390/RS12010070

Schweitzer, S. A., & Cowen, E. A. (2021). Instantaneous River-Wide Water Surface Velocity Field Measurements at Centimeter Scales Using Infrared Quantitative Image Velocimetry. *Water Resources Research*, *57*(8). https://doi.org/10.1029/2020WR029279

Shavit, U., Lowe, R. J., & Steinbuck, J. V. (2007). Intensity Capping: A simple method to improve cross-correlation PIV results. *Experiments in Fluids*, *42*(2), 225–240. https://doi.org/10.1007/s00348-006-0233-7

Sontek. (n.d.). *Sontek M9 Specifications https://www.ysi.com/sontek-m9*.

Tauro, F., Porfiri, M., & Grimaldi, S. (2014). Orienting the camera and firing lasers to enhance large scale particle image velocimetry for streamflow monitoring. *Water Resources Research*, *50*(9), 7470–7483. https://doi.org/10.1002/2014WR015952

Tauro, F., Tosi, F., Mattoccia, S., Toth, E., Piscopia, R., & Grimaldi, S. (2018). Optical tracking velocimetry (OTV): Leveraging optical flow and trajectory-based filtering for surface streamflow observations. *Remote Sensing*, *10*(12). https://doi.org/10.3390/rs10122010

Teledyne Marine. (2006). *StreamPro ADCP Shallow Streamflow Measurement System*. www.teledynemarine.com

Teledyne Marine. (2023). *RiverPro 600 ADCP River Discharge Measurement System for Advanced Applications*. www.teledynemarine.com

Teledyne RD Instruments. (2021). *WinRiver II Software User's Guide*.

Thielicke, W. (2014). *The Flapping Flight of Birds - Analysis and Application* [University of Groningen]. http://PIVlab.blogspot.com

Thielicke, W., & Sonntag, R. (2021). Particle Image Velocimetry for MATLAB: Accuracy and enhanced algorithms in PIVlab. *Journal of Open Research Software*, *9*, 1–14. https://doi.org/10.5334/JORS.334

USGS. (n.d.). *Known Issues*. USGS.

WaMSTeC. (2021). *National Industry Guidelines for hydrometric monitoring PART 11: APPLICATION OF SURFACE VELOCITY METHODS FOR VELOCITY AND OPEN CHANNEL DISCHARGE MEASUREMENTS*.

Westoby, M. J., Brasington, J., Glasser, N. F., Hambrey, M. J., & Reynolds, J. M. (2012). "Structure-from-Motion" photogrammetry: A low-cost, effective tool for geoscience applications. *Geomorphology*, *179*, 300–314. https://doi.org/10.1016/j.geomorph.2012.08.021

Zhang, C., Sun, A., Hassan, M. A., & Qin, C. (2022). Assessing Through-Water Structure-from-Motion Photogrammetry in Gravel-Bed Rivers under Controlled Conditions. *Remote Sensing*, *14*(21). https://doi.org/10.3390/rs14215351

Appendices

Appendix A – Combined Camera Calculations

March 21st, 2022

x	Midsection	z	vvel			Area	Discharge
4.616627	4.897547	4.352	LB			0.572785	0.319692
5.178467	5.939457	3.872					
6.700446	7.251989	3.439	1.578888	LB		1.198342	1.892047
7.803531	8.392183	3.239	1.752636			1.269036	2.224158
8.980834	9.052395	3.097	1.57674			0.828567	1.306435
9.123956	9.821989	2.723	1.559398			1.253669	1.954968
10.52002	11.21251	2.761	1.462756			2.212321	3.236085
11.905	12.53203	2.6	1.499097			2.311797	3.465608
13.15906	13.63889	2.625	1.568081			1.911554	2.997472
14.11873	14.76764	2.541	1.591307			2.044155	3.252878
15.41655	16.03461	2.513	1.565748			2.329954	3.64812
16.65266	16.73136	2.739	1.621924			1.123865	1.822823
16.81006	17.23427	3.082	1.621924			0.638695	1.035915
17.65848	17.75892	3.049	1.654636			0.683625	1.13115
17.85937	18.2897	2.652	1.67353			0.902319	1.510057
18.72003	18.76987	2.616	1.661412			0.833573	1.384908
18.8197	18.93313	2.812	1.686514			0.251424	0.424031
19.04656	19.36394	2.547	1.686514			0.777608	1.311446
19.68132	20.3097	2.583	1.661853	RB		1.673053	2.780368
20.93808	21.5153	2.615	1.596547			2.094127	3.343373
22.09252	22.61921	2.599	1.673411			1.935147	3.238296
23.1459	23.33318	2.626	1.783372			1.232311	2.197669
23.52046	23.77594	2.767	1.783372			0.701781	1.251537
24.03142	24.50851	2.597	1.827217			1.285667	2.349191
24.9856	25.4408	2.614	1.89996			1.620318	3.078539
25.896	26.38628	2.597	1.883843			1.659318	3.125894
26.87656	27.41762	2.843	1.863639			1.556291	2.900364
27.95868	28.44494	2.925	1.793064			1.465985	2.628605
28.9312	29.08366	2.997	1.64181			0.865464	1.420927
29.23612	29.42897	3.157	1.64181			0.412649	0.677492
29.62183	30.04546	2.977	1.596908			0.847673	1.353655
30.4691	30.97807	3.085	1.393916			1.181612	1.647068
31.48704	32.1849	3.323	0.275061			1.241832	0.341579
32.88276	33.57301	3.651	0.021432			0.97306	0.020854
34.26325	34.2652	3.982	0.00975			0.25611	0.002497
34.26714	34.86604	4.052					
35.46493	36.02287	4.187					
36.5808		4.352	RB			0.856774	0.006491
							65.28219
						Alpha	0.895
						LSPIV Q	58.42756
						ADCP Q	55.5
						% diff	4.77%

April 8th, 2022

x	Midsection	z	v-vel		Area	Discharge
4.836681	5.007574	4.164	LB		0.799512	0.47029
5.178467	5.939457	3.872				
6.700446	7.251989	3.439	1.66399		0.951586	1.583429
7.803531	8.392183	3.239	1.818159		1.05468	1.917575
8.980834	9.052395	3.097	1.806631		0.704447	1.272675
9.123956	9.821989	2.723	1.80921		1.108985	2.006387
10.52002	11.21251	2.761	1.777337		1.950903	3.467411
11.905	12.53203	2.6	1.814861		2.063728	3.745379
13.15906	13.63889	2.625	1.74674		1.703464	2.975508
14.11873	14.76764	2.541	1.905586		1.831951	3.490941
15.41655	16.03461	2.513	1.960146		2.091764	4.100162
16.65266	16.73136	2.739	1.935594		0.992875	1.921803
16.81006	17.23427	3.082	1.935594		0.544148	1.05325
17.65848	17.75892	3.049	1.893807		0.58499	1.107857
17.85937	18.2897	2.652	1.886261		0.802533	1.513786
18.72003	18.76987	2.616	1.887534		0.743301	1.403006
18.8197	18.93313	2.812	1.844408		0.220731	0.407118
19.04656	19.36394	2.547	1.844408		0.696616	1.284844
19.68132	20.3097	2.583	1.836439		1.49525	2.745935
20.93808	21.5153	2.615	1.800175		1.867474	3.36178
22.09252	22.61921	2.599	1.75526		1.727613	3.03241
23.1459	23.33318	2.626	1.900653		1.098085	2.087079
23.52046	23.77594	2.767	1.900653		0.618542	1.175633
24.03142	24.50851	2.597	2.005564		1.147943	2.302272
24.9856	25.4408	2.614	2.144523		1.445047	3.098937
25.896	26.38628	2.597	2.088008		1.481568	3.093525
26.87656	27.41762	2.843	2.219207		1.362399	3.023447
27.95868	28.44494	2.925	2.103813		1.272849	2.677837
28.9312	29.08366	2.997	1.913491		0.745385	1.426288
29.23612	29.42897	3.157	1.913491		0.347731	0.665379
29.62183	30.04546	2.977	1.913491		0.731773	1.400241
30.4691	30.97807	3.085	1.741336		1.006282	1.752274
31.48704	32.1849	3.323	1.453974		1.014947	1.475707
32.88276	33.57301	3.651	0.208159		0.712097	0.14823
34.26325	34.2652	3.982			0.865871	0.063714
34.26714	34.764	4.052				
35.26086		4.164	RB			
						67.25211
					Alpha	0.892
					ADCP Q	53.8
					LSPIV Q	59.98888
					% diff	11.49%

May 5th, 2023

Combined Camera						
x	Midpoint	z	velmag		Area	Discharge
6.032603	6.366525	3.629	LB		0.063445	0.029563
6.700446	7.251989	3.439	1.318139		0.168238	0.221761
7.803531	8.392183	3.239	1.607774		0.444676	0.714938
8.980834	9.052395	3.097	1.520358		0.351233	0.534
9.123956	9.821989	2.723	1.439771		0.697252	1.003883
10.52002	11.21251	2.761	1.393594		1.206973	1.682031
11.905	12.53203	2.6	1.442464		1.357785	1.958556
13.15906	13.63889	2.625	1.396919		1.111291	1.552384
14.11873	14.76764	2.541	1.32346		1.228073	1.625305
15.41655	16.03461	2.513	1.30725		1.413936	1.848368
16.65266	16.73136	2.739	1.305728		0.620111	0.809697
16.81006	17.23427	3.082	1.305728		0.275092	0.359195
17.65848	17.75892	3.049	1.300666		0.3043	0.395792
17.85937	18.2897	2.652	1.371162		0.518568	0.71104
18.72003	18.76987	2.616	1.349653		0.486411	0.656486
18.8197	18.93313	2.812	1.349653		0.133386	0.180024
19.04656	19.36394	2.547	1.349653		0.466134	0.629119
19.68132	20.3097	2.583	1.32368		0.989267	1.309473
20.93808	21.5153	2.615	1.288282		1.222478	1.574896
22.09252	22.61921	2.599	1.356251		1.137023	1.542089
23.1459	23.33318	2.626	1.411177		0.716111	1.01056
23.52046	23.77594	2.767	1.411177		0.381663	0.538594
24.03142	24.50851	2.597	1.493606		0.756016	1.12919
24.9856	25.4408	2.614	1.562161		0.946273	1.47823
25.896	26.38628	2.597	1.57245		0.975736	1.534295
26.87656	27.41762	2.843	1.52056		0.810633	1.232616
27.95868	28.44494	2.925	1.454919		0.723233	1.052246
28.9312	29.08366	2.997	1.368256		0.40367	0.552324
29.23612	29.42897	3.157	1.185408		0.162988	0.193207
29.62183	30.04546	2.977	1.185408		0.401951	0.476476
30.4691	30.97807	3.085	0.903159		0.507338	0.458206
31.48704	32.1381	3.323	0.499801		0.354968	0.177413
32.78915		3.629	RB		0.199222	0.035199
						29.20716
					Alpha	0.806
					LSPIV Q	23.54097
					ADCP Q	25.1
					% diff	-6.22%

March 6th, 2024

x	Midsection Point	z	v-vel		Area	Discharge
5.863885	6.282165485	3.677	LB		0.099551	0.036343
6.700446	7.251988508	3.439	1.032729	Cam1	0.230818	0.238372
7.803531	8.392182577	3.239	1.408105		0.499405	0.703215
8.980834	9.052395181	3.097	1.378315		0.382923	0.527789
9.123956	9.82198928	2.723	1.378315		0.734193	1.011949
10.52002	11.21251146	2.761	1.27658		1.273718	1.626003
11.905	12.53203039	2.6	1.219046		1.421122	1.732414
13.15906	13.63889439	2.625	1.02375		1.164421	1.192076
14.11873	14.76763812	2.541	0.957277		1.282253	1.227472
15.41655	16.03460583	2.513	1.028209		1.47475	1.516351
16.65266	16.73136024	2.739	1.08098		0.653556	0.70648
16.81006	17.23426998	3.082	1.130552		0.299231	0.338296
17.65848	17.75892433	3.049	1.159008		0.329483	0.381873
17.85937	18.28969992	2.652	1.159008		0.544045	0.630552
18.72003	18.76986861	2.616	1.1354		0.509459	0.57844
18.8197	18.93313116	2.812	1.1354		0.141222	0.160344
19.04656	19.36393874	2.547	1.1354		0.486813	0.552727
19.68132	20.30970067	2.583	1.241168	RB	1.034664	1.284191
20.93808	21.51530062	2.615	1.20697		1.280347	1.54534
22.09252	22.61920655	2.599	1.318575		1.190011	1.569119
23.1459	23.33317592	2.626	1.302327		0.750382	0.977242
23.52046	23.77594013	2.767	1.302327		0.402915	0.524727
24.03142	24.50851371	2.597	1.413535		0.791179	1.11836
24.9856	25.44080236	2.614	1.547868		0.991023	1.533972
25.896	26.38628269	2.597	1.475829		1.021119	1.506996
26.87656	27.41762215	2.843	1.49852		0.860137	1.288932
27.95868	28.44494204	2.925	1.344388		0.772545	1.0386
28.9312	29.08366104	2.997	1.220932		0.434329	0.530286
29.23612	29.4289744	3.157	1.220932		0.179563	0.219234
29.62183	30.04546364	2.977	1.060583		0.431542	0.457687
30.4691	30.97806941	3.085	0.77682		0.552103	0.428884
31.48704	32.18490334	3.323			1.191774	0.327268
32.88276	32.93698289	3.651				
32.9912		3.677	RB			
						27.51153
					Alpha	0.803
					LSPIV Q	22.09176
					ADCP Q	23.3
					% Diff	-5.19%

May 15th, 2024

x	Midsection	z	v-vel		Area	Discharge
7.450544	7.627037	3.303	LB		0.193978	0.024581
7.803531	8.392183	3.239				
8.980834	9.052395	3.097	0.358477	Cam1	0.136004	0.048754
9.123956	9.821989	2.723	0.358477		0.446365	0.160011
10.52002	11.21251	2.761	0.477625		0.753663	0.359968
11.905	12.53203	2.6	0.382712		0.927622	0.355012
13.15906	13.63889	2.625	0.420653		0.750454	0.315681
14.11873	14.76764	2.541	0.42881		0.860103	0.368821
15.41655	16.03461	2.513	0.415166		1.000904	0.415542
16.65266	16.73136	2.739	0.401192		0.392969	0.157656
16.81006	17.23427	3.082	0.401192		0.111143	0.04459
17.65848	17.75892	3.049	0.33101		0.133262	0.044111
17.85937	18.2897	2.652	0.214446		0.345535	0.074099
18.72003	18.76987	2.616	0.27897		0.329876	0.092026
18.8197	18.93313	2.812	0.27897		0.080162	0.022363
19.04656	19.36394	2.547	0.358192		0.325691	0.11666
19.68132	20.3097	2.583	0.389282	RB	0.680949	0.265081
20.93808	21.5153	2.615	0.447595		0.829453	0.371259
22.09252	22.61921	2.599	0.497865		0.77715	0.386916
23.1459	23.33318	2.626	0.597279		0.483357	0.288699
23.52046	23.77594	2.767	0.639898		0.237322	0.151862
24.03142	24.50851	2.597	0.639898		0.517197	0.330953
24.9856	25.4408	2.614	0.728583		0.642347	0.468003
25.896	26.38628	2.597	0.770557		0.667509	0.514354
26.87656	27.41762	2.843	0.739353		0.474416	0.350761
27.95868	28.44494	2.925	0.64948		0.388327	0.25221
28.9312	29.08366	2.997	0.261301		0.195448	0.051071
29.23612	29.42897	3.157			0.733558	0.067759
29.62183	30.04546	2.977				
30.4691	30.975	3.085				
31.48091		3.303	RB			
						6.098802
					Alpha	0.75
					LSPIV Q	4.574101
					ADCP Q	5.29
					% diff	-13.61%

Appendix B – Velocity Difference Plots

This section contains all of the velocity difference plots that have were scaled based on the maximum differences of each survey.

March 18th, 2022

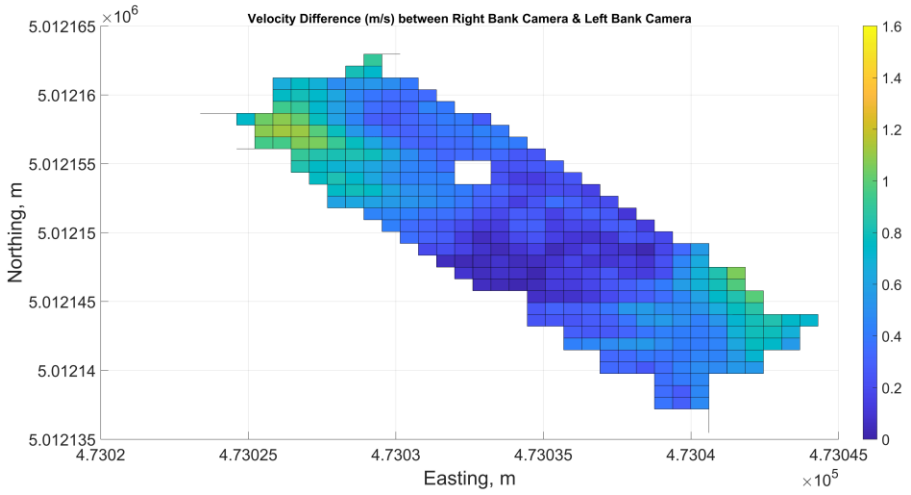

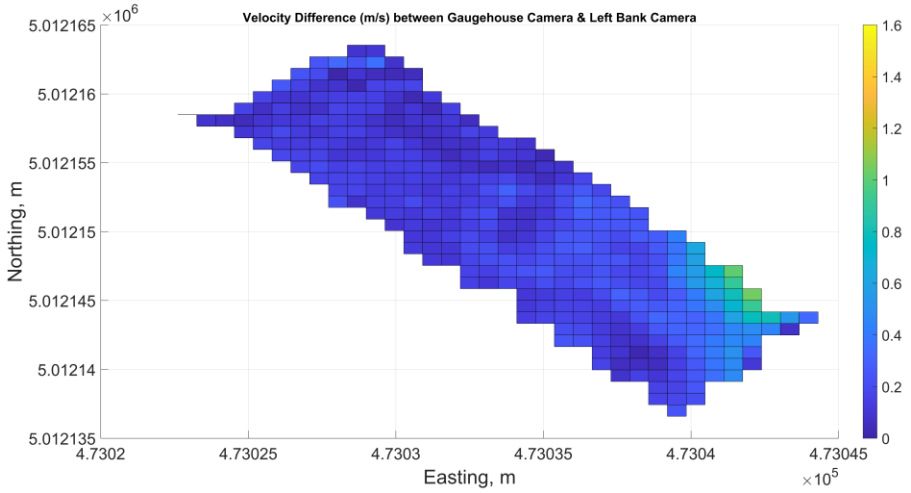

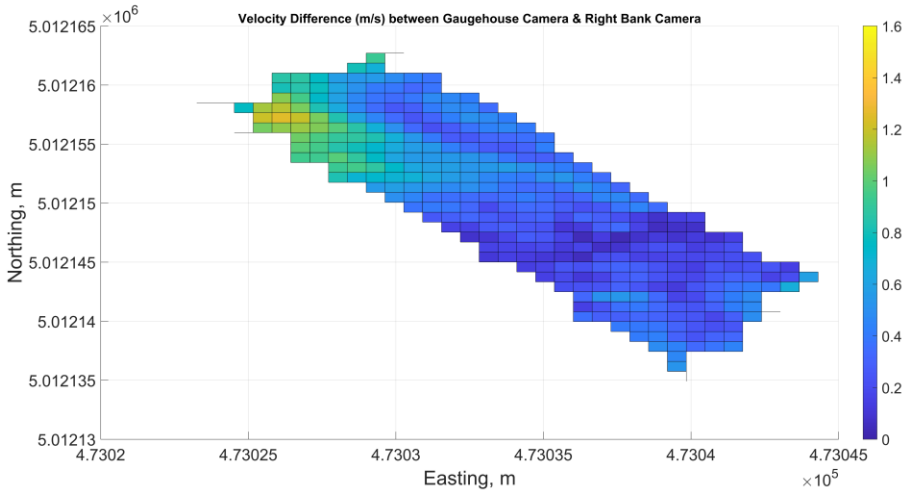

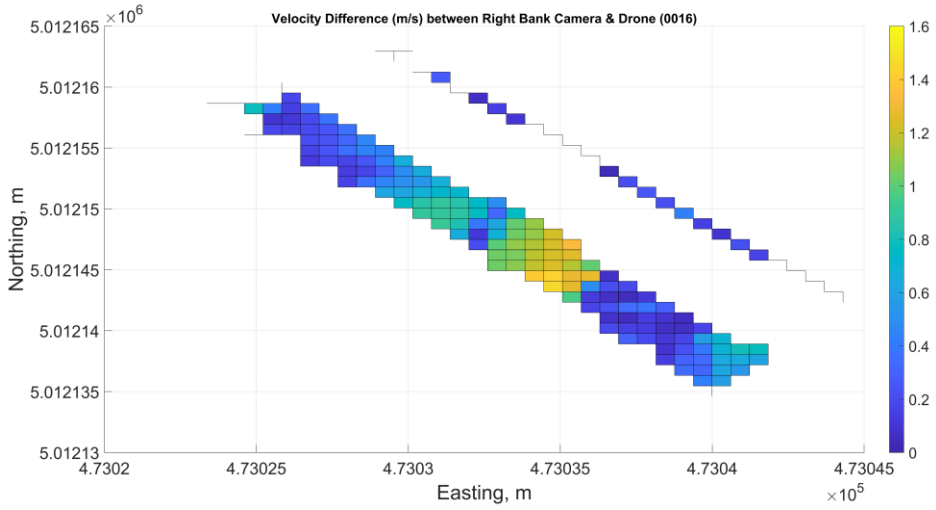
Velocity Difference (m/s) between Right Bank Camera & Drone (0016)
×10^6
5.012165
5.01216
5.012155
5.01215
5.012145
5.01214
5.012135
5.01213
Northing, m
4.7302
4.73025
4.7303
4.73035
4.7304
4.73045
×10^5
Easting, m
1.6
1.4
1.2
1
0.8
0.6
0.4
0.2
0

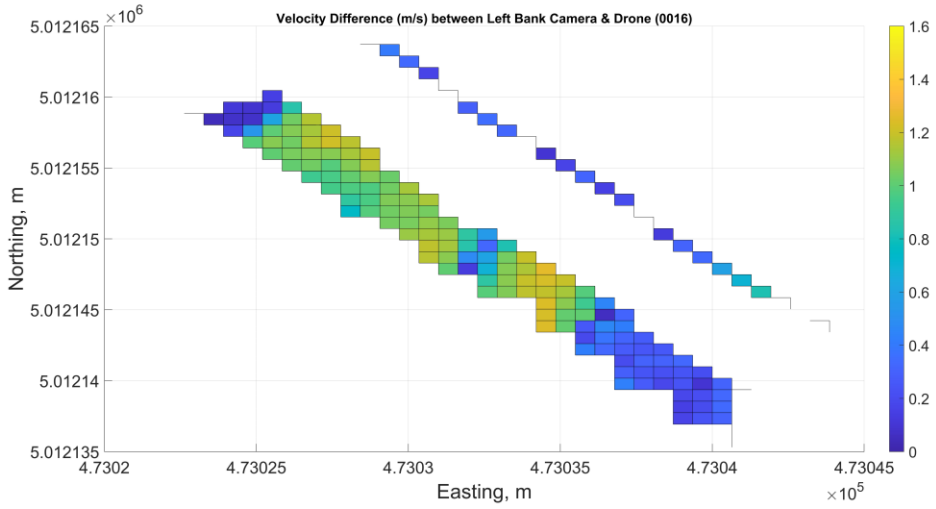
Velocity Difference (m/s) between Left Bank Camera & Drone (0016)
×10^6
5.012165
5.01216
5.012155
5.01215
5.012145
5.01214
5.012135
Northing, m
4.7302
4.73025
4.7303
4.73035
4.7304
4.73045
×10^5
Easting, m
1.6
1.4
1.2
1
0.8
0.6
0.4
0.2
0

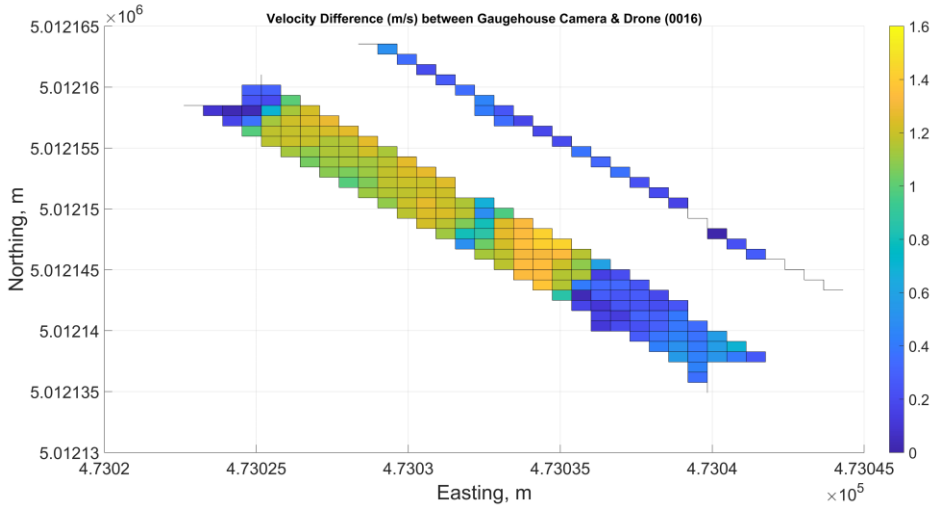
Velocity Difference (m/s) between Gaugehouse Camera & Drone (0016)
×10^6
5.012165
5.01216
5.012155
5.01215
5.012145
5.01214
5.012135
5.01213
Northing, m
4.7302
4.73025
4.7303
4.73035
4.7304
4.73045
×10^5
Easting, m
1.6
1.4
1.2
1
0.8
0.6
0.4
0.2
0

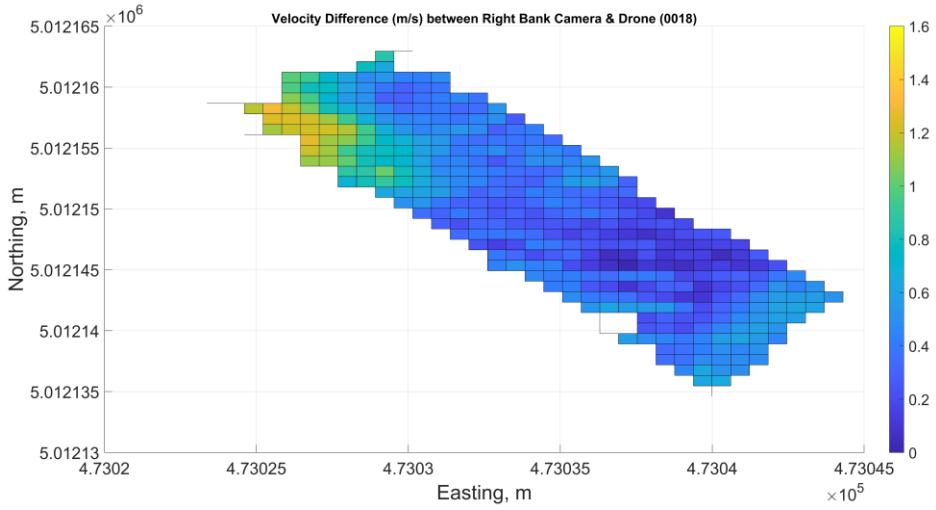
Velocity Difference (m/s) between Right Bank Camera & Drone (0018)
×10^6
5.012165
5.01216
5.012155
5.01215
5.012145
5.01214
5.012135
5.01213
Northing, m
4.7302
4.73025
4.7303
4.73035
4.7304
4.73045
×10^5
Easting, m
1.6
1.4
1.2
1
0.8
0.6
0.4
0.2
0

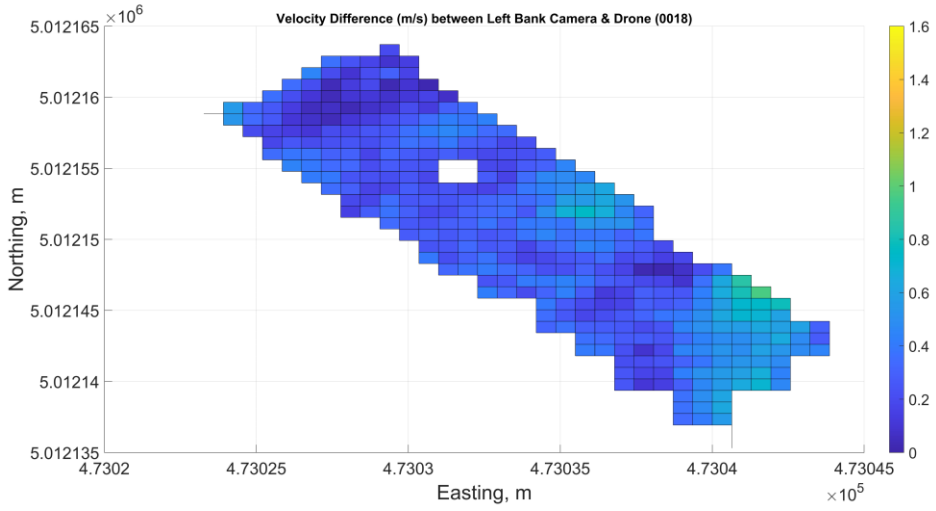
Velocity Difference (m/s) between Left Bank Camera & Drone (0018)
×10^6
5.012165
5.01216
5.012155
5.01215
5.012145
5.01214
5.012135
Northing, m
4.7302
4.73025
4.7303
4.73035
4.7304
4.73045
×10^5
Easting, m
1.6
1.4
1.2
1
0.8
0.6
0.4
0.2
0

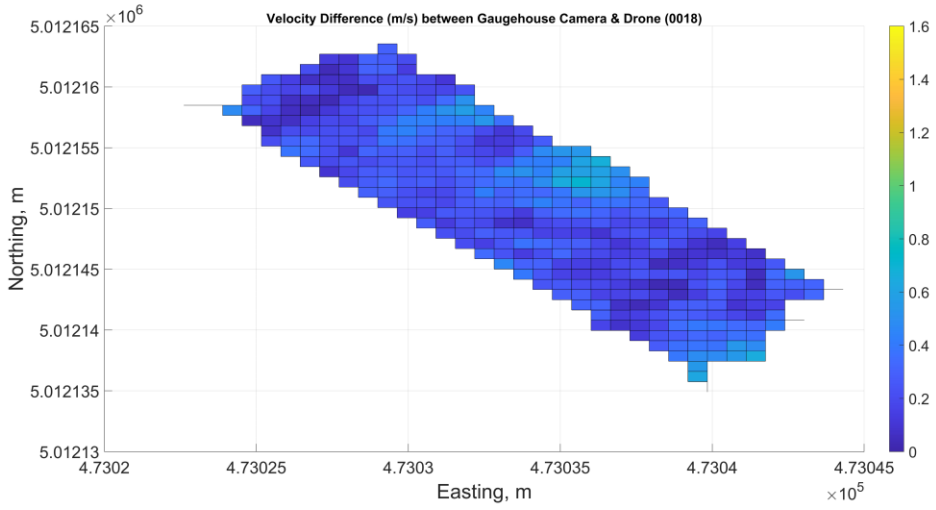
Velocity Difference (m/s) between Gaugehouse Camera & Drone (0018)
×10^6
5.012165
5.01216
5.012155
5.01215
5.012145
5.01214
5.012135
5.01213
Northing, m
4.7302
4.73025
4.7303
4.73035
4.7304
4.73045
×10^5
Easting, m
1.6
1.4
1.2
1
0.8
0.6
0.4
0.2
0

March 21st, 2022

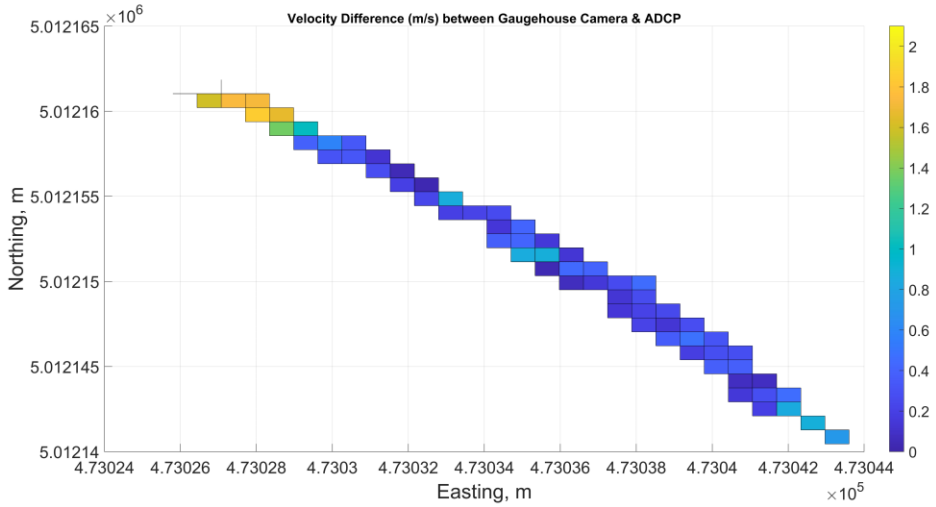

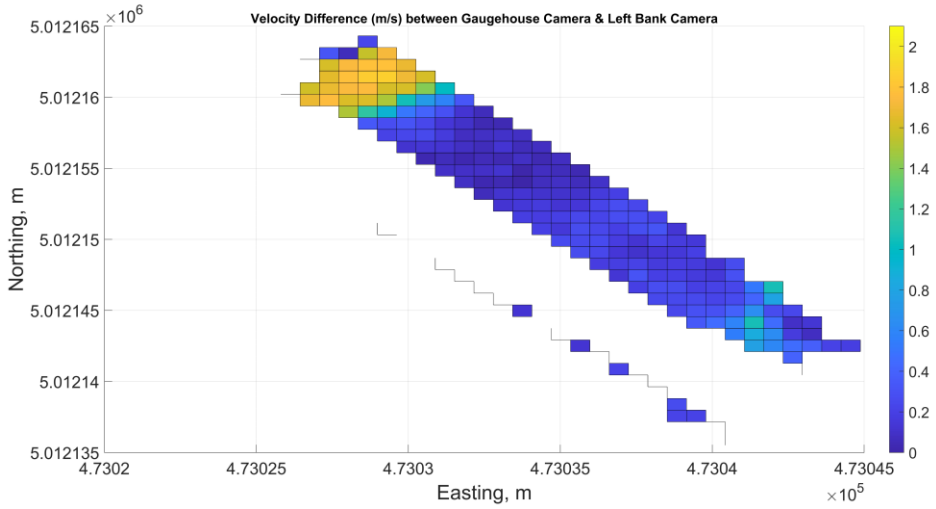

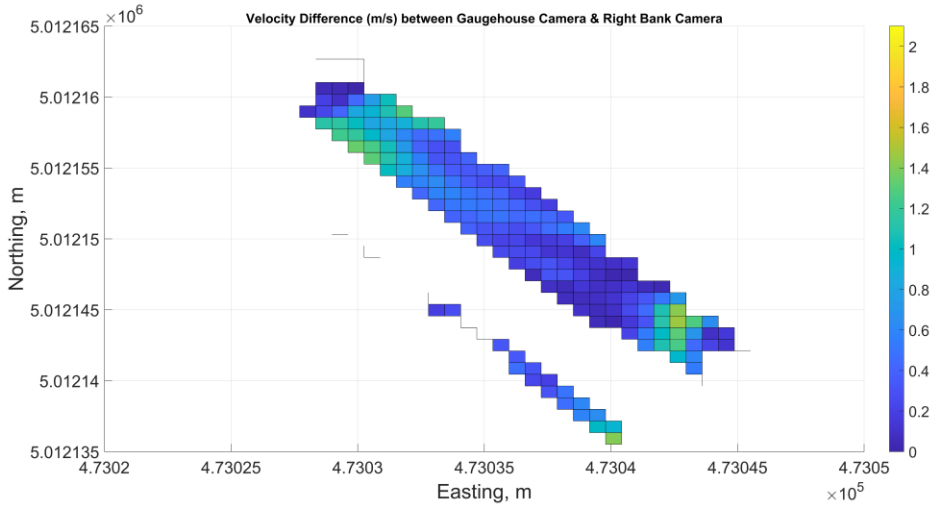

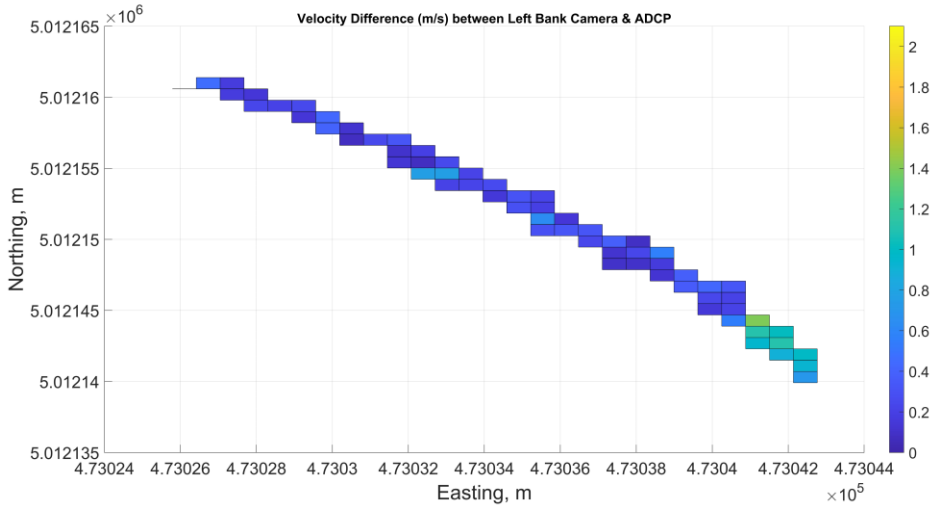
Velocity Difference (m/s) between Left Bank Camera & ADCP
Northing, m
Easting, m
×10^6
×10^5
5.012165
5.01216
5.012155
5.01215
5.012145
5.01214
5.012135
4.73024
4.73026
4.73028
4.7303
4.73032
4.73034
4.73036
4.73038
4.7304
4.73042
4.73044
2
1.8
1.6
1.4
1.2
1
0.8
0.6
0.4
0.2
0

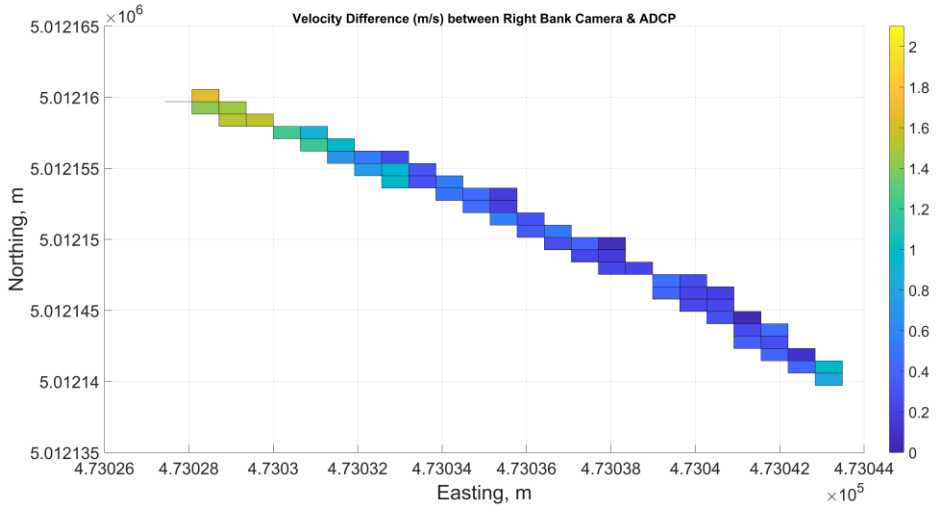
Velocity Difference (m/s) between Right Bank Camera & ADCP
Northing, m
Easting, m
×10^6
×10^5
5.012165
5.01216
5.012155
5.01215
5.012145
5.01214
5.012135
4.73026
4.73028
4.7303
4.73032
4.73034
4.73036
4.73038
4.7304
4.73042
4.73044
2
1.8
1.6
1.4
1.2
1
0.8
0.6
0.4
0.2
0

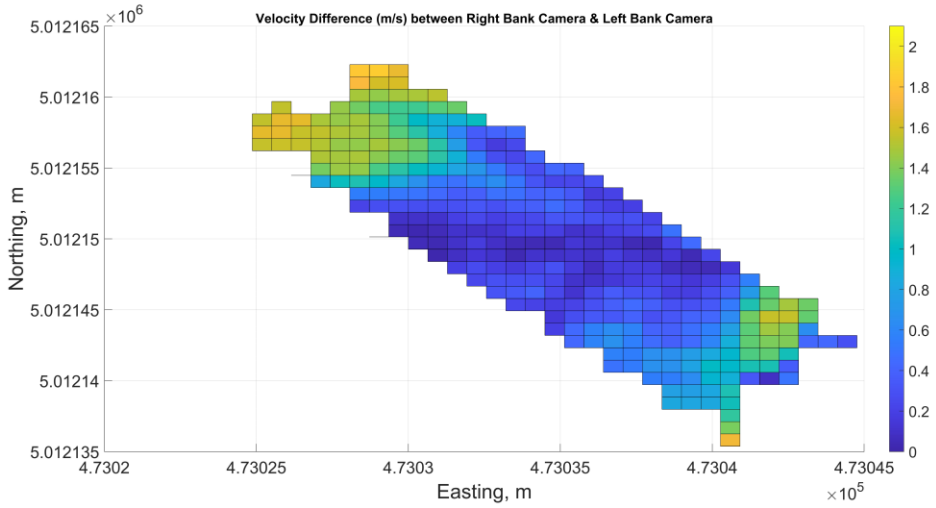
Velocity Difference (m/s) between Right Bank Camera & Left Bank Camera
Northing, m
Easting, m
×10^6
×10^5
5.012165
5.01216
5.012155
5.01215
5.012145
5.01214
5.012135
4.7302
4.73025
4.7303
4.73035
4.7304
4.73045
2
1.8
1.6
1.4
1.2
1
0.8
0.6
0.4
0.2
0

April 8th, 2022

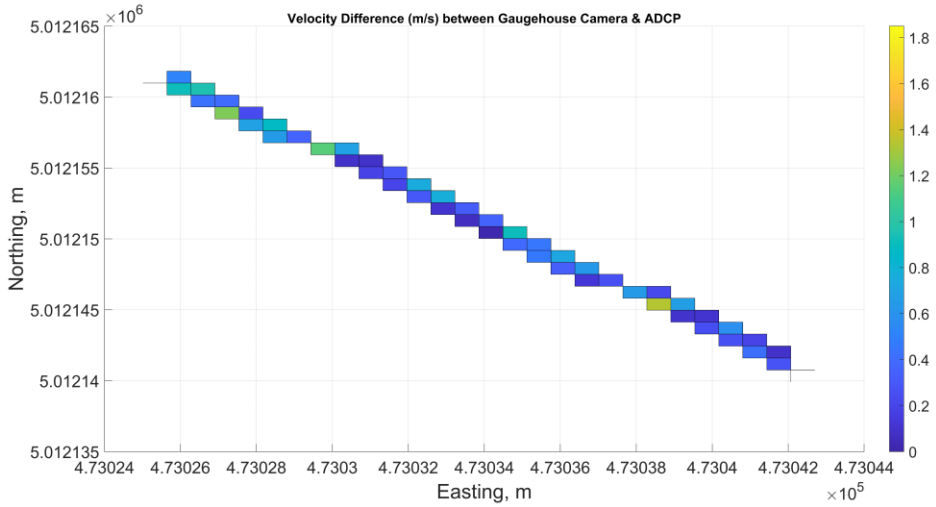

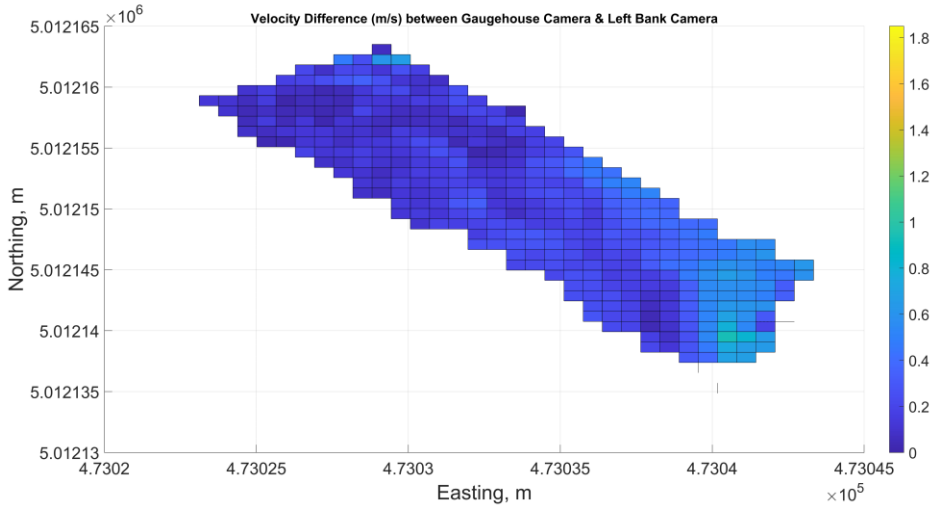

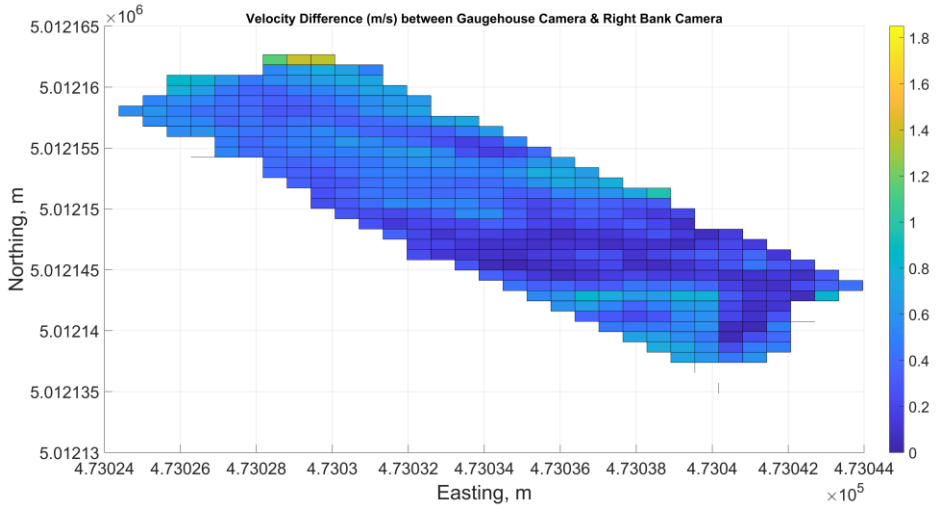
Velocity Difference (m/s) between Gaugehouse Camera & Right Bank Camera
×10^6
5.012165
5.01216
5.012155
5.01215
5.012145
5.01214
5.012135
5.01213
Northing, m
4.73024
4.73026
4.73028
4.7303
4.73032
4.73034
4.73036
4.73038
4.7304
4.73042
4.73044
×10^5
Easting, m
1.8
1.6
1.4
1.2
1
0.8
0.6
0.4
0.2
0

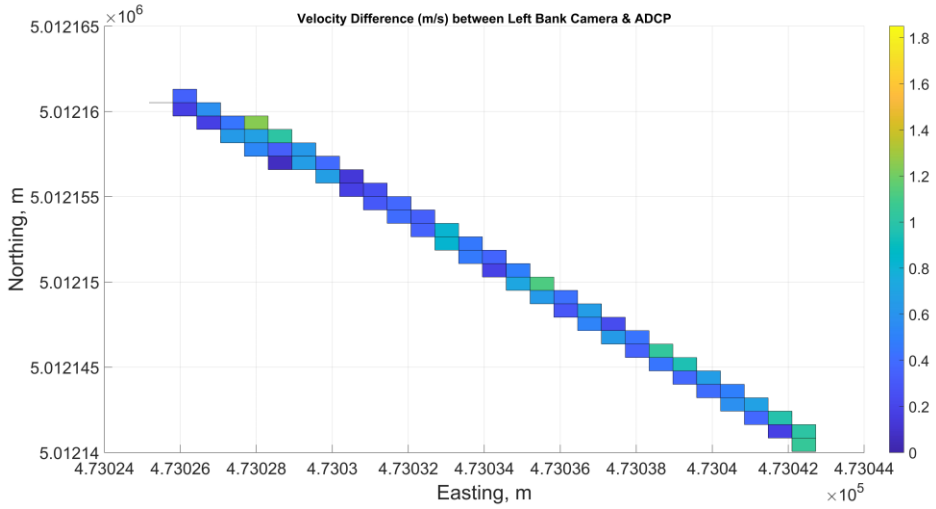
Velocity Difference (m/s) between Left Bank Camera & ADCP
×10^6
5.012165
5.01216
5.012155
5.01215
5.012145
5.01214
Northing, m
4.73024
4.73026
4.73028
4.7303
4.73032
4.73034
4.73036
4.73038
4.7304
4.73042
4.73044
×10^5
Easting, m
1.8
1.6
1.4
1.2
1
0.8
0.6
0.4
0.2
0

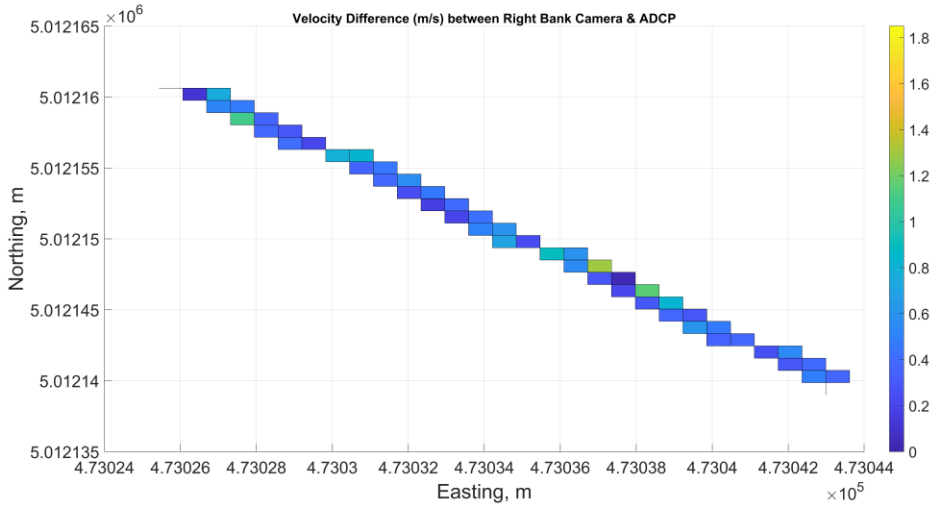
Velocity Difference (m/s) between Right Bank Camera & ADCP
×10^6
5.012165
5.01216
5.012155
5.01215
5.012145
5.01214
5.012135
Northing, m
4.73024
4.73026
4.73028
4.7303
4.73032
4.73034
4.73036
4.73038
4.7304
4.73042
4.73044
×10^5
Easting, m
1.8
1.6
1.4
1.2
1
0.8
0.6
0.4
0.2
0

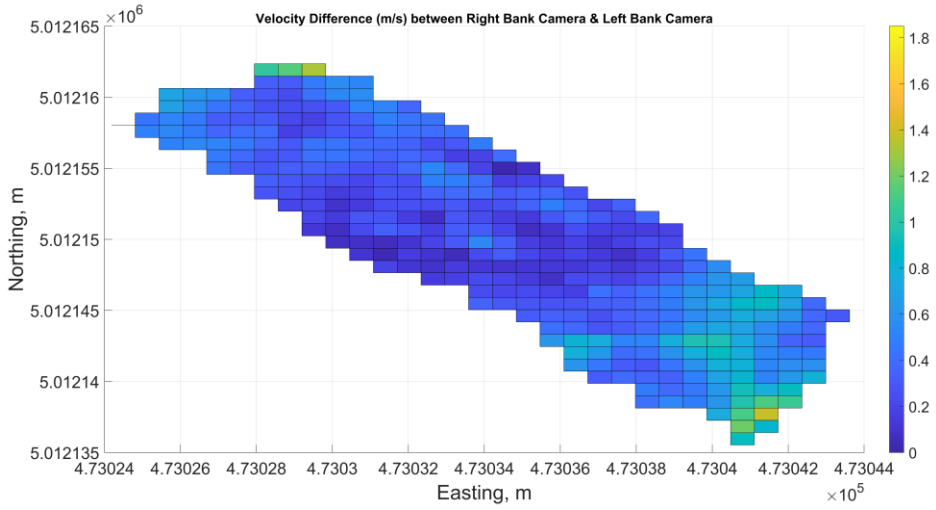
Velocity Difference (m/s) between Right Bank Camera & Left Bank Camera
×10^6
5.012165
5.01216
5.012155
5.01215
5.012145
5.01214
5.012135
Northing, m
4.73024
4.73026
4.73028
4.7303
4.73032
4.73034
4.73036
4.73038
4.7304
4.73042
4.73044
Easting, m
×10^5
1.8
1.6
1.4
1.2
1
0.8
0.6
0.4
0.2
0

May 5th, 2022

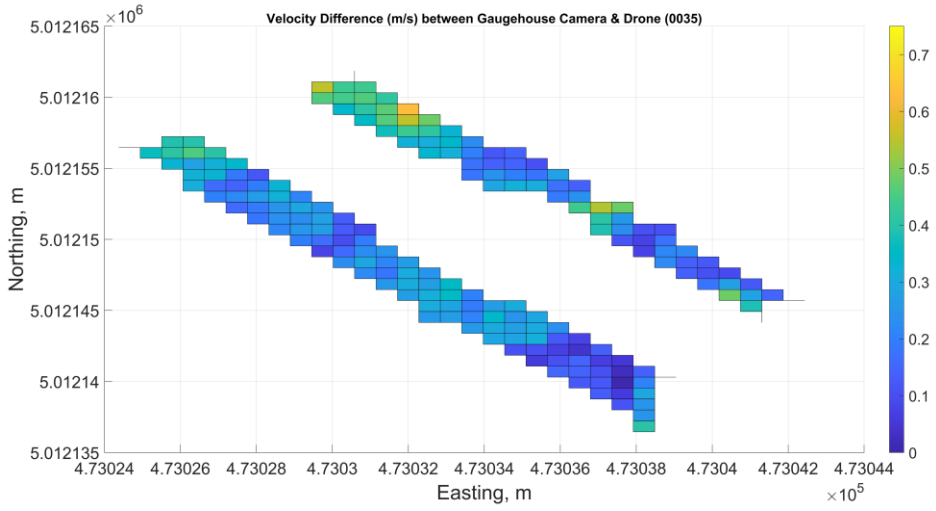
Velocity Difference (m/s) between Gaugehouse Camera & Drone (0035)
×10^6
5.012165
5.01216
5.012155
5.01215
5.012145
5.01214
5.012135
Northing, m
4.73024
4.73026
4.73028
4.7303
4.73032
4.73034
4.73036
4.73038
4.7304
4.73042
4.73044
Easting, m
×10^5
0.7
0.6
0.5
0.4
0.3
0.2
0.1
0

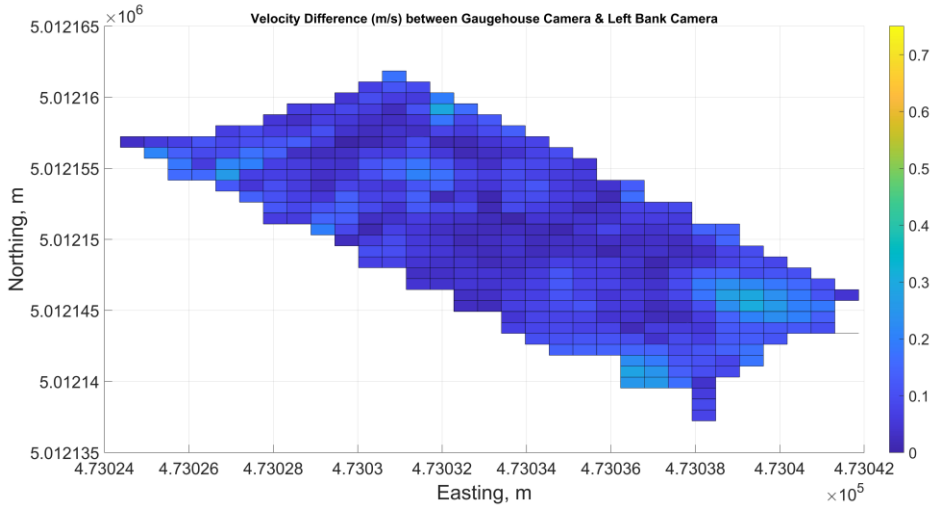
Velocity Difference (m/s) between Gaugehouse Camera & Left Bank Camera
×10^6
5.012165
5.01216
5.012155
5.01215
5.012145
5.01214
5.012135
Northing, m
4.73024
4.73026
4.73028
4.7303
4.73032
4.73034
4.73036
4.73038
4.7304
4.73042
×10^5
Easting, m
0.7
0.6
0.5
0.4
0.3
0.2
0.1
0

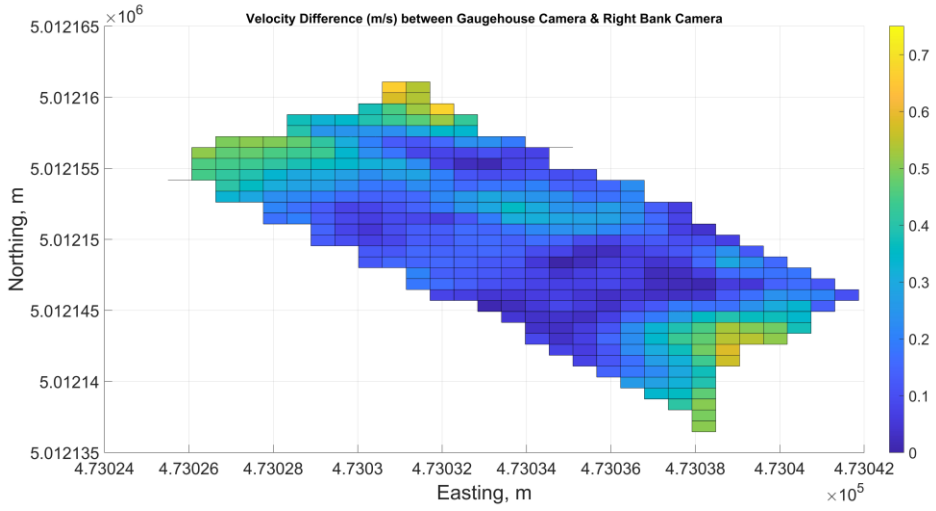
Velocity Difference (m/s) between Gaugehouse Camera & Right Bank Camera
×10^6
5.012165
5.01216
5.012155
5.01215
5.012145
5.01214
5.012135
Northing, m
4.73024
4.73026
4.73028
4.7303
4.73032
4.73034
4.73036
4.73038
4.7304
4.73042
×10^5
Easting, m
0.7
0.6
0.5
0.4
0.3
0.2
0.1
0

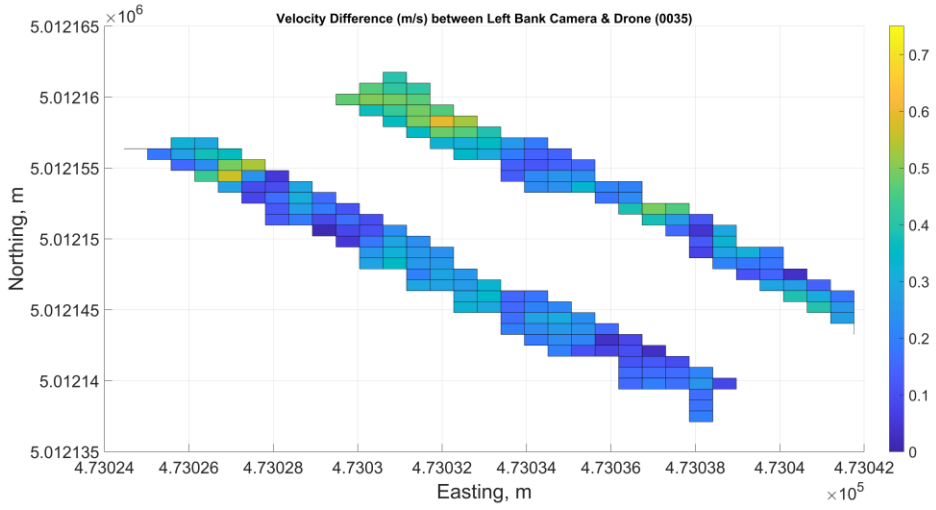
Velocity Difference (m/s) between Left Bank Camera & Drone (0035)
×10^6
5.012165
5.01216
5.012155
5.01215
5.012145
5.01214
5.012135
Northing, m
4.73024
4.73026
4.73028
4.7303
4.73032
4.73034
4.73036
4.73038
4.7304
4.73042
×10^5
Easting, m
0.7
0.6
0.5
0.4
0.3
0.2
0.1
0

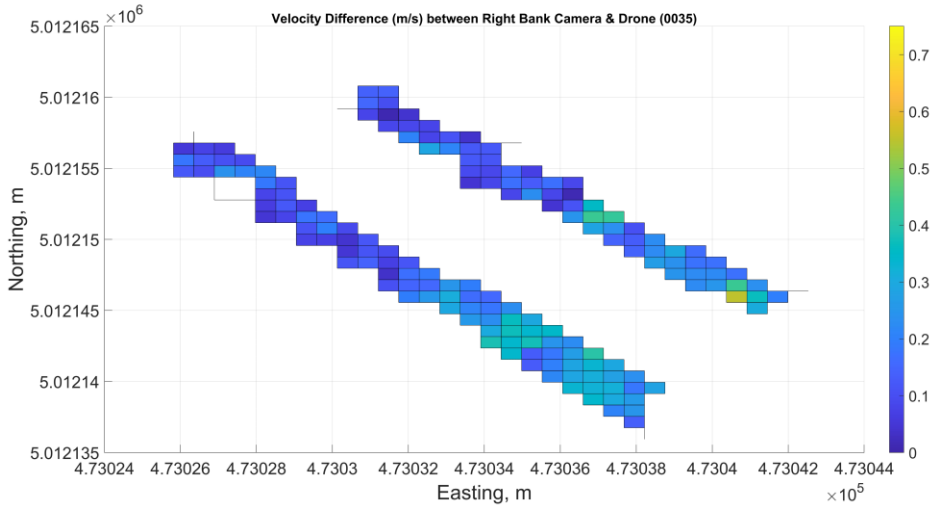
Velocity Difference (m/s) between Right Bank Camera & Drone (0035)
×10^6
5.012165
5.01216
5.012155
5.01215
5.012145
5.01214
5.012135
Northing, m
4.73024
4.73026
4.73028
4.7303
4.73032
4.73034
4.73036
4.73038
4.7304
4.73042
4.73044
Easting, m
×10^5
0.7
0.6
0.5
0.4
0.3
0.2
0.1
0

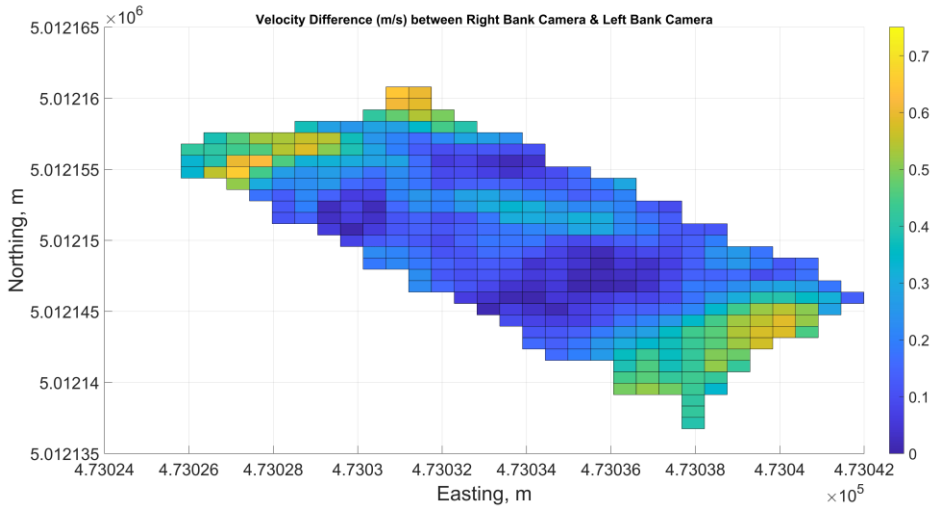
Velocity Difference (m/s) between Right Bank Camera & Left Bank Camera
×10^6
5.012165
5.01216
5.012155
5.01215
5.012145
5.01214
5.012135
Northing, m
4.73024
4.73026
4.73028
4.7303
4.73032
4.73034
4.73036
4.73038
4.7304
4.73042
Easting, m
×10^5
0.7
0.6
0.5
0.4
0.3
0.2
0.1
0

May 5th, 2023

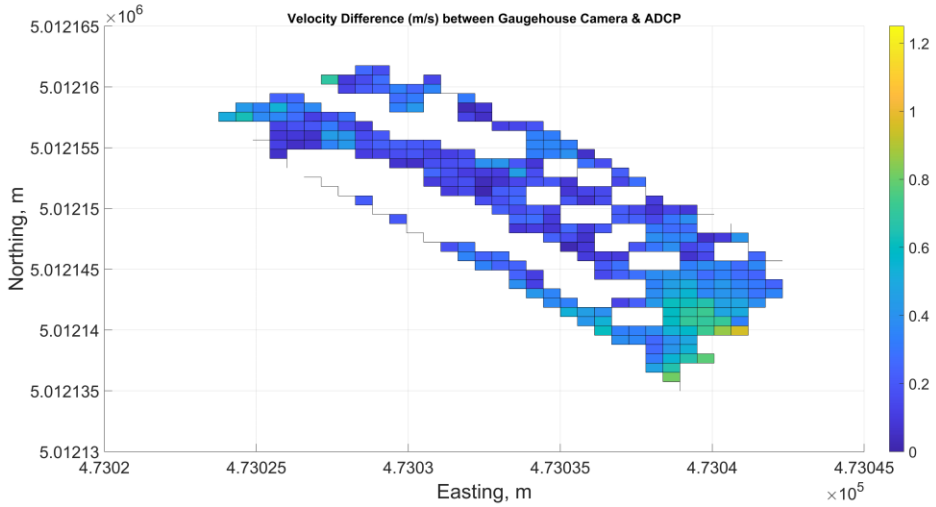
Velocity Difference (m/s) between Gaugehouse Camera & ADCP
×10^6
5.012165
5.01216
5.012155
5.01215
5.012145
5.01214
5.012135
5.01213
Northing, m
4.7302
4.73025
4.7303
4.73035
4.7304
4.73045
×10^5
Easting, m
1.2
1
0.8
0.6
0.4
0.2
0

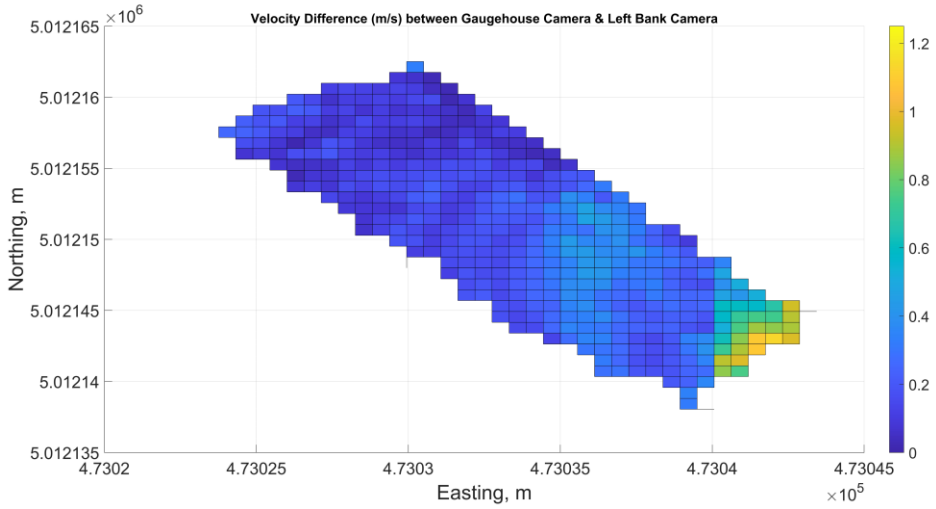
Velocity Difference (m/s) between Gaugehouse Camera & Left Bank Camera
×10^6
5.012165
5.01216
5.012155
5.01215
5.012145
5.01214
5.012135
Northing, m
4.7302
4.73025
4.7303
4.73035
4.7304
4.73045
×10^5
Easting, m
1.2
1
0.8
0.6
0.4
0.2
0

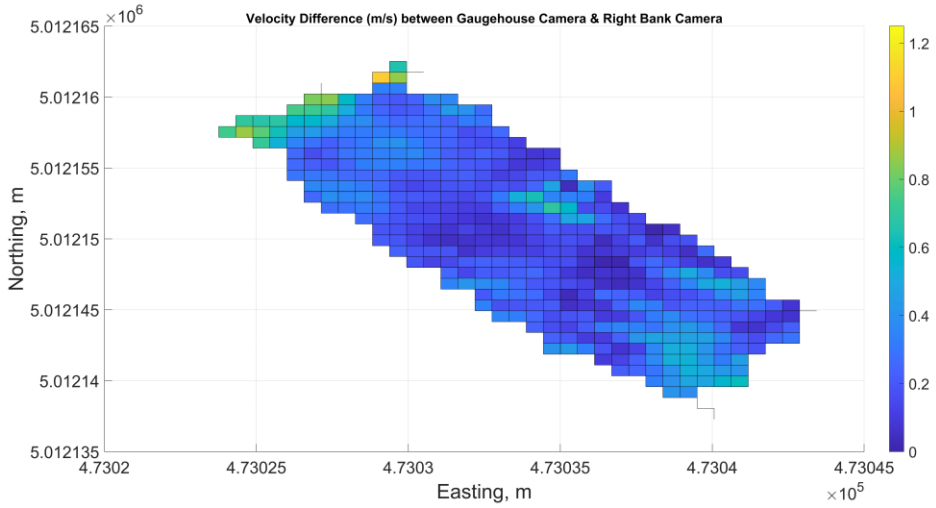
Velocity Difference (m/s) between Gaugehouse Camera & Right Bank Camera
×10^6
5.012165
5.01216
5.012155
5.01215
5.012145
5.01214
5.012135
Northing, m
4.7302
4.73025
4.7303
4.73035
4.7304
4.73045
×10^5
Easting, m
1.2
1
0.8
0.6
0.4
0.2
0

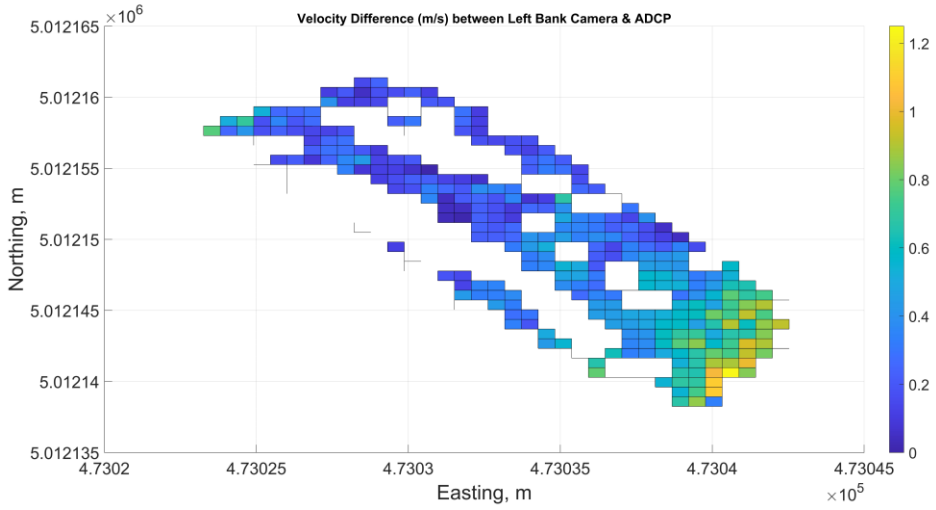
Velocity Difference (m/s) between Left Bank Camera & ADCP
×10^6
5.012165
5.01216
5.012155
5.01215
5.012145
5.01214
5.012135
Northing, m
4.7302
4.73025
4.7303
4.73035
4.7304
4.73045
Easting, m
×10^5
1.2
1
0.8
0.6
0.4
0.2
0

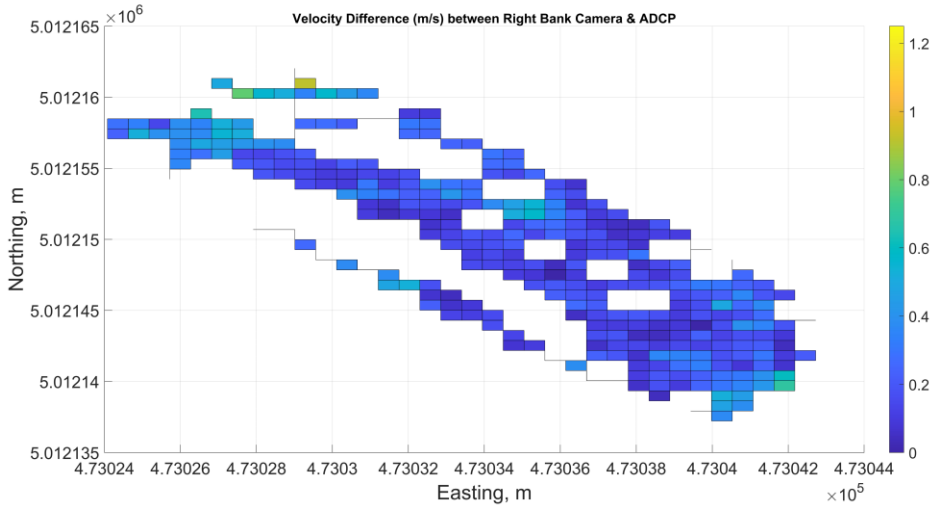
Velocity Difference (m/s) between Right Bank Camera & ADCP
×10^6
5.012165
5.01216
5.012155
5.01215
5.012145
5.01214
5.012135
Northing, m
4.73024
4.73026
4.73028
4.7303
4.73032
4.73034
4.73036
4.73038
4.7304
4.73042
4.73044
Easting, m
×10^5
1.2
1
0.8
0.6
0.4
0.2
0

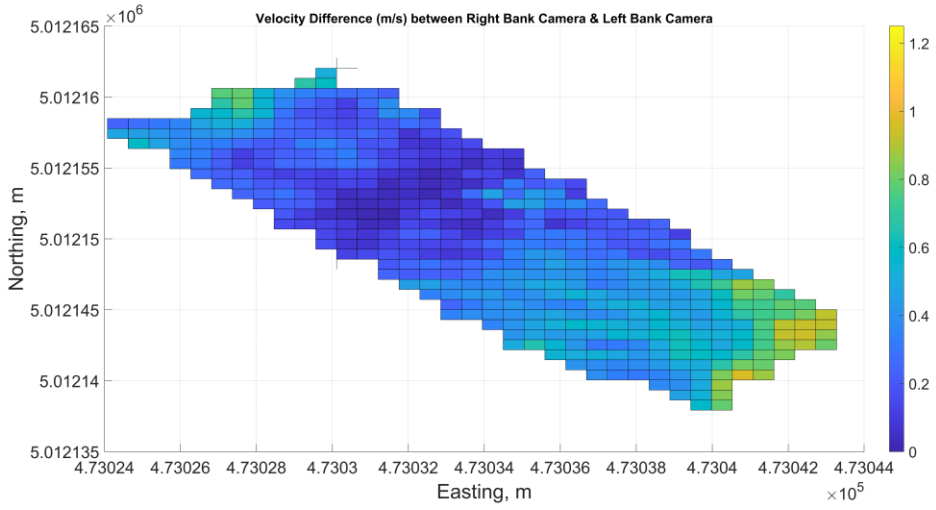
Velocity Difference (m/s) between Right Bank Camera & Left Bank Camera
×10^6
5.012165
5.01216
5.012155
5.01215
5.012145
5.01214
5.012135
Northing, m
4.73024
4.73026
4.73028
4.7303
4.73032
4.73034
4.73036
4.73038
4.7304
4.73042
4.73044
Easting, m
×10^5
1.2
1
0.8
0.6
0.4
0.2
0

March 6th, 2024

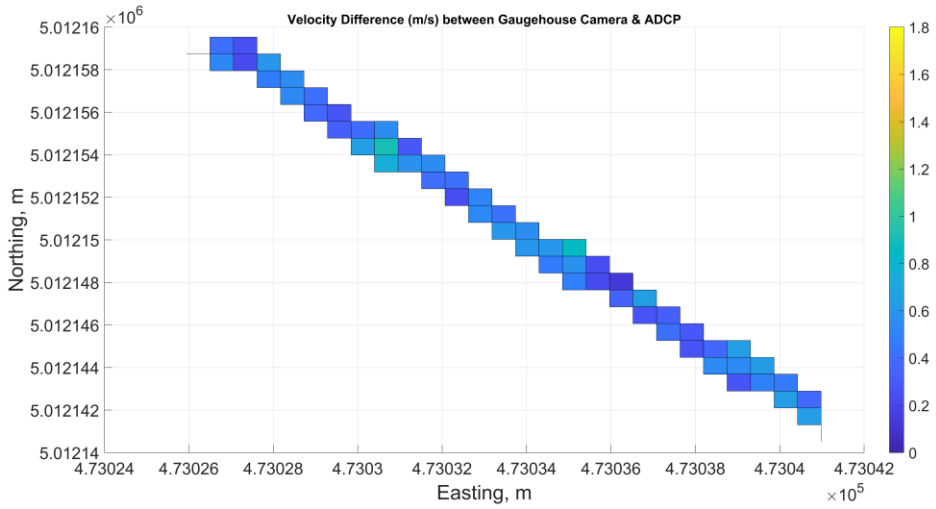

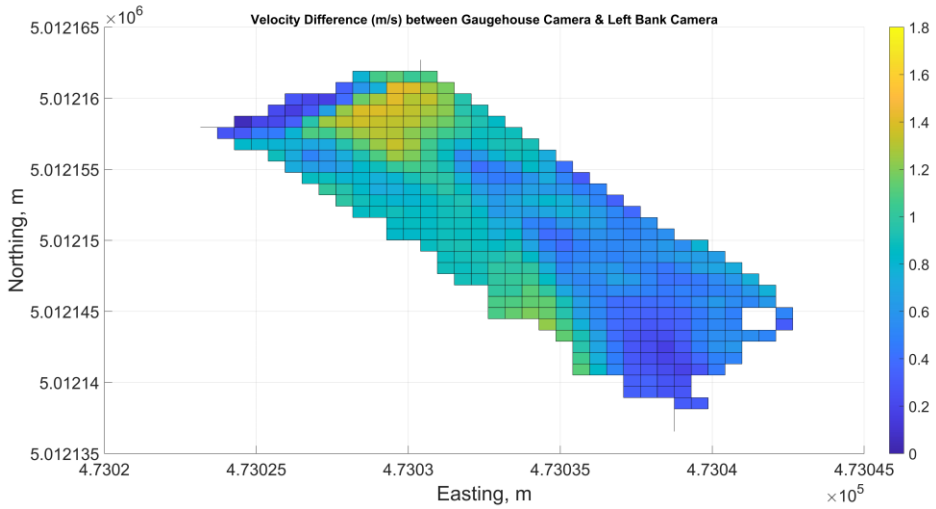

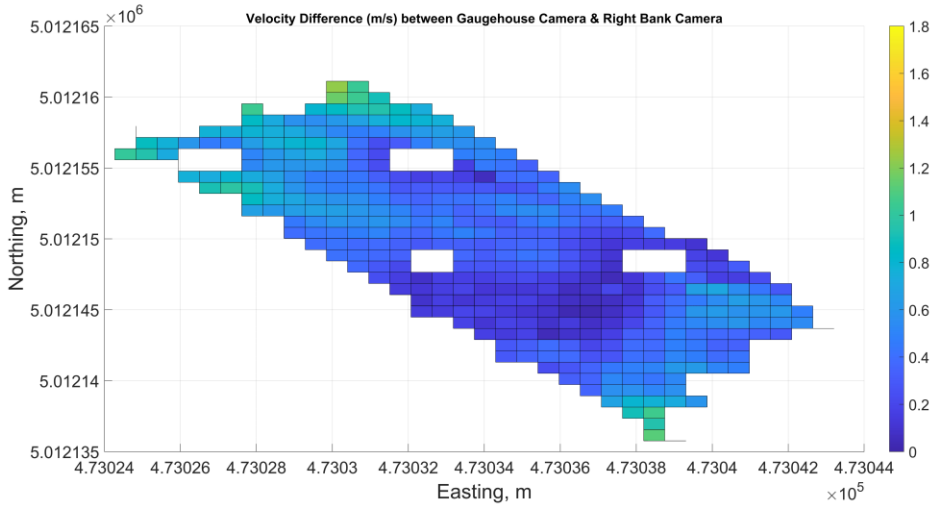

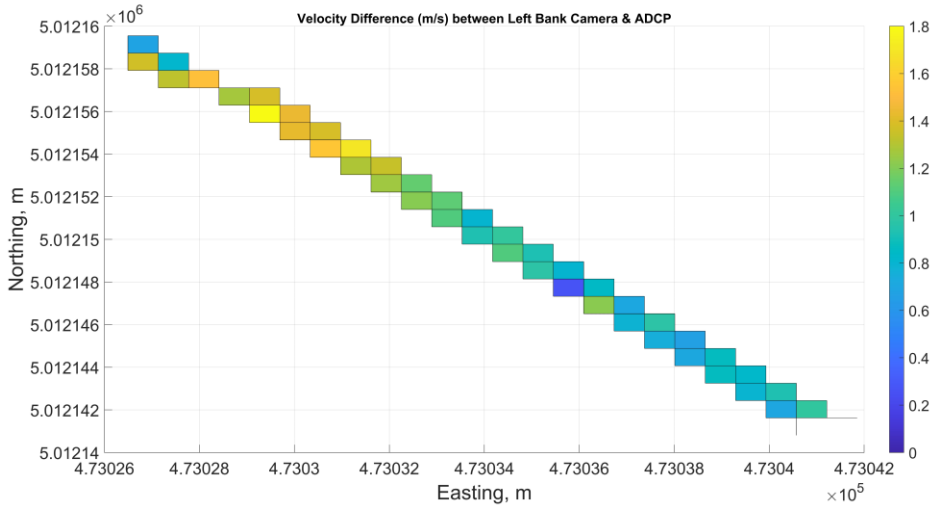
Velocity Difference (m/s) between Left Bank Camera & ADCP
×10^6
5.01216
5.012158
5.012156
5.012154
5.012152
5.01215
5.012148
5.012146
5.012144
5.012142
5.01214
Northing, m
4.73026
4.73028
4.7303
4.73032
4.73034
4.73036
4.73038
4.7304
4.73042
×10^5
Easting, m
1.8
1.6
1.4
1.2
1
0.8
0.6
0.4
0.2
0

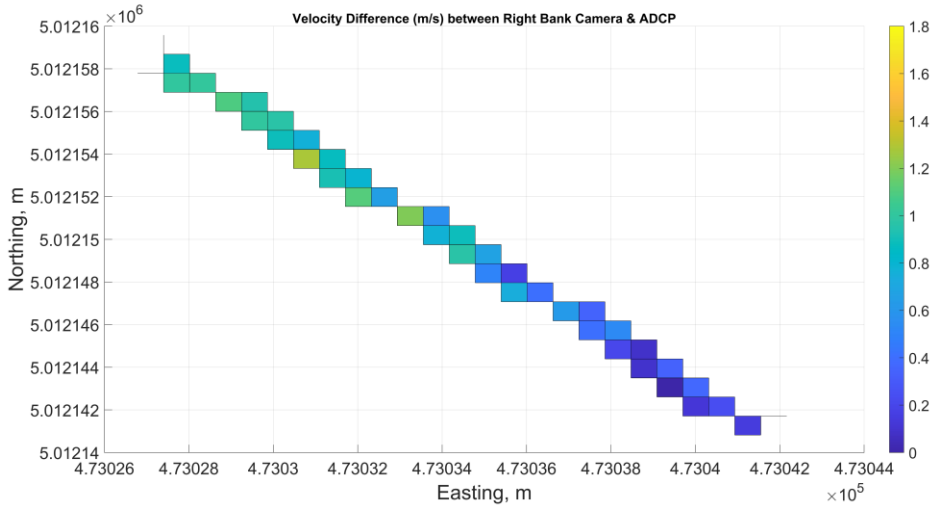
Velocity Difference (m/s) between Right Bank Camera & ADCP
×10^6
5.01216
5.012158
5.012156
5.012154
5.012152
5.01215
5.012148
5.012146
5.012144
5.012142
5.01214
Northing, m
4.73026
4.73028
4.7303
4.73032
4.73034
4.73036
4.73038
4.7304
4.73042
4.73044
×10^5
Easting, m
1.8
1.6
1.4
1.2
1
0.8
0.6
0.4
0.2
0

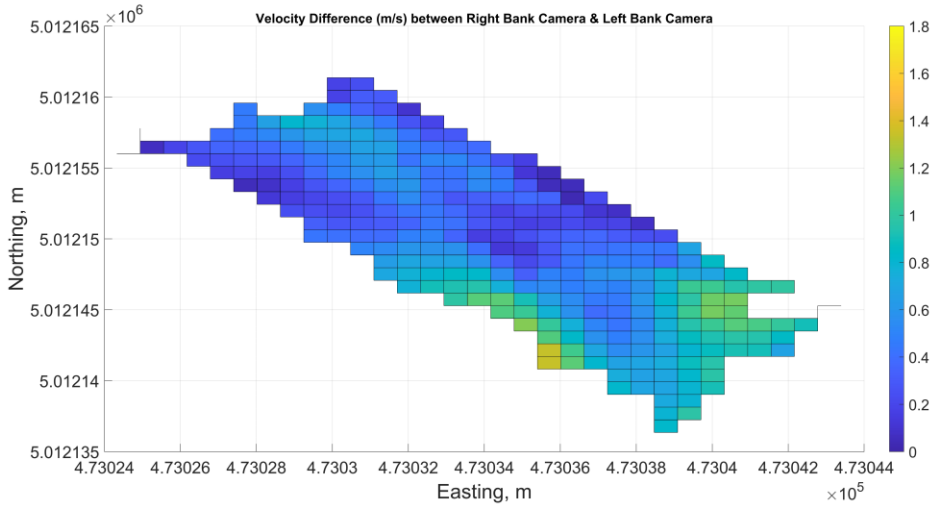
Velocity Difference (m/s) between Right Bank Camera & Left Bank Camera
×10^6
5.012165
5.01216
5.012155
5.01215
5.012145
5.01214
5.012135
Northing, m
4.73024
4.73026
4.73028
4.7303
4.73032
4.73034
4.73036
4.73038
4.7304
4.73042
4.73044
×10^5
Easting, m
1.8
1.6
1.4
1.2
1
0.8
0.6
0.4
0.2
0

May 15th, 2024

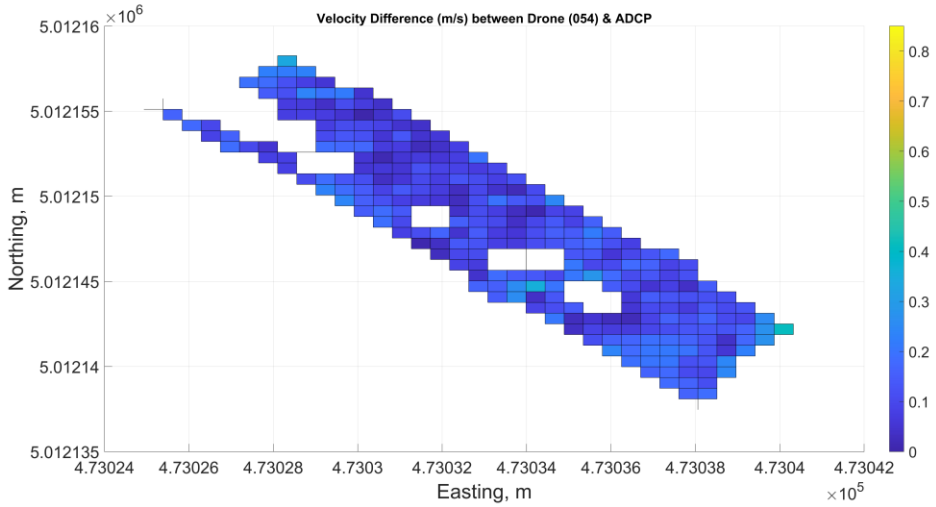

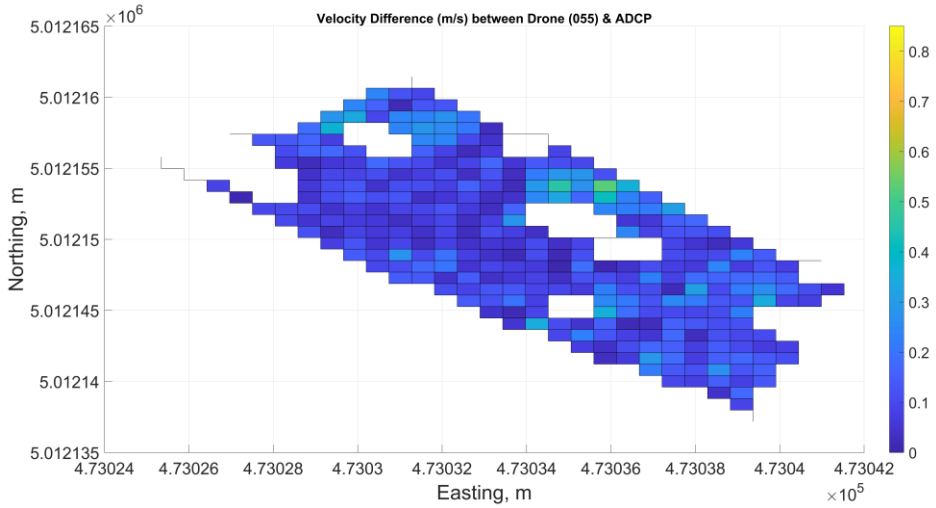

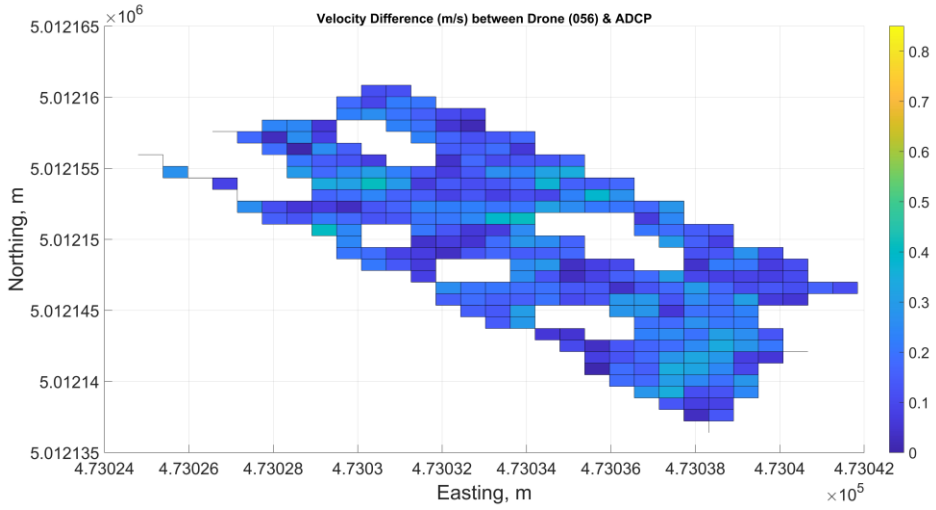
Velocity Difference (m/s) between Drone (056) & ADCP
×10^6
5.012165
5.01216
5.012155
5.01215
5.012145
5.01214
5.012135
Northing, m
4.73024
4.73026
4.73028
4.7303
4.73032
4.73034
4.73036
4.73038
4.7304
4.73042
×10^5
Easting, m
0.8
0.7
0.6
0.5
0.4
0.3
0.2
0.1
0

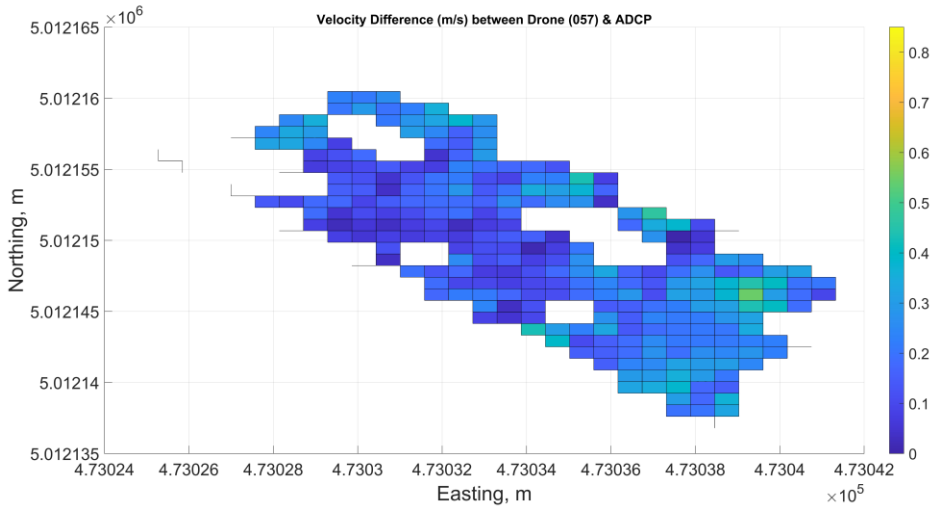
Velocity Difference (m/s) between Drone (057) & ADCP
×10^6
5.012165
5.01216
5.012155
5.01215
5.012145
5.01214
5.012135
Northing, m
4.73024
4.73026
4.73028
4.7303
4.73032
4.73034
4.73036
4.73038
4.7304
4.73042
×10^5
Easting, m
0.8
0.7
0.6
0.5
0.4
0.3
0.2
0.1
0

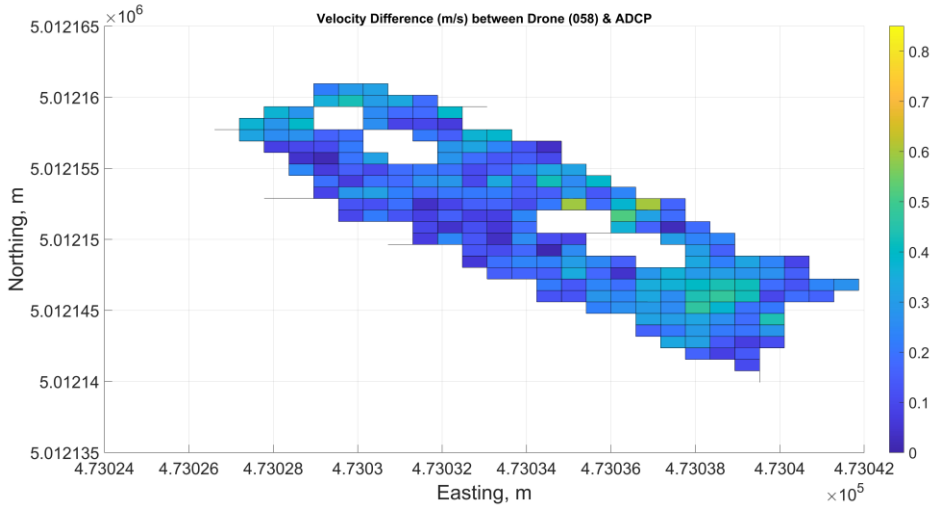
Velocity Difference (m/s) between Drone (058) & ADCP
×10^6
5.012165
5.01216
5.012155
5.01215
5.012145
5.01214
5.012135
Northing, m
4.73024
4.73026
4.73028
4.7303
4.73032
4.73034
4.73036
4.73038
4.7304
4.73042
×10^5
Easting, m
0.8
0.7
0.6
0.5
0.4
0.3
0.2
0.1
0

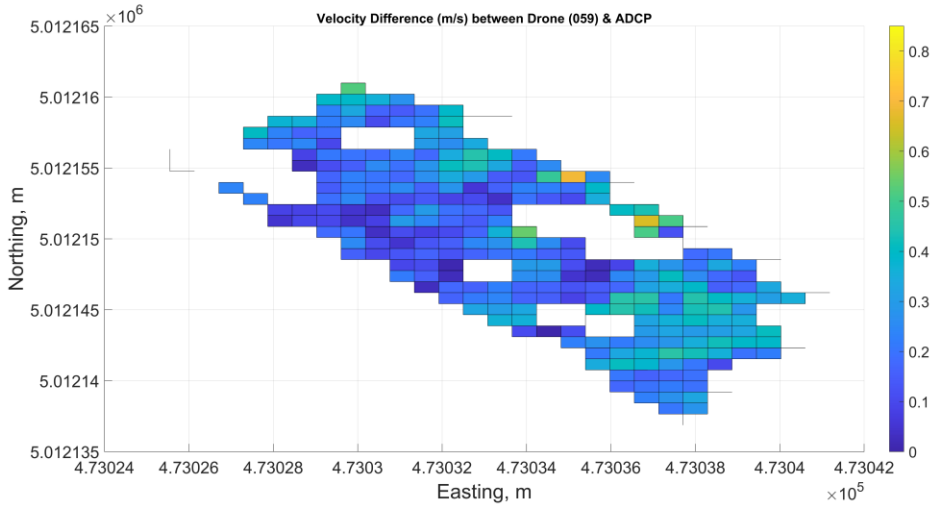
Velocity Difference (m/s) between Drone (059) & ADCP
×10^6
5.012165
5.01216
5.012155
5.01215
5.012145
5.01214
5.012135
Northing, m
4.73024
4.73026
4.73028
4.7303
4.73032
4.73034
4.73036
4.73038
4.7304
4.73042
×10^5
Easting, m
0.8
0.7
0.6
0.5
0.4
0.3
0.2
0.1
0

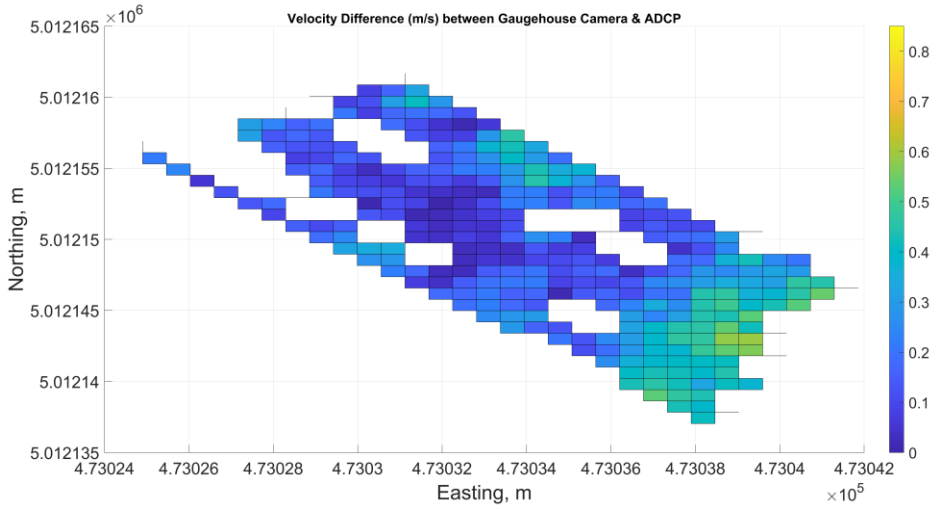
Velocity Difference (m/s) between Gaugehouse Camera & ADCP
×10^6
5.012165
5.01216
5.012155
5.01215
5.012145
5.01214
5.012135
Northing, m
4.73024
4.73026
4.73028
4.7303
4.73032
4.73034
4.73036
4.73038
4.7304
4.73042
×10^5
Easting, m
0.8
0.7
0.6
0.5
0.4
0.3
0.2
0.1
0

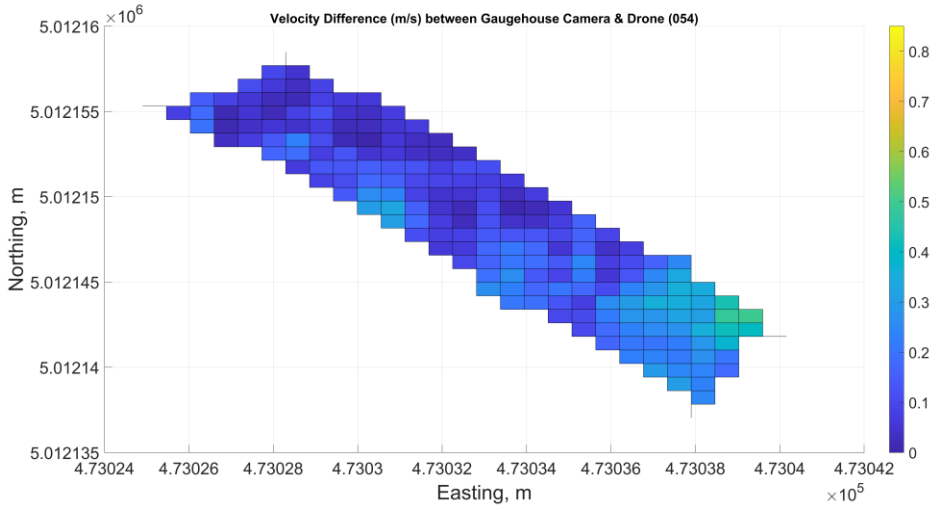
Velocity Difference (m/s) between Gaugehouse Camera & Drone (054)
×10^6
5.01216
5.012155
5.01215
5.012145
5.01214
5.012135
Northing, m
4.73024
4.73026
4.73028
4.7303
4.73032
4.73034
4.73036
4.73038
4.7304
4.73042
×10^5
Easting, m
0.8
0.7
0.6
0.5
0.4
0.3
0.2
0.1
0

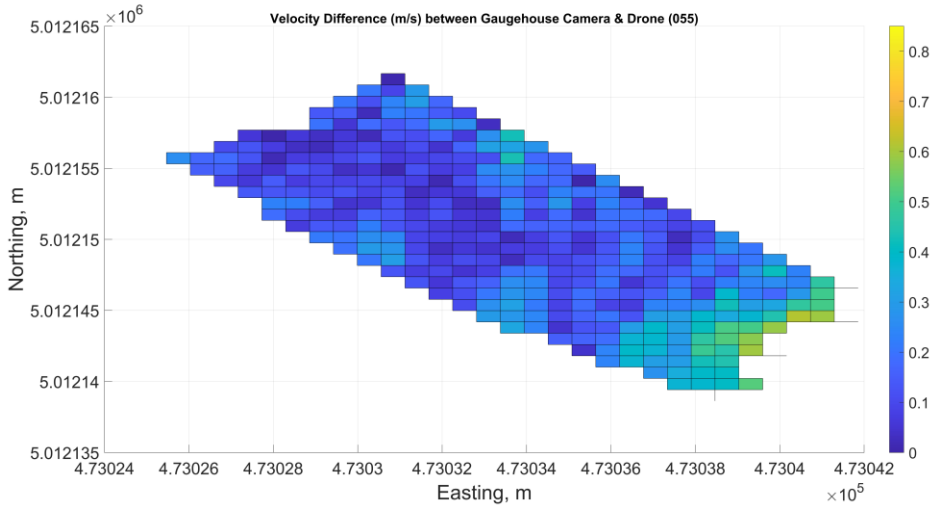
Velocity Difference (m/s) between Gaugehouse Camera & Drone (055)
×10^6
5.012165
5.01216
5.012155
5.01215
5.012145
5.01214
5.012135
Northing, m
4.73024
4.73026
4.73028
4.7303
4.73032
4.73034
4.73036
4.73038
4.7304
4.73042
×10^5
Easting, m
0.8
0.7
0.6
0.5
0.4
0.3
0.2
0.1
0

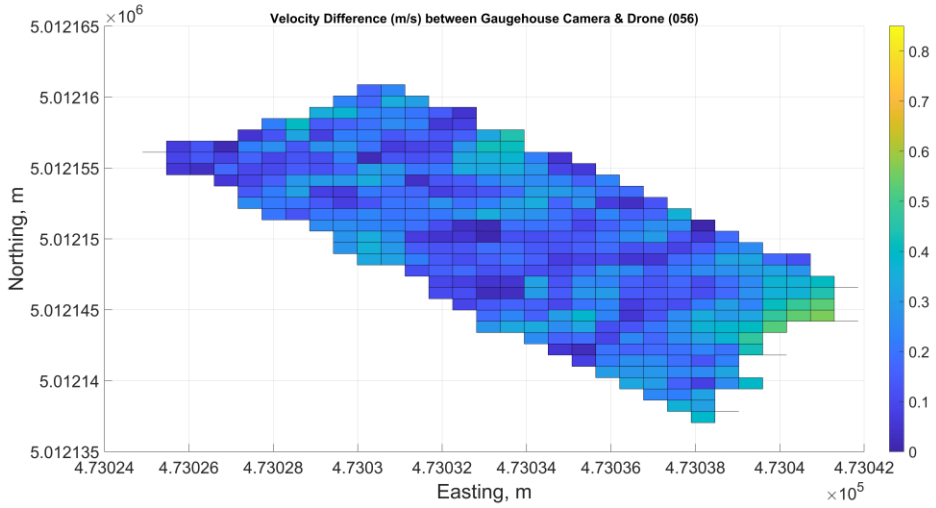
Velocity Difference (m/s) between Gaugehouse Camera & Drone (056)
×10^6
5.012165
5.01216
5.012155
5.01215
5.012145
5.01214
5.012135
Northing, m
4.73024
4.73026
4.73028
4.7303
4.73032
4.73034
4.73036
4.73038
4.7304
4.73042
×10^5
Easting, m
0.8
0.7
0.6
0.5
0.4
0.3
0.2
0.1
0

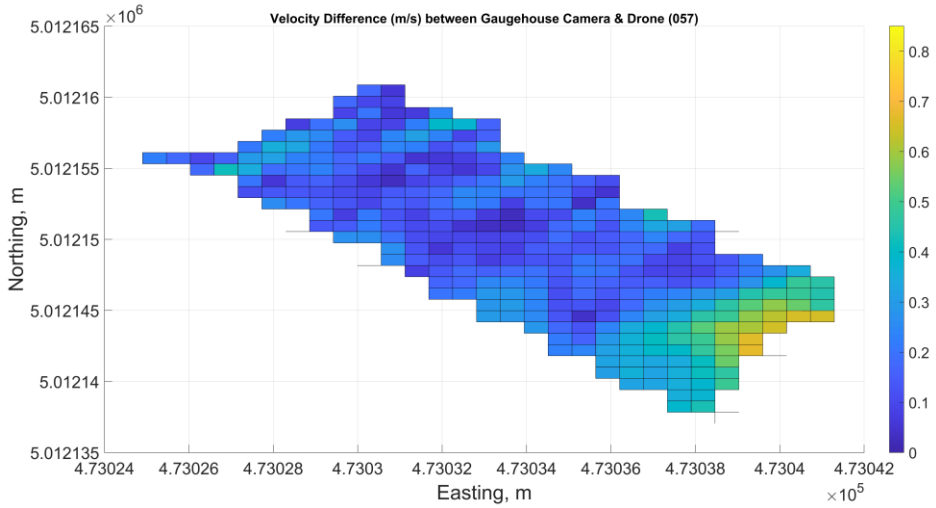
Velocity Difference (m/s) between Gaugehouse Camera & Drone (057)
×10^6
5.012165
5.01216
5.012155
5.01215
5.012145
5.01214
5.012135
Northing, m
4.73024
4.73026
4.73028
4.7303
4.73032
4.73034
4.73036
4.73038
4.7304
4.73042
×10^5
Easting, m
0.8
0.7
0.6
0.5
0.4
0.3
0.2
0.1
0

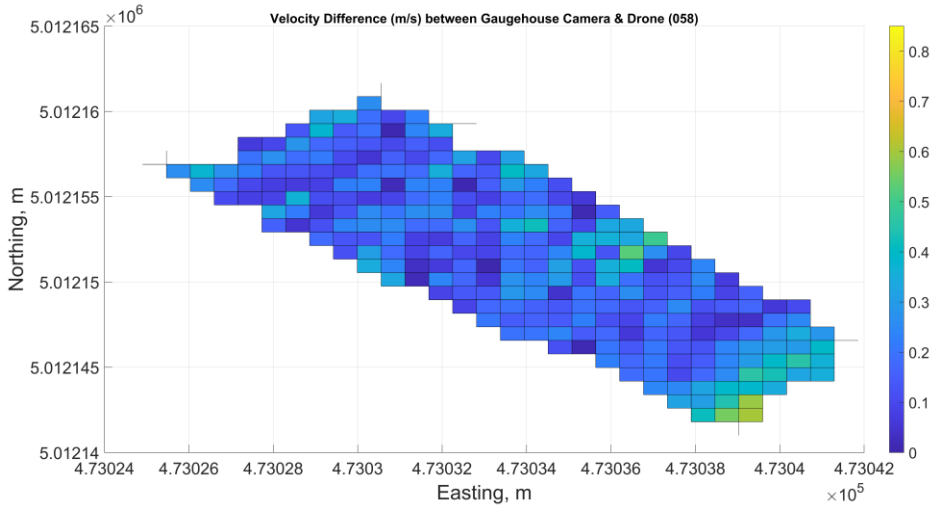
Velocity Difference (m/s) between Gaugehouse Camera & Drone (058)
×10^6
5.012165
5.01216
5.012155
5.01215
5.012145
5.01214
Northing, m
4.73024
4.73026
4.73028
4.7303
4.73032
4.73034
4.73036
4.73038
4.7304
4.73042
×10^5
Easting, m
0.8
0.7
0.6
0.5
0.4
0.3
0.2
0.1
0

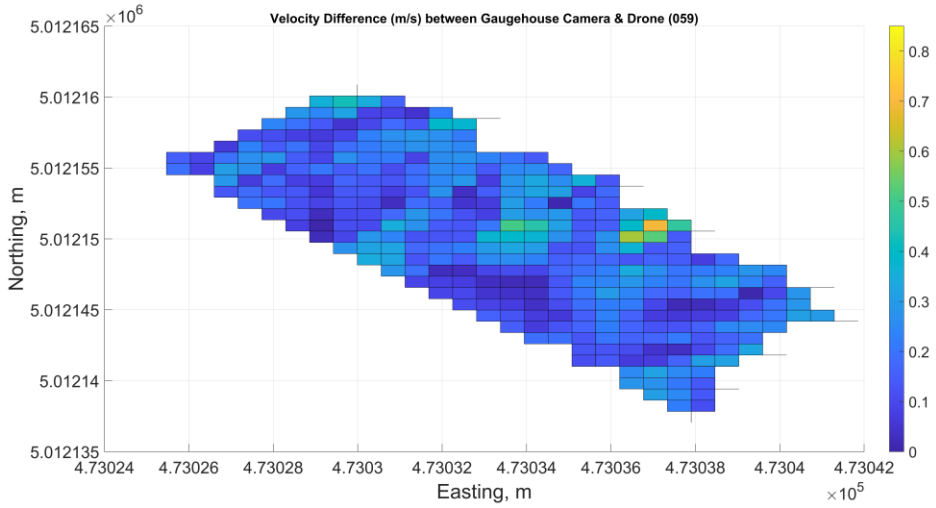
Velocity Difference (m/s) between Gaugehouse Camera & Drone (059)
×10^6
5.012165
5.01216
5.012155
5.01215
5.012145
5.01214
5.012135
Northing, m
4.73024
4.73026
4.73028
4.7303
4.73032
4.73034
4.73036
4.73038
4.7304
4.73042
×10^5
Easting, m
0.8
0.7
0.6
0.5
0.4
0.3
0.2
0.1
0

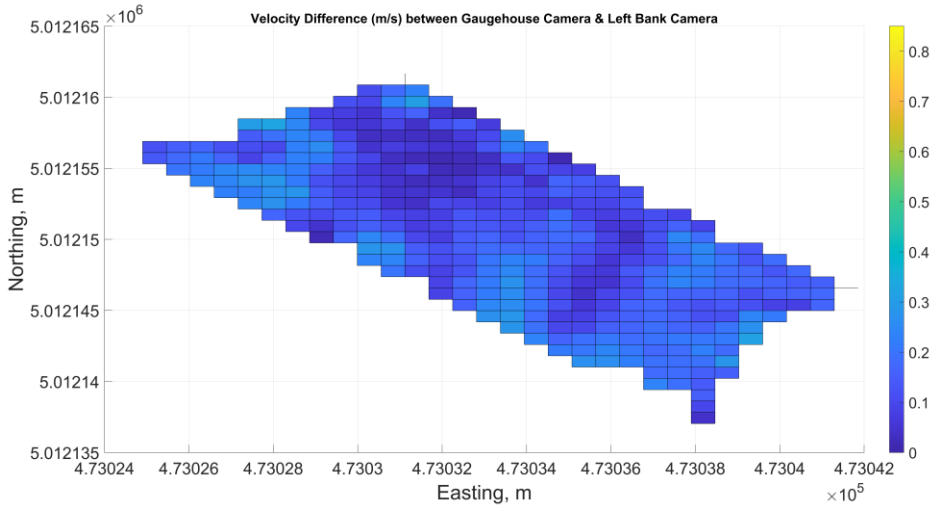
Velocity Difference (m/s) between Gaugehouse Camera & Left Bank Camera
×10^6
5.012165
5.01216
5.012155
5.01215
5.012145
5.01214
5.012135
Northing, m
4.73024
4.73026
4.73028
4.7303
4.73032
4.73034
4.73036
4.73038
4.7304
4.73042
Easting, m
×10^5
0.8
0.7
0.6
0.5
0.4
0.3
0.2
0.1
0

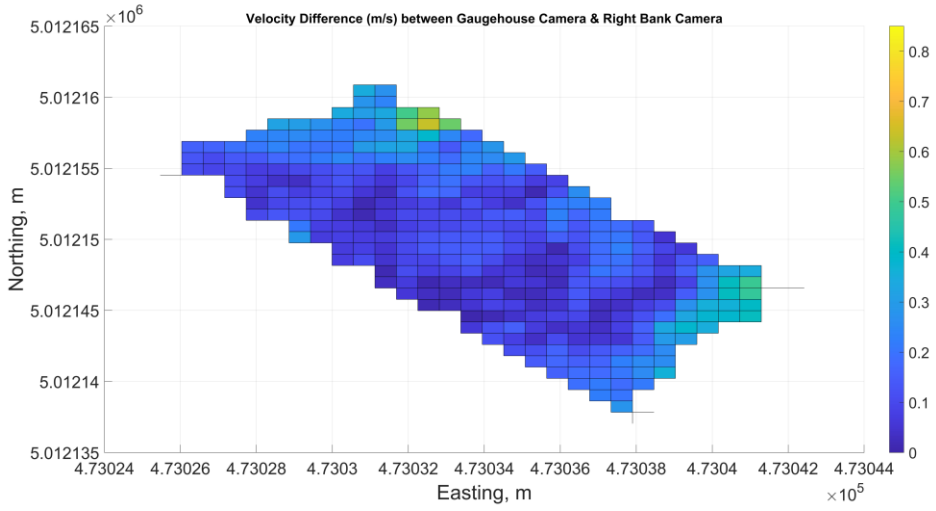
Velocity Difference (m/s) between Gaugehouse Camera & Right Bank Camera
×10^6
5.012165
5.01216
5.012155
5.01215
5.012145
5.01214
5.012135
Northing, m
4.73024
4.73026
4.73028
4.7303
4.73032
4.73034
4.73036
4.73038
4.7304
4.73042
4.73044
Easting, m
×10^5
0.8
0.7
0.6
0.5
0.4
0.3
0.2
0.1
0

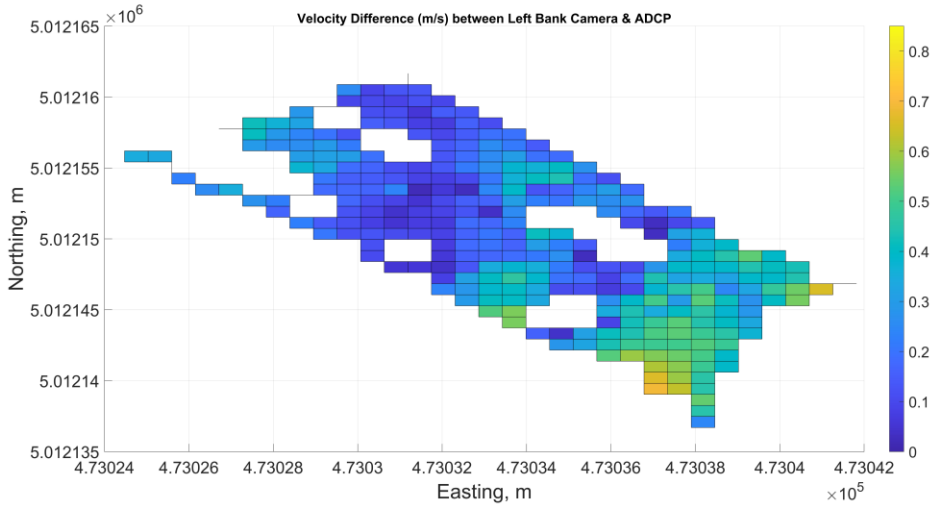
Velocity Difference (m/s) between Left Bank Camera & ADCP
×10^6
5.012165
5.01216
5.012155
5.01215
5.012145
5.01214
5.012135
Northing, m
4.73024
4.73026
4.73028
4.7303
4.73032
4.73034
4.73036
4.73038
4.7304
4.73042
Easting, m
×10^5
0.8
0.7
0.6
0.5
0.4
0.3
0.2
0.1
0

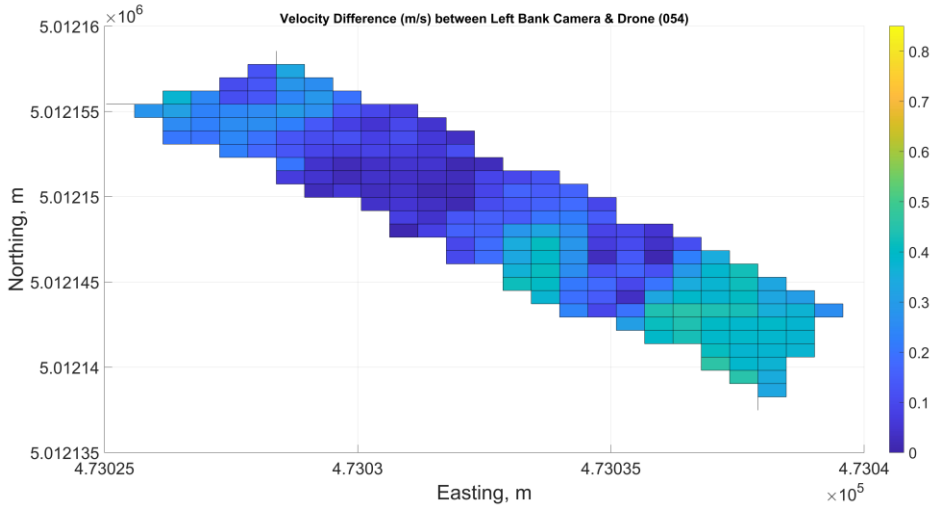
Velocity Difference (m/s) between Left Bank Camera & Drone (054)
×10^6
5.01216
5.012155
5.01215
5.012145
5.01214
5.012135
Northing, m
4.73025
4.7303
4.73035
4.7304
Easting, m
×10^5
0.8
0.7
0.6
0.5
0.4
0.3
0.2
0.1
0

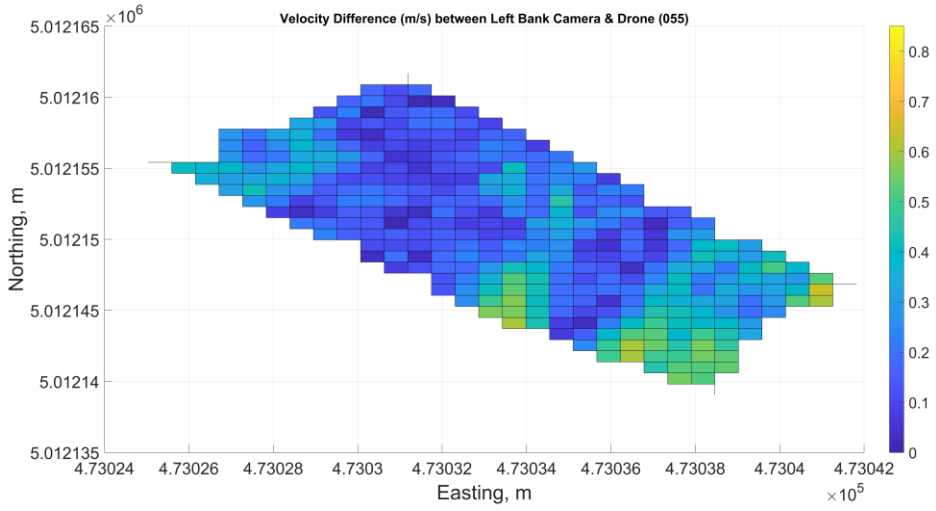
Velocity Difference (m/s) between Left Bank Camera & Drone (055)
×10^6
5.012165
5.01216
5.012155
5.01215
5.012145
5.01214
5.012135
Northing, m
4.73024
4.73026
4.73028
4.7303
4.73032
4.73034
4.73036
4.73038
4.7304
4.73042
Easting, m
×10^5
0.8
0.7
0.6
0.5
0.4
0.3
0.2
0.1
0

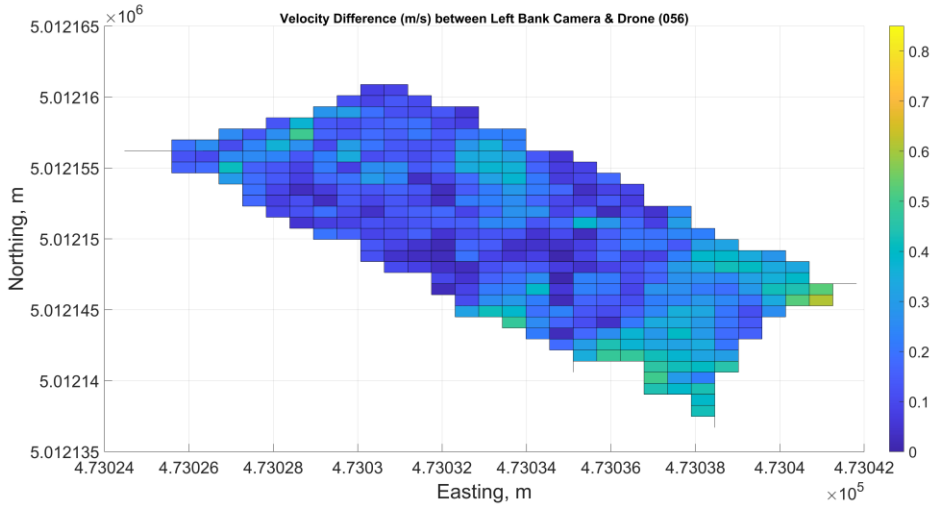
Velocity Difference (m/s) between Left Bank Camera & Drone (056)
×10^6
5.012165
5.01216
5.012155
5.01215
5.012145
5.01214
5.012135
Northing, m
4.73024
4.73026
4.73028
4.7303
4.73032
4.73034
4.73036
4.73038
4.7304
4.73042
Easting, m
×10^5
0.8
0.7
0.6
0.5
0.4
0.3
0.2
0.1
0

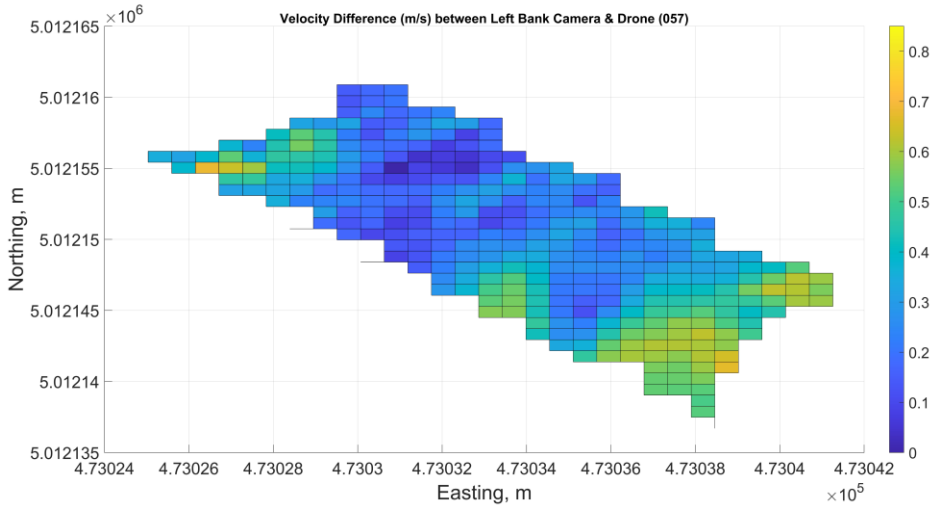
Velocity Difference (m/s) between Left Bank Camera & Drone (057)
×10^6
5.012165
5.01216
5.012155
5.01215
5.012145
5.01214
5.012135
Northing, m
4.73024
4.73026
4.73028
4.7303
4.73032
4.73034
4.73036
4.73038
4.7304
4.73042
×10^5
Easting, m
0.8
0.7
0.6
0.5
0.4
0.3
0.2
0.1
0

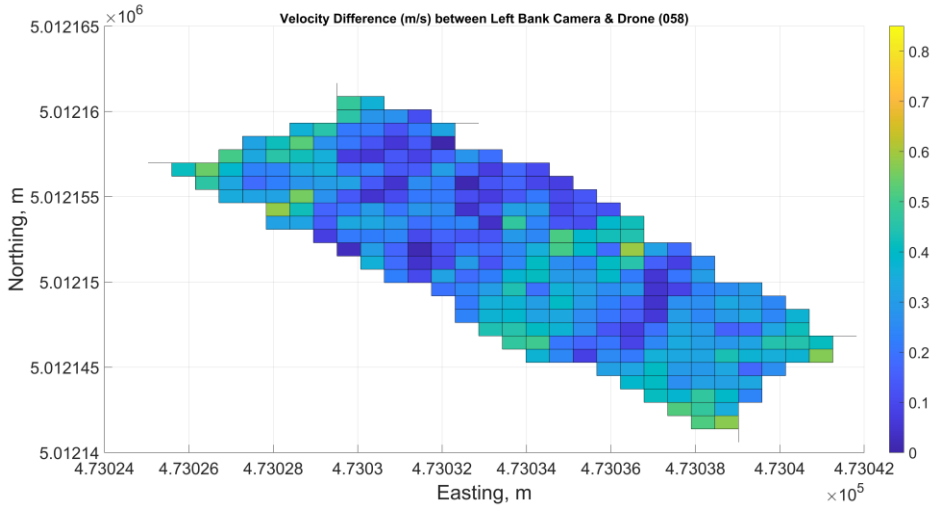
Velocity Difference (m/s) between Left Bank Camera & Drone (058)
×10^6
5.012165
5.01216
5.012155
5.01215
5.012145
5.01214
Northing, m
4.73024
4.73026
4.73028
4.7303
4.73032
4.73034
4.73036
4.73038
4.7304
4.73042
×10^5
Easting, m
0.8
0.7
0.6
0.5
0.4
0.3
0.2
0.1
0

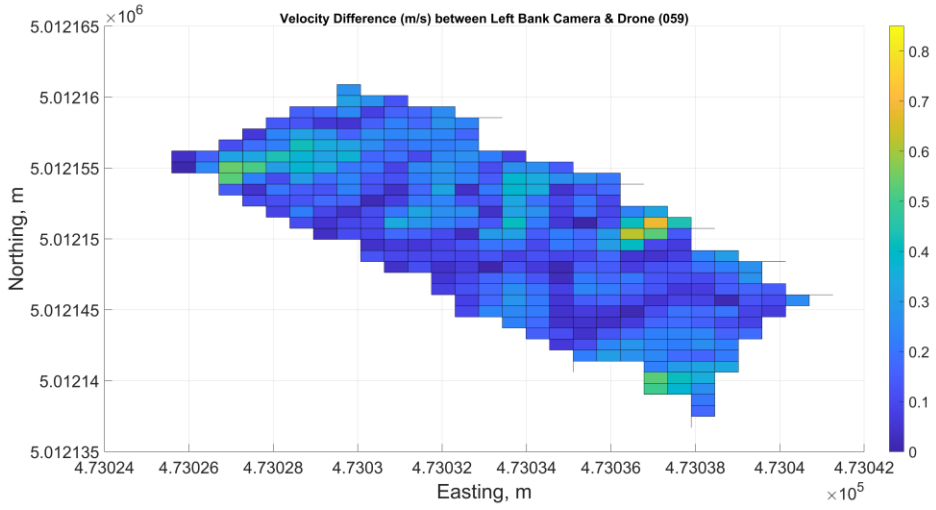
Velocity Difference (m/s) between Left Bank Camera & Drone (059)
×10^6
5.012165
5.01216
5.012155
5.01215
5.012145
5.01214
5.012135
Northing, m
4.73024
4.73026
4.73028
4.7303
4.73032
4.73034
4.73036
4.73038
4.7304
4.73042
×10^5
Easting, m
0.8
0.7
0.6
0.5
0.4
0.3
0.2
0.1
0

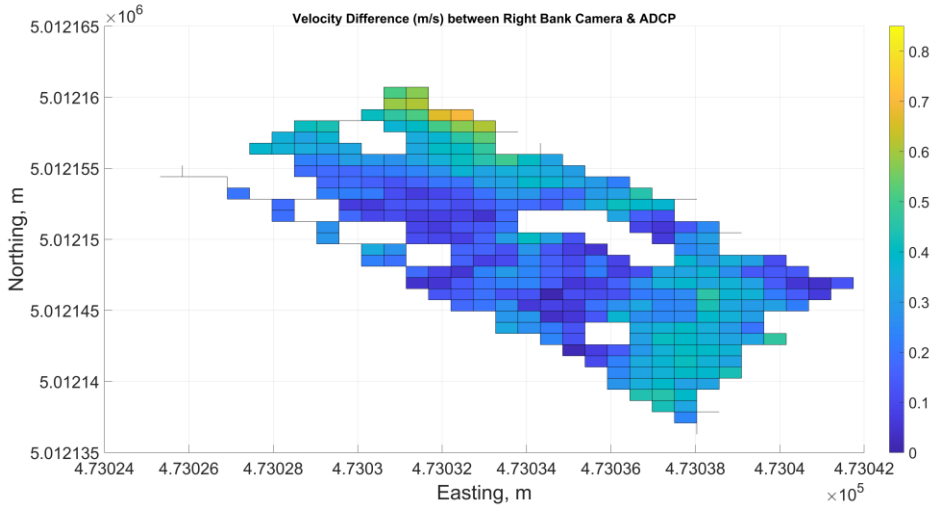
Velocity Difference (m/s) between Right Bank Camera & ADCP
×10^6
5.012165
5.01216
5.012155
5.01215
5.012145
5.01214
5.012135
Northing, m
4.73024
4.73026
4.73028
4.7303
4.73032
4.73034
4.73036
4.73038
4.7304
4.73042
×10^5
Easting, m
0.8
0.7
0.6
0.5
0.4
0.3
0.2
0.1
0

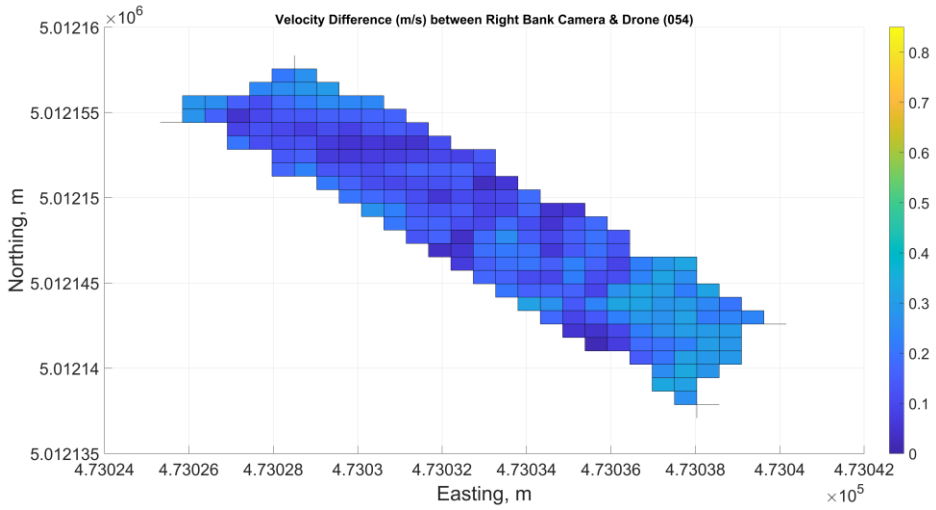
Velocity Difference (m/s) between Right Bank Camera & Drone (054)
×10^6
5.01216
5.012155
5.01215
5.012145
5.01214
5.012135
Northing, m
4.73024
4.73026
4.73028
4.7303
4.73032
4.73034
4.73036
4.73038
4.7304
4.73042
×10^5
Easting, m
0.8
0.7
0.6
0.5
0.4
0.3
0.2
0.1
0

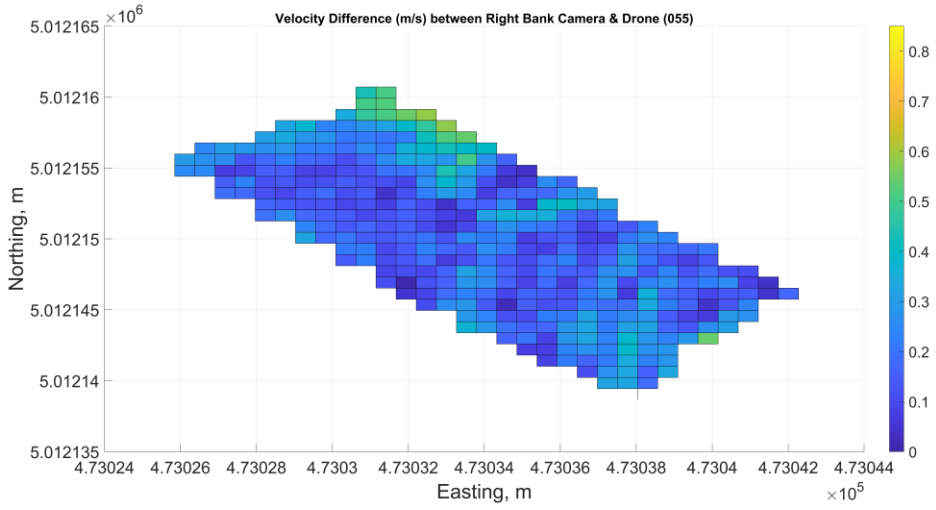
Velocity Difference (m/s) between Right Bank Camera & Drone (055)
×10^6
5.012165
5.01216
5.012155
5.01215
5.012145
5.01214
5.012135
Northing, m
4.73024
4.73026
4.73028
4.7303
4.73032
4.73034
4.73036
4.73038
4.7304
4.73042
4.73044
×10^5
Easting, m
0.8
0.7
0.6
0.5
0.4
0.3
0.2
0.1
0

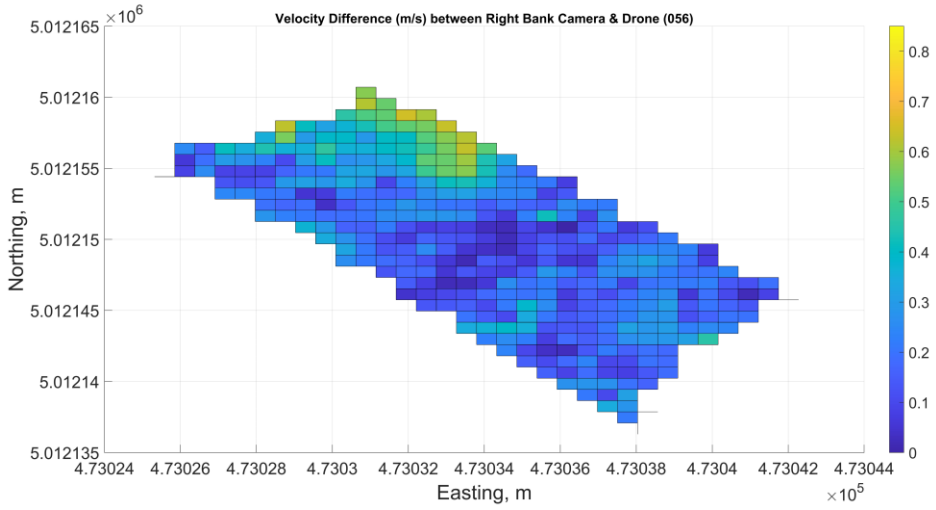
Velocity Difference (m/s) between Right Bank Camera & Drone (056)
×10^6
5.012165
5.01216
5.012155
5.01215
5.012145
5.01214
5.012135
Northing, m
4.73024
4.73026
4.73028
4.7303
4.73032
4.73034
4.73036
4.73038
4.7304
4.73042
4.73044
×10^5
Easting, m
0.8
0.7
0.6
0.5
0.4
0.3
0.2
0.1
0

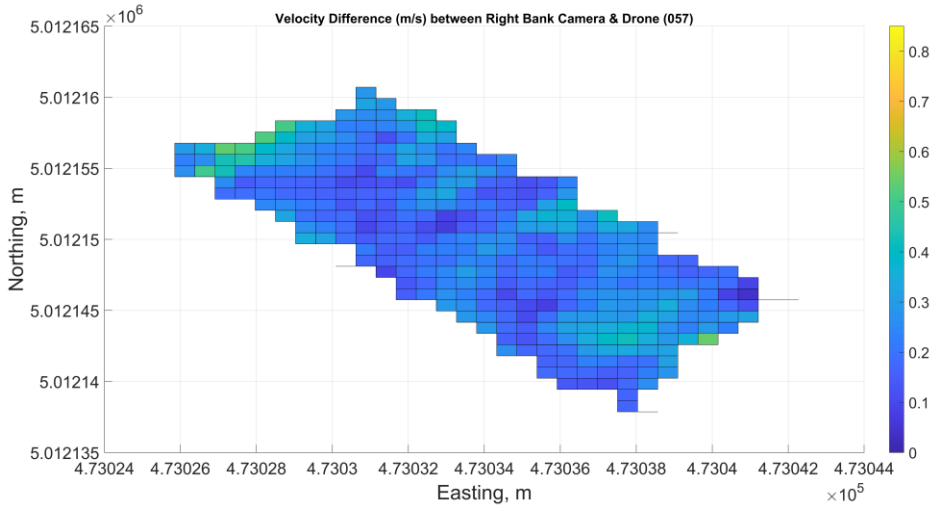
Velocity Difference (m/s) between Right Bank Camera & Drone (057)
×10^6
5.012165
5.01216
5.012155
5.01215
5.012145
5.01214
5.012135
Northing, m
4.73024
4.73026
4.73028
4.7303
4.73032
4.73034
4.73036
4.73038
4.7304
4.73042
4.73044
×10^5
Easting, m
0.8
0.7
0.6
0.5
0.4
0.3
0.2
0.1
0

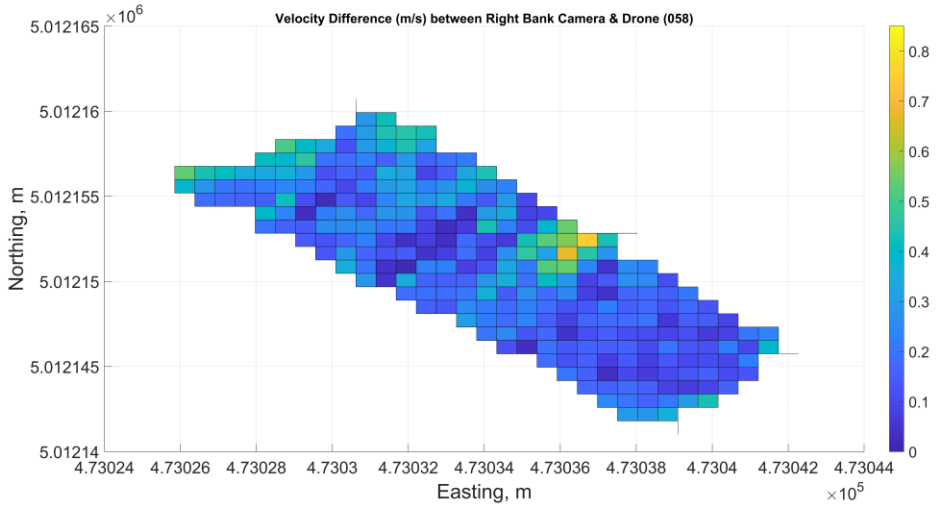
Velocity Difference (m/s) between Right Bank Camera & Drone (058)
×10^6
5.012165
5.01216
5.012155
5.01215
5.012145
5.01214
Northing, m
4.73024
4.73026
4.73028
4.7303
4.73032
4.73034
4.73036
4.73038
4.7304
4.73042
4.73044
×10^5
Easting, m
0.8
0.7
0.6
0.5
0.4
0.3
0.2
0.1
0

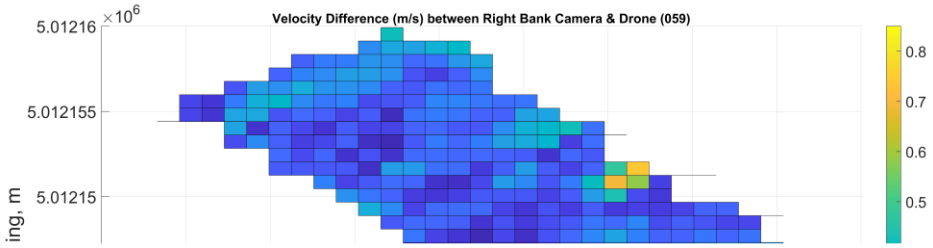
Velocity Difference (m/s) between Right Bank Camera & Drone (059)
×10^6
5.01216
5.012155
5.01215
ing, m
0.8
0.7
0.6
0.5

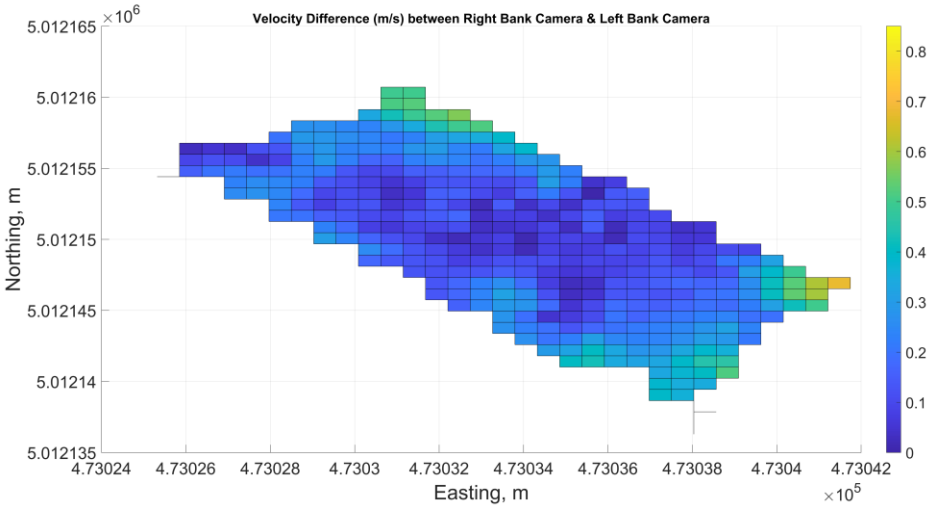
Velocity Difference (m/s) between Right Bank Camera & Left Bank Camera
×10^6
5.012165
5.01216
5.012155
5.01215
5.012145
5.01214
5.012135
Northing, m
4.73024
4.73026
4.73028
4.7303
4.73032
4.73034
4.73036
4.73038
4.7304
4.73042
Easting, m
×10^5
0.8
0.7
0.6
0.5
0.4
0.3
0.2
0.1
0

Appendix C – Normalized Velocity Difference Plots

This section contains all of the normalized velocity difference plots that were scaled by finding the average surface velocity from the ADCP or gauge station data.

March 18th, 2022

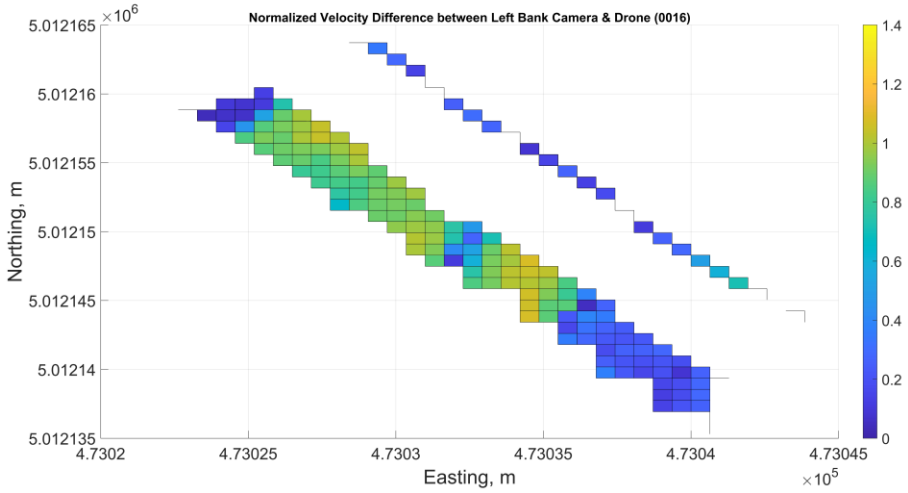

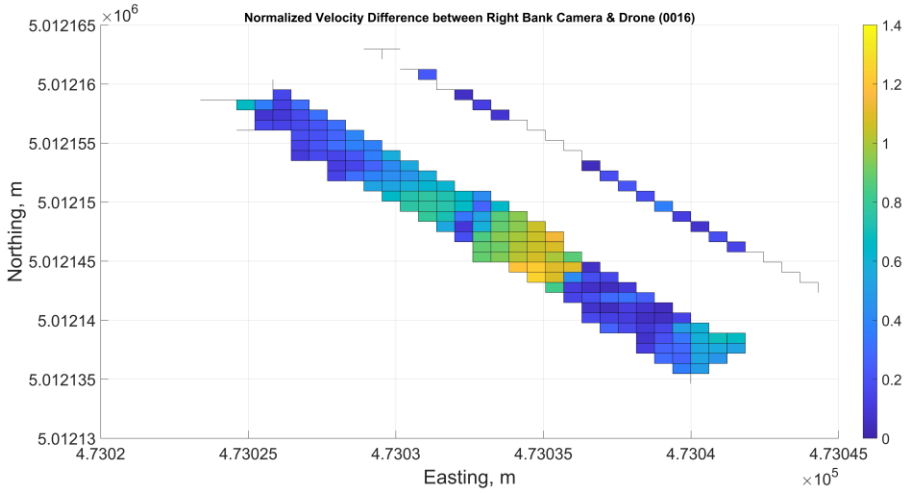

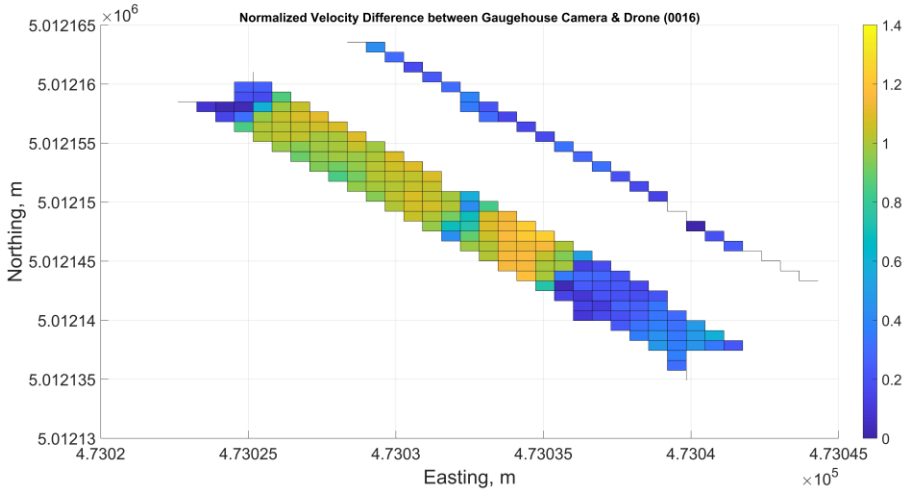

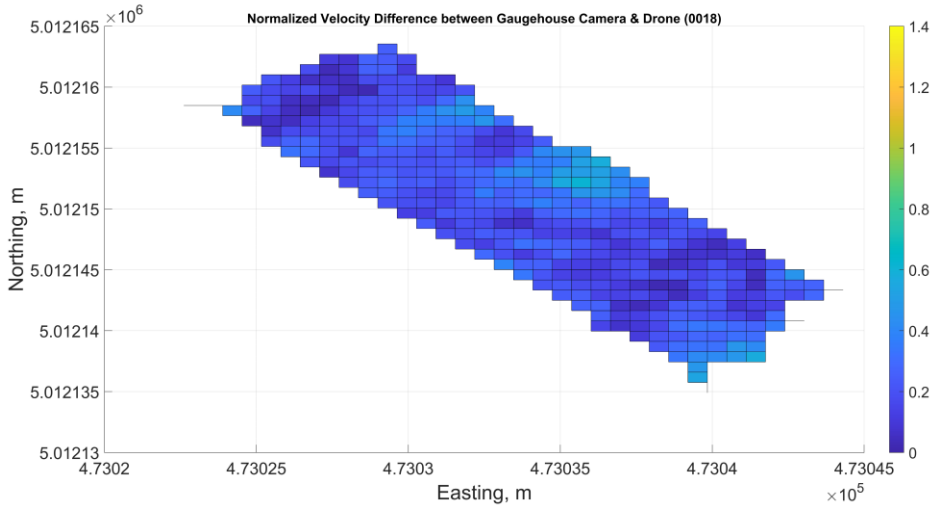

March 21st, 2022

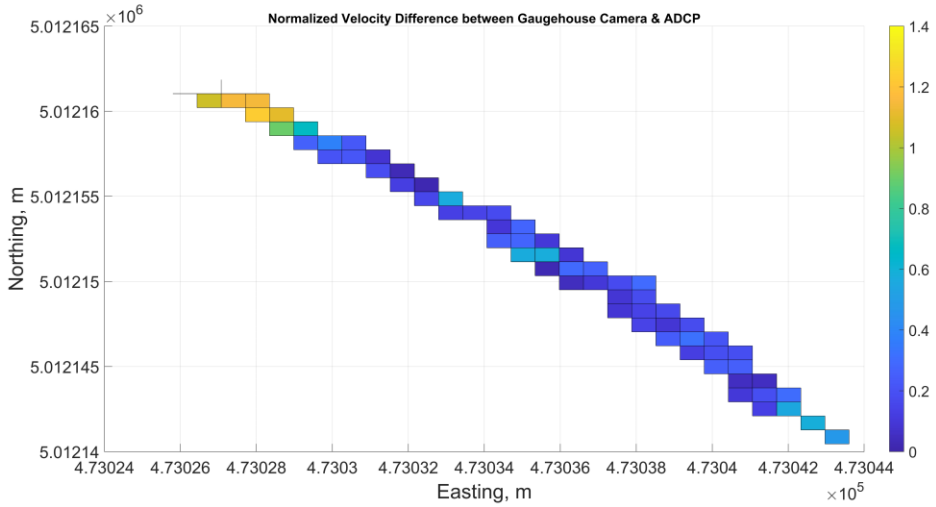

April 8th, 2022

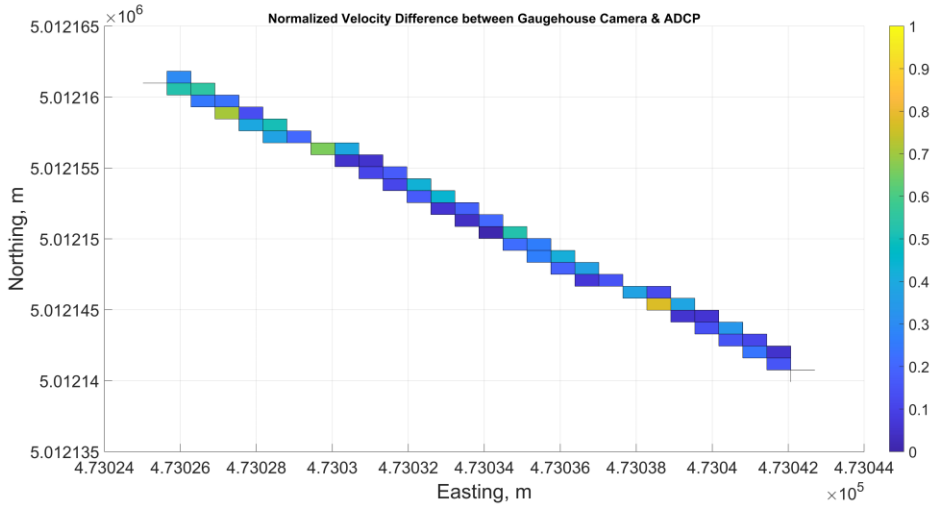

May 5th, 2022

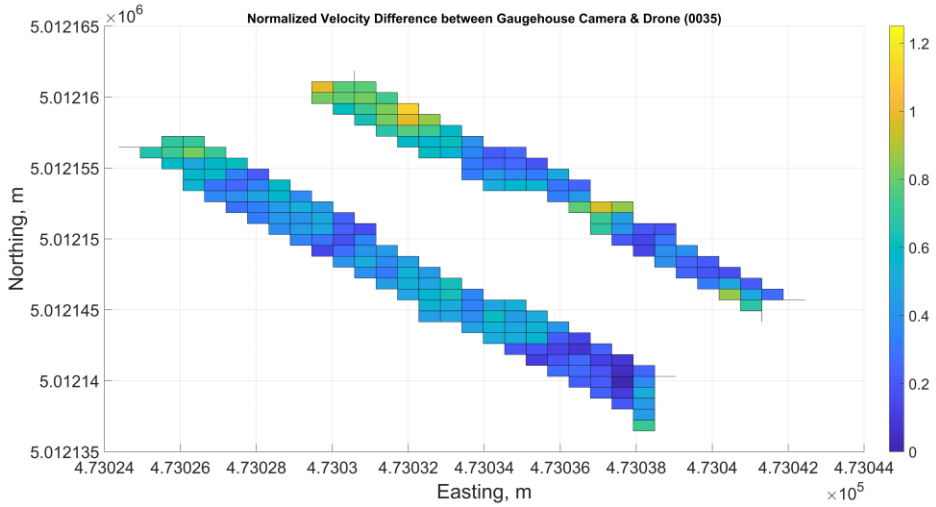

March 6th, 2024

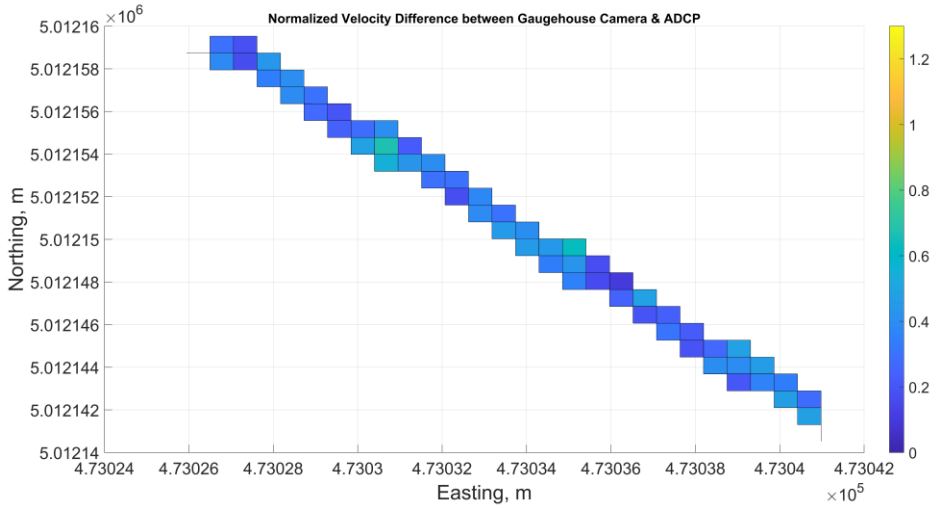

May 15th, 2024

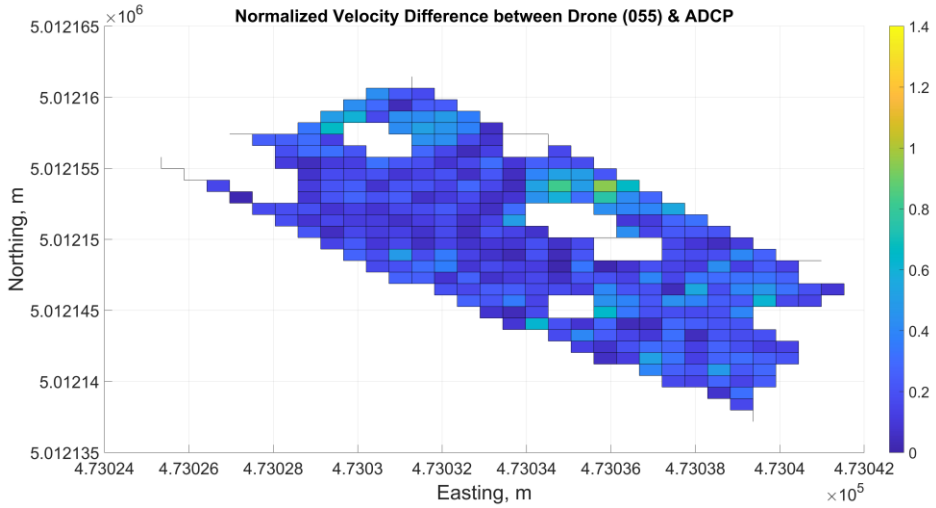

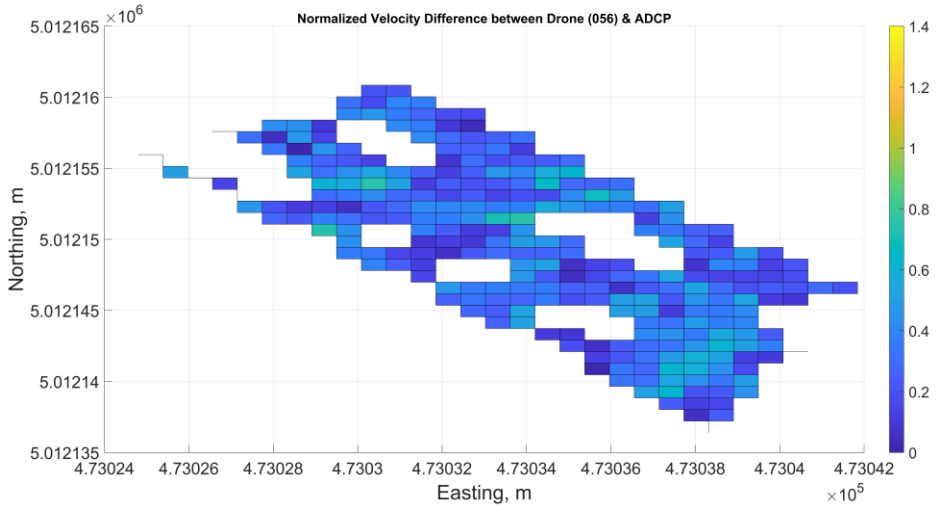
Normalized Velocity Difference between Drone (056) & ADCP
×10^6
5.012165
5.01216
5.012155
5.01215
5.012145
5.01214
5.012135
Northing, m
4.73024
4.73026
4.73028
4.7303
4.73032
4.73034
4.73036
4.73038
4.7304
4.73042
×10^5
Easting, m
1.4
1.2
1
0.8
0.6
0.4
0.2
0

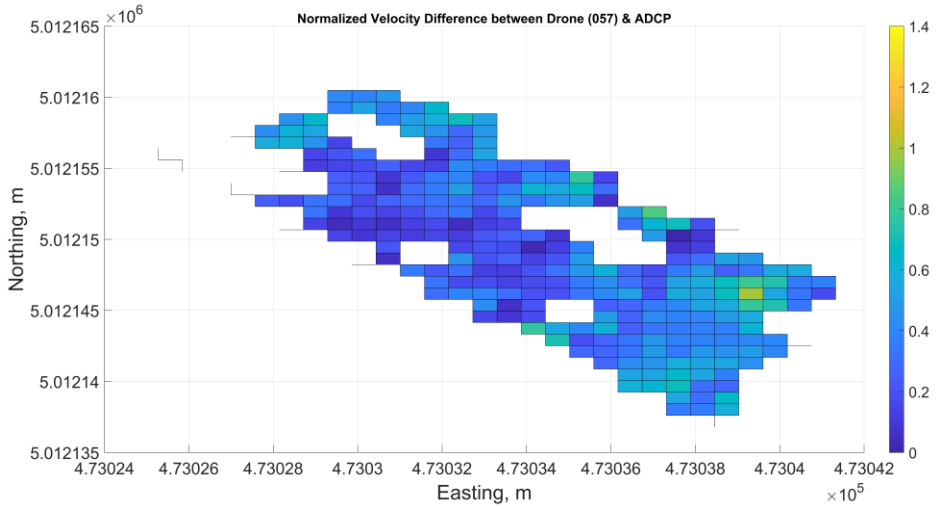
Normalized Velocity Difference between Drone (057) & ADCP
×10^6
5.012165
5.01216
5.012155
5.01215
5.012145
5.01214
5.012135
Northing, m
4.73024
4.73026
4.73028
4.7303
4.73032
4.73034
4.73036
4.73038
4.7304
4.73042
×10^5
Easting, m
1.4
1.2
1
0.8
0.6
0.4
0.2
0

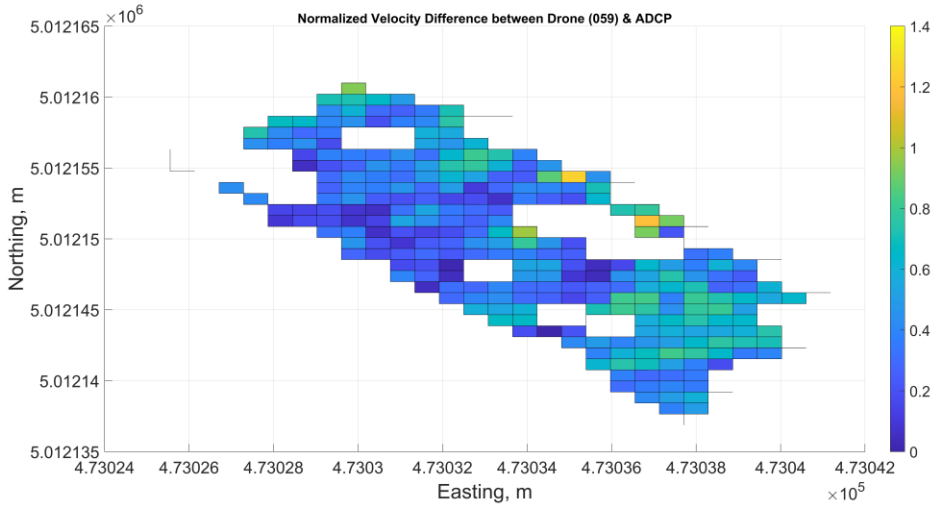
Normalized Velocity Difference between Drone (059) & ADCP
×10^6
5.012165
5.01216
5.012155
5.01215
5.012145
5.01214
5.012135
Northing, m
4.73024
4.73026
4.73028
4.7303
4.73032
4.73034
4.73036
4.73038
4.7304
4.73042
×10^5
Easting, m
1.4
1.2
1
0.8
0.6
0.4
0.2
0

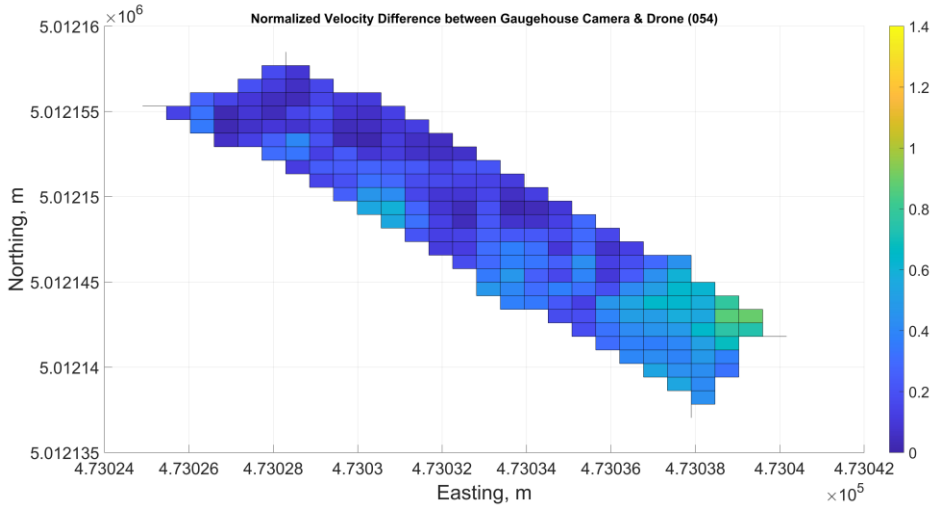
Normalized Velocity Difference between Gaugehouse Camera & Drone (054)
×10^6
5.01216
5.012155
5.01215
5.012145
5.01214
5.012135
Northing, m
4.73024
4.73026
4.73028
4.7303
4.73032
4.73034
4.73036
4.73038
4.7304
4.73042
×10^5
Easting, m
1.4
1.2
1
0.8
0.6
0.4
0.2
0

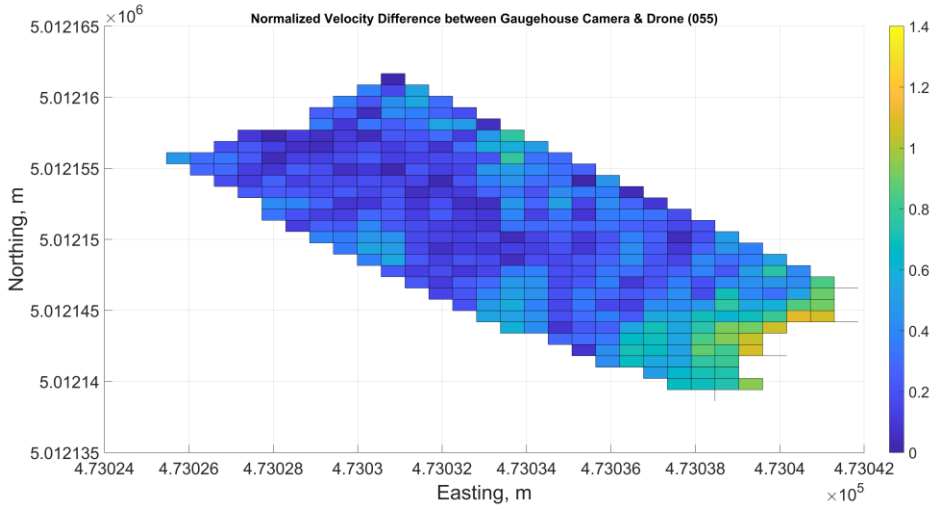
Normalized Velocity Difference between Gaugehouse Camera & Drone (055)
×10^6
5.012165
5.01216
5.012155
5.01215
5.012145
5.01214
5.012135
Northing, m
4.73024
4.73026
4.73028
4.7303
4.73032
4.73034
4.73036
4.73038
4.7304
4.73042
×10^5
Easting, m
1.4
1.2
1
0.8
0.6
0.4
0.2
0

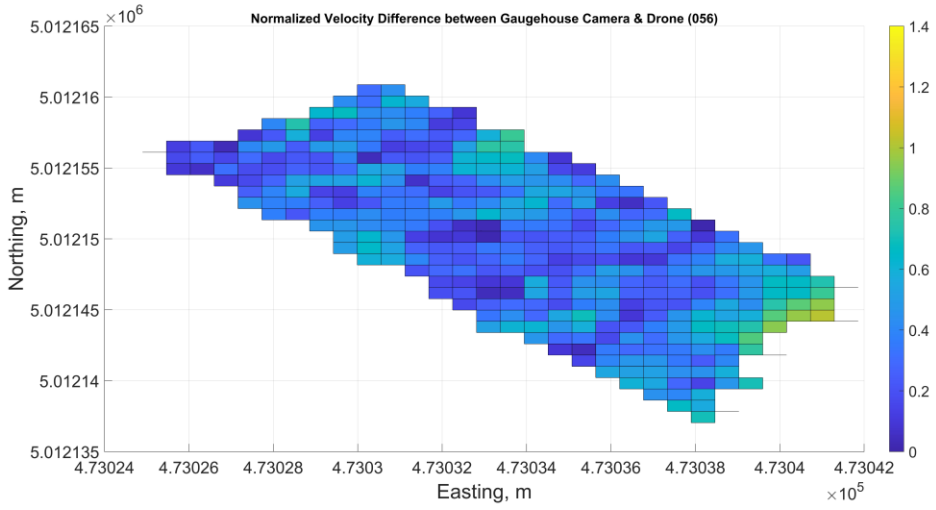
Normalized Velocity Difference between Gaugehouse Camera & Drone (056)
×10^6
5.012165
5.01216
5.012155
5.01215
5.012145
5.01214
5.012135
Northing, m
4.73024
4.73026
4.73028
4.7303
4.73032
4.73034
4.73036
4.73038
4.7304
4.73042
×10^5
Easting, m
1.4
1.2
1
0.8
0.6
0.4
0.2
0

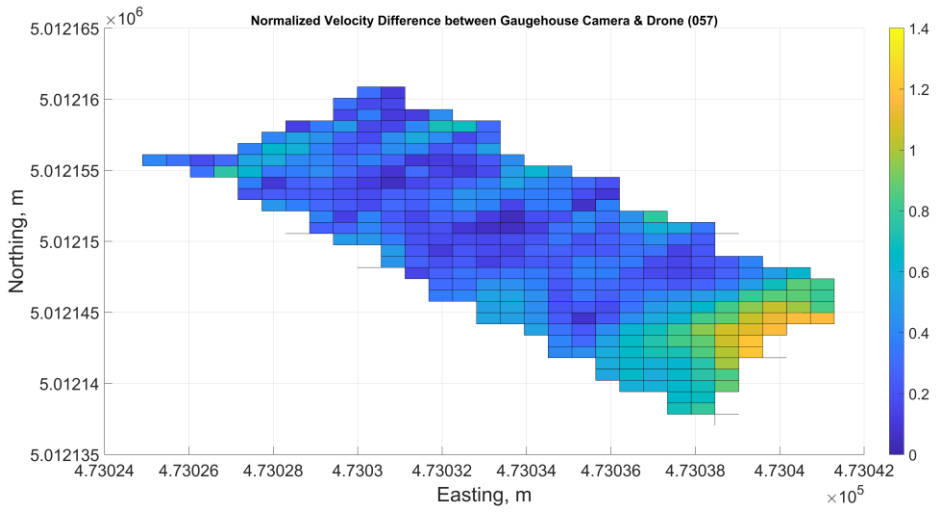
Normalized Velocity Difference between Gaugehouse Camera & Drone (057)
×10^6
5.012165
5.01216
5.012155
5.01215
5.012145
5.01214
5.012135
Northing, m
4.73024
4.73026
4.73028
4.7303
4.73032
4.73034
4.73036
4.73038
4.7304
4.73042
×10^5
Easting, m
1.4
1.2
1
0.8
0.6
0.4
0.2
0

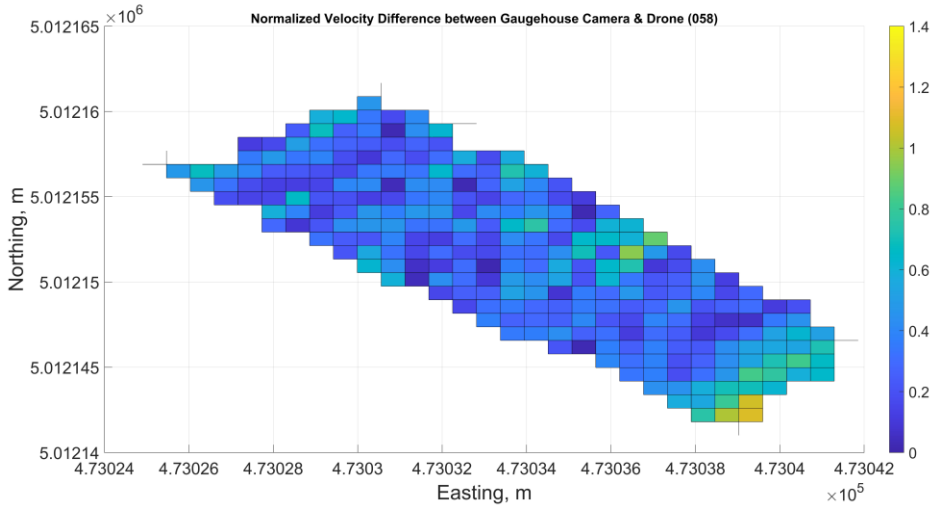
Normalized Velocity Difference between Gaugehouse Camera & Drone (058)
×10^6
5.012165
5.01216
5.012155
5.01215
5.012145
5.01214
Northing, m
4.73024
4.73026
4.73028
4.7303
4.73032
4.73034
4.73036
4.73038
4.7304
4.73042
×10^5
Easting, m
1.4
1.2
1
0.8
0.6
0.4
0.2
0

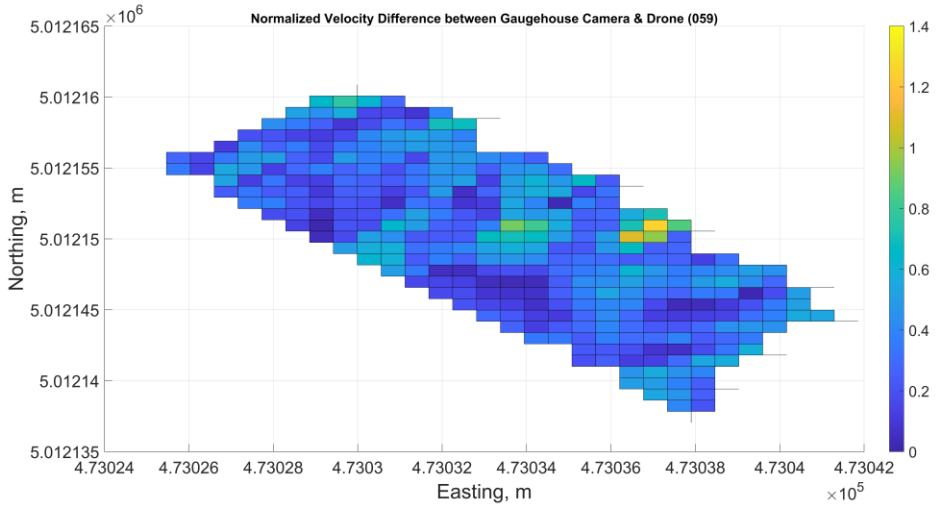
Normalized Velocity Difference between Gaugehouse Camera & Drone (059)
×10^6
5.012165
5.01216
5.012155
5.01215
5.012145
5.01214
5.012135
Northing, m
4.73024
4.73026
4.73028
4.7303
4.73032
4.73034
4.73036
4.73038
4.7304
4.73042
×10^5
Easting, m
1.4
1.2
1
0.8
0.6
0.4
0.2
0

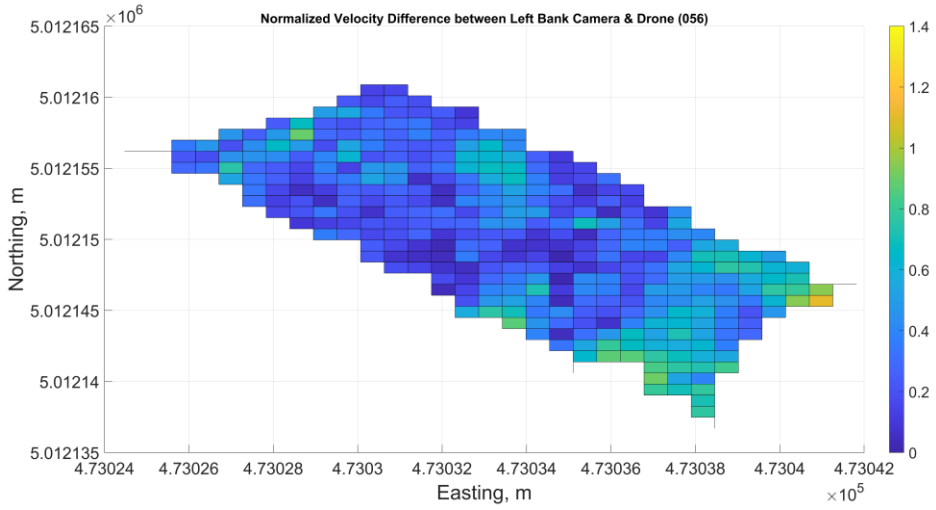
Normalized Velocity Difference between Left Bank Camera & Drone (056)
Northing, m
Easting, m
×10^6
×10^5
5.012165
5.01216
5.012155
5.01215
5.012145
5.01214
5.012135
4.73024
4.73026
4.73028
4.7303
4.73032
4.73034
4.73036
4.73038
4.7304
4.73042
1.4
1.2
1
0.8
0.6
0.4
0.2
0

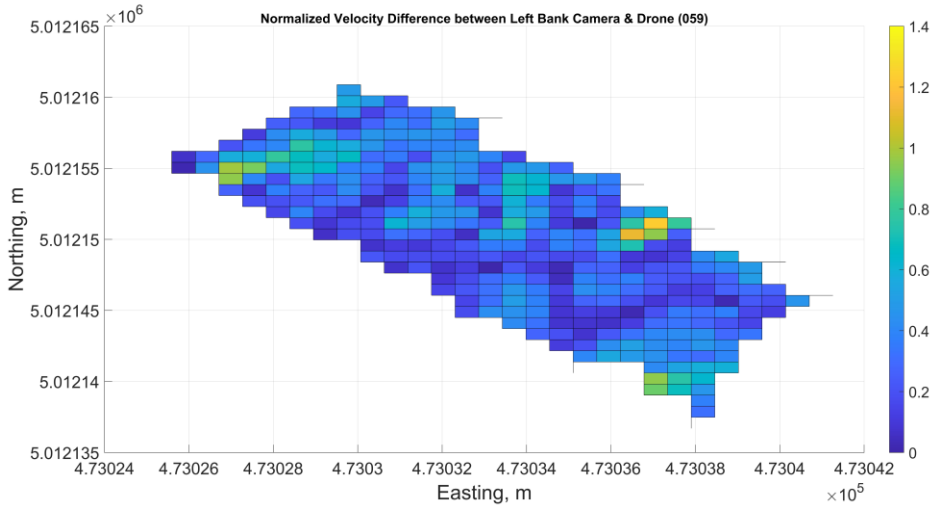
Normalized Velocity Difference between Left Bank Camera & Drone (059)
Northing, m
Easting, m
×10^6
×10^5
5.012165
5.01216
5.012155
5.01215
5.012145
5.01214
5.012135
4.73024
4.73026
4.73028
4.7303
4.73032
4.73034
4.73036
4.73038
4.7304
4.73042
1.4
1.2
1
0.8
0.6
0.4
0.2
0

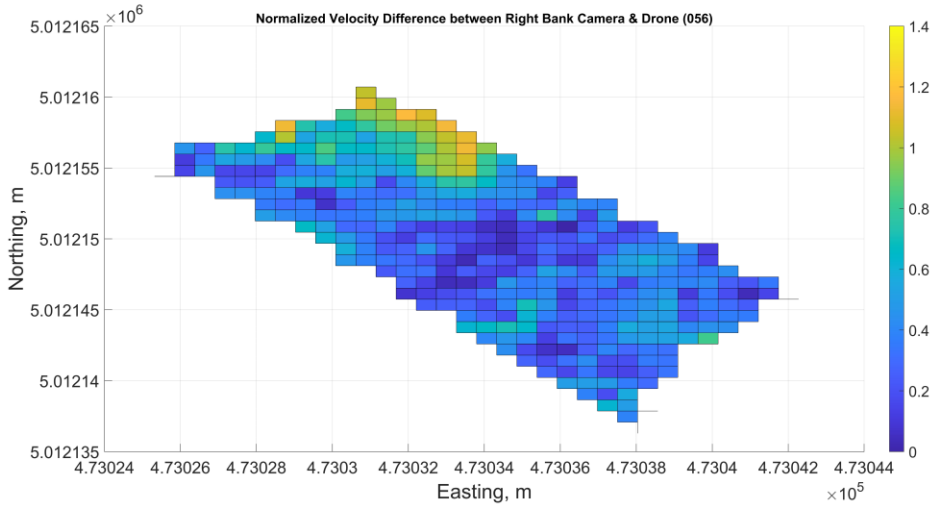
Normalized Velocity Difference between Right Bank Camera & Drone (056)
Northing, m
Easting, m
×10^6
×10^5
5.012165
5.01216
5.012155
5.01215
5.012145
5.01214
5.012135
4.73024
4.73026
4.73028
4.7303
4.73032
4.73034
4.73036
4.73038
4.7304
4.73042
4.73044
1.4
1.2
1
0.8
0.6
0.4
0.2
0

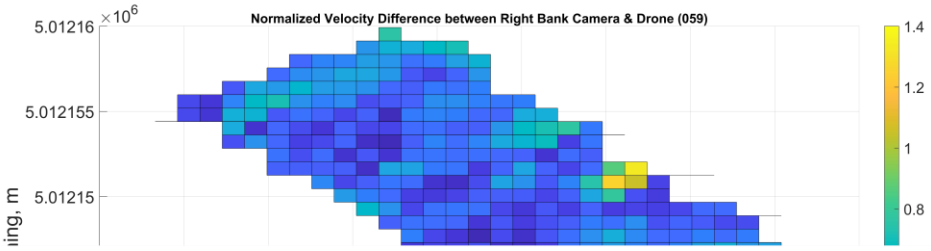
Normalized Velocity Difference between Right Bank Camera & Drone (059)
×10^6
5.01216
5.012155
5.01215
ing, m
1.4
1.2
1
0.8

Appendix D – Velocity Vector Plots

This section contains all of the vector plot comparisons between methods.

March 18th, 2022

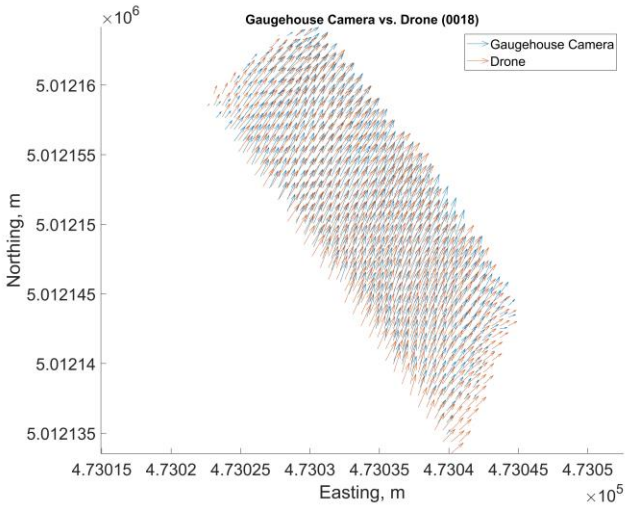

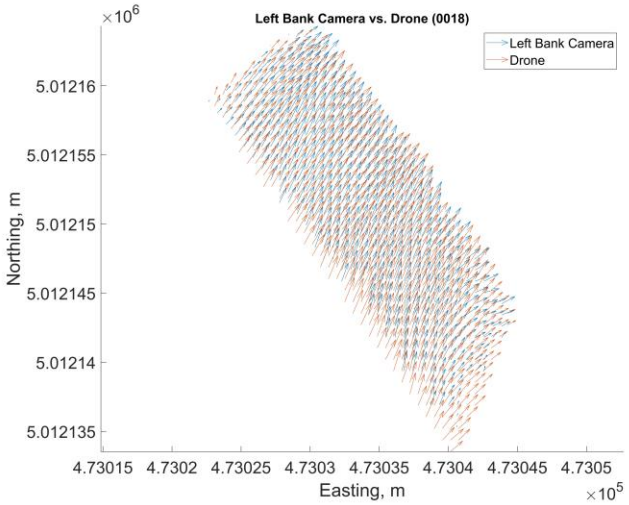

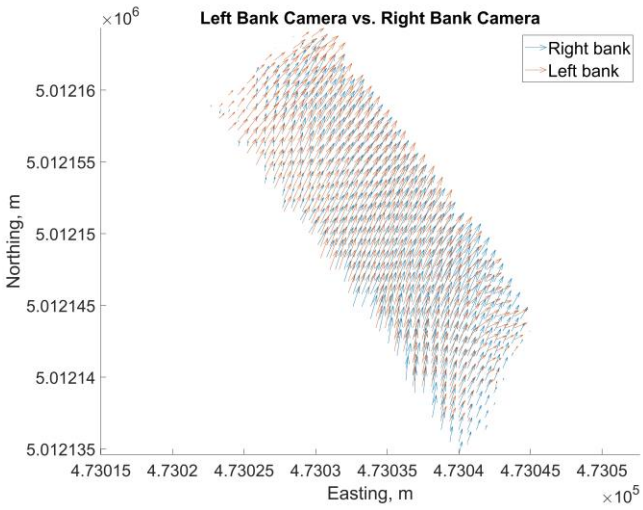
Left Bank Camera vs. Right Bank Camera
Right bank
Left bank
×10^6
5.01216
5.012155
5.01215
5.012145
5.01214
5.012135
Northing, m
4.73015 4.7302 4.73025 4.7303 4.73035 4.7304 4.73045 4.7305
Easting, m
×10^5

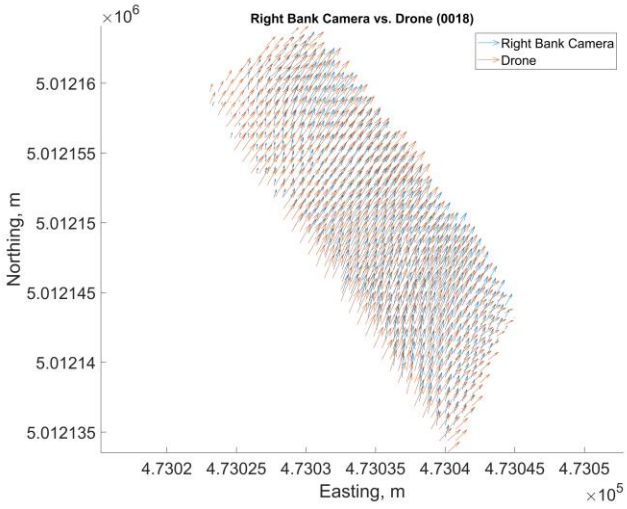
Right Bank Camera vs. Drone (0018)
Right Bank Camera
Drone
×10^6
5.01216
5.012155
5.01215
5.012145
5.01214
5.012135
Northing, m
4.7302 4.73025 4.7303 4.73035 4.7304 4.73045 4.7305
Easting, m
×10^5

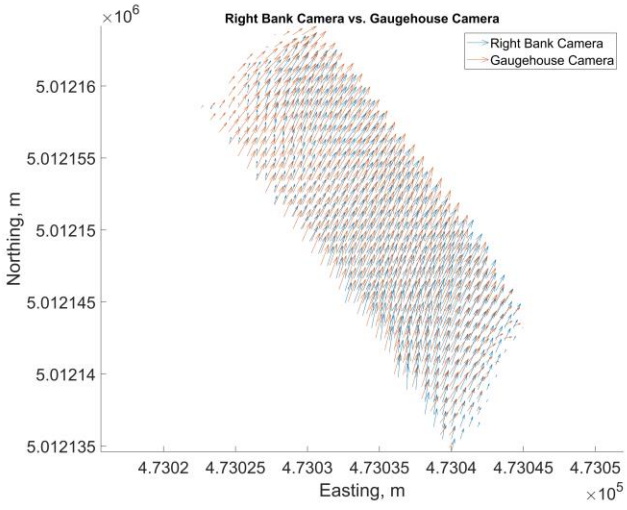
Right Bank Camera vs. Gaugehouse Camera
Right Bank Camera
Gaugehouse Camera
×10^6
5.01216
5.012155
5.01215
5.012145
5.01214
5.012135
Northing, m
4.7302 4.73025 4.7303 4.73035 4.7304 4.73045 4.7305
Easting, m
×10^5

March 21st, 2022

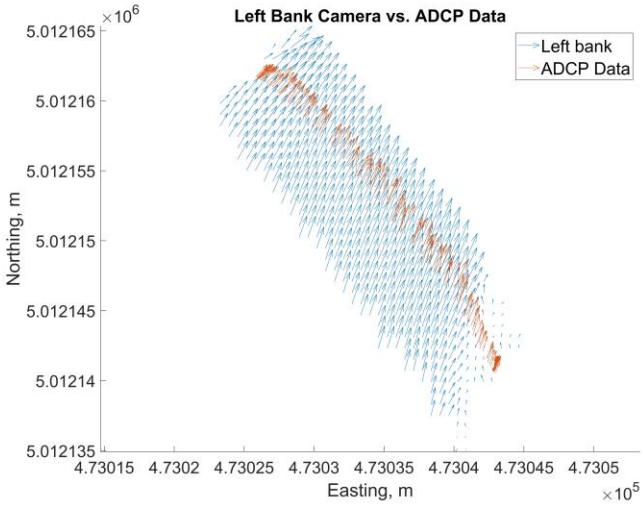

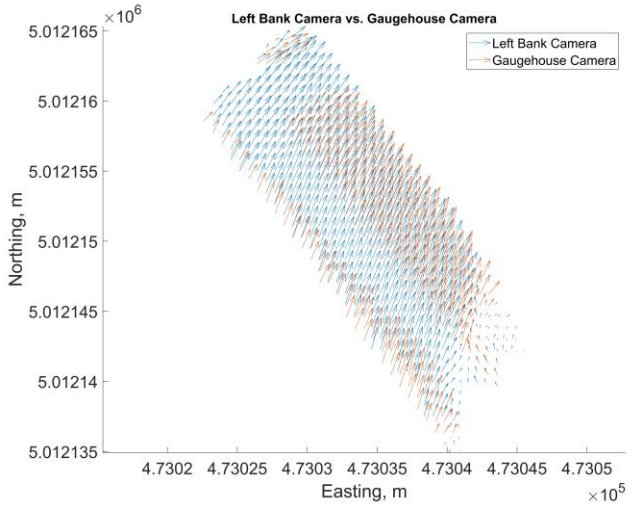

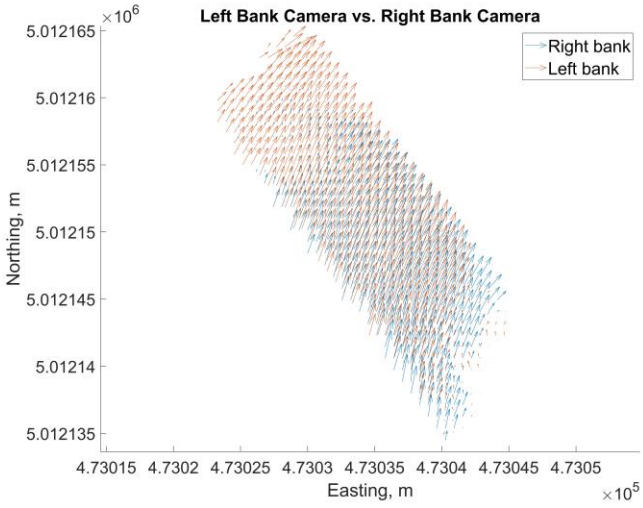

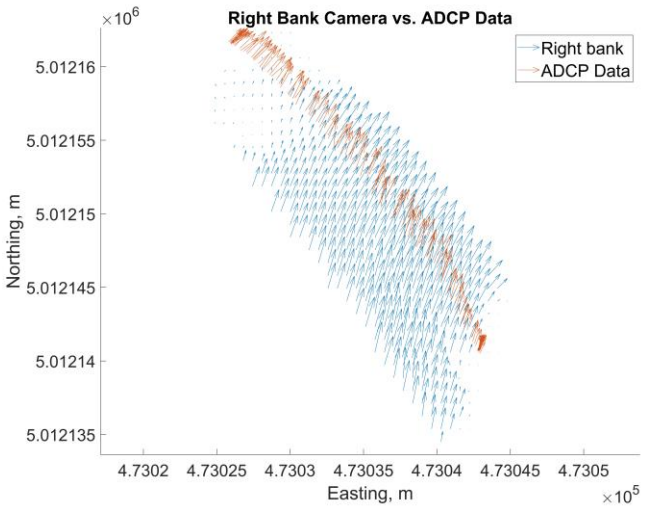

April 8th, 2022

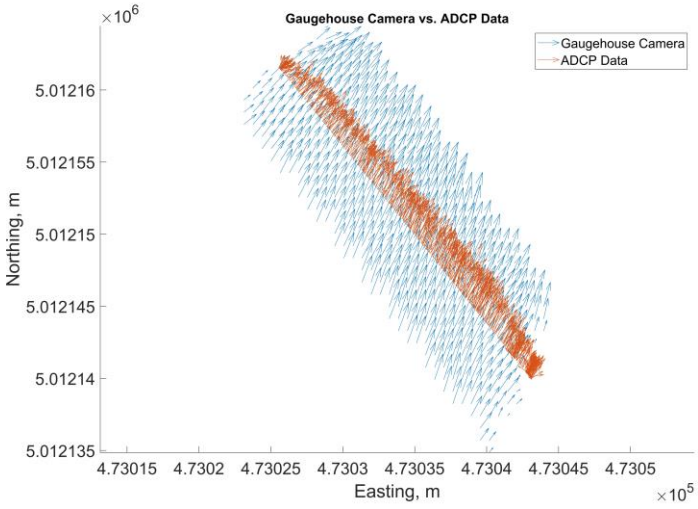

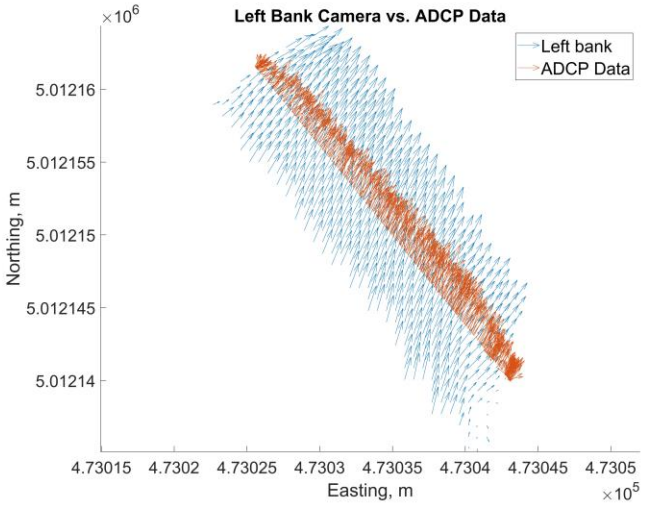

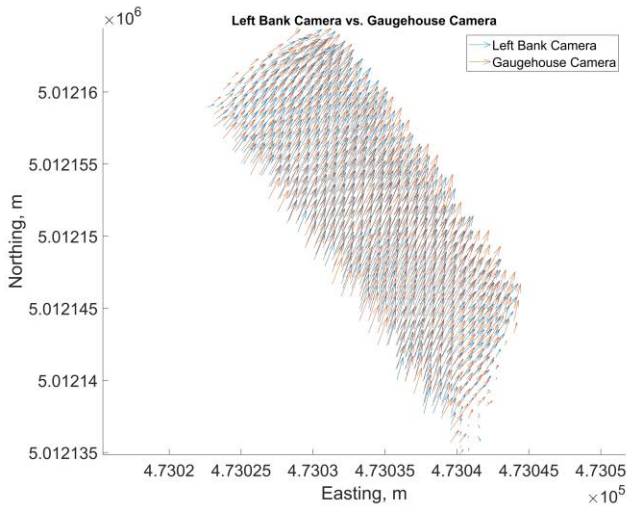
Left Bank Camera vs. Gaugehouse Camera
Left Bank Camera
Gaugehouse Camera
×10^6
5.01216
5.012155
5.01215
5.012145
5.01214
5.012135
Northing, m
4.7302
4.73025
4.7303
4.73035
4.7304
4.73045
4.7305
Easting, m
×10^5

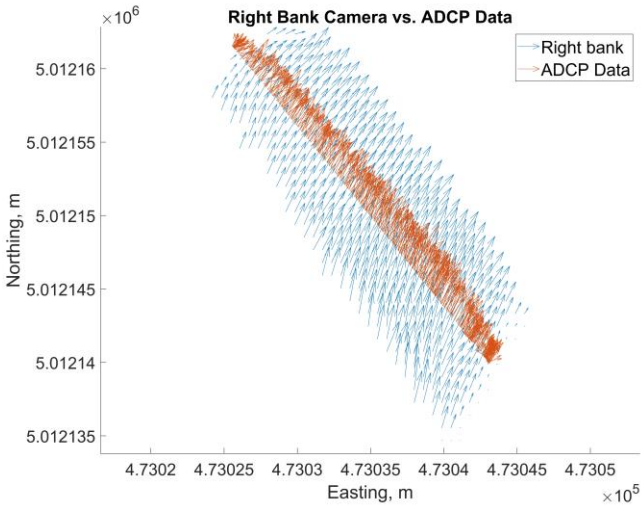
Right Bank Camera vs. ADCP Data
Right bank
ADCP Data
×10^6
5.01216
5.012155
5.01215
5.012145
5.01214
5.012135
Northing, m
4.7302
4.73025
4.7303
4.73035
4.7304
4.73045
4.7305
Easting, m
×10^5

May 5th, 2022

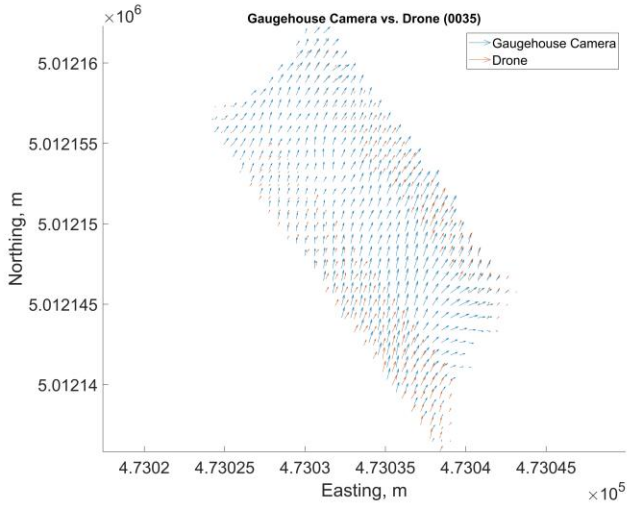
Gaugehouse Camera vs. Drone (0035)
Gaugehouse Camera
Drone
×10^6
5.01216
5.012155
5.01215
5.012145
5.01214
Northing, m
4.7302
4.73025
4.7303
4.73035
4.7304
4.73045
Easting, m
×10^5

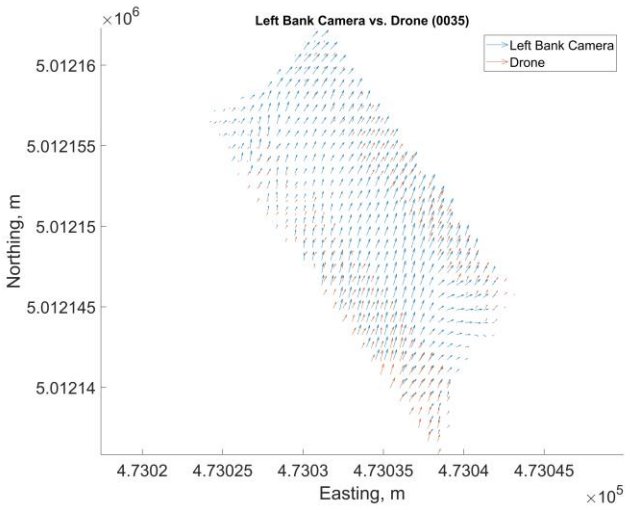
Left Bank Camera vs. Drone (0035)
Left Bank Camera
Drone
×10^6
5.01216
5.012155
5.01215
5.012145
5.01214
Northing, m
4.7302
4.73025
4.7303
4.73035
4.7304
4.73045
Easting, m
×10^5

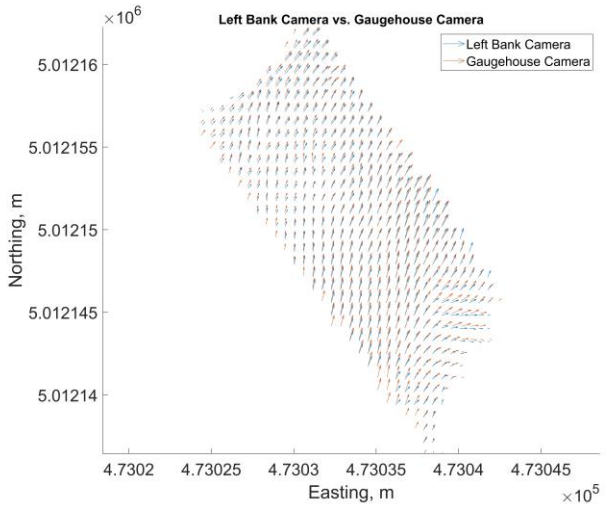
Left Bank Camera vs. Gaugehouse Camera
Left Bank Camera
Gaugehouse Camera
×10^6
5.01216
5.012155
5.01215
5.012145
5.01214
Northing, m
4.7302
4.73025
4.7303
4.73035
4.7304
4.73045
Easting, m
×10^5

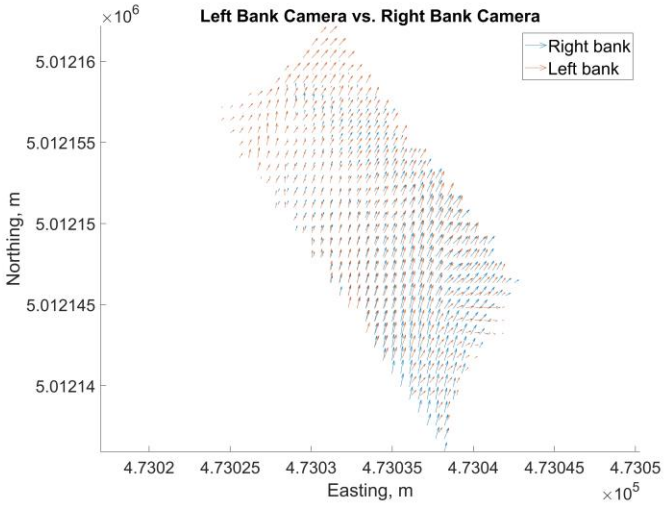
Left Bank Camera vs. Right Bank Camera
Right bank
Left bank
×10^6
5.01216
5.012155
5.01215
5.012145
5.01214
Northing, m
4.7302
4.73025
4.7303
4.73035
4.7304
4.73045
4.7305
Easting, m
×10^5

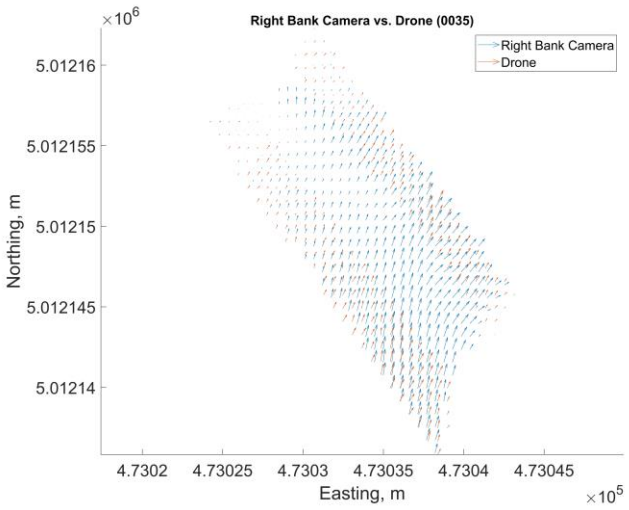
Right Bank Camera vs. Drone (0035)
Right Bank Camera
Drone
×10^6
5.01216
5.012155
5.01215
5.012145
5.01214
Northing, m
4.7302
4.73025
4.7303
4.73035
4.7304
4.73045
Easting, m
×10^5

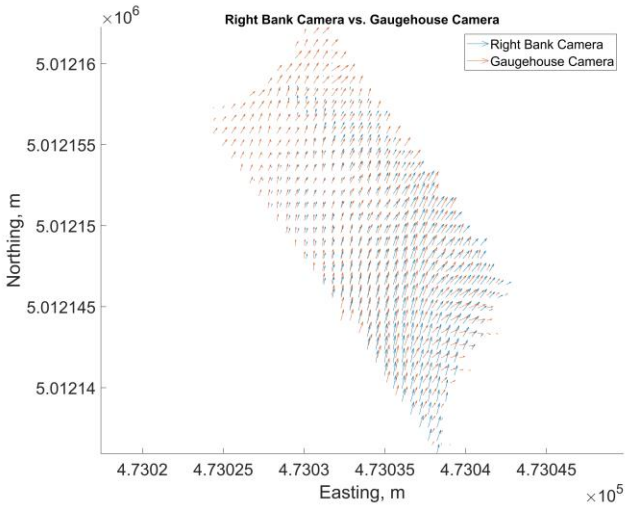
Right Bank Camera vs. Gaugehouse Camera
Right Bank Camera
Gaugehouse Camera
×10^6
5.01216
5.012155
5.01215
5.012145
5.01214
Northing, m
4.7302
4.73025
4.7303
4.73035
4.7304
4.73045
Easting, m
×10^5

May 5th, 2023

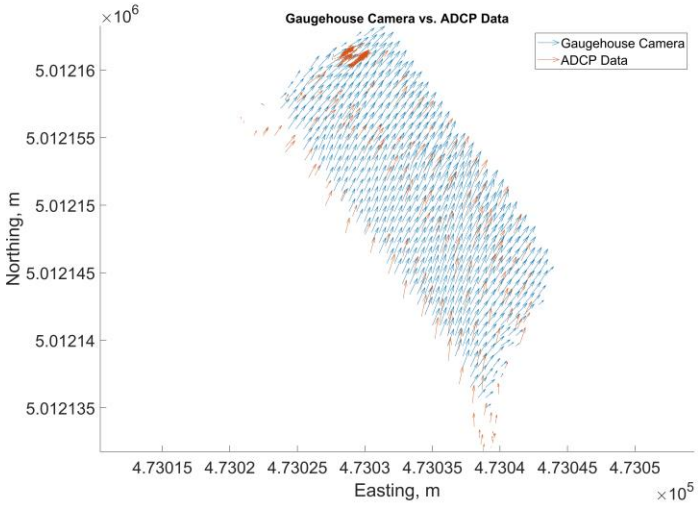
Gaugehouse Camera vs. ADCP Data
Gaugehouse Camera
ADCP Data
×10^6
5.01216
5.012155
5.01215
5.012145
5.01214
5.012135
Northing, m
4.73015
4.7302
4.73025
4.7303
4.73035
4.7304
4.73045
4.7305
Easting, m
×10^5

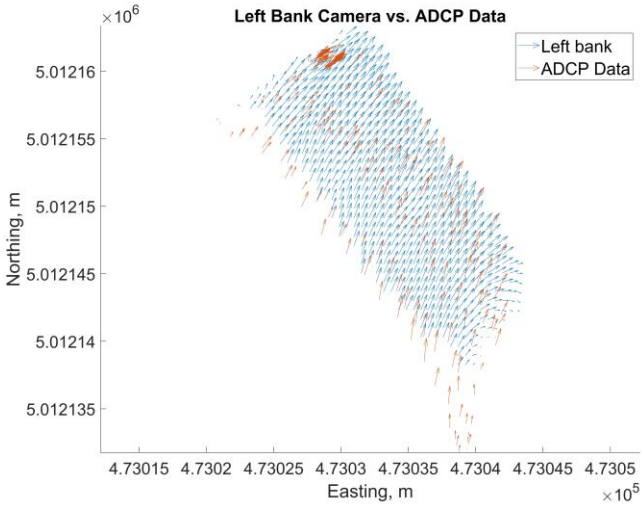
Left Bank Camera vs. ADCP Data
Left bank
ADCP Data
×10^6
5.01216
5.012155
5.01215
5.012145
5.01214
5.012135
Northing, m
4.73015 4.7302 4.73025 4.7303 4.73035 4.7304 4.73045 4.7305
Easting, m
×10^5

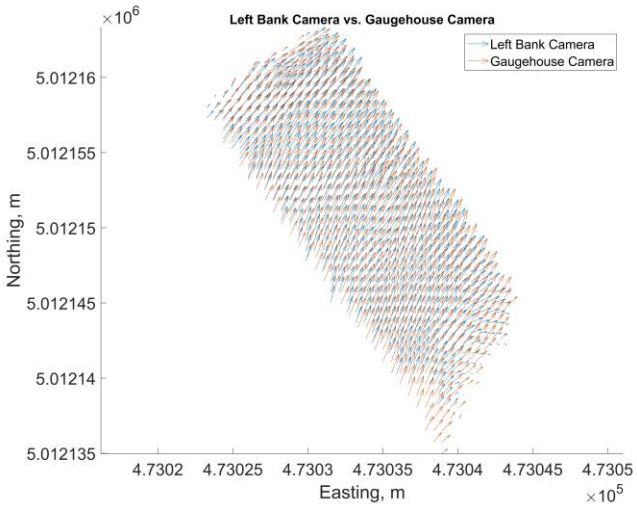
Left Bank Camera vs. Gaugehouse Camera
Left Bank Camera
Gaugehouse Camera
×10^6
5.01216
5.012155
5.01215
5.012145
5.01214
5.012135
Northing, m
4.7302 4.73025 4.7303 4.73035 4.7304 4.73045 4.7305
Easting, m
×10^5

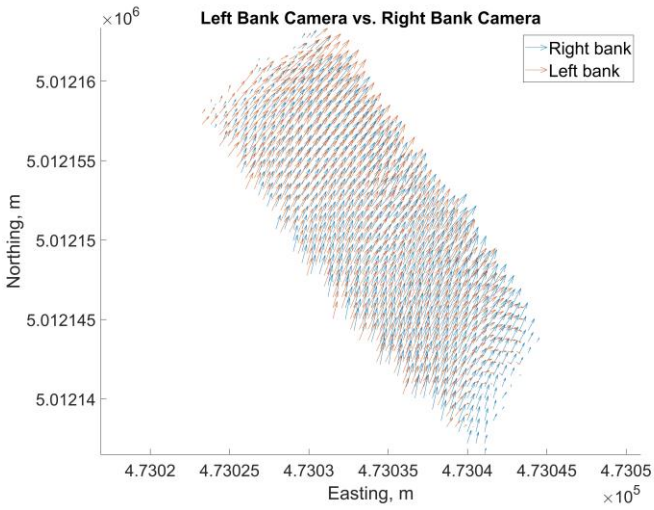
Left Bank Camera vs. Right Bank Camera
Right bank
Left bank
×10^6
5.01216
5.012155
5.01215
5.012145
5.01214
Northing, m
4.7302
4.73025
4.7303
4.73035
4.7304
4.73045
4.7305
Easting, m
×10^5

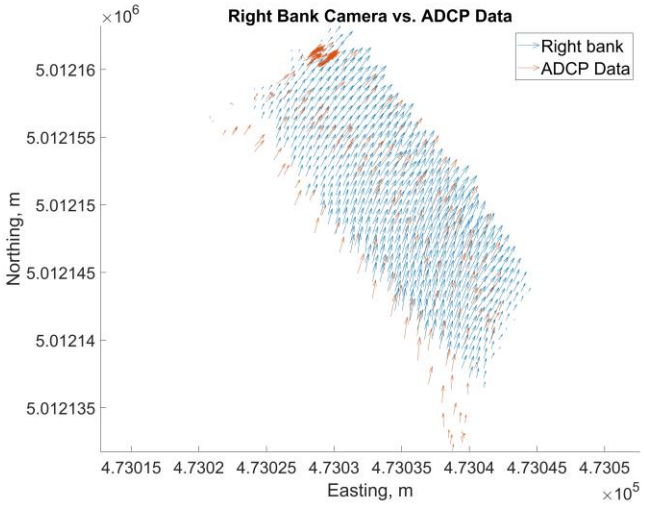
Right Bank Camera vs. ADCP Data
Right bank
ADCP Data
×10^6
5.01216
5.012155
5.01215
5.012145
5.01214
5.012135
Northing, m
4.73015
4.7302
4.73025
4.7303
4.73035
4.7304
4.73045
4.7305
Easting, m
×10^5

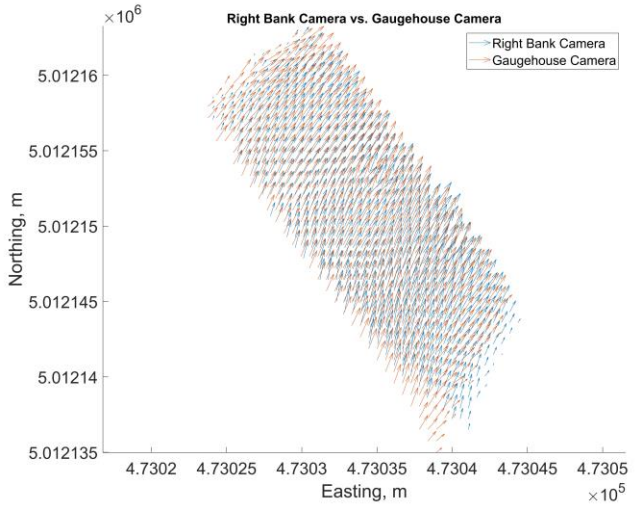
Right Bank Camera vs. Gaugehouse Camera
Right Bank Camera
Gaugehouse Camera
×10^6
5.01216
5.012155
5.01215
5.012145
5.01214
5.012135
Northing, m
4.7302
4.73025
4.7303
4.73035
4.7304
4.73045
4.7305
Easting, m
×10^5

March 6th, 2024

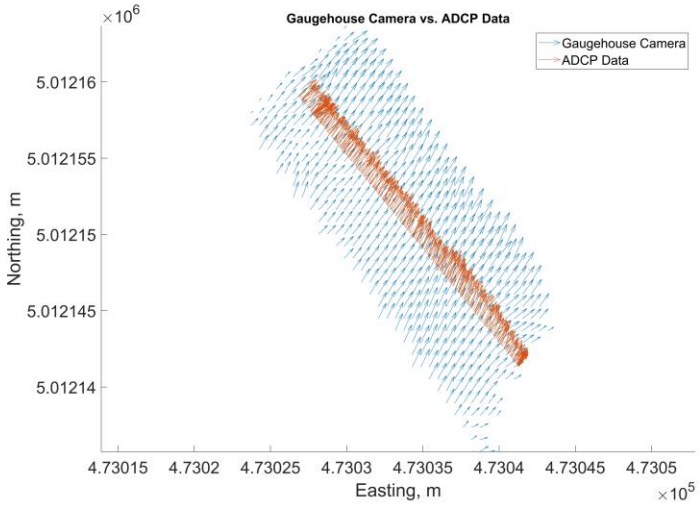

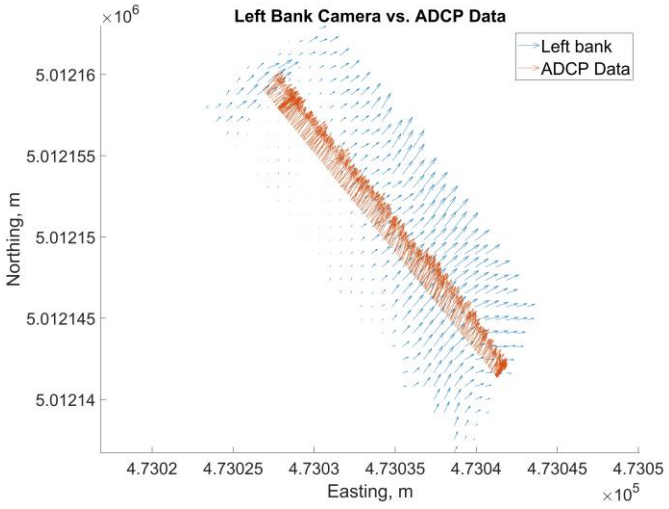

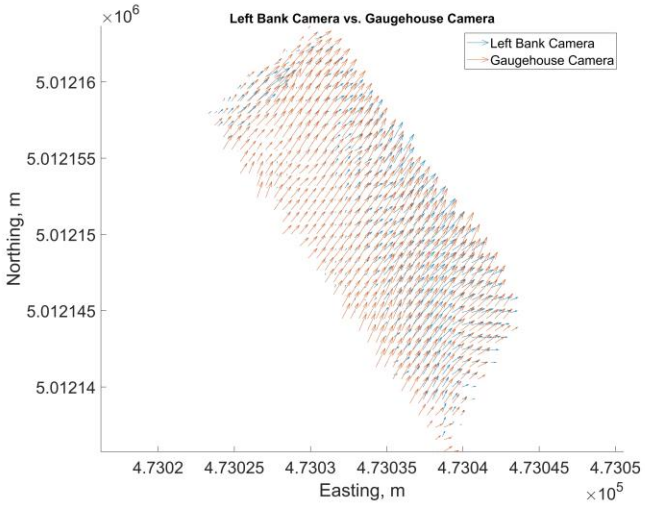

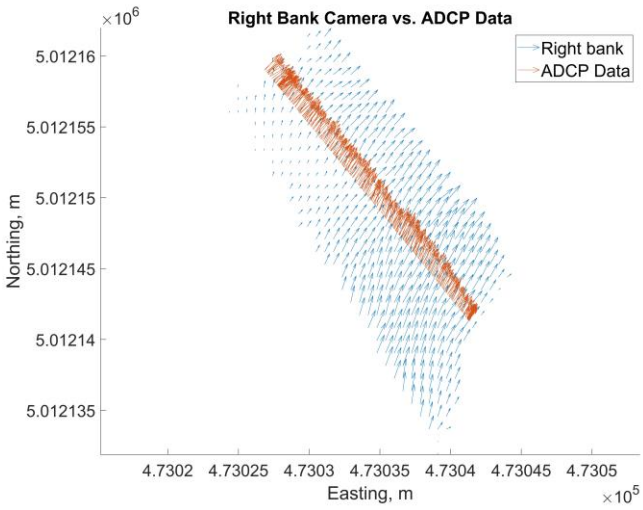

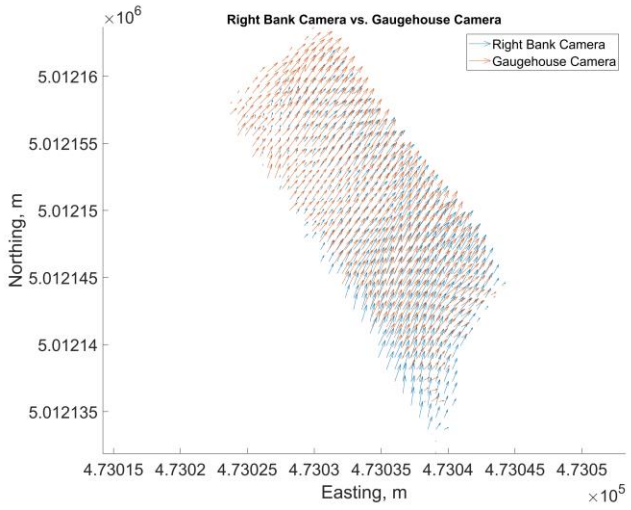

May 15th, 2024

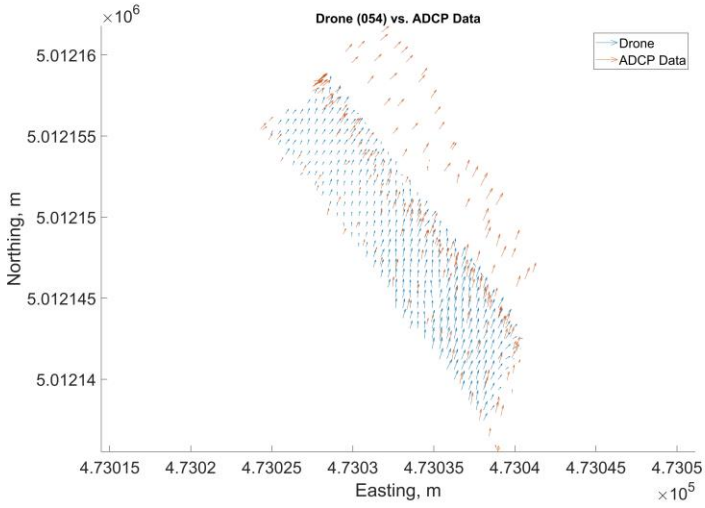

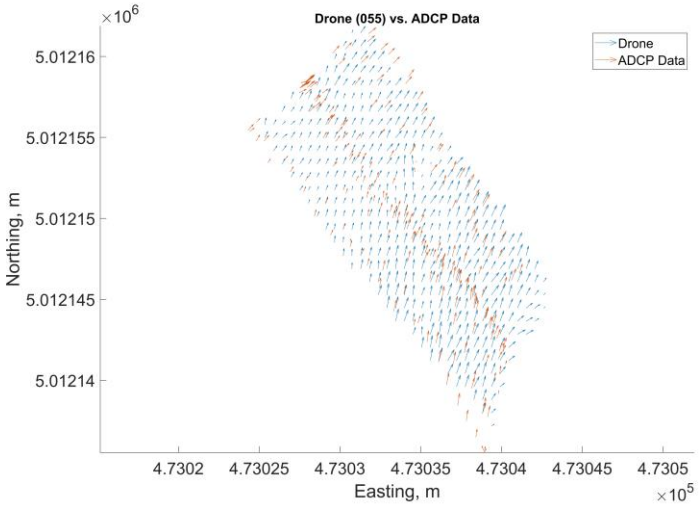
Drone (055) vs. ADCP Data
Drone
ADCP Data
×10^6
5.01216
5.012155
5.01215
5.012145
5.01214
Northing, m
4.7302
4.73025
4.7303
4.73035
4.7304
4.73045
4.7305
Easting, m
×10^5

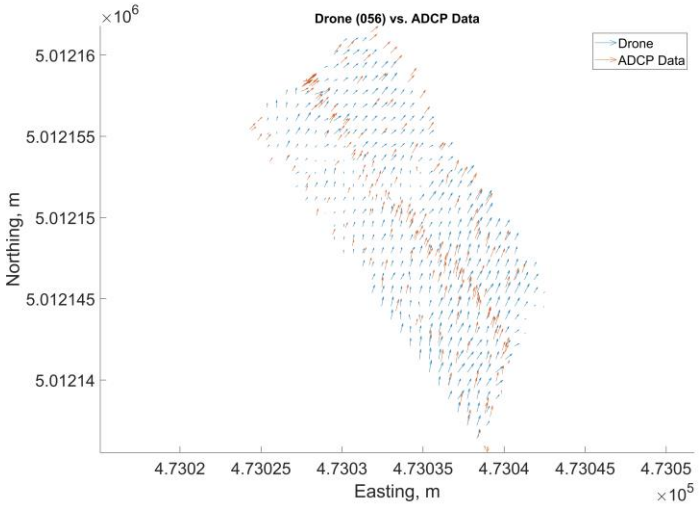
Drone (056) vs. ADCP Data
Drone
ADCP Data
×10^6
5.01216
5.012155
5.01215
5.012145
5.01214
Northing, m
4.7302
4.73025
4.7303
4.73035
4.7304
4.73045
4.7305
Easting, m
×10^5

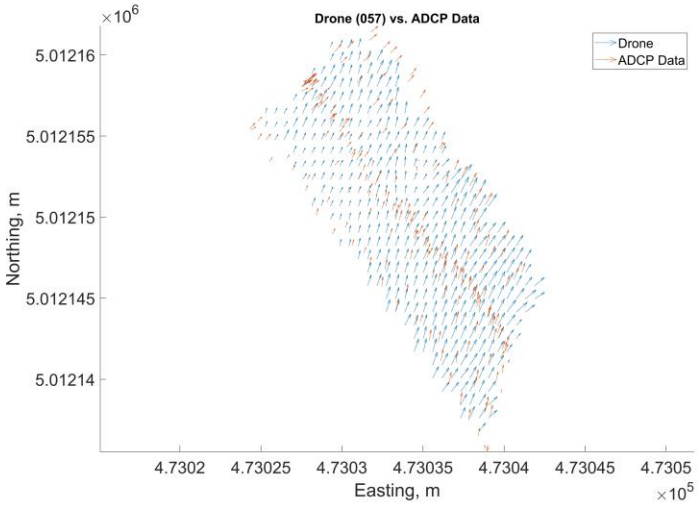
Drone (057) vs. ADCP Data
Drone
ADCP Data
×10^6
5.01216
5.012155
5.01215
5.012145
5.01214
Northing, m
4.7302
4.73025
4.7303
4.73035
4.7304
4.73045
4.7305
Easting, m
×10^5

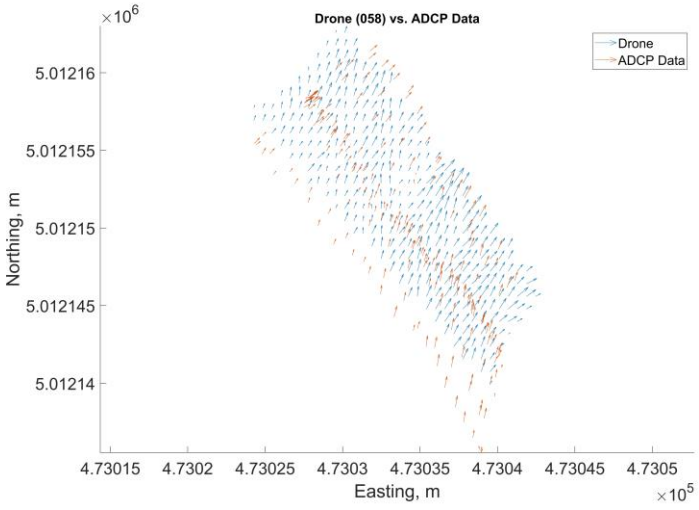
Drone (058) vs. ADCP Data
Drone
ADCP Data
×10^6
5.01216
5.012155
5.01215
5.012145
5.01214
Northing, m
4.73015
4.7302
4.73025
4.7303
4.73035
4.7304
4.73045
4.7305
Easting, m
×10^5

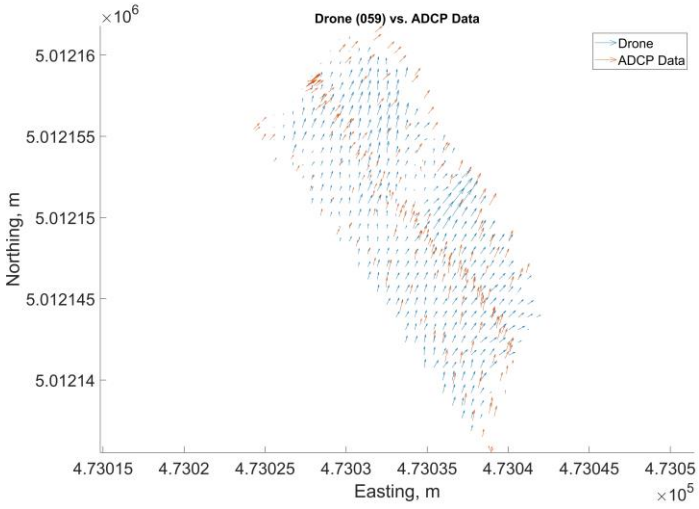
Drone (059) vs. ADCP Data
Drone
ADCP Data
×10^6
5.01216
5.012155
5.01215
5.012145
5.01214
Northing, m
4.73015
4.7302
4.73025
4.7303
4.73035
4.7304
4.73045
4.7305
Easting, m
×10^5

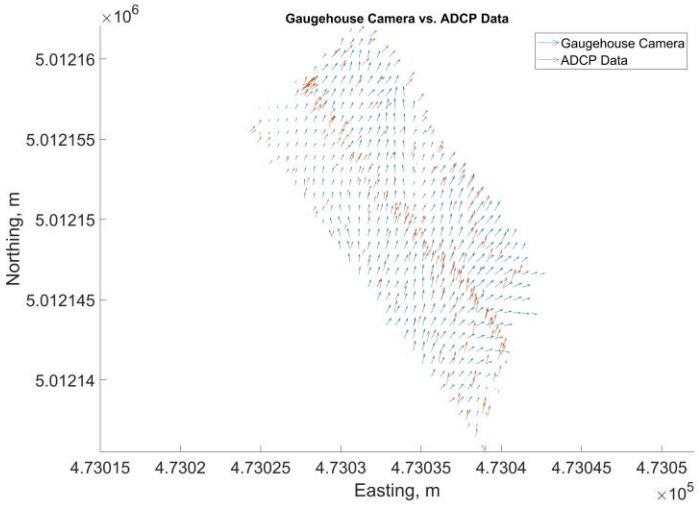
Gaugehouse Camera vs. ADCP Data
Gaugehouse Camera
ADCP Data
×10^6
5.01216
5.012155
5.01215
5.012145
5.01214
Northing, m
4.73015
4.7302
4.73025
4.7303
4.73035
4.7304
4.73045
4.7305
Easting, m
×10^5

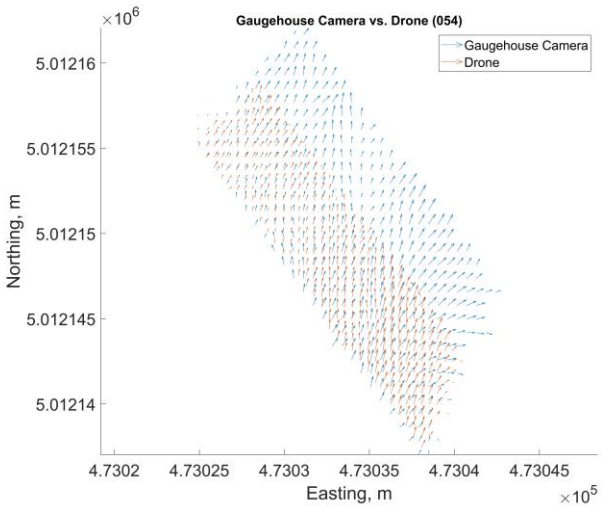
Gaugehouse Camera vs. Drone (054)
Gaugehouse Camera
Drone
×10^6
5.01216
5.012155
5.01215
5.012145
5.01214
Northing, m
4.7302
4.73025
4.7303
4.73035
4.7304
4.73045
Easting, m
×10^5

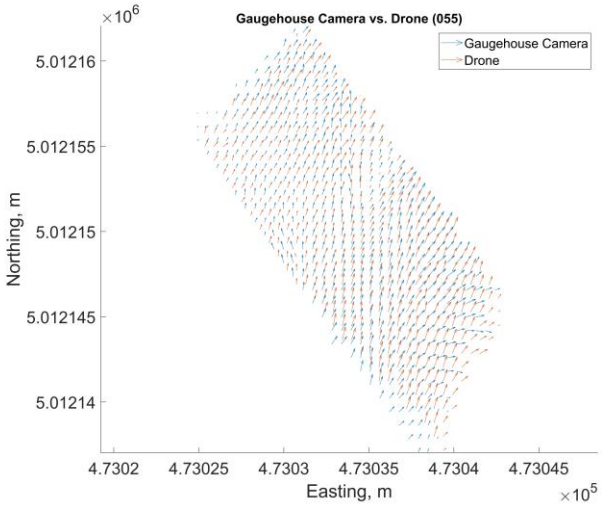
Gaugehouse Camera vs. Drone (055)
Gaugehouse Camera
Drone
×10^6
5.01216
5.012155
5.01215
5.012145
5.01214
Northing, m
4.7302
4.73025
4.7303
4.73035
4.7304
4.73045
Easting, m
×10^5

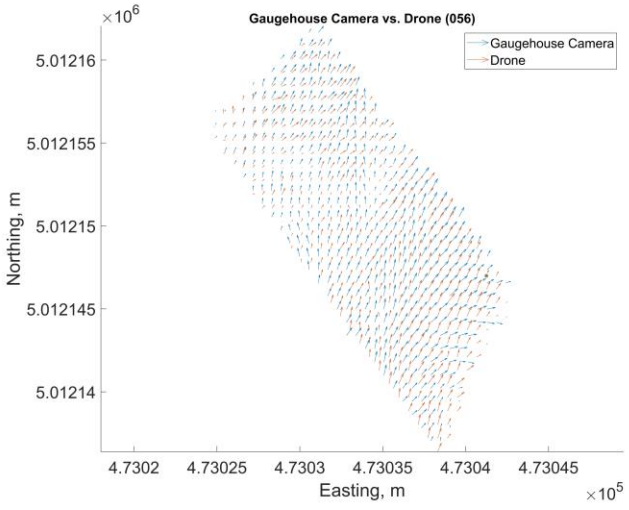
Gaugehouse Camera vs. Drone (056)
Gaugehouse Camera
Drone
×10^6
5.01216
5.012155
5.01215
5.012145
5.01214
Northing, m
4.7302
4.73025
4.7303
4.73035
4.7304
4.73045
Easting, m
×10^5

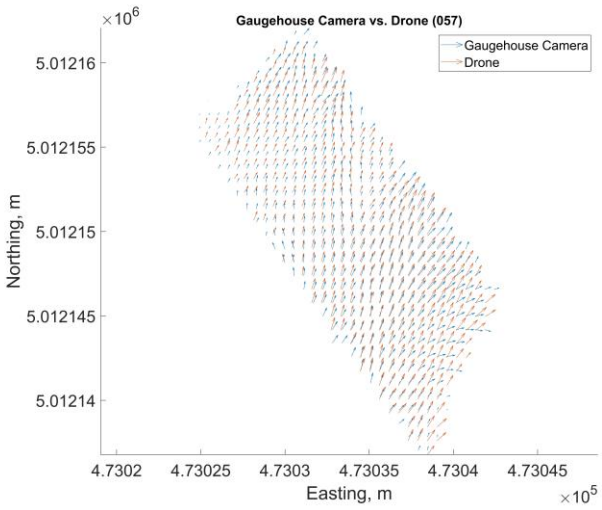
Gaugehouse Camera vs. Drone (057)
Gaugehouse Camera
Drone
×10^6
5.01216
5.012155
5.01215
5.012145
5.01214
Northing, m
4.7302
4.73025
4.7303
4.73035
4.7304
4.73045
Easting, m
×10^5

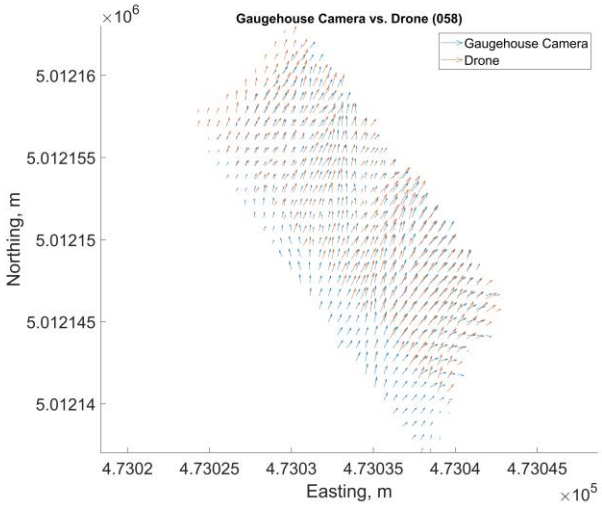
Gaugehouse Camera vs. Drone (058)
Gaugehouse Camera
Drone
×10^6
5.01216
5.012155
5.01215
5.012145
5.01214
Northing, m
4.7302
4.73025
4.7303
4.73035
4.7304
4.73045
Easting, m
×10^5

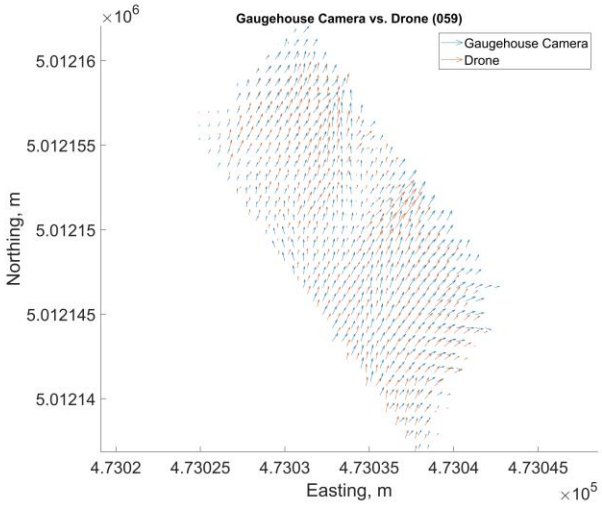
Gaugehouse Camera vs. Drone (059)
Gaugehouse Camera
Drone
×10^6
5.01216
5.012155
5.01215
5.012145
5.01214
Northing, m
4.7302
4.73025
4.7303
4.73035
4.7304
4.73045
Easting, m
×10^5

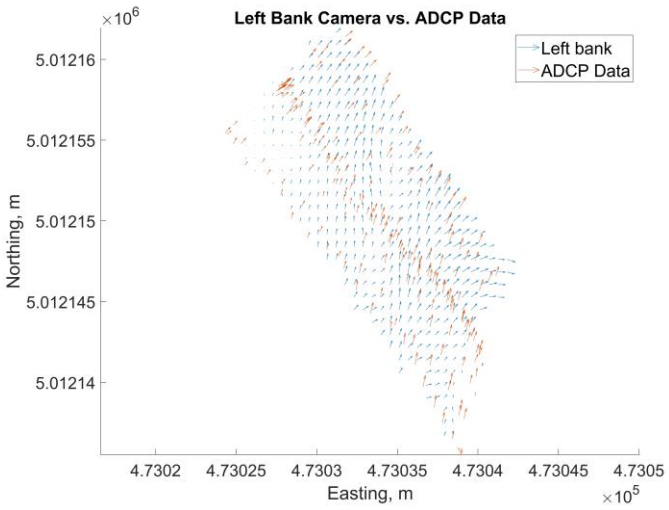
Left Bank Camera vs. ADCP Data
Left bank
ADCP Data
×10^6
5.01216
5.012155
5.01215
5.012145
5.01214
Northing, m
4.7302
4.73025
4.7303
4.73035
4.7304
4.73045
4.7305
×10^5
Easting, m

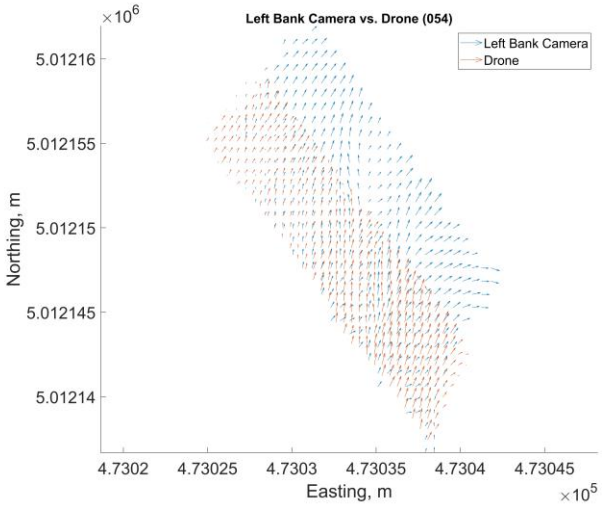
Left Bank Camera vs. Drone (054)
Left Bank Camera
Drone
×10^6
5.01216
5.012155
5.01215
5.012145
5.01214
Northing, m
4.7302
4.73025
4.7303
4.73035
4.7304
4.73045
×10^5
Easting, m

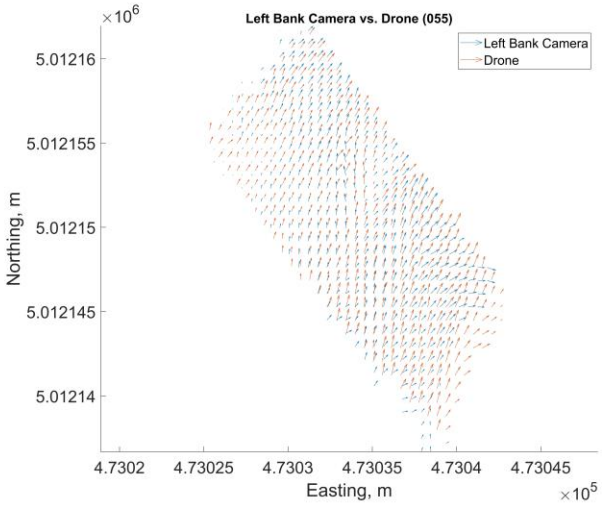
Left Bank Camera vs. Drone (055)
Left Bank Camera
Drone
×10^6
5.01216
5.012155
5.01215
5.012145
5.01214
Northing, m
4.7302
4.73025
4.7303
4.73035
4.7304
4.73045
×10^5
Easting, m

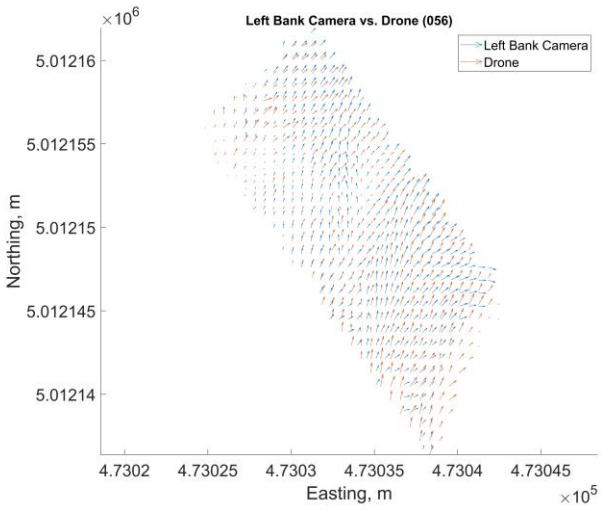
Left Bank Camera vs. Drone (056)
Left Bank Camera
Drone
×10^6
5.01216
5.012155
5.01215
5.012145
5.01214
Northing, m
4.7302
4.73025
4.7303
4.73035
4.7304
4.73045
×10^5
Easting, m

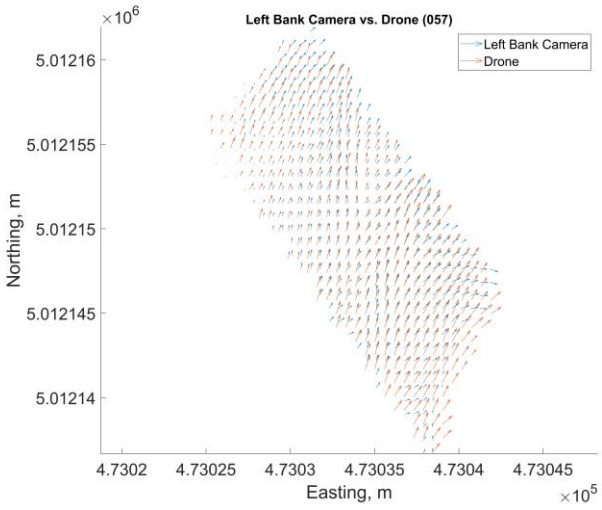
Left Bank Camera vs. Drone (057)
Left Bank Camera
Drone
×10^6
5.01216
5.012155
5.01215
5.012145
5.01214
Northing, m
4.7302
4.73025
4.7303
4.73035
4.7304
4.73045
×10^5
Easting, m

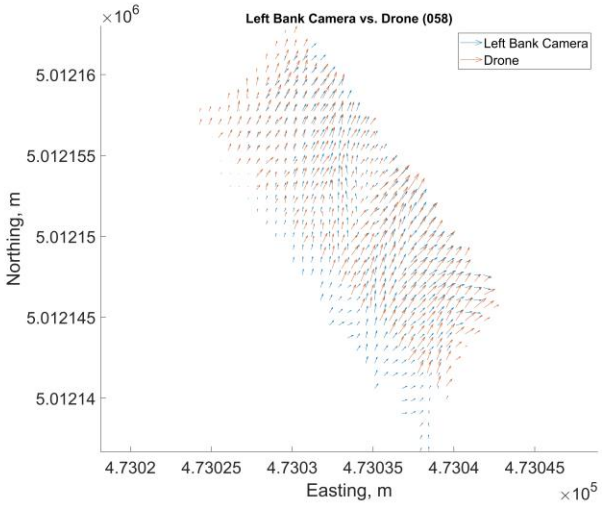
Left Bank Camera vs. Drone (058)
Left Bank Camera
Drone
×10^6
5.01216
5.012155
5.01215
5.012145
5.01214
Northing, m
4.7302
4.73025
4.7303
4.73035
4.7304
4.73045
×10^5
Easting, m

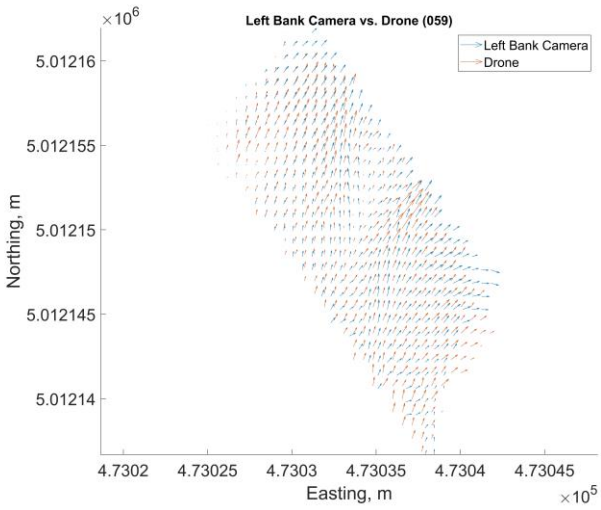
Left Bank Camera vs. Drone (059)
Left Bank Camera
Drone
×10^6
5.01216
5.012155
5.01215
5.012145
5.01214
Northing, m
4.7302
4.73025
4.7303
4.73035
4.7304
4.73045
Easting, m
×10^5

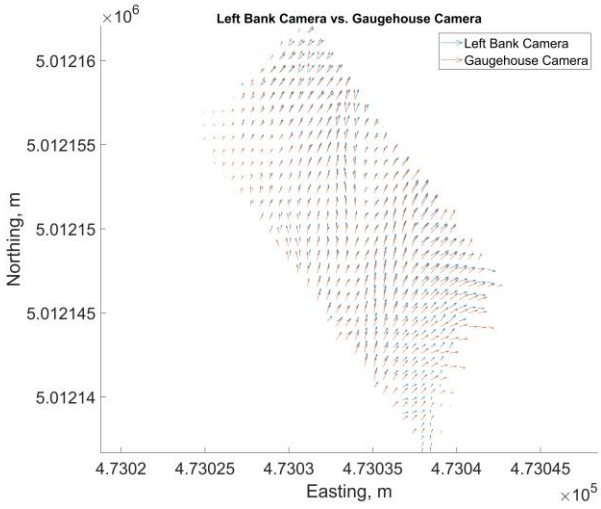
Left Bank Camera vs. Gaugehouse Camera
Left Bank Camera
Gaugehouse Camera
×10^6
5.01216
5.012155
5.01215
5.012145
5.01214
Northing, m
4.7302
4.73025
4.7303
4.73035
4.7304
4.73045
Easting, m
×10^5

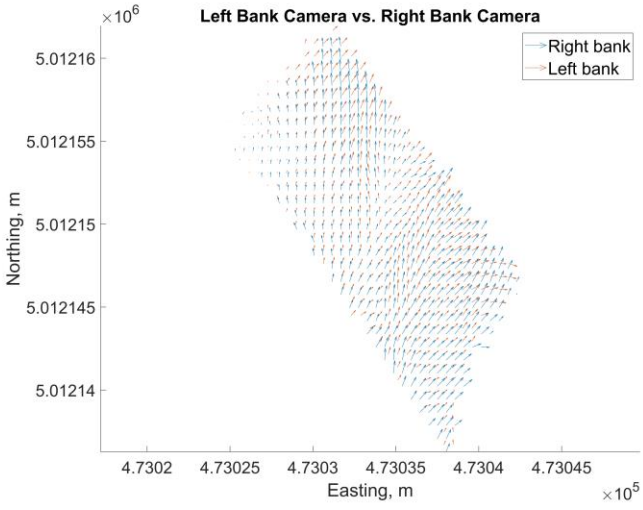
Left Bank Camera vs. Right Bank Camera
Right bank
Left bank
×10^6
5.01216
5.012155
5.01215
5.012145
5.01214
Northing, m
4.7302
4.73025
4.7303
4.73035
4.7304
4.73045
Easting, m
×10^5

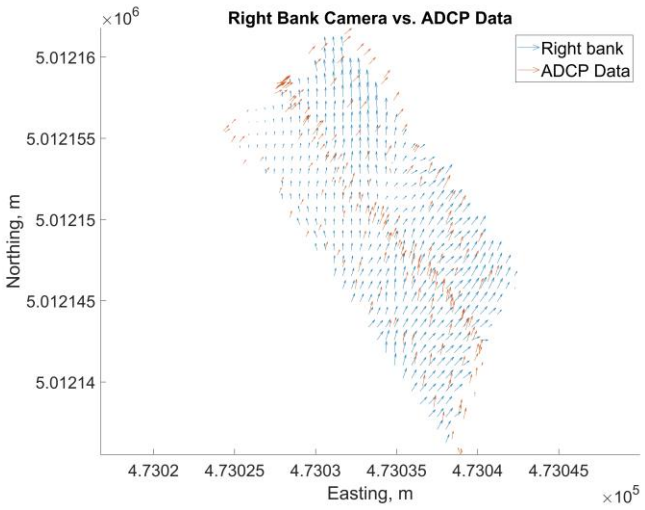
Right Bank Camera vs. ADCP Data
Right bank
ADCP Data
×10^6
5.01216
5.012155
5.01215
5.012145
5.01214
Northing, m
4.7302
4.73025
4.7303
4.73035
4.7304
4.73045
Easting, m
×10^5

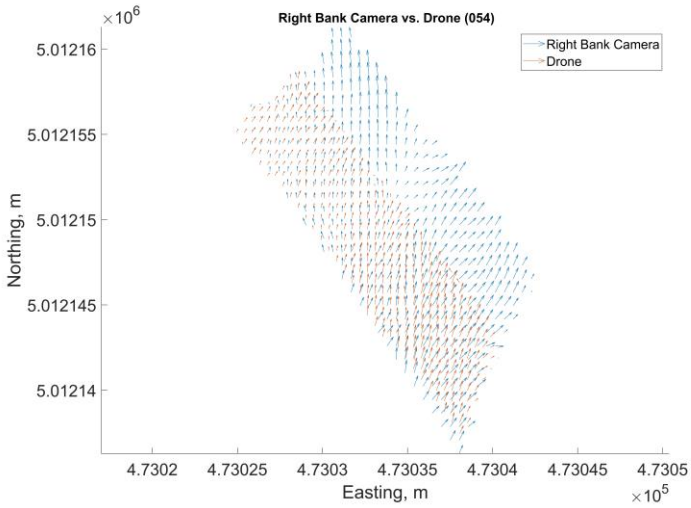
Right Bank Camera vs. Drone (054)
Right Bank Camera
Drone
×10^6
5.01216
5.012155
5.01215
5.012145
5.01214
Northing, m
4.7302
4.73025
4.7303
4.73035
4.7304
4.73045
4.7305
Easting, m
×10^5

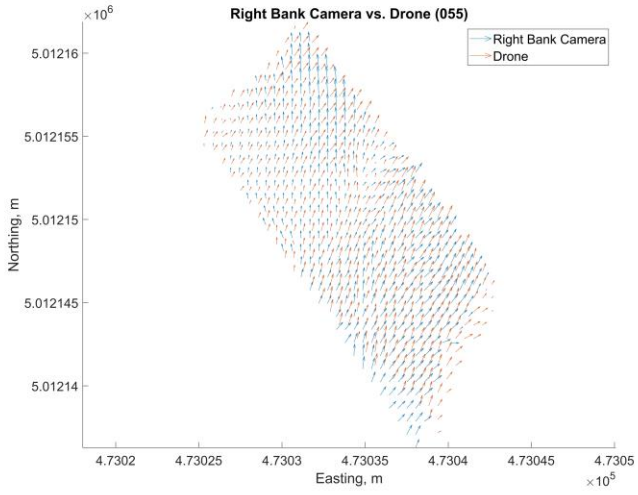
Right Bank Camera vs. Drone (055)
Right Bank Camera
Drone
×10^6
5.01216
5.012155
5.01215
5.012145
5.01214
Northing, m
4.7302
4.73025
4.7303
4.73035
4.7304
4.73045
4.7305
Easting, m
×10^5

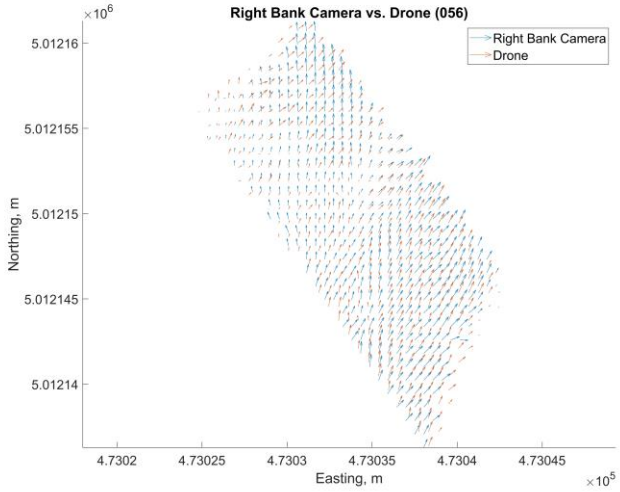
Right Bank Camera vs. Drone (056)
Right Bank Camera
Drone
×10^6
5.01216
5.012155
5.01215
5.012145
5.01214
Northing, m
4.7302
4.73025
4.7303
4.73035
4.7304
4.73045
Easting, m
×10^5

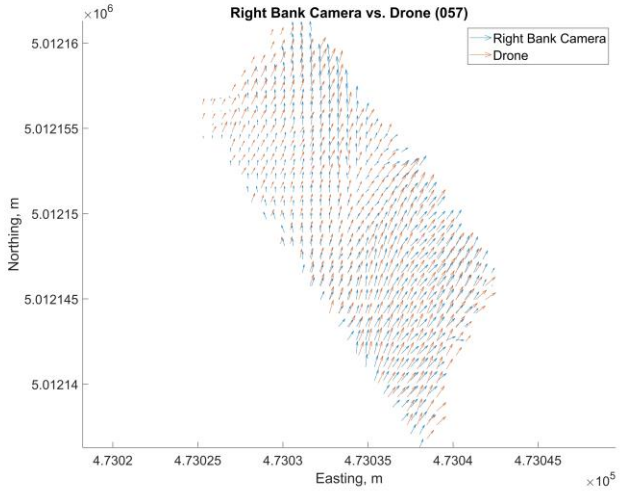
Right Bank Camera vs. Drone (057)
Right Bank Camera
Drone
×10^6
5.01216
5.012155
5.01215
5.012145
5.01214
Northing, m
4.7302
4.73025
4.7303
4.73035
4.7304
4.73045
Easting, m
×10^5

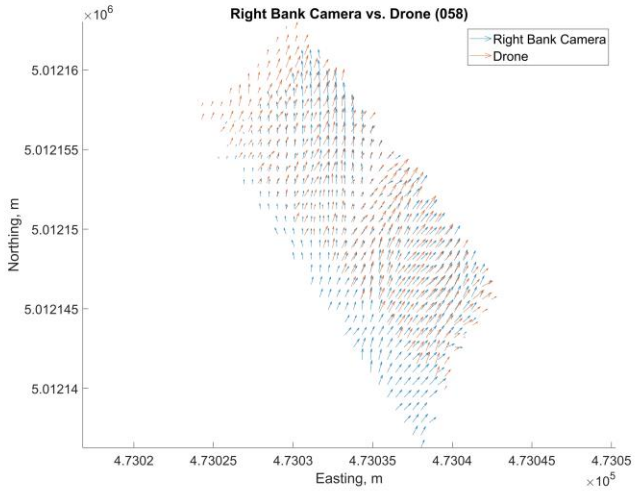
Right Bank Camera vs. Drone (058)
Right Bank Camera
Drone
×10^6
5.01216
5.012155
5.01215
5.012145
5.01214
Northing, m
4.7302
4.73025
4.7303
4.73035
4.7304
4.73045
4.7305
Easting, m
×10^5

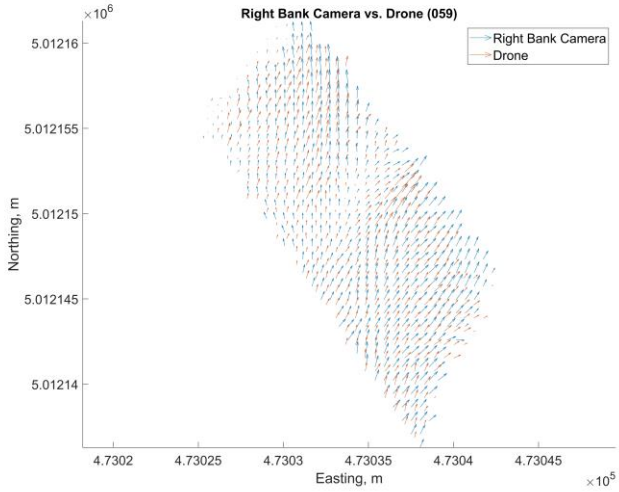

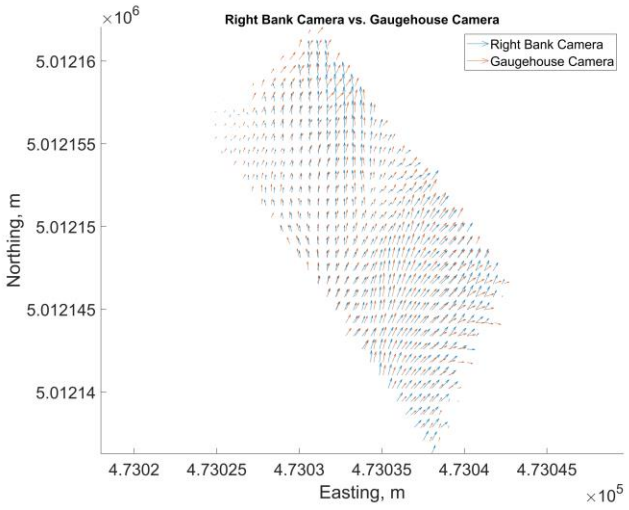

Appendix E – Other Plots & MATLAB Scripts

This final section contains additional surface velocity cross-section plots, distance plots and the key MATLAB scripts used in the study.

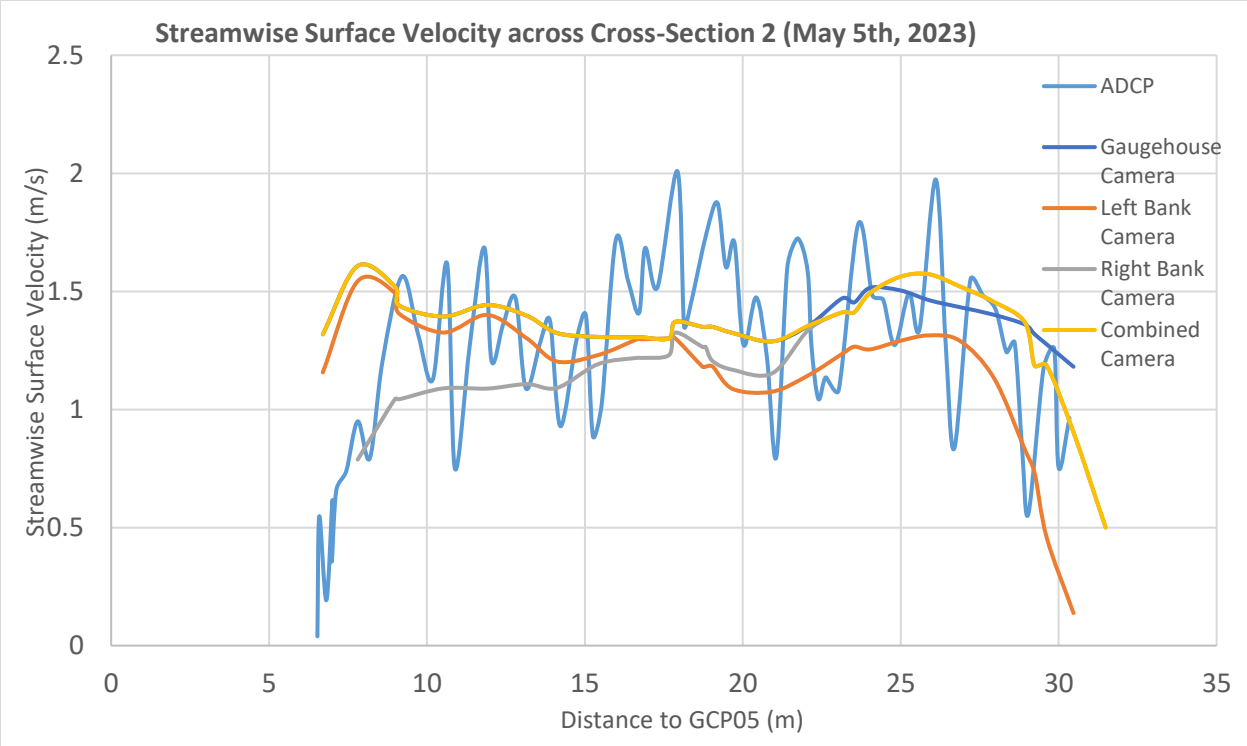
Streamwise Surface Velocity across Cross-Section 2 (May 5th, 2023)
Streamwise Surface Velocity (m/s)
Distance to GCP05 (m)
ADCP
Gaugehouse Camera
Left Bank Camera
Right Bank Camera
Combined Camera

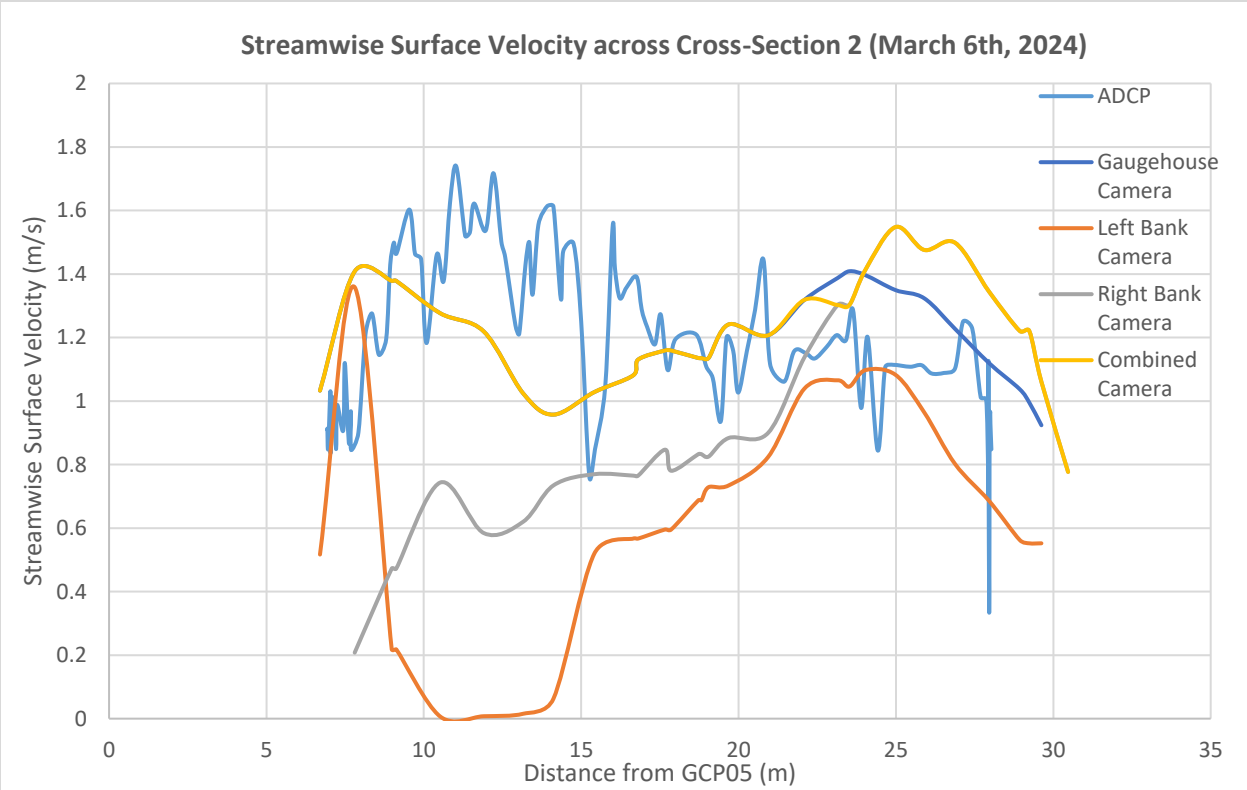
Streamwise Surface Velocity across Cross-Section 2 (March 6th, 2024)
Streamwise Surface Velocity (m/s)
Distance from GCP05 (m)
ADCP
Gaugehouse Camera
Left Bank Camera
Right Bank Camera
Combined Camera

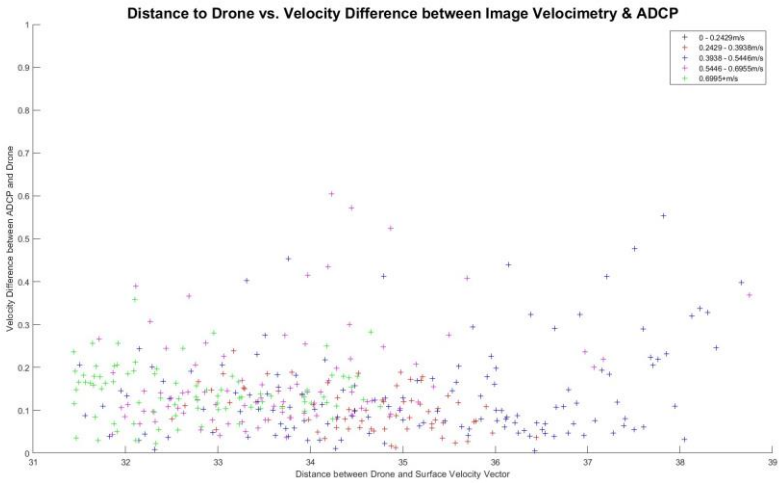

Figure E 1: Distance to drone versus velocity difference plot for DJI054 video

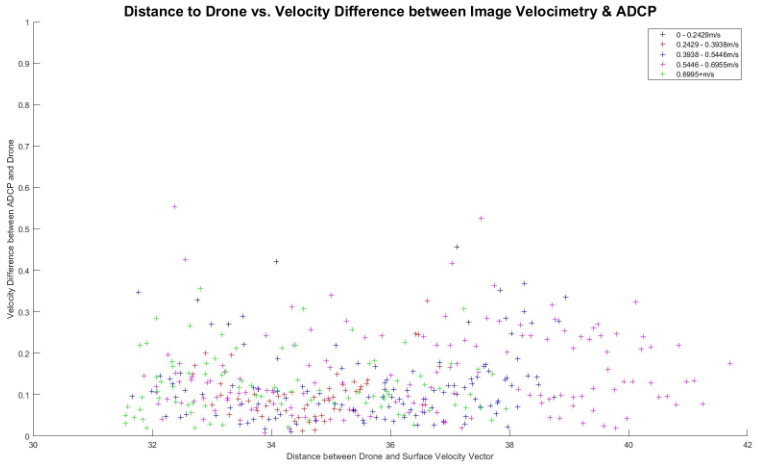

Figure E 2: Distance to drone versus velocity difference plot for DJI055 video

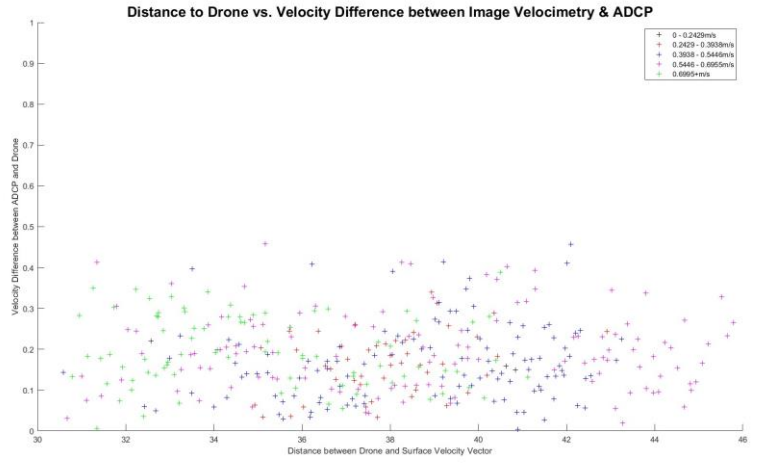

Figure E 3: Distance to drone versus velocity difference plot for DJI056 video

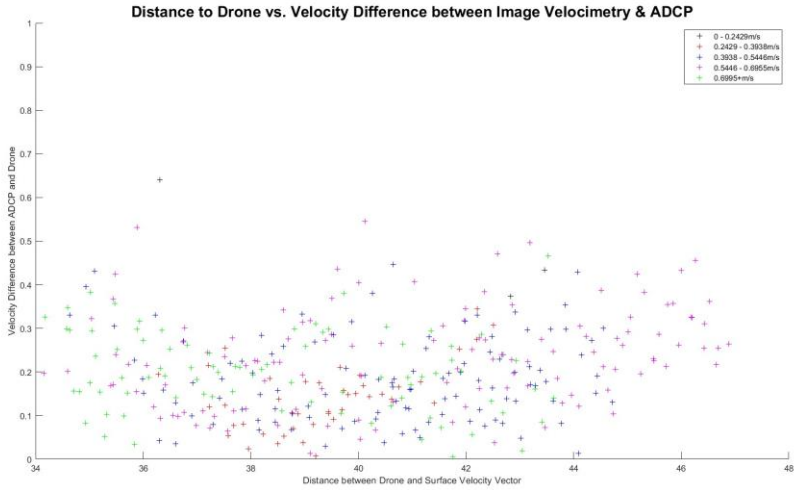

Figure E 4: Distance to drone versus velocity difference plot for DJI057 video

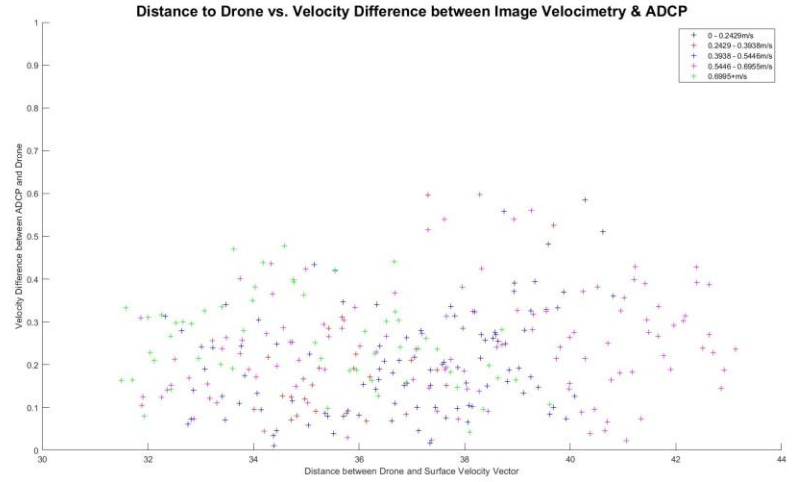

Figure E 5: Distance to drone versus velocity difference plot for DJI058 video

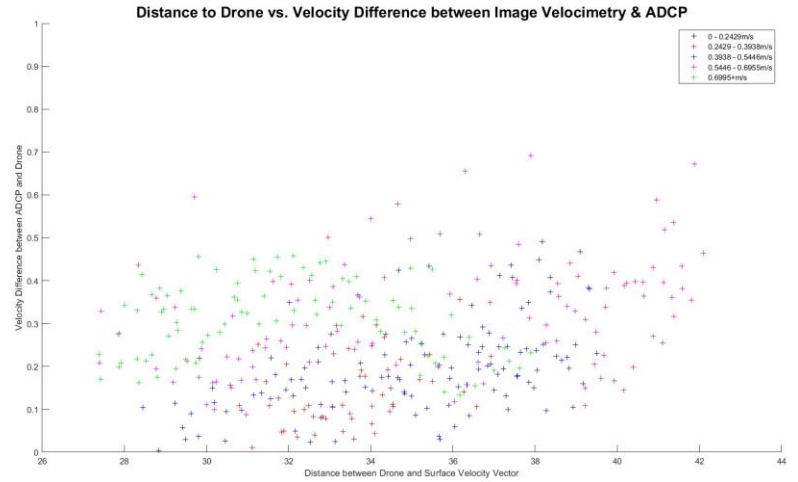

Figure E 6: Distance to drone versus velocity difference plot for DJI059 video

Velocity Difference Code

```
 rb_range=input('input the sheet range for rb data, ie x#:x# in single quotes ')
%changes for every dataset
 lb_range=input('input the sheet range for lb data, ie x#:x# in single quotes ')
 % drone_range=input('input the sheet range for the drone data in single
quotes')
 cam1_range=input('input the sheet range for the Cam1 data in single quotes ')

 u_rb = readmatrix('U_RB03062024.csv');
 u_lb = readmatrix('U_LB03062024.csv');
 v_rb = readmatrix('V_RB03062024.csv');
 v_lb = readmatrix('V_LB03062024.csv');
 x_rb = readmatrix('X_RB03062024.csv','range',rb_range);
 x_lb = readmatrix('X_LB03062024.csv','range',lb_range);
 y_rb = readmatrix('Y_RB03062024.csv','range',rb_range);
 y_lb = readmatrix('Y_LB03062024.csv','range',lb_range);
 % drone_uvel = readmatrix('U_DJ0018.csv');
 % drone_vvel = readmatrix('V_DJ0018.csv');
 % drone_x = readmatrix('X_DJ0018.csv', 'range', drone_range);
 % drone_y = readmatrix('Y_DJ0018.csv', 'range', drone_range);
 u_cam1 = readmatrix('U_Cam103062024.csv');
 v_cam1 = readmatrix('V_Cam103062024.csv');
 x_cam1 = readmatrix('X_Cam103062024.csv', 'range',cam1_range);
 y_cam1 = readmatrix('Y_Cam103062024.csv', 'range',cam1_range);
 adcpdata = readmatrix('March6th2024ADCPData.csv'); %can go back &
 % forth with line 16 (boxcar average data) and line 18 (single ping)
 %LB & RB comparison
 for k=1:size(x_rb,2)
     for m=1:size(y_rb,1)
         for p=1:size(x_lb,2)
             for q=1:size(y_lb,1)
                 diff(q,p)=sqrt((x_rb(1,k)-x_lb(1,p))^2+(y_rb(m,1)-
y_lb(q,1))^2);
             end
         end
          smallestdiff(m,k)=min(min(diff));
          for t=1:q
              for s=1:p
                  if diff(t,s)==smallestdiff(m,k)
                                  smallestdiff_x_lb_cellnumber(m,k)=s;
                                  smallestdiff_y_lb_cellnumber(m,k)=t;
                  end
              end
          end
     end
```

```
 end

 %now find velocity difference for matched points for RB & LB
 for k=1:size(u_rb,2)
     for m=1:size(u_rb,1)
         if smallestdiff(m,k) > 0.5 %needs a sensitivity analysis
            uveldiff(m,k) = NaN;
            vveldiff(m,k) = NaN;
         else
         uveldiff(m,k)=u_rb(m,k)-
u_lb(smallestdiff_y_lb_cellnumber(m,k),smallestdiff_x_lb_cellnumber(m,k));
         vveldiff(m,k)=v_rb(m,k)-
v_lb(smallestdiff_y_lb_cellnumber(m,k),smallestdiff_x_lb_cellnumber(m,k));
         end
     end
 end
 clear diff
 %set up adcp vel scaling comparison
 [adcpangle,adcpmagnitude] = cart2pol(adcpdata(:,3),adcpdata(:,4));
 meanmag=mean(adcpmagnitude)
 maxmag=max(adcpmagnitude)
 stdmag=std(adcpmagnitude)
 lowestvel=meanmag - stdmag*2
 lowvel=meanmag - stdmag
 mediumvel=meanmag
 mediumhighvel=meanmag+stdmag
 highvel=meanmag + stdmag*2
 %compare ADCP to RB camera
 ADCPRBdiff(length(adcpdata),size(y_rb,1),size(x_rb,2))=NaN;
 for k=1:size(x_rb,2)
     for m=1:size(y_rb,1)
         for q=1:length(adcpdata)
             ADCPRBdiff(q,m,k)=sqrt((x_rb(1,k)-adcpdata(q,1))^2+(y_rb(m,1)-
adcpdata(q,2))^2);

         end
             smallestADCPRBdiff(m,k)=min(min(ADCPRBdiff(:,m,k)));
             for q=1:length(adcpdata)
                 for t=1:size(y_rb,1)
                     for s=1:size(x_rb,2)
                         if ADCPRBdiff(q,t,s)==smallestADCPRBdiff(m,k)
                                     smallestADCPRBdiff_x_rb_cellnumber(m,k)=s;
                                     smallestADCPRBdiff_y_rb_cellnumber(m,k)=t;
                            smallestADCPRBdiff_ADCPCellRB(m,k)=q;
                         end
                     end
```

```
                end
            end
    end
end


%now find velocity difference for matched points for RB & ADCP camera

ADCPRBvelmagdiff_lowestvel= NaN(m,k);
ADCPRBvelmagdiff_lowvel= NaN(m,k);
ADCPRBvelmagdiff_mediumvel= NaN(m,k);
ADCPRBvelmagdiff_mediumhighvel= NaN(m,k);
ADCPRBvelmagdiff_highvel= NaN(m,k);

for k=1:size(u_rb,2)
    for m=1:size(u_rb,1)
        if smallestADCPRBdiff(m,k) > 1.0 %needs a sensitivity analysis
           uveldiffADCPRB(m,k) = NaN;
           vveldiffADCPRB(m,k) = NaN;
        else
        uveldiffADCPRB(m,k)=adcpdata(smallestADCPRBdiff_ADCPCellRB(m,k),3)-
u_rb(smallestADCPRBdiff_y_rb_cellnumber(m,k),smallestADCPRBdiff_x_rb_cellnumber(
m,k));
        vveldiffADCPRB(m,k)=adcpdata(smallestADCPRBdiff_ADCPCellRB(m,k),4)-
v_rb(smallestADCPRBdiff_y_rb_cellnumber(m,k),smallestADCPRBdiff_x_rb_cellnumber(
m,k));

%added to bin by velocity

ADCPRBvelmagdiff_forplot(m,k)=sqrt(uveldiffADCPRB(m,k).^2+vveldiffADCPRB(m,k).^2
);
    if adcpmagnitude(smallestADCPRBdiff_ADCPCellRB(m,k)) < lowestvel
        ADCPRBvelmagdiff_lowestvel(m,k)=ADCPRBvelmagdiff_forplot(m,k);
    elseif adcpmagnitude(smallestADCPRBdiff_ADCPCellRB(m,k)) < lowvel
        ADCPRBvelmagdiff_lowvel(m,k)=ADCPRBvelmagdiff_forplot(m,k);
    elseif adcpmagnitude(smallestADCPRBdiff_ADCPCellRB(m,k)) < mediumvel
        ADCPRBvelmagdiff_mediumvel(m,k)=ADCPRBvelmagdiff_forplot(m,k);
    elseif adcpmagnitude(smallestADCPRBdiff_ADCPCellRB(m,k)) < mediumhighvel
        ADCPRBvelmagdiff_mediumhighvel(m,k)=ADCPRBvelmagdiff_forplot(m,k);
    else %high vel
        ADCPRBvelmagdiff_highvel(m,k)=ADCPRBvelmagdiff_forplot(m,k);
    end

        end
    end
end
```

```
 clear diff
 %compare ADCP to LB camera
 ADCPLBdiff(length(adcpdata),size(y_lb,1),size(x_lb,2))=NaN;
 for k=1:size(x_lb,2)
     for m=1:size(y_lb,1)
             for q=1:length(adcpdata)
                 ADCPLBdiff(q,m,k)=sqrt((x_lb(1,k)-adcpdata(q,1))^2+(y_lb(m,1)-
adcpdata(q,2))^2);
             end
             smallestADCPLBdiff(m,k)=min(min(ADCPLBdiff(:,m,k)));
             for q=1:length(adcpdata)
             for t=1:size(y_lb,1)
              for s=1:size(x_lb,2)
                  if ADCPLBdiff(q,t,s)==smallestADCPLBdiff(m,k)
                                     smallestADCPLBdiff_x_lb_cellnumber(m,k)=s;
                                     smallestADCPLBdiff_y_lb_cellnumber(m,k)=t;
                           smallestADCPLBdiff_ADCPCellLB(m,k)=q;
                   end
                end
             end
         end
     end
 end


 %now find velocity difference for matched points for LB and ADCP

 ADCPLBvelmagdiff_lowestvel= NaN(m,k);
 ADCPLBvelmagdiff_lowvel= NaN(m,k);
 ADCPLBvelmagdiff_mediumvel= NaN(m,k);
 ADCPLBvelmagdiff_mediumhighvel= NaN(m,k);
 ADCPLBvelmagdiff_highvel= NaN(m,k);

 for k=1:size(u_lb,2)
     for m=1:size(u_lb,1)
         if smallestADCPLBdiff(m,k) > 1.0 %needs a sensitivity analysis
            uveldiffADCPLB(m,k) = NaN;
            vveldiffADCPLB(m,k) = NaN;
         else
         uveldiffADCPLB(m,k)=adcpdata(smallestADCPLBdiff_ADCPCellLB(m,k),3)-
u_lb(smallestADCPLBdiff_y_lb_cellnumber(m,k),smallestADCPLBdiff_x_lb_cellnumber(
m,k));
         vveldiffADCPLB(m,k)=adcpdata(smallestADCPLBdiff_ADCPCellLB(m,k),4)-
v_lb(smallestADCPLBdiff_y_lb_cellnumber(m,k),smallestADCPLBdiff_x_lb_cellnumber(
m,k));
```

```
 %added to bin by velocity

ADCPLBvelmagdiff_forplot(m,k)=sqrt(uveldiffADCPLB(m,k).^2+vveldiffADCPLB(m,k).^2
);
     if adcpmagnitude(smallestADCPLBdiff_ADCPCellLB(m,k)) < lowestvel
         ADCPLBvelmagdiff_lowestvel(m,k)=ADCPLBvelmagdiff_forplot(m,k);
     elseif adcpmagnitude(smallestADCPLBdiff_ADCPCellLB(m,k)) < lowvel
         ADCPLBvelmagdiff_lowvel(m,k)=ADCPLBvelmagdiff_forplot(m,k);
     elseif adcpmagnitude(smallestADCPLBdiff_ADCPCellLB(m,k)) < mediumvel
         ADCPLBvelmagdiff_mediumvel(m,k)=ADCPLBvelmagdiff_forplot(m,k);
     elseif adcpmagnitude(smallestADCPLBdiff_ADCPCellLB(m,k)) < mediumhighvel
         ADCPLBvelmagdiff_mediumhighvel(m,k)=ADCPLBvelmagdiff_forplot(m,k);
     else %high vel
         ADCPLBvelmagdiff_highvel(m,k)=ADCPLBvelmagdiff_forplot(m,k);
     end

         end
     end
 end
 clear diff
 % %drone comparison to RB
 % for k=1:size(x_rb,2)
 %     for m=1:size(y_rb,1)
 %         for p=1:size(drone_x,2)
 %             for q=1:size(drone_y,1)
 %                 diff(q,p)=sqrt((x_rb(1,k)-drone_x(1,p))^2+(y_rb(m,1)-
drone_y(q,1))^2);
 %             end
 %         end
 %          smallestRBDronediff(m,k)=min(min(diff));
 %          for t=1:q
 %              for s=1:p
 %                  if diff(t,s)==smallestRBDronediff(m,k)
 %
      smallestRBDronediff_drone_x_cellnumber(m,k)=s;
 %
      smallestRBDronediff_drone_y_cellnumber(m,k)=t;
 %                  end
 %              end
 %          end
 %     end
 % end
 %
 % %now find velocity difference for matched points for RB & Drone
 % for k=1:size(u_rb,2)
 %     for m=1:size(u_rb,1)
```

```
 %         if smallestRBDronediff(m,k) > 0.5 %needs a sensitivity analysis
 %            uvelRBDronediff(m,k) = NaN;
 %            vvelRBDronediff(m,k) = NaN;
 %         else
 %         uvelRBDronediff(m,k)=u_rb(m,k)-
drone_uvel(smallestRBDronediff_drone_y_cellnumber(m,k),smallestRBDronediff_drone
_x_cellnumber(m,k));
 %         vvelRBDronediff(m,k)=v_rb(m,k)-
drone_vvel(smallestRBDronediff_drone_y_cellnumber(m,k),smallestRBDronediff_drone
_x_cellnumber(m,k));
 %         end
 %     end
 % end
 % clear diff
 % %drone comparison to LB
 % for k=1:size(x_lb,2)
 %     for m=1:size(y_lb,1)
 %         for p=1:size(drone_x,2)
 %             for q=1:size(drone_y,1)
 %                 diff(q,p)=sqrt((x_lb(1,k)-drone_x(1,p))^2+(y_lb(m,1)-
drone_y(q,1))^2);
 %             end
 %         end
 %          smallestLBDronediff(m,k)=min(min(diff));
 %          for t=1:q
 %              for s=1:p
 %                  if diff(t,s)==smallestLBDronediff(m,k)
 %
      smallestLBDronediff_drone_x_cellnumber(m,k)=s;
 %
      smallestLBDronediff_drone_y_cellnumber(m,k)=t;
 %                 end
 %              end
 %          end
 %     end
 % end
 %
 % %now find velocity difference for matched points for LB & Drone
 % for k=1:size(u_lb,2)
 %     for m=1:size(u_lb,1)
 %         if smallestLBDronediff(m,k) > 0.5 %needs a sensitivity analysis
 %            uvelLBDronediff(m,k) = NaN;
 %            vvelLBDronediff(m,k) = NaN;
 %         else
```

```
 %         uvelLBDronediff(m,k)=u_lb(m,k)-
drone_uvel(smallestLBDronediff_drone_y_cellnumber(m,k),smallestLBDronediff_drone
_x_cellnumber(m,k));
 %         vvelLBDronediff(m,k)=v_lb(m,k)-
drone_vvel(smallestLBDronediff_drone_y_cellnumber(m,k),smallestLBDronediff_drone
_x_cellnumber(m,k));
 %         end
 %     end
 % end
 % clear diff
 % %drone comparison to Cam1
 % for k=1:size(x_cam1,2)
 %     for m=1:size(y_cam1,1)
 %         for p=1:size(drone_x,2)
 %             for q=1:size(drone_y,1)
 %                 diff(q,p)=sqrt((x_cam1(1,k)-drone_x(1,p))^2+(y_cam1(m,1)-
drone_y(q,1))^2);
 %             end
 %         end
 %          smallestCam1Dronediff(m,k)=min(min(diff));
 %          for t=1:q
 %              for s=1:p
 %                  if diff(t,s)==smallestCam1Dronediff(m,k)
 %
      smallestCam1Dronediff_drone_x_cellnumber(m,k)=s;
 %
      smallestCam1Dronediff_drone_y_cellnumber(m,k)=t;
 %                  end
 %              end
 %          end
 %     end
 % end
 %
 % %now find velocity difference for matched points for Cam1 & Drone
 % for k=1:size(u_cam1,2)
 %     for m=1:size(u_cam1,1)
 %         if smallestCam1Dronediff(m,k) > 0.5 %needs a sensitivity analysis
 %            uvelCam1Dronediff(m,k) = NaN;
 %            vvelCam1Dronediff(m,k) = NaN;
 %         else
 %         uvelCam1Dronediff(m,k)=u_cam1(m,k)-
drone_uvel(smallestCam1Dronediff_drone_y_cellnumber(m,k),smallestCam1Dronediff_d
rone_x_cellnumber(m,k));
 %         vvelCam1Dronediff(m,k)=v_cam1(m,k)-
drone_vvel(smallestCam1Dronediff_drone_y_cellnumber(m,k),smallestCam1Dronediff_d
rone_x_cellnumber(m,k));
```

```
 %         end
 %     end
 % end
 % clear diff
 %Cam1 to LB
 for k=1:size(x_cam1,2)
     for m=1:size(y_cam1,1)
         for p=1:size(x_lb,2)
             for q=1:size(y_lb,1)
                 diff(q,p)=sqrt((x_cam1(1,k)-x_lb(1,p))^2+(y_cam1(m,1)-
y_lb(q,1))^2);
             end
         end
          smallestLBCam1diff(m,k)=min(min(diff));
          for t=1:q
              for s=1:p
                  if diff(t,s)==smallestLBCam1diff(m,k)
                                      smallestLBCam1diff_x_lb_cellnumber(m,k)=s;
                                      smallestLBCam1diff_y_lb_cellnumber(m,k)=t;

                  end
              end
          end
     end
 end

 %now find velocity difference for matched points for Cam1 & LB
 for k=1:size(u_cam1,2)
     for m=1:size(u_cam1,1)
         if smallestLBCam1diff(m,k) > 0.5 %needs a sensitivity analysis
            uvelCam1LBdiff(m,k) = NaN;
            vvelCam1LBdiff(m,k) = NaN;
         else
         uvelCam1LBdiff(m,k)=u_cam1(m,k)-
u_lb(smallestLBCam1diff_y_lb_cellnumber(m,k),smallestLBCam1diff_x_lb_cellnumber(
m,k));
         vvelCam1LBdiff(m,k)=v_cam1(m,k)-
v_lb(smallestLBCam1diff_y_lb_cellnumber(m,k),smallestLBCam1diff_x_lb_cellnumber(
m,k));
         end
     end
 end
 clear diff
 %Cam1 to RB
 for k=1:size(x_cam1,2)
     for m=1:size(y_cam1,1)
```

```
         for p=1:size(x_rb,2)
             for q=1:size(y_rb,1)
                 diff(q,p)=sqrt((x_cam1(1,k)-x_rb(1,p))^2+(y_cam1(m,1)-
y_rb(q,1))^2);
             end
         end
          smallestCam1RBdiff(m,k)=min(min(diff));
          for t=1:q
              for s=1:p
              % for s=1
                  if diff(t,s)==smallestCam1RBdiff(m,k)
                                      smallestCam1RBdiff_x_rb_cellnumber(m,k)=s;
                            smallestCam1RBdiff_y_rb_cellnumber(m,k)=t;
                  end
              end
          end
     end
 end

 %now find velocity difference for matched points for Cam1 & RB
 for k=1:size(u_cam1,2)
     for m=1:size(u_cam1,1)
         if smallestCam1RBdiff(m,k) > 0.5 %needs a sensitivity analysis
            uvelCam1RBdiff(m,k) = NaN;
            vvelCam1RBdiff(m,k) = NaN;
         else
         uvelCam1RBdiff(m,k)=u_cam1(m,k)-
u_rb(smallestCam1RBdiff_y_rb_cellnumber(m,k),smallestCam1RBdiff_x_rb_cellnumber(
m,k));
         vvelCam1RBdiff(m,k)=v_cam1(m,k)-
v_rb(smallestCam1RBdiff_y_rb_cellnumber(m,k),smallestCam1RBdiff_x_rb_cellnumber(
m,k));
         end
     end
 end
 clear diff
 % %compare ADCP to drone
 % ADCPDronediff(length(adcpdata),size(drone_y,1),size(drone_x,2))=NaN;
 % for k=1:size(drone_x,2)
 %     for m=1:size(drone_y,1)
 %             for q=1:length(adcpdata)
 %                 ADCPDronediff(q,m,k)=sqrt((drone_x(1,k)-
adcpdata(q,1))^2+(drone_y(m,1)-adcpdata(q,2))^2);
 %             end
 %             smallestADCPDronediff(m,k)=min(min(ADCPDronediff(:,m,k)));
 %             for q=1:length(adcpdata)
```

```
 %             for t=1:size(drone_y,1)
 %              for s=1:size(drone_x,2)
 %                  if ADCPDronediff(q,t,s)==smallestADCPDronediff(m,k)
 %
      smallestADCPDronediff_drone_x_cellnumber(m,k)=s;
 %
      smallestADCPDronediff_drone_y_cellnumber(m,k)=t;
 %                      smallestADCPDronediff_ADCPCellDrone(m,k)=q;
 %                   end
 %                end
 %             end
 %         end
 %     end
 % end
 %
 % %now find velocity difference for matched points for drone and ADCP
 % uvelADCPDronediff = NaN(m,k);
 % vvelADCPDronediff = NaN(m,k);
 %
 % ADCPdronevelmagdiff_lowestvel= NaN(m,k);
 % ADCPdronevelmagdiff_lowvel= NaN(m,k);
 % ADCPdronevelmagdiff_mediumvel= NaN(m,k);
 % ADCPdronevelmagdiff_mediumhighvel= NaN(m,k);
 % ADCPdronevelmagdiff_highvel= NaN(m,k);
 %
 % for k=1:size(drone_uvel,2)
 %     for m=1:size(drone_uvel,1)
 %         if smallestADCPDronediff(m,k) > 1.0
 %            uveldiffADCPDrone(m,k) = NaN;
 %            vveldiffADCPDrone(m,k) = NaN;
 %         else
 %
uvelADCPDronediff(m,k)=adcpdata(smallestADCPDronediff_ADCPCellDrone(m,k),3)-
drone_uvel(smallestADCPDronediff_drone_y_cellnumber(m,k),smallestADCPDronediff_d
rone_x_cellnumber(m,k));
 %
vvelADCPDronediff(m,k)=adcpdata(smallestADCPDronediff_ADCPCellDrone(m,k),4)-
drone_vvel(smallestADCPDronediff_drone_y_cellnumber(m,k),smallestADCPDronediff_d
rone_x_cellnumber(m,k));
 %
 %         %added to bin by velocity
 %
ADCPDronevelmagdiff_forplot(m,k)=sqrt(uvelADCPDronediff(m,k).^2+vvelADCPDronedif
f(m,k).^2);
 %     if adcpmagnitude(smallestADCPDronediff_ADCPCellDrone(m,k)) <= lowestvel
 %         ADCPdronevelmagdiff_lowestvel(m,k)=ADCPDronevelmagdiff_forplot(m,k);
```

```
 %     elseif adcpmagnitude(smallestADCPDronediff_ADCPCellDrone(m,k)) <= lowvel
 %         ADCPdronevelmagdiff_lowvel(m,k)=ADCPDronevelmagdiff_forplot(m,k);
 %     elseif adcpmagnitude(smallestADCPDronediff_ADCPCellDrone(m,k)) <=
mediumvel
 %         ADCPdronevelmagdiff_mediumvel(m,k)=ADCPDronevelmagdiff_forplot(m,k);
 %     elseif adcpmagnitude(smallestADCPDronediff_ADCPCellDrone(m,k)) <=
mediumhighvel
 %
ADCPdronevelmagdiff_mediumhighvel(m,k)=ADCPDronevelmagdiff_forplot(m,k);
 %     else %high vel
 %         ADCPdronevelmagdiff_highvel(m,k)=ADCPDronevelmagdiff_forplot(m,k);
 %     end
 %         end
 %     end
 % end
 % clear diff
 %compare ADCP to cam1
 ADCPCam1diff(length(adcpdata),size(y_cam1,1),size(x_cam1,2))=NaN;
 for k=1:size(x_cam1,2)
     for m=1:size(y_cam1,1)
             for q=1:length(adcpdata)
                 ADCPCam1diff(q,m,k)=sqrt((x_cam1(1,k)-
adcpdata(q,1))^2+(y_cam1(m,1)-adcpdata(q,2))^2);
             end
             smallestADCPCam1diff(m,k)=min(min(ADCPCam1diff(:,m,k)));
             for q=1:length(adcpdata)
             for t=1:size(y_cam1,1)
              for s=1:size(x_cam1,2)
                  if ADCPCam1diff(q,t,s)==smallestADCPCam1diff(m,k)

      smallestADCPCam1diff_x_cam1_cellnumber(m,k)=s;

      smallestADCPCam1diff_y_cam1_cellnumber(m,k)=t;
                          smallestADCPCam1diff_ADCPCellCam1(m,k)=q;
                  end
                end
             end
         end
     end
 end


 %now find velocity difference for matched points for cam1 and ADCP

 ADCPCam1velmagdiff_lowestvel= NaN(m,k);
 ADCPCam1velmagdiff_lowvel= NaN(m,k);
```

```
 ADCPCam1velmagdiff_mediumvel= NaN(m,k);
 ADCPCam1velmagdiff_mediumhighvel= NaN(m,k);
 ADCPCam1velmagdiff_highvel= NaN(m,k);

 for k=1:size(u_cam1,2)
     for m=1:size(v_cam1,1)
         if smallestADCPCam1diff(m,k) > 1.0 %needs a sensitivity analysis
            uvelADCPCam1diff(m,k) = NaN;
            vvelADCPCam1diff(m,k) = NaN;
         else

uvelADCPCam1diff(m,k)=adcpdata(smallestADCPCam1diff_ADCPCellCam1(m,k),3)-
u_cam1(smallestADCPCam1diff_y_cam1_cellnumber(m,k),smallestADCPCam1diff_x_cam1_c
ellnumber(m,k));

vvelADCPCam1diff(m,k)=adcpdata(smallestADCPCam1diff_ADCPCellCam1(m,k),4)-
v_cam1(smallestADCPCam1diff_y_cam1_cellnumber(m,k),smallestADCPCam1diff_x_cam1_c
ellnumber(m,k));

 %added to bin by velocity

ADCPCam1velmagdiff_forplot(m,k)=sqrt(uvelADCPCam1diff(m,k).^2+vvelADCPCam1diff(m
,k).^2);
     if adcpmagnitude(smallestADCPCam1diff_ADCPCellCam1(m,k)) < lowestvel
         ADCPCam1velmagdiff_lowestvel(m,k)=ADCPCam1velmagdiff_forplot(m,k);
     elseif adcpmagnitude(smallestADCPCam1diff_ADCPCellCam1(m,k)) < lowvel
         ADCPCam1velmagdiff_lowvel(m,k)=ADCPCam1velmagdiff_forplot(m,k);
     elseif adcpmagnitude(smallestADCPCam1diff_ADCPCellCam1(m,k)) < mediumvel
         ADCPCam1velmagdiff_mediumvel(m,k)=ADCPCam1velmagdiff_forplot(m,k);
     elseif adcpmagnitude(smallestADCPCam1diff_ADCPCellCam1(m,k)) <
mediumhighvel
         ADCPCam1velmagdiff_mediumhighvel(m,k)=ADCPCam1velmagdiff_forplot(m,k);
     else %high vel
         ADCPCam1velmagdiff_highvel(m,k)=ADCPCam1velmagdiff_forplot(m,k);
     end

         end
     end
 end
 clear diff
 March18=1.163;
 March21=1.5114;
 April8=1.7337;
 May522=0.5631;
 May523=1.5133;
 March6=1.3557;
```

```
 May15=0.5539;

 %velocity differences for cameras & ADCP data, use above to scale

 % ADCPRBvelmagdiff=sqrt(uveldiffADCPRB.^2+vveldiffADCPRB.^2);
 % ADCPLBvelmagdiff=sqrt(uveldiffADCPLB.^2+vveldiffADCPLB.^2);
 % velmagdiff=sqrt(uveldiff.^2+vveldiff.^2); %LB & RB camera
 % % DroneRBvelmagdiff=sqrt(uvelRBDronediff.^2+vvelRBDronediff.^2);
 % % DroneLBvelmagdiff=sqrt(uvelLBDronediff.^2+vvelLBDronediff.^2);
 % % DroneCam1velmagdiff=sqrt(uvelCam1Dronediff.^2+vvelCam1Dronediff.^2);
 % Cam1RBvelmagdiff=sqrt(uvelCam1RBdiff.^2+vvelCam1RBdiff.^2);
 % Cam1LBvelmagdiff=sqrt(uvelCam1LBdiff.^2+vvelCam1LBdiff.^2);
 % % ADCPDronevelmagdiff=sqrt(uvelADCPDronediff.^2+vvelADCPDronediff.^2);
 % ADCPCam1velmagdiff=sqrt(uvelADCPCam1diff.^2+vvelADCPCam1diff.^2);

 %scaled velocity differences

 ADCPRBvelmagdiff=(sqrt(uveldiffADCPRB.^2+vveldiffADCPRB.^2))./March6;
 ADCPLBvelmagdiff=(sqrt(uveldiffADCPLB.^2+vveldiffADCPLB.^2))./March6;
 velmagdiff=(sqrt(uveldiff.^2+vveldiff.^2))./March6; %LB & RB camera
 % % % DroneRBvelmagdiff=(sqrt(uvelRBDronediff.^2+vvelRBDronediff.^2))./March18;
 % % % DroneLBvelmagdiff=(sqrt(uvelLBDronediff.^2+vvelLBDronediff.^2))./March18;
 % % %
DroneCam1velmagdiff=(sqrt(uvelCam1Dronediff.^2+vvelCam1Dronediff.^2))./March18;
 Cam1RBvelmagdiff=(sqrt(uvelCam1RBdiff.^2+vvelCam1RBdiff.^2))./March6;
 Cam1LBvelmagdiff=(sqrt(uvelCam1LBdiff.^2+vvelCam1LBdiff.^2))./March6;
 % % % %
ADCPDronevelmagdiff=(sqrt(uvelADCPDronediff.^2+vvelADCPDronediff.^2))./May523;
 ADCPCam1velmagdiff=(sqrt(uvelADCPCam1diff.^2+vvelADCPCam1diff.^2))./March6;


 %plots for difference between cameras
 % plot for RB & LB
 figure
 surf(x_rb, y_rb, velmagdiff) %surf plots in planar looks better than contour
 title('Velocity Difference (m/s) between Right Bank Camera & Left Bank Camera',
'FontSize', 8) %for absolute values
 % title('Normalized Velocity Difference between Right Bank Camera & Left Bank
Camera', 'FontSize', 8) %for normalized values
 fontsize(gcf, scale=2.25)
 xlabel('Easting, m', 'FontSize', 28)
 ylabel('Northing, m', 'FontSize', 28)
 shading faceted
 % clim([0 1.8]) %colorbar limits for absolute differences
 clim([0 1.3]) %colorbar limits for normalized differences
 colorbar
```

```
 % plots for RB & ADCB
 figure
 surf(x_rb, y_rb, ADCPRBvelmagdiff)
 title('Velocity Difference (m/s) between Right Bank Camera & ADCP', 'FontSize',
8)
 % title('Normalized Velocity Difference between Right Bank Camera & ADCP',
'FontSize', 8) %for normalized values
 fontsize(gcf, scale=2.25)
 xlabel('Easting, m', 'FontSize', 28)
 ylabel('Northing, m', 'FontSize', 28)
 shading faceted
 % clim([0 1.8])
 clim([0 1.3]) %colorbar limits for normalized differences
 colorbar

 % plots for LB & ADCP
 figure
 surf(x_lb, y_lb, ADCPLBvelmagdiff)
 title('Velocity Difference (m/s) between Left Bank Camera & ADCP', 'FontSize',
8)
 % title('Normalized Velocity Difference between Left Bank Camera & ADCP',
'FontSize', 8) %for normalized values
 fontsize(gcf, scale=2.25)
 xlabel('Easting, m', 'FontSize', 28)
 ylabel('Northing, m', 'FontSize', 28)
 shading faceted
 % clim([0 1.8])
 clim([0 1.3]) %colorbar limits for normalized differences
 colorbar

 % %plot for RB & Drone
 % figure
 % surf(x_rb, y_rb, DroneRBvelmagdiff)
 % title('Velocity Difference (m/s) between Right Bank Camera & Drone (054)',
'FontSize', 8)
 % % title('Normalized Velocity Difference between Right Bank Camera & Drone
(054)', 'FontSize', 8) %for normalized values
 % fontsize(gcf, scale=2.25)
 % xlabel('Easting, m', 'FontSize', 28)
 % ylabel('Northing, m', 'FontSize', 28)
 % shading faceted
 % % clim([0 2.1])
 % clim([0 1]) %colorbar limits for normalized differences
 % colorbar
```

```
 %
 % %plot for LB & Drone
 % figure
 % surf(x_lb, y_lb, DroneLBvelmagdiff)
 % title('Velocity Difference (m/s) between Left Bank Camera & Drone (054)',
'FontSize', 8)
 % % title('Normalized Velocity Difference between Left Bank Camera & Drone
(054)', 'FontSize', 8) %for normalized values
 % fontsize(gcf, scale=2.25)
 % xlabel('Easting, m', 'FontSize', 28)
 % ylabel('Northing, m', 'FontSize', 28)
 % shading faceted
 % % clim([0 2.1])
 % clim([0 1]) %colorbar limits for normalized differences
 % colorbar
 %
 % %plot for Cam1 & Drone
 % figure
 % surf(x_cam1, y_cam1, DroneCam1velmagdiff)
 % title('Velocity Difference (m/s) between Gaugehouse Camera & Drone (054)',
'FontSize', 8)
 % % title('Normalized Velocity Difference between Gaugehouse Camera & Drone
(054)', 'FontSize', 8) %for normalized values
 % fontsize(gcf, scale=2.25)
 % xlabel('Easting, m', 'FontSize', 28)
 % ylabel('Northing, m', 'FontSize', 28)
 % shading faceted
 % % clim([0 2.1])
 % clim([0 1]) %colorbar limits for normalized differences
 % colorbar

 % plot for Cam1 & RB
 figure
 surf(x_cam1, y_cam1, Cam1RBvelmagdiff)
 title('Velocity Difference (m/s) between Gaugehouse Camera & Right Bank
Camera', 'FontSize', 8)
 % title('Normalized Velocity Difference between Gaugehouse Camera & Right Bank
Camera', 'FontSize', 8) %for normalized values
 fontsize(gcf, scale=2.25)
 xlabel('Easting, m', 'FontSize', 28)
 ylabel('Northing, m', 'FontSize', 28)
 shading faceted
 % clim([0 1.8])
 clim([0 1.3]) %colorbar limits for normalized differences
 colorbar
```

```
 %plot for Cam1 & LB
 figure
 surf(x_cam1, y_cam1, Cam1LBvelmagdiff)
 title('Velocity Difference (m/s) between Gaugehouse Camera & Left Bank Camera',
'FontSize', 8)
 % title('Normalized Velocity Difference between Gaugehouse Camera & Left Bank
Camera', 'FontSize', 8) %for normalized values
 fontsize(gcf, scale=2.25)
 xlabel('Easting, m', 'FontSize', 28)
 ylabel('Northing, m', 'FontSize', 28)
 shading faceted
 % clim([0 1.8])
 clim([0 1.3]) %colorbar limits for normalized differences
 colorbar

 % plot for Cam1 & ADCP
 figure
 surf(x_cam1, y_cam1, ADCPCam1velmagdiff)
 title('Velocity Difference (m/s) between Gaugehouse Camera & ADCP', 'FontSize',
8)
 % title('Normalized Velocity Difference between Gaugehouse Camera & ADCP',
'FontSize', 8) %for normalized values
 fontsize(gcf, scale=2.25)
 xlabel('Easting, m', 'FontSize', 28)
 ylabel('Northing, m', 'FontSize', 28)
 shading faceted
 % clim([0 1.8])
 clim([0 1.3]) %colorbar limits for normalized differences
 colorbar

 %plot for Drone & ADCP
 % figure
 % surf(drone_x, drone_y, ADCPDronevelmagdiff)
 % title('Velocity Difference (m/s) between Drone (054) & ADCP', 'FontSize', 8)
 % % title('Normalized Velocity Difference between Drone (054) & ADCP',
'FontSize', 8) %for normalized values
 % fontsize(gcf, scale=2.25)
 % xlabel('Easting, m', 'FontSize', 28)
 % ylabel('Northing, m', 'FontSize', 28)
 % shading faceted
 % % clim([0 1.25])
 % clim([0 0.8]) %colorbar limits for normalized differences
 % colorbar
 %error metrics
 meanabserror=mean(abs(velmagdiff(:)), 'omitnan')
 meanabsRBADCPerror=mean(abs(ADCPRBvelmagdiff(:)), 'omitnan')
```

```
meanabsLBADCPerror=mean(abs(ADCPLBvelmagdiff(:)), 'omitnan')
% meanabsDroneRBerror=mean(abs(DroneRBvelmagdiff(:)), 'omitnan')
% meanabsDroneLBerror=mean(abs(DroneLBvelmagdiff(:)), 'omitnan')
% meanabsDroneCam1error=mean(abs(DroneCam1velmagdiff(:)), 'omitnan')
meanabsCam1RBerror=mean(abs(Cam1RBvelmagdiff(:)), 'omitnan')
meanabsCam1LBerror=mean(abs(Cam1LBvelmagdiff(:)), 'omitnan')
meanabsCam1ADCPerror=mean(abs(ADCPCam1velmagdiff(:)), 'omitnan')
% meanabsADCPDroneerror=mean(abs(ADCPDronevelmagdiff(:)), 'omitnan')

maxdiff = max(velmagdiff(:))
maxADCPRBdiff = max(ADCPRBvelmagdiff(:))
maxADCPLBdiff = max(ADCPLBvelmagdiff(:))
% maxDroneRBdiff = max(DroneRBvelmagdiff(:))
% maxDroneLBdiff = max(DroneLBvelmagdiff(:))
% maxDroneCam1diff = max(DroneCam1velmagdiff(:))
maxCam1RBdiff = max(Cam1RBvelmagdiff(:))
maxCam1LBdiff = max(Cam1LBvelmagdiff(:))
maxCam1ADCPdiff = max(ADCPCam1velmagdiff(:))
% maxDroneADCPdiff = max(ADCPDronevelmagdiff(:))
LBCameraE=473025.727;
LBCameraN=5012172.741;
LBCameraEl=10.79;
RBCameraE=473052.715;
RBCameraN=5012136.16;
RBCameraEl=10.777;
Cam1E=473017.15;
Cam1N=5012169.649;
Cam1El=13.429;
WSE_March21 = 4.352;
WSE_April8 = 4.164;
WSE_May5 = 3.629;
WSE_March6 = 3.677;
WSE_May15 = 3.303;
D054_E = 473030.43;
D054_N = 5012142.005;
D054_Alt = 31.276;
D055_E = 473020.887;
D055_N = 5012130.269;
D055_Alt = 28.976;
D056_E = 473020.376;
D056_N = 5012120.717;
D056_Alt = 22.476;
D057_E = 473011.351;
D057_N = 5012120.2;
D057_Alt = 17.076;
D058_E = 473014.574;
```

```
 D058_N = 5012121.742;
 D058_Alt = 11.176;
 D059_E = 473014.889;
 D059_N = 5012121.852;
 D059_Alt = 5.776;


 distancetoLBcamera=sqrt((x_lb-LBCameraE).^2+(y_lb-LBCameraN).^2+(WSE_March6-
LBCameraEl).^2); %need to change WSE each time
 distancetoRBcamera=sqrt((x_rb-RBCameraE).^2+(y_rb-RBCameraN).^2+(WSE_March6-
RBCameraEl).^2);
 distancetoCam1=sqrt((x_cam1-Cam1E).^2+(y_cam1-Cam1N).^2+(WSE_March6-
Cam1El).^2);
 % distancetoDrone=sqrt((drone_x-D059_E).^2+(drone_y-D059_N).^2+(WSE_May15-
D059_Alt).^2); %need to change drone file name
 %
 % figure
 % hold on
 % plot(distancetoDrone(:),ADCPdronevelmagdiff_lowestvel(:),'+','Color','k')
 % plot(distancetoDrone(:),ADCPdronevelmagdiff_lowvel(:),'+','Color','r')
 % plot(distancetoDrone(:),ADCPdronevelmagdiff_mediumvel(:), '+', 'Color', 'b')
 % plot(distancetoDrone(:),ADCPdronevelmagdiff_mediumhighvel(:), '+', 'Color',
'magenta')
 % plot(distancetoDrone(:),ADCPdronevelmagdiff_highvel(:), '+', 'Color', 'g')
 % fontsize(gcf, scale=2.5)
 % xlabel('Distance between Drone and Surface Velocity Vector', 'FontSize', 22)
 % ylabel('Velocity Difference between ADCP and Drone', 'FontSize', 22)
 % ylim([0 1.0])
 % legend('0 - 0.2429m/s', '0.2429 - 0.3938m/s', '0.3938 - 0.5446m/s','0.5446 -
0.6955m/s', '0.6995+m/s', 'FontSize', 8)
 % title('Distance to Drone vs. Velocity Difference between Image Velocimetry &
ADCP', 'FontSize', 16)
 % hold off
 %
 %
 figure
 hold on
 plot(distancetoCam1(:),ADCPCam1velmagdiff_lowestvel(:),'+','Color','k')
 plot(distancetoCam1(:),ADCPCam1velmagdiff_lowvel(:),'+','Color','r')
 plot(distancetoCam1(:),ADCPCam1velmagdiff_mediumvel(:), '+', 'Color', 'b')
 plot(distancetoCam1(:),ADCPCam1velmagdiff_mediumhighvel(:), '+', 'Color',
'magenta')
 fontsize(gcf, scale=2.5)
 plot(distancetoCam1(:),ADCPCam1velmagdiff_highvel(:), '+', 'Color', 'g')
 xlabel('Distance between Gaugehouse Camera and Surface Velocity Vector',
'FontSize', 22)
```

```
 ylabel('Velocity Difference between ADCP and Gaugehouse Camera', 'FontSize',
22)
 ylim([0 2.0])
 legend('0 - 0.9792m/s', '0.9792 - 1.2130m/s', '1.2130 - 1.4468m/s','1.4468 -
1.6806m/s', '1.6806+m/s', 'FontSize', 18)
 title('Distance to Gaugehouse Camera vs. Velocity Difference between Image
Velocimetry & ADCP', 'FontSize', 16)
 hold off

 figure
 hold on
 plot(distancetoLBcamera(:),ADCPLBvelmagdiff_lowestvel(:),'+','Color','k')
 plot(distancetoLBcamera(:),ADCPLBvelmagdiff_lowvel(:),'+','Color','r')
 plot(distancetoLBcamera(:),ADCPLBvelmagdiff_mediumvel(:), '+', 'Color', 'b')
 plot(distancetoLBcamera(:),ADCPLBvelmagdiff_mediumhighvel(:), '+', 'Color',
'magenta')
 fontsize(gcf, scale=2.5)
 plot(distancetoLBcamera(:),ADCPLBvelmagdiff_highvel(:), '+', 'Color', 'g')
 xlabel('Distance between Left Bank Camera and Surface Velocity Vector',
'FontSize', 22)
 ylabel('Velocity Difference between ADCP and Left Bank Camera', 'FontSize', 22)
 ylim([0 2.0])
 legend('0 - 0.9792m/s', '0.9792 - 1.2130m/s', '1.2130 - 1.4468m/s','1.4468 -
1.6806m/s', '1.6806+m/s', 'FontSize', 18)
 title('Distance to Left Bank Camera vs. Velocity Difference between Image
Velocimetry & ADCP', 'FontSize', 16)
 hold off

 figure
 hold on
 plot(distancetoRBcamera(:),ADCPRBvelmagdiff_lowestvel(:),'+','Color','k')
 plot(distancetoRBcamera(:),ADCPRBvelmagdiff_lowvel(:),'+','Color','r')
 plot(distancetoRBcamera(:),ADCPRBvelmagdiff_mediumvel(:), '+', 'Color', 'b')
 plot(distancetoRBcamera(:),ADCPRBvelmagdiff_mediumhighvel(:), '+', 'Color',
'magenta')
 plot(distancetoRBcamera(:),ADCPRBvelmagdiff_highvel(:), '+', 'Color', 'g')
 fontsize(gcf, scale=2.5)
 xlabel('Distance between Rigth Bank Camera and Surface Velocity Vector',
'FontSize', 22)
 ylabel('Velocity Difference between ADCP and Right Bank Camera', 'FontSize',
22)
 ylim([0 2.0])
 legend('0 - 0.9792m/s', '0.9792 - 1.2130m/s', '1.2130 - 1.4468m/s','1.4468 -
1.6806m/s', '1.6806+m/s', 'FontSize', 18)
 title('Distance to Right Bank Camera vs. Velocity Difference between Image
Velocimetry & ADCP', 'FontSize', 16)
```

```
 hold off

 % figure
 % plot(distancetoRBcamera, ADCPRBvelmagdiff, '+','Color', 'k')
 % xlabel('Distance to Camera (m)')
 % ylabel('Velocity Difference compared to ADCP (m/s)')
 % title('May 5th, 2023', 'Distance to Right Bank Camera vs Velocity Difference
Compared to ADCP')
 %
 % figure
 % plot(distancetoCam1, ADCPCam1velmagdiff, '+','Color', 'k')
 % xlabel('Distance to Camera (m)')
 % ylabel('Velocity Difference compared to ADCP (m/s)')
 % title('May 5th, 2023','Distance to Camera 1 vs Velocity Difference Compared
to ADCP')
 %angle plots vs error

 % % angleLB=asin(7.161./distancetoLBcamera);
 % % angleRB=asin(7.161./distancetoRBcamera);
 % % angleCam1=asin(9.8./distancetoCam1);
 % %
 % % figure
 % % plot(angleLB, ADCPLBvelmagdiff, '+', 'Color', 'k')
 % % xlabel('Angle between camera and Vector')
 % % ylabel('Velocity Difference compared to ADCP (m/s)')
 % %
 % % figure
 % % plot(angleCam1, ADCPCam1velmagdiff, '+', 'Color', 'k')
 %
 % writematrix(ADCPRBvelmagdiff, 'ADCPRBvelmagdiff.csv');
 % writematrix(ADCPLBvelmagdiff, 'ADCPLBvelmagdiff.csv');
 % writematrix(ADCPCam1velmagdiff, 'ADCPCam1velmagdiff.csv');
 % % writematrix(ADCPDronevelmagdiff, 'ADCPDronevelmagdiff.csv');
 % writematrix(distancetoLBcamera, 'DistancetoLBcamera.csv');
 % writematrix(distancetoRBcamera, 'DistancetoRBcamera.csv');
 % writematrix(distancetoCam1, 'DistancetoCam1.csv');
 % % writematrix(distancetoDrone, 'DistancetoDrone.csv');
```

Combining Discharge Code

```
 % GCPS=readmatrix('DistanceMadeGoodGCPs_Upper.csv', 'Range', 'B2:E3'); %load
file with both Real-World Coordinates & Camera coords
 %
 % GCPS_EN=GCPS(1:2,3:4)-GCPS(1,3:4); %need to change this to be based on upper
gcps
 % GCPS_xy=GCPS(1:2, 1:2);
 %
 % theta=[];
 % theta=0:0.01:2*pi;
 % for k=1:length(theta)
 %     Estar(k)=GCPS_xy(2,1).*cos(theta(k))-GCPS_xy(2,2).*sin(theta(k)); %is
this set up right?
 %     Nstar(k)=GCPS_xy(2,2).*cos(theta(k))+GCPS_xy(2,1).*sin(theta(k));
 %     diffE(k)=Estar(k)-GCPS_EN(2,1);
 %     diffN(k)=Nstar(k)-GCPS_EN(2,2);
 % end
 %
 % %diffE and diffN = 542.5 for upper GCPs
 %
 %     %test this by putting an xy gcp onto EN gcp
 %  % GCPS_xy(2,1).*cos(5.42)-GCPS_xy(2,2).*sin(5.42)=26.13
 % %this is 3cm off (26.10)
 x = readmatrix('April8XSData.csv', 'Range', 'A2:A40'); %cross-section x
 y = readmatrix('April8XSData.csv', 'Range', 'B2:B40'); %cross-section y

 theta = 5.42 %when including upper control points
 % theta = 5.395 %when starting at left bank
 % theta=2.255; %when starting at right bank, shouldn't need this
 GCP05x = 473022.077;
 GCP05y = 5012165.405;
 GCP08x = 473048.18;
 GCP08y = 5012134.838;
 %for surveys with water levels past lower gcps I will need to redo
 %everything with the upper level gcps including finding a new angle

     Easting=x.*cos(theta)-y.*sin(theta); %rotate EN coordinates
     Northing=y.*cos(theta)+x.*sin(theta);

     x_xs = Easting + GCP05x;
     y_xs = Northing + GCP05y;

 %test plot to confirm line makes sense
 % figure
 % hold on
```

```
 % plot(x_xs, y_xs)
 % plot(GCP05x, GCP05y, 'x')
 % plot(GCP08x, GCP08y, 'o')
 % hold off
 z_xs = readmatrix('April8XSData.csv', 'Range', 'C2:C460'); %xs elevation data
 wse = 4.164; %this has to be changed with each survey
 %add bank coordinates manually, Idk how to do it here

 for k=1:length(z_xs)
      if z_xs(k)>=wse
            z_xs(k)=NaN;
            x_xs(k)=NaN;
            y_xs(k)=NaN;
      end
 end
 rb_range=input('input the sheet range for rb data, ie x#:x# in single quotes ')
%changes for every dataset
 lb_range=input('input the sheet range for lb data, ie x#:x# in single quotes ')

 u_rb = readmatrix('U_RB04082022.csv');
 u_lb = readmatrix('U_LB04082022.csv');
 v_rb = readmatrix('V_RB04082022.csv');
 v_lb = readmatrix('V_LB04082022.csv');
 x_rb = readmatrix('X_RB04082022.csv','range',rb_range);
 x_lb = readmatrix('X_LB04082022.csv','range',lb_range);
 y_rb = readmatrix('Y_RB04082022.csv','range',rb_range);
 y_lb = readmatrix('Y_LB04082022.csv','range',lb_range);
 for k=1:size(x_rb,2)
     for m=1:size(y_rb,1)
         if y_rb(m,1) - x_rb(1,k)*1.5 <= 4302593  %based on dividing line in
river
             keep_u_rb(m,k) = u_rb(m,k);
             keep_v_rb(m,k) = v_rb(m,k);
         else
             keep_u_rb(m,k) = NaN;
             keep_v_rb(m,k) = NaN;
         end
     end
 end

 for k=1:size(x_lb,2)
     for m=1:size(y_lb,1)
         if y_lb(m,1) - x_lb(1,k)*1.5 >= 4302593
             keep_u_lb(m,k) = u_lb(m,k);
             keep_v_lb(m,k) = v_lb(m,k);
         else
```

```
            keep_u_lb(m,k) = NaN;
            keep_v_lb(m,k) = NaN;
        end
    end
end

% figure
% hold on
% quiver(x_rb, y_rb, keep_u_rb, keep_v_rb)
% quiver(x_lb, y_lb, keep_u_lb, keep_v_lb)
%section for matching cross-section points to surface velocity points, then
%assigning those points as the u and v velocities for rb camera

for q=1:length(y_xs)
    for k=1:size(x_rb,2)
        for m=1:size(y_rb,1)

                diffRB(q,m,k)=sqrt((x_rb(1,k)-x_xs(q))^2+(y_rb(m,1)-
y_xs(q))^2);
            end

    end
end
for q=1:length(y_xs)
    smallestdiffRB(q)=min(min(min(diffRB(q,:,:))));
end



%now find velocity difference for matched points
for q=1:length(y_xs)
        if isnan(smallestdiffRB(q))
            uvel_rb(q)=NaN;
            vvel_rb(q)=NaN;
        else
            for k=1:size(u_rb,2)
            for m=1:size(u_rb,1)
                if diffRB(q,m,k)==smallestdiffRB(q)
                    uvel_rb(q)=keep_u_rb(m,k);
                    vvel_rb(q)=keep_v_rb(m,k);
                    kcheckRB(q)=k;
                    mcheckRB(q)=m;
                end
            end
            end
        end
```

```
end
%for the left bank camera
for q=1:length(y_xs)
    for k=1:size(x_lb,2)
        for m=1:size(y_lb,1)
            diffLB(q,m,k)=sqrt((x_lb(1,k)-x_xs(q))^2+(y_lb(m,1)-y_xs(q))^2);

        end
    end
end

for q=1:length(y_xs)
    smallestdiffLB(q)=min(min(min(diffLB(q,:,:))));
end

%now find velocity difference for matched points

for q=1:length(y_xs)
    if isnan(smallestdiffLB(q))
       uvel_lb(q)=NaN;
       vvel_lb(q)=NaN;
    else
       for k=1:size(u_lb,2)
           for m=1:size(u_lb,1)
               if diffLB(q,m,k)==smallestdiffLB(q)
                   uvel_lb(q)=keep_u_lb(m,k);
                   vvel_lb(q)=keep_v_lb(m,k);
                   kcheckLB(q) = k;
                   mcheckLB(q) = m;
               end
           end
       end
    end
end

figure
hold on
quiver(x_xs, y_xs, uvel_rb', vvel_rb')
quiver(x_xs, y_xs, uvel_lb', vvel_lb')
axis equal
plot(x_xs, y_xs)
plot(GCP05x, GCP05y, 'x')
plot(GCP08x, GCP08y, 'o')
hold off

velmagLB = sqrt((uvel_lb).^2+(vvel_lb).^2);
```

```
velmagRB = sqrt((uvel_rb).^2+(vvel_rb).^2);
velmagLB = rmmissing(velmagLB);
velmagRB = rmmissing(velmagRB);
%concecate the 2 velmagdiffs
vvelLB = rmmissing(vvel_lb);
vvelRB = rmmissing(vvel_rb);
uvelLB = rmmissing(uvel_lb);
uvelRB = rmmissing(uvel_rb);
combinedVvel = [vvelLB vvelRB];
combinedUvel = [uvelLB uvelRB];
combinedvelmag = [velmagLB velmagRB];
rotatedStreamwise = sin(-5.42)*combinedUvel + cos(-5.42)* combinedVvel;
rotatedCrossstream =  combinedUvel*cos(-5.42) - combinedVvel*sin(-5.42);
rotatedvelmag = sqrt((rotatedStreamwise).^2+(rotatedCrossstream).^2);
% z_xs = rmmissing(z_xs);
% x_xs = rmmissing(x_xs);
% y_xs = rmmissing(y_xs);



%calculate discharge, area for the points closest to the bank will have to
%be interpolated using wse
```

Vector Plots Code

```
 rb_range=input('input the sheet range for rb data, ie x#:x# in single quotes ')
%changes for every dataset
 lb_range=input('input the sheet range for lb data, ie x#:x# in single quotes ')
 % drone_range=input('input the sheet range for the drone data in single
quotes')
 cam1_range=input('input the sheet range for the Cam1 data in single quotes ')

 u_rb = readmatrix('U_RB03062024.csv');
 u_lb = readmatrix('U_LB03062024.csv');
 v_rb = readmatrix('V_RB03062024.csv');
 v_lb = readmatrix('V_LB03062024.csv');
 x_rb = readmatrix('X_RB03062024.csv','range',rb_range);
 x_lb = readmatrix('X_LB03062024.csv','range',lb_range);
 y_rb = readmatrix('Y_RB03062024.csv','range',rb_range);
 y_lb = readmatrix('Y_LB03062024.csv','range',lb_range);
 % drone_uvel = readmatrix('U_DJ0018.csv');
 % drone_vvel = readmatrix('V_DJ0018.csv');
 % drone_x = readmatrix('X_DJ0018.csv', 'range', drone_range);
 % drone_y = readmatrix('Y_DJ0018.csv', 'range', drone_range);
 u_cam1 = readmatrix('U_Cam103062024.csv');
 v_cam1 = readmatrix('V_Cam103062024.csv');
 x_cam1 = readmatrix('X_Cam103062024.csv', 'range',cam1_range);
 y_cam1 = readmatrix('Y_Cam103062024.csv', 'range',cam1_range);
 adcpdata = readmatrix('March6th2024ADCPData.csv'); %can go back &
 % forth with line 16 (boxcar average data) and line 18 (single ping)
 % adcpdata = readmatrix('050523SinglePing_AllData.csv');


 % figure
 % hold on
 % quiver(x_rb, y_rb, u_rb, v_rb, 'Autoscale', 'off')
 % quiver(x_lb, y_lb, u_lb, v_lb, 'Autoscale', 'off')
 % quiver(adcpdata(:,1), adcpdata(:,2), adcpdata(:,3), adcpdata(:,4),
'Autoscale', 'off')
 % plot(473043.068, 5012139.943, "Marker","o") %change these points based on the
region of interest for each dataset
 % plot(473044.964,5012143.388, "Marker","o")
 % plot(473022.484,5012158.021, "Marker","o")
 % plot(473029.736,5012164.295, "Marker","o")
 % axis equal
 % title('Left Bank Camera vs. Right Bank Camera vs. ADCP Data')
 % xlabel('Easting, m')
 % ylabel('Northing, m')
 % legend('right bank','left bank', 'ADCP Data')
```

```
% hold off
figure
hold on
quiver(x_rb, y_rb, u_rb, v_rb, 'autoscale', 'off')
quiver(x_lb, y_lb, u_lb, v_lb, 'autoscale', 'off')
axis equal
fontsize(gcf, scale=2.25)
title('Left Bank Camera vs. Right Bank Camera', 'FontSize', 24)
xlabel('Easting, m')
ylabel('Northing, m')
legend('Right bank','Left bank', 'FontSize', 24)
hold off

figure
hold on
quiver(x_rb, y_rb, u_rb, v_rb, 'Autoscale', 'off')
quiver(adcpdata(:,1), adcpdata(:,2), adcpdata(:,3), adcpdata(:,4), 'Autoscale',
'off')
axis equal
fontsize(gcf, scale=2.25)
title('Right Bank Camera vs. ADCP Data', 'FontSize', 24)
xlabel('Easting, m')
ylabel('Northing, m')
legend('Right bank', 'ADCP Data', 'FontSize', 24)
hold off

figure
hold on
quiver(x_lb, y_lb, u_lb, v_lb, 'Autoscale', 'off')
quiver(adcpdata(:,1), adcpdata(:,2), adcpdata(:,3), adcpdata(:,4), 'Autoscale',
'off')
axis equal
fontsize(gcf, scale=2.25)
title('Left Bank Camera vs. ADCP Data', 'FontSize', 24)
xlabel('Easting, m')
ylabel('Northing, m')
legend('Left bank', 'ADCP Data', 'FontSize', 24)
hold off

figure
hold on
quiver(x_lb, y_lb, u_lb, v_lb, 'autoscale', 'off')
quiver(x_cam1, y_cam1, u_cam1, v_cam1, 'autoScale', 'off')
fontsize(gcf, scale=2.25)
title('Left Bank Camera vs. Gaugehouse Camera', 'FontSize', 18)
legend('Left Bank Camera', 'Gaugehouse Camera', 'FontSize', 18)
```

```
xlabel('Easting, m')
ylabel('Northing, m')
axis equal
hold off

figure
hold on
quiver(x_rb, y_rb, u_rb, v_rb, 'autoscale', 'off')
quiver(x_cam1, y_cam1, u_cam1, v_cam1, 'autoScale', 'off')
fontsize(gcf, scale=2.25)
title('Right Bank Camera vs. Gaugehouse Camera', 'FontSize', 18)
legend('Right Bank Camera', 'Gaugehouse Camera', 'FontSize', 18)
xlabel('Easting, m')
ylabel('Northing, m')
axis equal
hold off

% figure
% hold on
% quiver(x_rb, y_rb, u_rb, v_rb, 'autoscale', 'off')
% quiver(drone_x, drone_y, drone_uvel, drone_vvel, 'autoscale', 'off')
% fontsize(gcf, scale=2.25)
% title('Right Bank Camera vs. Drone (059)', 'FontSize', 18)
% legend('Right Bank Camera', 'Drone', 'FontSize', 18)
% xlabel('Easting, m')
% ylabel('Northing, m')
% axis equal
% hold off
%
% figure
% hold on
% quiver(x_lb, y_lb, u_lb, v_lb, 'autoscale', 'off')
% quiver(drone_x, drone_y, drone_uvel, drone_vvel, 'autoscale', 'off')
% fontsize(gcf, scale=2.25)
% title('Left Bank Camera vs. Drone (059)', 'FontSize', 18)
% legend('Left Bank Camera', 'Drone', 'FontSize', 18)
% xlabel('Easting, m')
% ylabel('Northing, m')
% axis equal
% hold off
%
% figure
% hold on
% quiver(x_cam1, y_cam1, u_cam1, v_cam1, 'autoscale', 'off')
% quiver(drone_x, drone_y, drone_uvel, drone_vvel, 'autoscale', 'off')
% fontsize(gcf, scale=2.25)
```

```
 % title('Gaugehouse Camera vs. Drone (059)', 'FontSize', 18)
 % legend('Gaugehouse Camera', 'Drone', 'FontSize', 18)
 % xlabel('Easting, m')
 % ylabel('Northing, m')
 % axis equal
 % hold off
 %
 % figure
 % hold on
 % quiver(drone_x, drone_y, drone_uvel, drone_vvel, 'Autoscale', 'off')
 % quiver(adcpdata(:,1), adcpdata(:,2), adcpdata(:,3), adcpdata(:,4),
'Autoscale', 'off')
 % fontsize(gcf, scale=2.25)
 % axis equal
 % title('Drone (059) vs. ADCP Data', 'FontSize', 18)
 % xlabel('Easting, m')
 % ylabel('Northing, m')
 % legend('Drone', 'ADCP Data', 'FontSize', 18)
 % hold off

 figure
 hold on
 quiver(x_cam1, y_cam1, u_cam1, v_cam1, 'Autoscale', 'off')
 quiver(adcpdata(:,1), adcpdata(:,2), adcpdata(:,3), adcpdata(:,4), 'Autoscale',
'off')
 fontsize(gcf, scale=2.25)
 axis equal
 title('Gaugehouse Camera vs. ADCP Data', 'FontSize', 18)
 xlabel('Easting, m')
 ylabel('Northing, m')
 legend('Gaugehouse Camera', 'ADCP Data', 'FontSize', 18)
 hold off
```

Distance Made Good Code

```
 GCPS=readmatrix('DistanceMadeGoodGCPs.csv', 'Range', 'B2:E3') %load file with
both Real-World Coordinates & Camera coords

 GCPS_EN=GCPS(1:2,3:4)-GCPS(1,3:4)
 GCPS_xy=GCPS(1:2, 1:2)
 % GCP06x = 473025.074;
 % GCP06y = 5012162.136;
 GCP07x = 473043.418;
 GCP07y = 5012138.713;

 theta=[];
 theta=0:0.01:2*pi;
 for k=1:length(theta)
     Estar(k)=GCPS_xy(2,1).*cos(theta(k))-GCPS_xy(2,2).*sin(theta(k)); %is this
set up right?
     Nstar(k)=GCPS_xy(2,2).*cos(theta(k))+GCPS_xy(2,1).*sin(theta(k));
     diffE(k)=Estar(k)-GCPS_EN(2,1);
     diffN(k)=Nstar(k)-GCPS_EN(2,2);
 end
 x = readmatrix('004_distancemadegoodMarch6th2024.csv','Range', 'C3:C118');
 y = readmatrix('004_distancemadegoodMarch6th2024.csv','Range', 'D3:D118');

 %findangle.m found theta=5.395 rad to convert xy to EN for April 8th and
 %theta = 2.255 for March 6th 2024
 theta=2.255;
 %     vE_rb=u_rb.*cos(theta)-v_rb.*sin(theta); %rotate velocity vectors
 %     vN_rb=v_rb.*cos(theta)+u_rb.*sin(theta);
     Easting=x.*cos(theta)-y.*sin(theta); %rotate EN coordinates
     Northing=y.*cos(theta)+x.*sin(theta);

     EastingTranslated = Easting + GCP07x;
     NorthingTranslated = Northing + GCP07y;

     %test this by putting an xy gcp onto EN gcp
  % GCPS_xy(2,1).*cos(5.395)-GCPS_xy(2,2).*sin(5.395)=18.38
 %this is 4cm off (18.34)
```

ADCP Variance Code

```
 adcpdata_1 =
readmatrix('averagewatervelforsurf_toptwobins_20240515133807_corrected.csv');
 adcpdata_2 =
readmatrix('averagewatervelforsurf_toptwobins_20240515134023_corrected.csv');

 for m=1:length(adcpdata_1)
     for k=1:length(adcpdata_2)
         ADCPvariance(m,k)=sqrt((adcpdata_1(m,1)-
adcpdata_2(k,1))^2+(adcpdata_1(m,2)-adcpdata_2(k,2))^2);
     end
 end
         % smallestADCPvariance(m,k)=min(min(ADCPvariance(m,k)));
         for t=1:length(adcpdata_1)
              smallestADCPvariance = ADCPvariance(t,1);
              % smallestADCPdiff_1(t)=smallestADCPvariance;
            for s=1:length(adcpdata_2)

                if ADCPvariance(t,s)<=smallestADCPvariance
                    smallestADCPvariance = ADCPvariance(t,s);
                         smallestADCPdiff_1(t)=smallestADCPvariance;
                         smallestADCPdiff_2(t)=s;
                end
            end
         end

 %now find velocity difference for matched points for drone and ADCP
 for m=1:length(adcpdata_1)
     % for k=1:length(adcpdata_2)
         if smallestADCPdiff_1(m) > 0.5
            uveldiffADCP(m) = NaN;
            vveldiffADCP(m) = NaN;
         else
         uveldiffADCP(m)=adcpdata_1(m,3)-adcpdata_2(smallestADCPdiff_2(m),3);
         vveldiffADCP(m)=adcpdata_1(m,4)-adcpdata_2(smallestADCPdiff_2(m),4);
         end
 end

 ADCP = sqrt((uveldiffADCP).^2+(vveldiffADCP).^2);
 writematrix(ADCP, '3vs4.csv');
```